THE UNIVERSITY OF CHICAGO

MASS COMPOSITION STUDIES WITH THE PIERRE AUGER OBSERVATORY SURFACE DETECTOR

A DISSERTATION SUBMITTED TO
THE FACULTY OF THE DIVISION OF THE PHYSICAL SCIENCES
IN CANDIDACY FOR THE DEGREE OF
DOCTOR OF PHILOSOPHY

DEPARTMENT OF PHYSICS

BY
JOHN MICHAEL FARMER

CHICAGO, ILLINOIS
DECEMBER 2021

Table of Contents

List of Figures

List of Tables

Acknowledgments

If I were to list in detail everyone whose contributions have been invaluable to my work, this section would extend for several pages, so please excuse my brevity. My thanks extend to my close collaborators over the years: Max, Radomir, Edivaldo, Toshihiro, Justin, Antonio, and many other members of both the FAST and Auger collaborations for their engagement and feedback. The contributions of my advisor and mentors were particularly crucial to my success: I extend special thanks to my advisor Paolo, for his support and insight; to Radomir, for his detailed feedback; and to Toshihiro, for his advice and role in FAST. And of course, my gratitude extends to the graduate student community at the University of Chicago, including countless close friendship forged at coffeeside chats, office conversations, and conferences.

Finally, I give my thanks to Toshihiro, Duşan, Max, and the many others present during the assembly, commissioning, and first light of the FAST@TA prototypes, both for the many fond memories during those long, cold desert nights and for the timeless experiences during our many scenic collaboration meetings.

Abstract

The origin and nature of Ultra-High-Energy Cosmic Rays (UHECRs) are still open questions. UHECRs are extreme astrophysical phenomena, single particles with macroscopic energies exceeding 10^{18} eV. Their study is complicated by their extremely minute flux at the highest energies (less than 1 particle per square kilometer per century), where recent results hint at interesting new physics. The cheif architect of these advances is the Pierre Auger Observatory, a cosmic ray detector in Argentina that covers $3000\,\mathrm{km}^2$ with both a surface array of 1660 water-Cherenkov detectors (with 100% uptime) and a set of 27 fluorescence telescopes (with 15% uptime). Its hybrid design uses the smaller, robust data sample collected by the fluorescence telescopes to calibrate the energy of surface array's larger dataset.

UHECRs cannot be studied directly; instead, their properties must be inferred from the statistical properties of the enormous air showers they produce upon entering the upper atmosphere. UHECR mass composition is studied through the shower depth of maximum development X_{max}, which is measured directly by the fluorescence detector. In recent years, Auger has extended its hybrid paradigm to mass composition measurements, using the fluorescence detector data to calibrate composition measurements with the surface array. One such technique is the Δ method, which exploits the composition sensitivity of signal rise-times in the water-Cherenkov tanks. This work presents an update and extension of the Δ technique to higher zenith angles and updates several data-driven parameterizations and studies of systematic uncertainties essential for the technique.

The Fluorescence detector Array of Single-pixel Telescopes (FAST) is a design concept for

a next-generation UHECR observatory, aimed at extending current exposures by an order of magnitude with inexpensive fluorescence detectors targeting the highest energy cosmic rays. This work outlines the design, installation, and results of four prototype telescopes running at the two largest UHECR observatories.

Chapter 1

Background

For most modern physics experiments, cosmic rays are background events, noise to be filtered from the detector. The task of cosmic ray astrophysics is to use this omnipresent "background" to study the universe. As cosmic rays have been observed over twenty decades of energy, they are effective probes of a huge variety of phenomena, from the geophysical (decaying radioactive isotopes) to the astrophysical (pulsars and gamma ray bursts) to the most extreme nonthermal phenomena in the universe. Ultra-high-energy cosmic rays (UHECRs, cosmic rays with energies exceeding 10^{18} eV) are so extreme that their origins and nature remain among the most puzzling open questions in astrophysics. Modern UHECR observatories seek to demystify their chemical composition, sources, and acceleration mechanisms; these experiments face challenges due to the extremely minute flux at the highest energies, only a single particle per square kilometer per century. My focus in this thesis is combating this scarcity of data by expanding the scope of our current analyses and providing R&D on prototypes for next-generation detectors.

This chapter builds context for the work presented in this thesis. First, I will briefly explore the history of cosmic rays, beginning with their discovery in the early 20th century. Next, I will review the basics of UHECR physics, including theories about their production and acceleration mechanisms, plus simple models for air shower development. I will then

walk through a number of historically-significant UHECR experiments that led the field to its current state. After briefly reviewing the current state of the major open questions in the field, I will close by describing prospects for next-generation UHECR observatories.

1.1 Discovery of Cosmic Rays

The first experimental evidence of what would later be known as cosmic rays emerged in 1909. Theodor Wulf designed and built the electrometer, a device to measure energetic charged particles in the atmosphere, and performed measurements at the Eiffel Tower's base and peak. At these two sites, he noted a difference in rate [26], but these results were controversial and were not immediately attributed to atmospheric radiation: motivated by Becquerel's discovery of radioactivity in 1896 [27], contemporary physicists attributed all atmospheric ionization to radioactive decays. Domenico Pacinis 1911 paper documenting ionization rates inside bodies of water [28] challenged this notion by noting a sharp decrease in underwater radiation levels, hinting that its origin may be atmospheric. These papers circled cosmic rays, but provided no direct confirmation of their existence.

The discovery of cosmic rays proper is often attributed to Victor Hesss 1911 balloon experiment [29]. Equipped with three electrometers, Hesss balloon flew to approximately 5000 meters and noted a significant increase in ionization rate with altitude (Figure 1.1, [1]). To exclude a solar origin, Hess performed a follow-up experiment during a solar eclipse and noted no difference in the results. This discovery won Hess the 1936 Nobel Prize in Physics and attracted the interest of several pre-eminent physicists in the early 1900s. Robert Milikan mistakenly believed these particles were photons and named them "cosmic rays" in analogy to gamma rays. He also proposed a production mechanism: that they were byproducts of interstellar hydrogen fusion [30]. This was challenged by the experiments of Jacob Clay in 1927, whose measurements at various latitudes demonstrated that cosmic rays interact with the geomagnetic field and hence must be charged particles, not photons. Milikan's

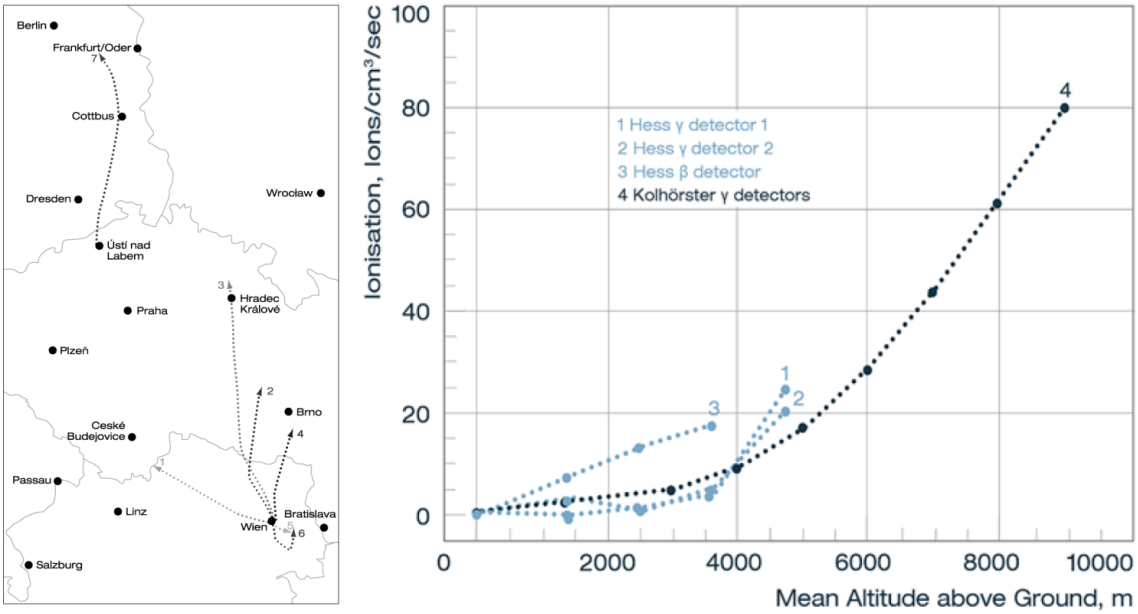

Figure 1.1: Left: diagram showing the flight paths of Hess's 1911 balloon experiment often attributed with the discovery of cosmic rays. Right: the measured ionization rates, with the Earth's background rate subtracted, of Hess's balloon flights superimposed with Kolhïster's 1914 follow-up, from [1].

hypothetical production mechanisms were contested in 1929 by Bothe and Kolhorster [31], who showed some cosmic ray particles were energetic enough to penetrate several centimeters of gold.

At this point, the literature suggested that cosmic rays were charged particles, but the precise details were unclear. Bruno Rossi proposed a method to measure the sign of their charge using the East-West effect, whereby interactions with the geomagnetic field cause differential intensities in the cosmic ray flux. In 1930, he determined that cosmic rays were positively charged [32]. Rossi also noted a larger-than-expected rate of coincidences between his detectors, the first evidence for Extensive Air Showers (EAS). These are showers of secondary particles produced by energetic primaries interacting with the atmosphere, and they are the mechanism by which we measure UHECRs today. Independently of Rossi, Pierre Auger et al. employed an array of Geiger-Muller detectors and experimentally verified the

existence of EAS events [33] [34].

In 1963, John Linsley reported the discovery of a cosmic ray primary with an energy of $1.2 \cdot 10^{20}$ eV (16 J) with the Volcano Ranch experiment [35], spurring renewed interest in Ultra-high-energy cosmic rays (UHECRs, cosmic rays with energies exceeding 10^{18} eV). Primaries with higher energies have since been observed, the most famous of which is the Oh-My-God particle observed by the Flys Eye experiment in Utah, with an energy of $3.2 \cdot 10^{20}$ eV. To this day, it remains the highest-energy particle ever seen by man.

In the half-century since, modern experiments have significantly advanced the hardware, systematics, and exposures of UHECR measurements. These will be covered in more depth in Section 1.3, but to understand the specific mechanics of UHECR detectors, we must first build an understanding of UHECR physics.

1.2 UHECR Physics

The three largest questions in UHECR physics are:

- Where are they produced?
- How are they accelerated?
- What is their chemical composition?

Modern observatories aim to significantly advance these questions by drawing inferences from the statistical properties of UHECRs. An understanding of air shower physics and common measurement techniques is essential for these measurements. This section will cover both pairs of topics: the physics of production and propagation, and the physics of shower development and measurement.

1.2.1 Production

The exact mechanisms for UHECR production are still unknown. Models are split into two categories: **bottom-up** and **top-down** models.

Top-down models [36, 37] propose that UHECRs originate from relic particles produced in the early universe. These may be particles with masses above $10^{18} - 10^{20}$ eV that decay directly into UHECRs, or lower-mass particles that decay into UHECRs with significant momenta. The properties of these particles are model-dependent, and there are no strict requirements on their sources. Although a detailed discussion of the physics behind these models is outside the scope of this thesis, they include theories such as neutrino interactions with a primordial neutrino background, known as Z-bursts [38, 39]; topological defects from spontaneous symmetry breaking of GUT theories, forming cosmic strings or monopoles [40, 41]; and super-heavy dark matter [42, 43, 44]. These models favor photons and neutrinos, so flux limits on these particles are effective discriminators between the two model categories. Results from the Pierre Auger collaboration suggest that top-down models do not dominate at high energies [45, 46, 47].

Bottom-up models involve the post-production acceleration of lower-energy particles to ultra-high energies. These mechanisms are discussed in the following subsection.

1.2.2 Propagation

The first mechanism for cosmic ray acceleration was proposed by Fermi [48]. Second-order Fermi acceleration details stochastic interactions with gas clouds in the interstellar medium, and since head-on collisions are more likely than head-tail ones, primary energy tends to increase in aggregate.

Consider Figure 1.2 [2]. Let v be the cloud velocity, E_1 and p_1 be the cosmic rays initial momentum and energy, and θ_1 by the incident angle with the cloud's velocity. Let S be the inertial frame of the laboratory and S' be that of the laboratory. In the cloud frame, the

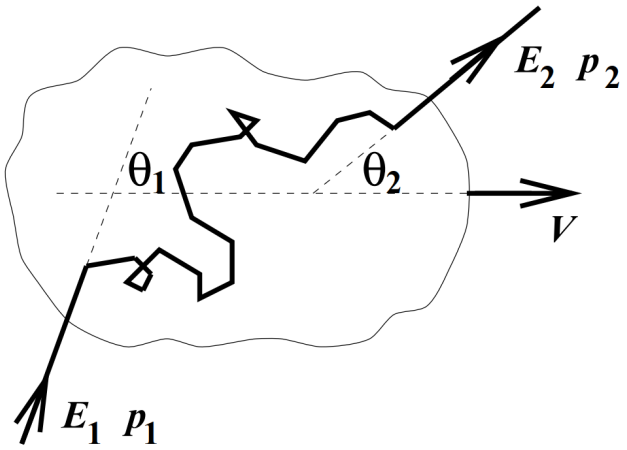

Figure 1.2: Diagram demonstrating the mechanism for second-order Fermi acceleration, where a particle scatters through an ISM cloud and experiences an energy change. From [2]

initial energy is

$$E_1' = \gamma E_1(1 - \beta \cos\theta_1), \tag{1.1}$$

where β is the relativistic velocity ratio and γ is the Lorentz factor. Inside the cloud, the particle scatters elastically a number of times and emerges with a new energy and momentum E_2 and p_2:

$$E_2 = \gamma E_2'(1 + \beta \cos\theta_2'). \tag{1.2}$$

The fractional change in energy is

$$\frac{\Delta E}{E} = \frac{1 - \beta\cos\theta_1 + \beta\cos\theta_2' - \beta^2\cos\theta_1\cos\theta_2'}{1 - \beta^2} - 1. \tag{1.3}$$

Since the direction is randomized, $\langle\cos\theta_2'\rangle = 0$. For an ultrarelativistic particles,

$$\langle\cos\theta_1\rangle = -\frac{\beta}{3}, \tag{1.4}$$

so that

$$f_{\mathrm{FA}} \equiv \frac{\langle \Delta E \rangle}{E} \approx \frac{4}{3}\beta^2, \tag{1.5}$$

assuming $\beta \ll 1$.

Diffusive Shock Acceleration (DSA) extends this to sequences of interactions experienced in strong astrophysical shocks, such as supernovae, that cause the accumulation of magnetic fields and ISM clouds. DSA is important because it can be used to estimate many important UHECR quantities, as we'll see. After interacting with an ISM cloud, the particle can be scattered back towards the shock and be re-injected back into ISM clouds. A similar analysis can be performed here, but the expectation values of the angles are different: $\langle \cos\theta_1 \rangle = -2/3$ and $\langle \cos\theta_2' \rangle = 2/3$, so

$$f_{\mathrm{DSA}} \equiv \frac{\langle \Delta E \rangle}{E} \approx \frac{4}{3}\beta. \tag{1.6}$$

The coefficient is identical to that of second-order Fermi acceleration, but the power on β is lower, yielding a much more effective acceleration mechanism. Conceptually, one can think of this as similar to second-order Fermi acceleration, but occuring inside a shock that is moving towards the particle, significantly increasing the likelihood of head-on collisions.

The DSA mechanism can be used to derive an estimate of the energy spectrum (the flux as a function of energy) by examining the escape probability P and the energy after n crossings, $E_n = E_0(1+f)^n$. This leads to a

$$\frac{\mathrm{d}N}{\mathrm{d}E} = \frac{N_0 P}{(1-P)E_0 \ln(1+f)} \frac{E_k}{E_0}^{\frac{\ln 1-P}{\ln 1+f}-1}. \tag{1.7}$$

The spectral index here evaluates to -2 for typical supernova shocks. Although this is significantly smaller than the observed index of -2.7 below the knee (see Section 1.4.1), this

is a promising starting point from such a remarkably simple model.

Finally, the DSA model can be used to examine possible UHECR sources through the Hillas criterion [3]. A source's energy is constrained by its Larmor radius

$$r_L = \frac{p_\perp}{ZeB}, \tag{1.8}$$

where $p_\perp$ is the perpendicular component of its momentum with respect to the magnetic field. As a particle's Larmor radius approaches the size of its accelerator, its escape probability rises sharply. The maximum acceleration energy of a source can be estimated by solving for the energy where these two distance scales match, a condition called the Hillas criterion. The maximum acceleration energy for DSA is hence

$$E_{\max} \leq \gamma ZeBr_L, \tag{1.9}$$

where γ is the shock's Lorentz factor (not the particle's). This can be used to estimate the theoretical acceleration limits for various astrophysical sources; this is referred to as a Hillas plot (Figure 1.3).

1.2.3 Shower Development

Upon entering the upper atmosphere, an UHECR interacts with the atmosphere to produce an enormous cascade of highly-energetic secondary particles. These secondaries subsequently interact again, producing further generations until ionization becomes the dominant dissipative process. This cascade generates a huge number of secondary particles—as many as 10^{10} for an event of $\sim 10^{19}$ eV—which is referred to collectively as an Extensive Air Shower (EAS). EAS footprints often span several kilometers at the ground level.

An UHECR shower consists of three components (Figure 1.4):

1. **The Electromagnetic Component:** consists of photons (γ) and electrons and

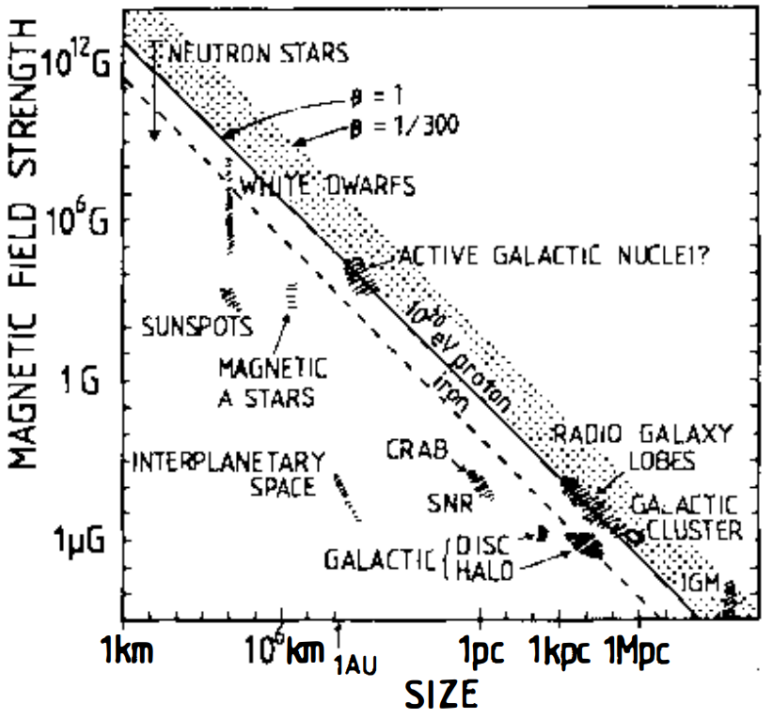

Figure 1.3: Hillas plot showing the theroetical acceleration limits for various sources under the assumption of diffusive shock acceleration [3].

positrons ($e^{\pm}$); originates from neutral pions (π^0), which decay into gamma rays and pair produce; $\mu^{\pm} \to e^{\pm}$ decays; and hadronic decays ($K^{\pm}/\pi^{\pm} \to \mu^{\pm}$, $K^0 \to \pi^0$ and their products, etc). Fluorescence and Cherenkov light also contribute. The dominant processes are

$$\pi^0 \to \gamma + \gamma \quad (\sim 99\%), \qquad \pi^0 \to \gamma + e^+ + e^- \quad (\sim 1\%) \tag{1.10}$$

$$\mu^- \to e^- + \bar{\nu}_e + \nu_\mu, \qquad \mu^+ \to e^+ + \nu_e + \bar{\nu}_\mu. \tag{1.11}$$

2. **The Muonic Component:** consists of muons ($\mu^{\pm}$) and neutrinos (ν_μ, $\bar{\nu}_\mu$); originates from charged pion ($\pi^{\pm}$) and kaon ($K^{\pm}$, K^0) decays. The dominant process is

$$\pi^+ \to \mu^+ + \nu_\mu, \qquad \pi^- \to \mu^- + \bar{\nu}_\mu \tag{1.12}$$

3. **The Hadronic Component:** consists of hadrons and nuclear fragments (p, n, $\pi^{\pm}$, $K^{\pm}$) that survive from the initial high-energy interactions through time dilation. The hadronic component is predominantly confined to near the shower core.

Of course, there exists some mixing between these components. Lower-energy muons typically decay into electrons and join the electromagnetic cascade prior to reaching ground level, while high-energy muons survive until the shower pancake's ground impact. Similarly, the various constituencies of the hadronic cascade may decay into muons, electrons, or photons. Nonetheless, for our purposes it suffices to think of these as three more-or-less discrete components. The highest-energy interactions predominantly produce hadrons and electromagnetic particles near the shower's core. These electromagnetic particles initiate the electromagnetic cascade, and as the hadronic shower develops, it in turn generates the muonic component through its atmospheric interactions and decay products.

For a more comprehensive understanding of air shower physics, we will briefly discuss

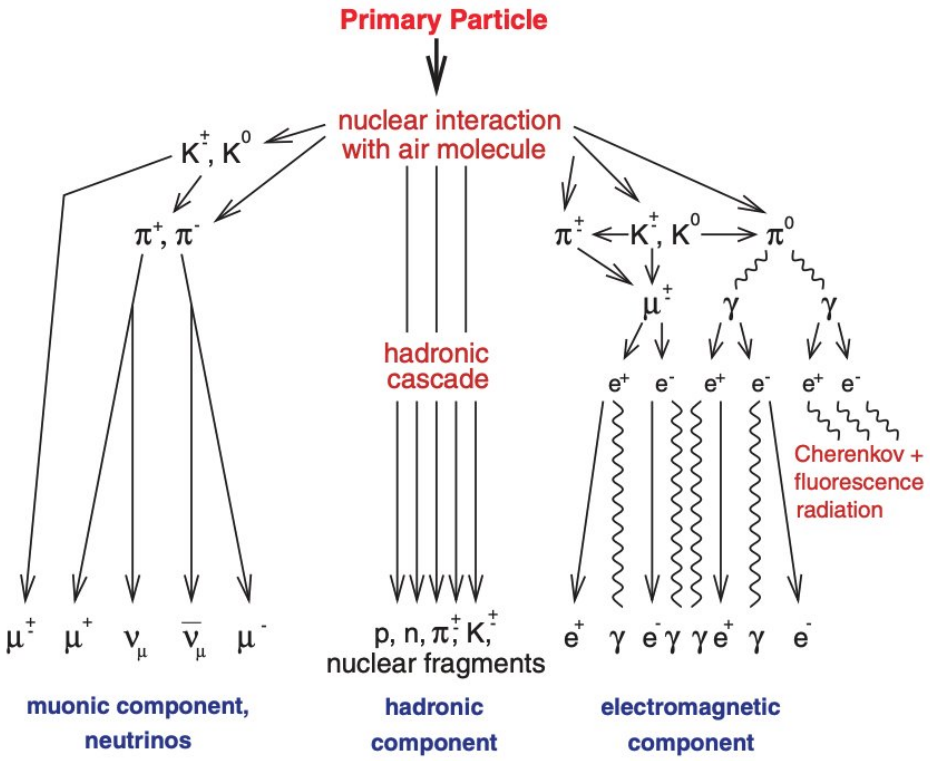

Figure 1.4: Diagram showing the three-component model for UHECR development.

simple models. Although showers may be modeled by sophisticated Monte Carlo simulation tools (such as CONEX [49], CORSIKA [50], and AIRES [51]), these naive models are important tools to understand the physics of shower development.

The Heitler Model

The traditional model for electromagnetic showers is the simple interative Heitler model, first developed in 1954 [52]. At each step, every electromagnetic particle (γ, $e_\pm$) travels one interaction length ($\lambda_r \ln 2$, where λ_r is the medium's radiation length) and interacts once. Photons interact with an atmospheric nucleus N via the process

$$\gamma + N \to N + e^+ + e^-. \tag{1.13}$$

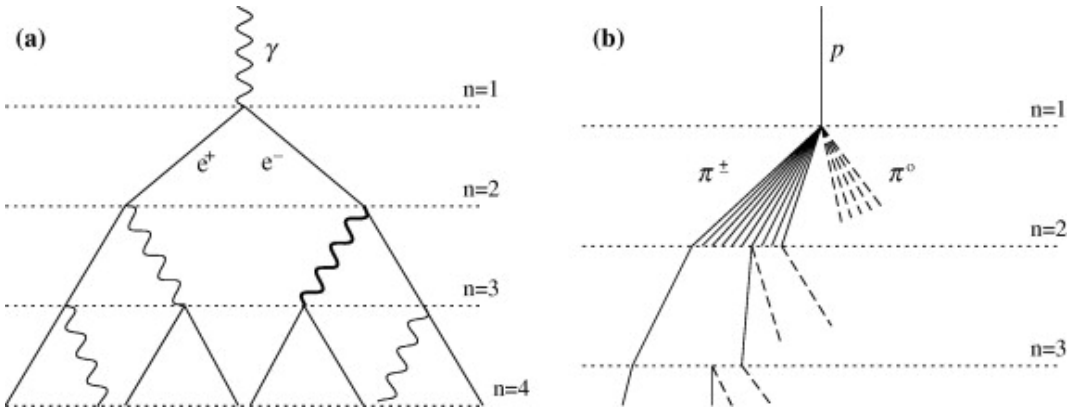

Figure 1.5: A schematic diagram of the Heitler model for development of the (a) electromagnetic and (b) hadronic components of an EAS. The dashed lines in the right figure represent neutral pions that decay into electromagnetic subshowers (not shown). Neither diagram is drawn to scale. Figure from [4].

This interaction results in energy loss of the particle and the production of an electron-positron pair. Electrons lose half their energy via Bremsstrahlung emission of one photon

$$e^{\pm} + N \to e^{\pm} + N + \gamma. \tag{1.14}$$

This continues until the energy of individual particles drops below the critical value where ionization overtakes Bremsstrahlung (approximately 80 MeV in air) as the primary energy-loss mechanism. This defines the maximum of the electromagnetic cascade.

Although these assumptions are extremely naive and neglect many subtleties about the number of particles and the distribution of energy among them, the resulting model makes several important (true) predictions:

- $X_{\max} \propto \ln E_0$;
- $N_{\max} \propto \ln E_0$;
- $X_{\max}$ evolves logarithmically with energy; and
- the elongation rate $D_{10} = \frac{\mathrm{d}X_{\max}}{\mathrm{d}\log E_0}$ is independent of energy.

Deriving these statements using the Heitler model is straightforward and requires only a few lines of algebra. After n radiation lengths in the electromagnetic cascade, there are $N_n = 2^n$ particles with energy E_0/N_n. The shower's maximum size is reached at

$$N_{\max} = \frac{E_0}{E_c}, \tag{1.15}$$

which implies a corresponding energy

$$E_c = \frac{E_0}{2^{n_{\max}}}, \tag{1.16}$$

from which we can find the number of radiation lengths at maximum

$$n_{\max} = \frac{\ln E_0/E_c}{\ln 2}. \tag{1.17}$$

The depth of maximum development is hence

$$X_{\max} = \lambda_r \ln(E_0/E_c), \tag{1.18}$$

which a corresponding elongation rate

$$\Lambda \equiv \frac{\mathrm{d}X_{\max}}{\mathrm{d}\log_{10} E_0} = 2.3\,\lambda \approx 85\,\mathrm{g\,cm^2\,dec^{-1}}. \tag{1.19}$$

The Matthews Extension

The Heitler model was extended to hadronic cascades by Matthews [4] by modeling charged pions in a similar fashion. (Neutral pions—approximately one third of the shower—are lost to the electromagnetic cascade.) Given a hadronic primary of energy E_0, after n steps, the

remaining energy is

$$E = \left(\frac{2}{3}\right)^n E_0. \tag{1.20}$$

We introduce a parameter $N_{\rm ch}$, the multiplicity of charged pions produced in the hadronic cascade. (Matthews assumes a constant $N_{\rm ch} = 10$ in his calculations). The number of pions at the nth step is then $N_\pi = N_{\rm ch}^n$, and so the energy per pion is

$$E_\pi = \frac{E_0}{((3/2)N_{\rm ch})^n}. \tag{1.21}$$

The neutral pions initiate electromagnetic subshowers of energy $E_0/(3N_{\rm ch})$. To estimate $X_{\rm max}$, we sum the initial interaction depth X_0 (which depends highly on the primary's mass) and the depth of these sub-showers:

$$X_{\rm max} = X_0 + \lambda_r \ln\left(\frac{E_0}{3N_{\rm ch}E_c}\right). \tag{1.22}$$

The elongation rate is

$$\Lambda = \Lambda^\gamma + X_0 - \lambda_r \ln(3N_{\rm ch}) = 58\,{\rm g\,cm^2\,dec^{-1}} \tag{1.23}$$

Because this model ignores second-generation neutral pions, it underestimates $X_{\rm max}$.

Higher-mass primaries (say, a particle of mass A) can be approximated by dividing the shower into A subshowers with equally-distributed energy. This is sometimes called the superposition model. Like the Heitler and Matthews models, it is physically naive (as it neglects the possibility for further nuclear interactions), but nonetheless makes important and useful predictions:

- Lighter showers develop more deeply than their heavier counterparts.

- The number of muons is higher for heavier primaries.
- The shower-to-shower fluctuations on $X_{\max}$ are smaller for heavier primaries.
- The elongation rate does not depend on primary mass.

A straightforward substitution reveals that

$$X^A_{\max} \propto \ln \frac{E_0}{A}. \tag{1.24}$$

Both the dependency upon E_0 and A are important. As with electromagnetic showers, $X_{\max}$ increases logarithmically with energy, but it decreases with higher primary mass. Hence we learn that the depth of maximum development $X_{\max}$ is composition-sensitive and can be used to infer the chemical composition of the shower's primary.

1.2.4 Measurement

UHECR primaries cannot be measured directly, and instead their properties must be inferred by measurement of the EAS they produce in the atmosphere. Two techniques are commonly used: sampling of the EAS secondaries at ground-level with particle detectors and direct observation of the shower's longitudinal atmospheric development.

Ground-level detectors employ grids of independent stations that sample the lateral particle density of the EAS. As there are no operational constraints from the night-sky background, they operate with close to 100% duty cycle. The spacing and elevation of the array determines its trigger efficiency, and there is a threshold E_{th} above which the array is fully efficient. This combination of 100% uptime and 100% efficiency is extremely attractive and trivializes the exposure calculation.

The timing information provided by sampling the shower pancake over several kilometers allows for precise reconstruction of the shower's axis. However, as surface detection techniques rely on post-LHC extrapolations of accelerator-tuned hadronic interaction models,

their energy resolution is poor. This can be alleviated with hybrid detection techniques that combine the SD and FD methods. This topic will be examined in more depth in Section 2.

Ground-level detectors are typically scintillator detectors or water-Cherenkov detectors. Scintillator detectors contain a scintillating material that absorbs and re-emits energy from passing particles, where it can be collected by photomultiplier tubes (PMTs). Water-Cherenkov detectors are tanks filled with purified water, which serves as a medium for the production of Cherenkov light from muons. They also measure energy deposited from pair production of electromagnetic particles. Scintillator detectors and water-Cherenkov detectors have different responses to electromagnetic and muonic components, and their projected volumes vary considerably as a function of incident zenith angle, so they have vastly different systematics and are difficult to directly compare. In recent years, radio detectors have also been explored. They measure radio emissions from interactions between shower particles and the geomagnetic field, and are highly effective at reconstructing the properties of inclined showers. For a deeper look into ground-level detectors, we will cover the Auger Surface Detector in depth in Section 2.1.

Fluorescence detectors measure the longitudinal development of showers as they traverse the atmosphere. They are typically telescopes with cameras consisting of PMT arrays mounted at the focal plane. These telescopes measure faint isotropically-emitted Nitrogen fluorescence light, and since the fluorescence yield of atmospheric Nitrogen can be measured precisely in the laboratory, they provide a robust calorimetric measurement of the shower energy. Further, by directly observing the longitudinal profile, one can straightforwardly measure the depth of maximum development $X_{\max}$. This is the point in shower development where ionization begins to dominate, and as we have seen in the previous subsection, it is our most useful estimator for particle composition. The precise details of this type of detector will be covered in exhaustive detail in Section 2.2, where we cover the Auger FD. Although FDs provide extremely robust measurements, their aperture is significantly more

complicated, and the requisite sensitivity of their cameras constrains their operations to clear moonless nights, yielding a duty cycle of $\sim 15\%$. Hence their datasets will be an order of magnitude smaller than that of an equivalent ground-level detector.

1.3 Significant UHECR Experiments

In this section, I will briefly cover some historically-significant UHECR experiments to provide context for the modern and future observatories studied in this thesis.

1.3.1 Volcano Ranch

Led by Bruno Rossi and John Linsley, the Volcano Ranch experiment in Albuquerque was the first modern UHECR detector [53]. It was the first experiment to reach several major milestones that are now standards of UHECR detectors, including observing UHECRs above $10^{20}\,\mathrm{eV}$ [35] and publishing measurements of the UHECR energy spectrum and anisotropy [5] (see Figure 1.6). It demonstrated the feasibility of using surface arrays as robust UHECR detectors. Originally featuring a triangular array of $3.3\,\mathrm{m}^2$ scintillator detectors with a $442\,\mathrm{m}$ spacing that covered $\sim 2\,\mathrm{km}^2$, it was later expanded with a larger spacing to cover $8\,\mathrm{km}^2$.

1.3.2 Haverah Park

The Haverah Park detector operated between 1967 and 1987 [54]. It is significant because it demonstrated the feasibility of water-Cherenkov detectors for UHECR detection. These detectors comprise the surface detector array of the largest current UHECR experiment, the Pierre Auger Observatory. Haverah Park originally consisted of four detector sites that each contained fifteen galvanized steel tanks filled with water, but was later extended with additional detectors, including scintillator detectors used for cross-calibration purposes with contemporary experiments.

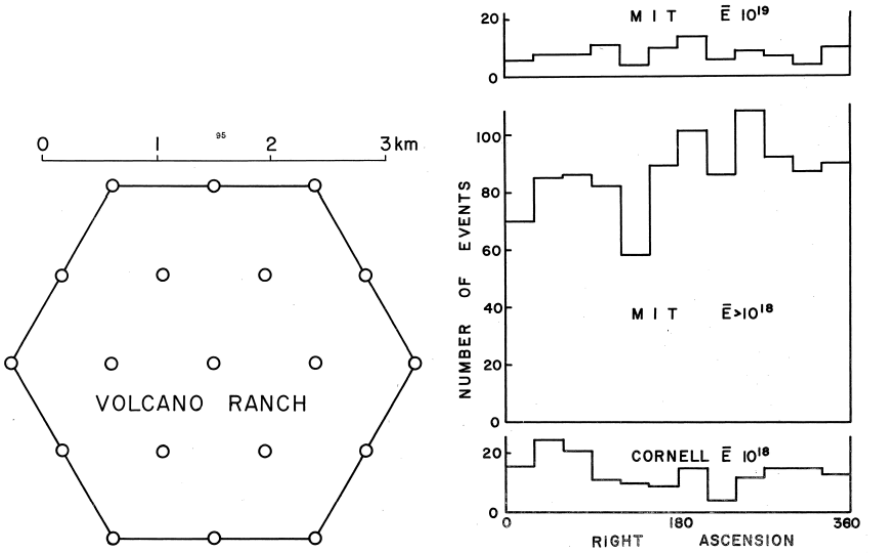

Figure 1.6: Left: diagram of the volcano ranch experiment, showing the triangular grid of 19 scintillator detectors. Right: arrival directions of 97 showers with 10^{19} eV average energy. Both figures from [5].

1.3.3 Fly's Eye

The Fly's Eye experiment was the first UHECR observatory to use fluorescence detection. It consisted of two detectors assembled in 1981 and 1986 at Dugway Proving Grounds, a U.S. Army site in Utah. The first detector featured 67 drums containing an array of 12-14 PMTs at the focal plane of a 1.5 m mirror in a steel drum (see Figure 1.7), and it covered the entire sky. The second detector was smaller and viewed only a portion of the night sky, but it enabled the stereoscopic measurement of UHECRs, significantly improving the data quality. Stereoscopic FD air shower measurements are to this day considered extremely robust.

Fly's Eye demonstrated the power of the fluorescence detection technique for understanding UHECR composition by directly measuring $X_{\max}$. It also observed the highest-energy UHECR to this day, often dubbed the "Oh-My-God" particle, at $3.2 \cdot 10^{10}$ eV [55].

Figure 1.7: Aerial view of the Fly's Eye 1 detector. Each of the steel drums contains a mirror and an array of PMTs [6].

1.3.4 HiRes

The High Resolution Fly's Eye (HiRes) experiment was a successor to Fly's Eye designed to improve its exposure at the highest energies by an order of magnitude and improve its signal-to-noise ratio by a factor of seven [56]. Operating from 1998 to 2006, it consisted of two FD stations (HiRes-I and HiRes-II) located 12.6 km apart at the Fly's Eye site. The HiRes experiment provided the first experimental evidence of the GZK effect at $6 \cdot 10^{19}$ eV [7], a flux suppression at the highest energies due to interactions with the cosmic microwave background radiation (Figure 1.8). This will be discussed in more detail in Section 1.4.1, where we cover major features of the UHECR energy spectrum.

1.3.5 AGASA

The Akeno Giant Air-Shower Array (AGASA) was the world's largest UHECR detector during its operation from 1990 to 2004 [57]. It was a Japanese experiment near Akeno that covered 100 km^2 with 111 2.2 m^2 scintillator detectors. It is particularly notable for observing a number of events above the GZK threshold and for publishing energy spectra

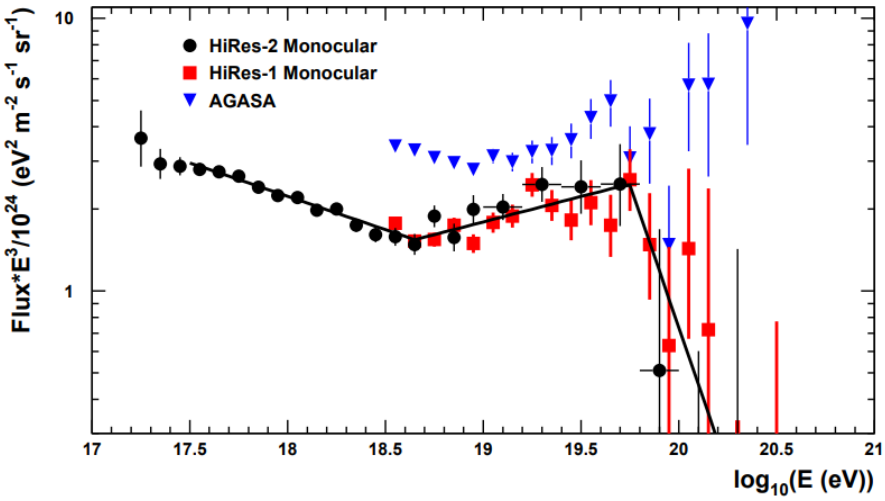

Figure 1.8: Energy spectrum reported by HiRes and AGASA. The HiRes monocular observations exihibit flux suppression at the highest energies, indicative of the GZK effect [7].

inconsistent with contemporary experiments [58]. The tension between HiRes and AGASA results provided compelling motivation for the construction of current-generation UHECR observatories.

1.3.6 Telescope Array

The Telescope Array experiment [59] is the world's second-largest UHECR observatory, superseded only by the Pierre Auger Observatory (which will be explored extensively in Section 2). Its location in the Northern hemisphere (near Delta, Utah) allows it to cover portions of the sky that Auger, which is located in the Southern hemisphere, cannot. Together, these experiments provide full-sky UHECR measurements with a shared declination band, useful for joint anisotropy studies.

The Telescope Array experiment is a hybrid detector that employs a square grid of surface detectors (507 3 m^2 scintillator stations) [60] overlooked by 38 FD telescopes [61], which employ a 3.3 m spherical mirror and a camera with 256 PMTs. The experiment covers approximately 700 km^2.

The TA experiment has been upgraded with a low-energy extension called the TA Low-energy Extension (TALE) [62], comprising of new SD stations with varying spacing and higher-elevation FD telescopes aimed at lower-energy events, and is currently undergoing an upgrade called TAx4 [8] aimed at expanding the array's size to approximately $3000\,\mathrm{km}^2$, which would rival that of Auger's. A diagram of the experiment, showing both the original array and the TAx4 upgrade, is shown in Figure 1.9.

1.3.7 The Pierre Auger Observatory

The Pierre Auger Observatory [63] is the world's largest cosmic ray detector. It is the subject of the analysis work performed in this thesis and will be covered in exhaustive detail in Chapter 2.

1.4 State of the Field

The three major studies published by UHECR observatories are:

- The Energy Spectrum
- Anisotropies (eg Arrival Directions)
- Mass Composition

This section will describe these measurements and briefly assess the state of the field in each.

1.4.1 Spectrum

The flux as a function of energy (the differential energy spectrum) is generally a power law with an index of roughly $\gamma = -2.7$. It is written as

$$\frac{\mathrm{d}N}{\mathrm{d}E} \propto E^{-\gamma}. \tag{1.25}$$

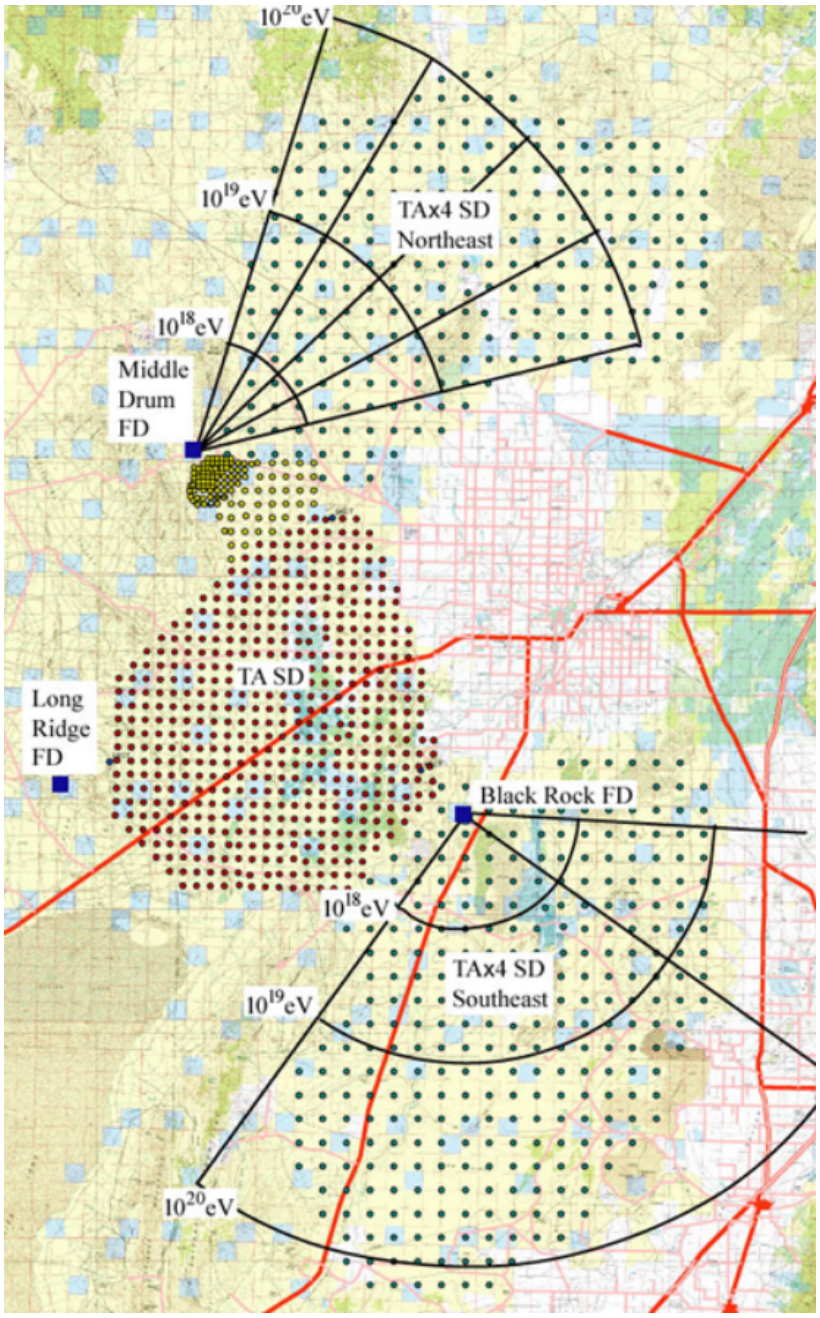

Figure 1.9: Diagram of the TA experiment, showing the original array and the TAx4 extension. [8].

Deviations and breaks in the spectrum encode important information about cosmic ray sources and production mechanisms [64]. Because the spectrum enfolds so much information, it is the topic of intense discussion and analysis. I will only briefly summarize the major features of the spectrum and their implications here, with a focus on features at the highest energies (since we are principally concerned with UHECRs here):

- **The Knee** at $\sim 3 \cdot 10^{15}\,\text{eV}$. Here the spectral index abruptly shifts to ~ 3.1. It is commonly interpreted as the result of either source depletion or galactic protons escaping the galaxy. Galactic sources are insufficient to accelerate cosmic rays significantly above $10^{15}\,\text{eV}$, and the proton's smaller Larmor radius enables it to escape the galaxy at approximately these same energies (via the Hillas criterion).

- **The Second Knee** at $\sim 4 \cdot 10^{17}\,\text{eV}$, a steeping of the spectrum that is typically interpreted as the result of a fall-off of heavier elements.

- **The Ankle** at $\sim 5 \cdot 10^{18}\,\text{eV}$, an abrupt flattening interpreted as the transition between galactic and extragalactic sources.

- **The Flux Suppression** at $\sim 6 \cdot 10^{19}\,\text{eV}$. First measured by the High Resolution Fly's Eye (HiRes) experiment [7], this is considered to be the result of either source depletion or the Greisen-Zatsepin-Kuzmin effect [65, 66], which proposes a theoretical limit to the cosmic ray spectrum due to pion production from scattering off the cosmic microwave background radiation photons through the Δ resonance:

$$\gamma_{\text{CMB}} + p \rightarrow \Delta^{+} \rightarrow p + \pi^{0} (\text{or } n + \pi^{+}). \tag{1.26}$$

  It follows that extremely high energy cosmic rays ($E > 10^{20}\,\text{eV}$) must be produced locally (within $\sim 100\,\text{Mpc}$).

For context, the Pierre Auger Observatory's 750 m and 1500 m arrays reach full trigger ef-

ficiency at $3 \cdot 10^{17}$ eV and $3 \cdot 10^{18}$ eV, respectively, which roughly coincides with the second knee and the ankle. The exact origins of these features are hotly debated, as it is unclear when the transition between galactic and extragalactic sources occurs, and this shift is not accompanied by a corresponding anisotropy in arrival directions. More precise interpretations of the spectral features require improvements in our understandings of production and acceleration mechanisms, anisotropies, and UHECR mass composition, as the spectrum measurement inherently encapsulates all these phenomena.

Because the spectral index is high, UHECR flux diminishes rapidly with increasing energy. This is the source UHECR observatories' greatest experimental challenge: collecting sufficient data at ultra-high energies to perform meaningful studies. Above the flux suppression, the typical flux of particles is approximately one per square kilometer per century, which necessitates instrumenting a huge area and collecting unprecedented exposures to draw inferences at high energies.

The most recent measurements from the Pierre Auger Observatory and the Telescope Array Experiment above $\sim 10^{18}$ eV are shown in Figure 1.10. The disagreement between these two experiments post-suppression (even in their common declination band and after removing events from the TA "hotspot", see Section 1.4.2) is a subject of active deliberation.

1.4.2 Anisotropy

Although UHECRs are charged and experience significant deflections in the galactic and extragalactic magnetic fields (unlike neutrinos, for instance), anistropies in their arrival directions are still useful source probes. An important quantity for anisotropy studies is the rigidity

$$R \equiv r_L B c = \frac{E}{Ze}, \tag{1.27}$$

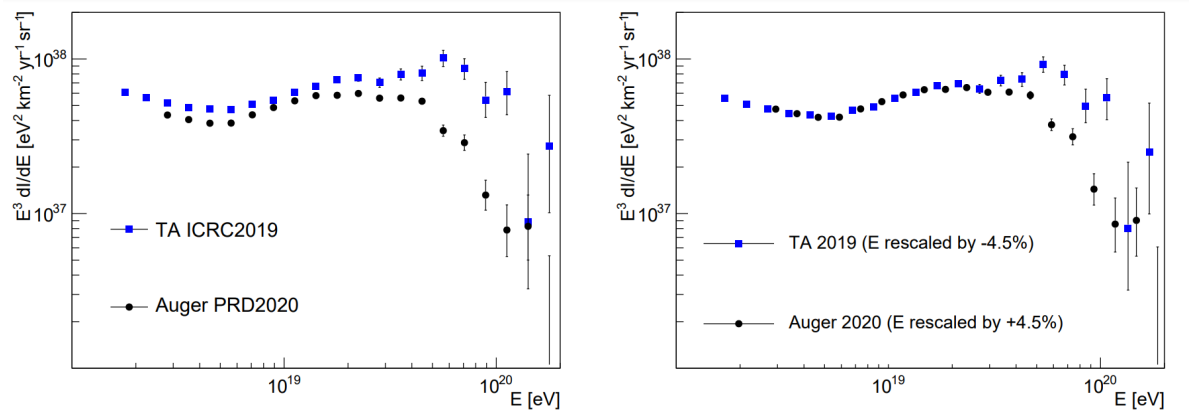

Figure 1.10: Energy spectrum reported by Auger (blue) and the Telescope Array Experiment (red), from [9].

where E is the particle energy and Z is its charge. The rigidity describes the resistance of a particle to magnetic deflections, and as it depends also on the primary charge, anisotropy studies are implicitly coupled with mass composition studies.

This field has greatly evolved in recent years. Anisotropy studies can be broadly broken into three categories:

- Large-scale anisotropy analyses that consider the entire sky. This includes techniques such as the Rayleigh analysis (unbinned Fourier analysis) and analysis of spherical harmonic amplitudes on the sky (with tools like HEALPIX).

- Local significance searches (typically using Li-Ma statistics) that search for overdensities.

- Small-and-intermediate-scale analyses that correlate observations with source catalogues.

Below is a brief overview of results using each of these techniques:

- In 2017, using Rayleigh analysis, the Pierre Auger Observatory has reported the discovery of a large-scale dipole in the arrival directions of UHECRs above 8 EeV with a significance of over 5σ (Figure 1.11) [67, 68]. With an amplitude of $\approx$6.5 % and a

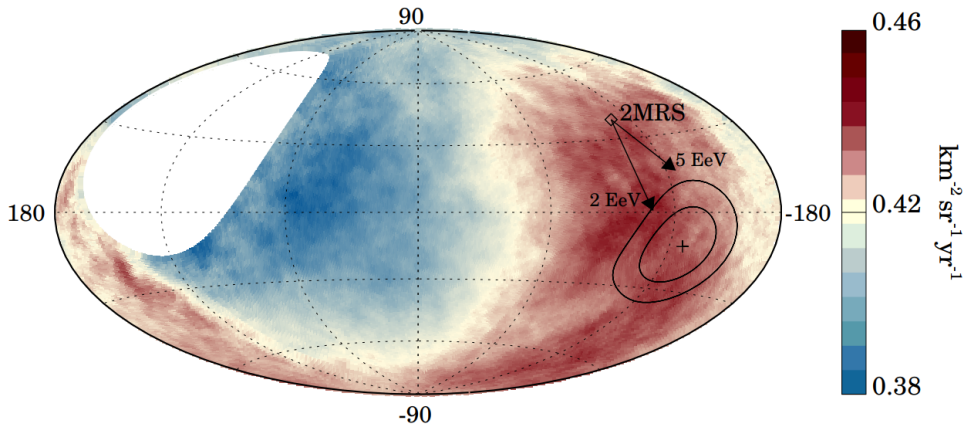

Figure 1.11: Flux map in galactic coordinates showing the large-scale dipole in arrival directions observed by Auger above $8 \cdot 10^{18}$ eV [10]. Arrows show the expected deflections from a model of the galactic magnetic field.

direction of $\alpha = 100 \pm 10$ degrees and $\delta = -24^{+12}_{-13}$ degrees, it suggests an extragalactic origin for these highest-energy cosmic rays. Further studies have confirmed the stability of this anisotropy and its growing amplitude with energy [69, 70].

- The Telescope Array experiment reported the discovery of a hotspot above 57 EeV in 2014, centered at $\alpha = 147°$ and $\delta = 43°$ with a significance of 3.4σ using oversampling and Li-Ma statistics [11] (see Figure 1.12). Further studies have tracked the continuing evolution of its statistics [71].

- At intermediate scales, the Pierre Auger Observatory reported the existence of a correlation with a flux pattern derived from starburst galaxies in 2018 (Figure 1.13), which was later extended and shown to have increased in significance from $4\,\sigma$ to $4.5\,\sigma$ [12, 70]. Auger also reported a $3.9\,\sigma$ correlation with Centaurus A for UHECRs above 37 EeV, using a 28° search radius [70].

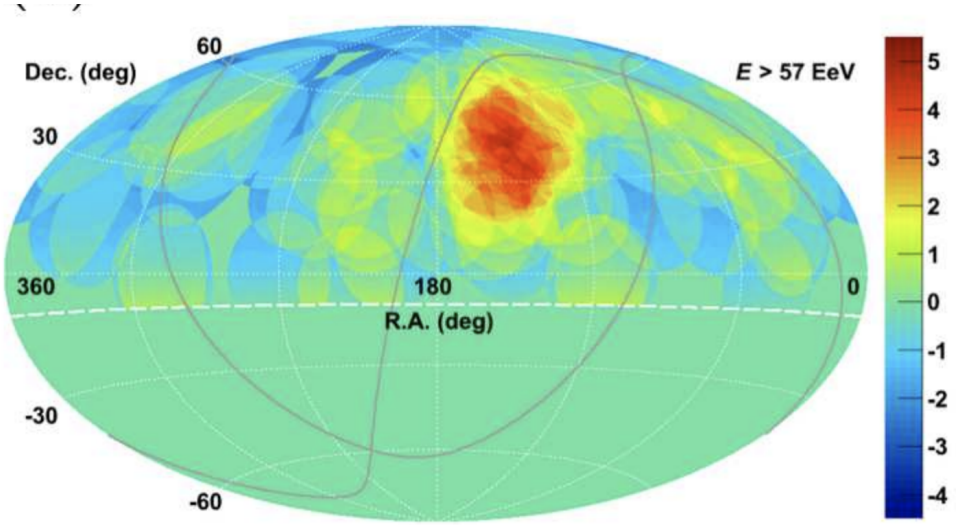

Figure 1.12: Significance map reported by the Telescope Array collaboration in [11], showing the five-sigma overdensity "hotspot."

1.4.3 Composition

Because UHECR primaries may only be measured indirectly through their EAs secondaries, direct determination of the parent particle is not possible. Instead, we measure quantities that are composition-sensitive and use our knowledge of their statistical properties to make inferences on primary masses.

For composition studies, we use the depth of maximum development, $X_{\max}$, which can be directly measured with fluorescence detectors. $X_{\max}$ depends strongly on the primary mass (Figure 1.14), but this dependence is complicated by shower-to-shower fluctuations that make discriminating the mass of single events impossible. The Heitler models (correctly) imply that these shower-to-shower fluctuations decrease with increasing primary mass. Hence we have two quantities we can use to make inferences on mass composition: $\langle X_{\max} \rangle$ and $\sigma(X_{\max})$.

To interpret these results, we need models for how showers of these energies develop. A number of hadronic interaction models fulfill this purpose. The most modern models are EPOS-LHC [72], Sibyll 2.3 [73, 74], and QGSJetII-04 [75, 76], all of which contain significant differences and implications. For composition studies, comparisons are typically made using

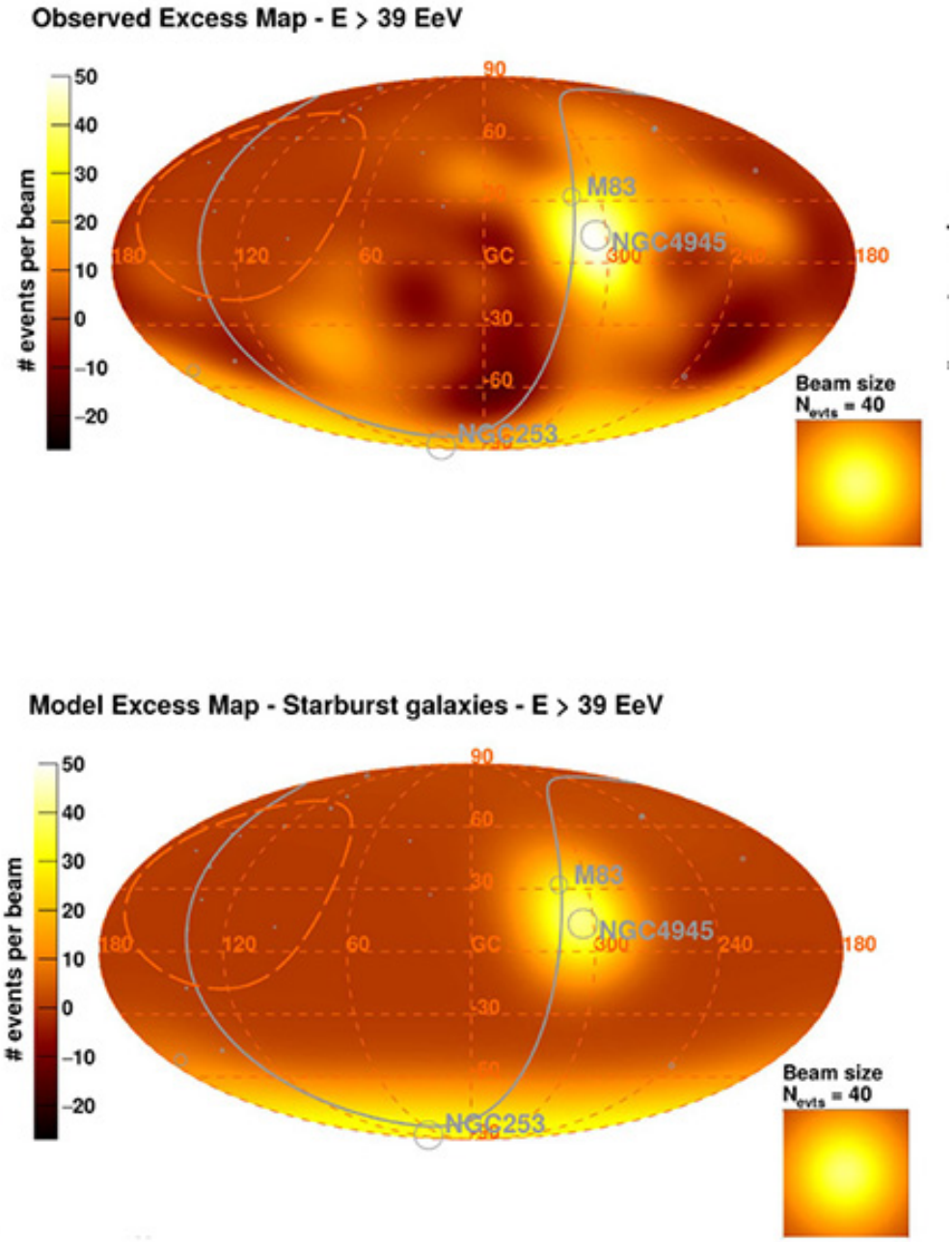

Figure 1.13: Top: measured background-subtracted flux map reported in [12]. Bottom: model flux map produced from Starburst galaxies.

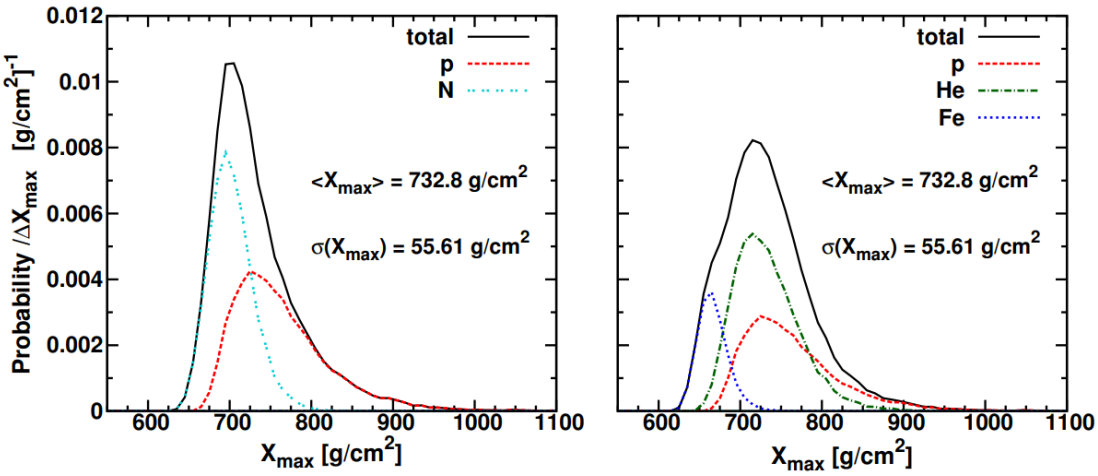

Figure 1.14: Longitudinal profiles generated with with the EPOS-LHC hadronic interaction model, showing how the dependence of $\langle X_{\max} \rangle$ and $\sigma(X_{\max})$ upon UHECR primary. This study involved 10^4 events of each primary in the energy range $10^{18.2} - 10^{18.3}$ [13].

all of these models. The Auger FD measurements of both these quantities are shown in Figure 1.15 [14]. They suggest an increasing mass above $3 \cdot 10^{18}$ eV, which could suggest proton extinction or source depletion.

In recent years a number of techniques have been developed to use SD information to draw inferences about mass composition. These include the Δ method [15] (which will be covered extensively in Chapter 3) and recent deep-learning based reconstructions of composition and muon content [77]. These emerging fields are promising because they unlock significantly larger datasts for composition studies, allowing robust science at higher energies. The elongation rate as reported in 2017 by the Δ method is shown in Figure 1.16, demonstrating remarkable agreement with FD measurements over their common energy range.

1.4.4 Joint Fits

Joint fits combine information from multiple of the above categories to improve their sensitivity. Joint fits of energy spectrum and composition track the evolution of a mixed composition with energy, providing valuable insight into the astrophysical origins of UHECRs. A

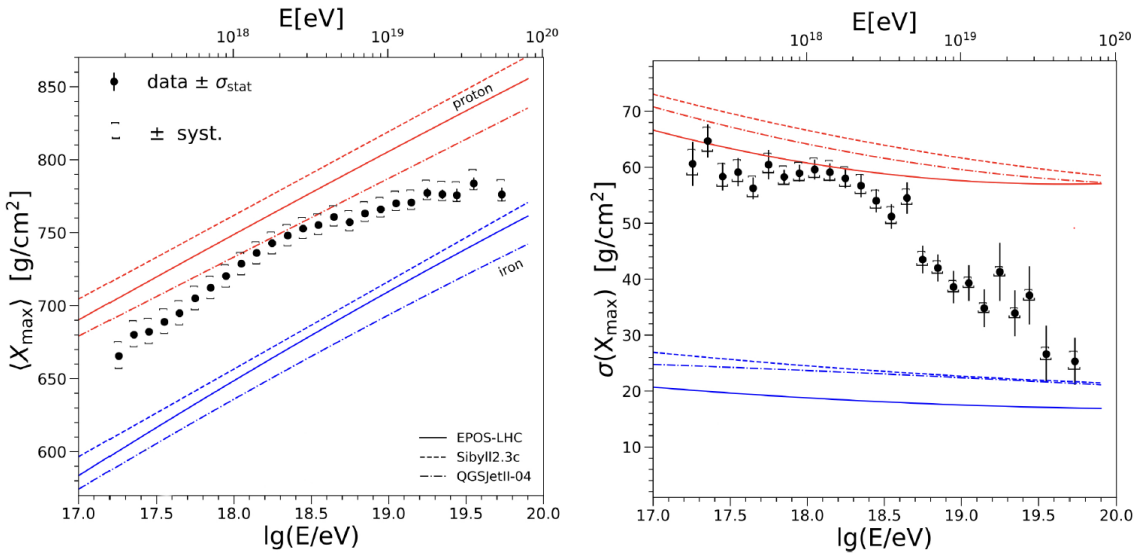

Figure 1.15: $\langle X_{\max} \rangle$ (left) and $\sigma(X_{\max})$ (right) from the Pierre Auger Observatory [14].

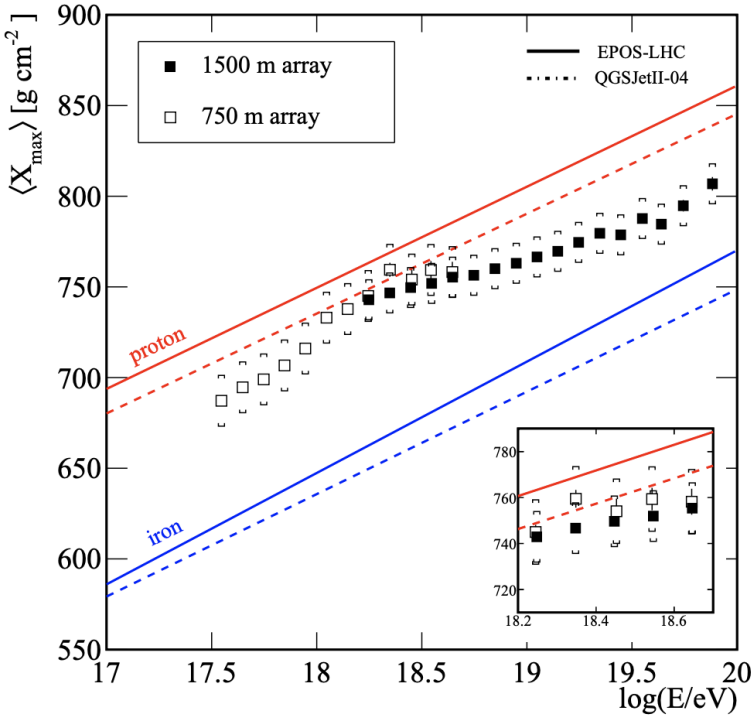

Figure 1.16: The elongation rate as reported by the Δ method in 2017 [15]. Additional information about the Δ technique is contained in Chapter 3.

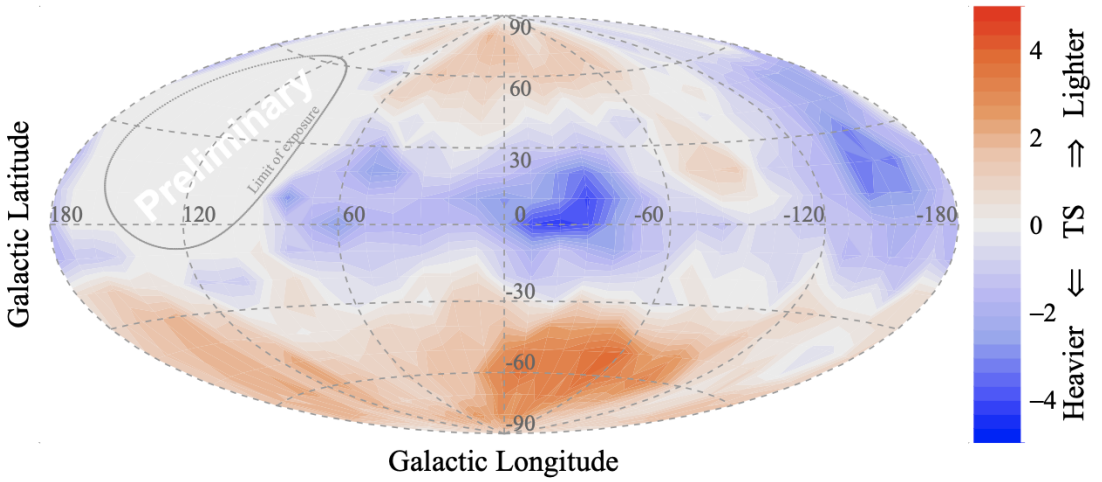

Figure 1.17: The galactic plane composition anisotropy observed above $10^{18.7}$ eV by the Pierre Auger Observatory hybrid data [16].

currently-emerging field is that of composition anisotropy, which combines information about the arrival directions and mass composition to study sources. The Pierre Auger Observatory recently reported indications of a mass-dependent anisotropy observed in alignment with the galactic plane [16] above $10^{18.7}$eV, shown in Figure 1.17. Statistics for these studies are limited due to their dependence on FD measurements of composition; however, the development of hybrid calibration methods for determining X_{max} with surface detector data, such as the work discussed in this thesis, could potentially unlock the ability to perform these studies in much greater detail.

1.5 Next-Generation Observatories

The steepness of the energy spectrum requires that future experiments drastically improve their exposures to expand upon current knowledge. Current-generation ground-based arrays (Auger and the TAx4 upgrade) cover $\sim 3000\,\mathrm{km}^2$, and building significantly-larger arrays without new design paradigms is likely unfeasible. But higher-energy events have larger footprints and brighter fluorescence signals than their lower-energy counterparts, so these

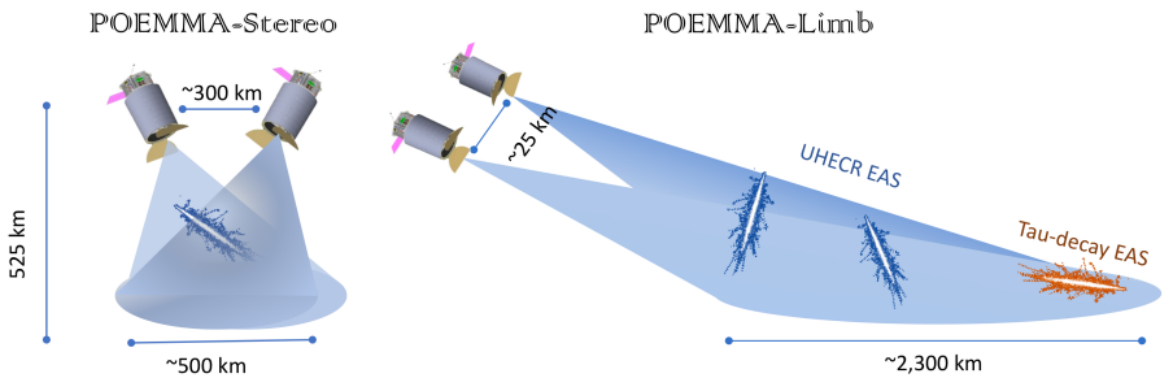

Figure 1.18: POEMMA-Stereo and POEMMA-Limb configurations [17].

increasing demands on exposure are somewhat mitigated by less-strict requirements on the resolution and signal-to-noise. There is less need to focus on the spectral regions that are already well-understood when many physics possibilities lie around and above the regime of flux suppression.

There are two categories of future observatories under consideration: ground-based observatories and satellite experiments.

1.5.1 POEMMA

The Probe of Extreme Multi-Messenger Astrophysics (POEMMA) [17], shown in Figure 1.18, is a prospective satellite-based experiment aimed at detecting UHECRs and cosmic neutrinos. It is an air fluorescence and Cherenkov detector consisting of two identical satellites with $6\,\mathrm{m}^2$ wide-angle Schmidt telescopes. It uses two sensor types: multi-anode photomultiplier tubes (MAPMTS) for fluorescence light and silicon photomultipliers (SiPMs) for Cherenkov light (see Figure 1.19).

These satellites will fly in one of two formations: POEMMA-Stereo or POEMMA-limb, each with different resolutions and reconstruction capabilities. It is projected to be a NASA Astrophysics Probe-class mission that will span five years, and its projected exposure, shown in Figure 1.20, will improve on that of current-generation observatories by two orders of

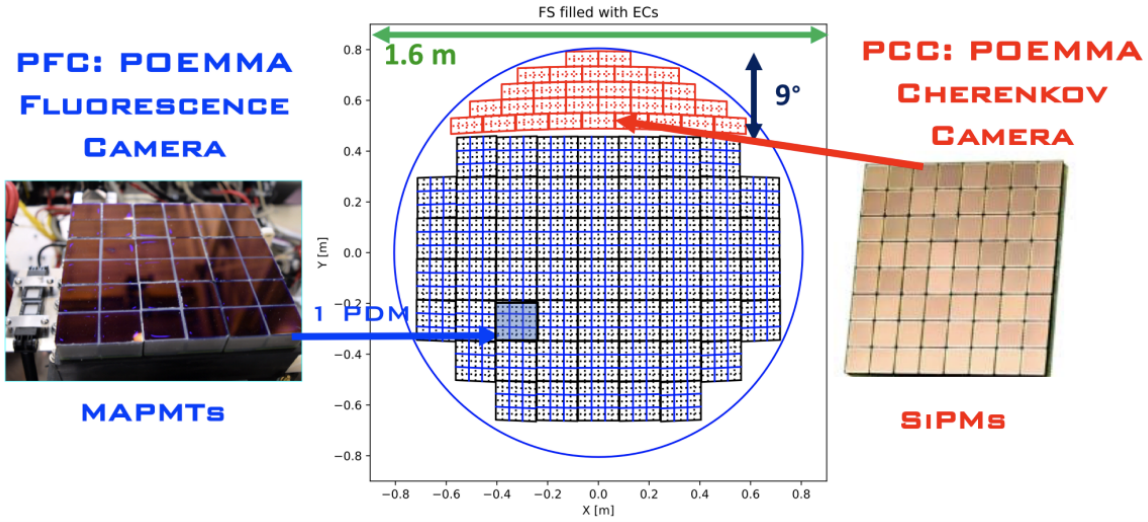

Figure 1.19: Layout of the sensors on the POEMMA "camera," consisting of a tiles containing two sensor types.

magnitude.

1.5.2 FAST

The Fluorescence detector Array of Single-pixel Telescopes (FAST) is a next-generation ground-based detector concept aimed at the highest-energy cosmic rays. It proposes a grid of FD stations using extremely coarse pixels: four PMTs span the same field-of-view that Auger observes with 440, resulting in much higher night-sky background. This significantly reduces both its signal-to-noise ratio and its cost. These relatively-inexpensive FD stations could theoretically be used to create a surface array of FD telescopes rather than SD stations. A detailed discussion of this concept, including the development and operation of several prototypes at the Auger and TA sites, comprises a major portion of this thesis, and further discussion of this venture will be reserved for Section 4.

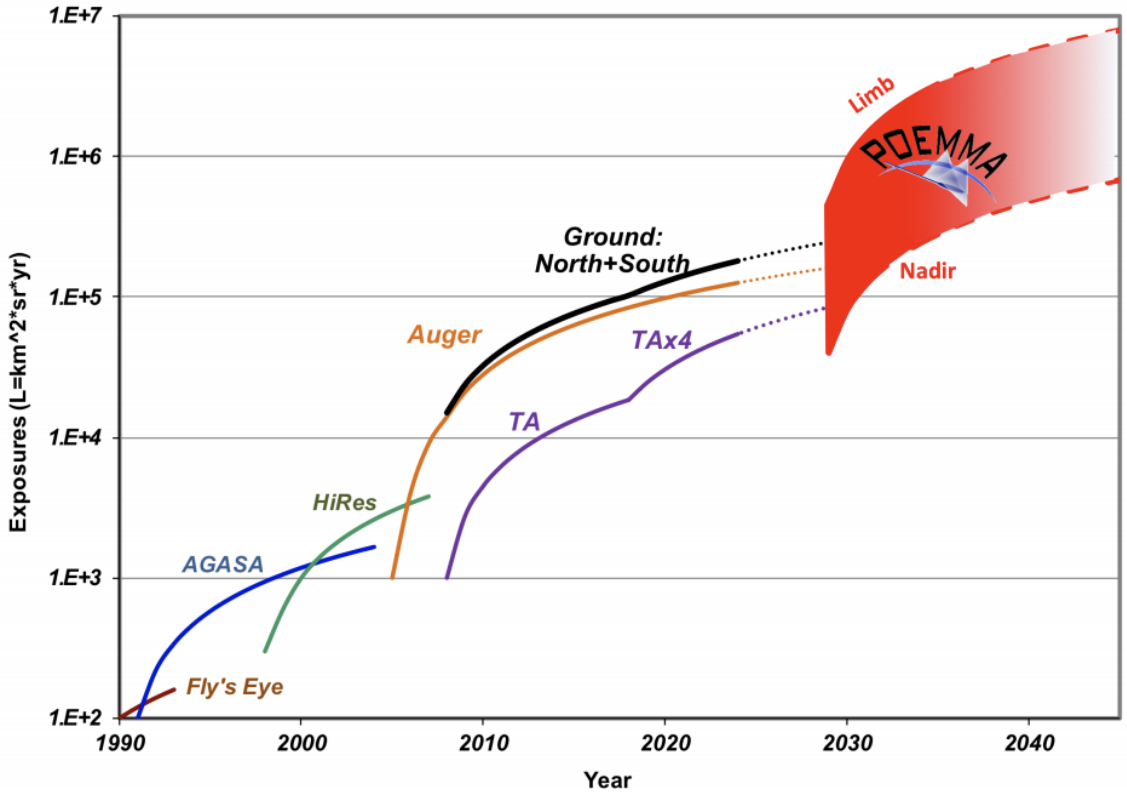

Figure 1.20: Projected exposure of POEMMA in both Limb and Stereo configurations [17].

Chapter 2

The Pierre Auger Observatory

The Pierre Auger Observatory (Auger) is the largest cosmic ray detector in the world. Located near the town of Malargüe in the province of Mendoza, Argentina, it covers approximately 3000 km^2 and targets UHECR events above approximately 10^{17} eV. First conceived by Jim Cronin and Alan Watson, it has been in operation since 2005 and has been completed since 2008 (but has since undergone a number of significant upgrades). In its decade and a half of operation, it has significantly expanded our understanding of UHECRs, with measurements of anistropy, energy spectrum, and composition that exceed the quality of any other instrument in the field's history.

The Pierre Auger Observatory is a hybrid detector that combines the two paradigms for UHECR measurement. A diagram of the experiment is shown in Figure 2.1. It features a surface detector (SD) array of 1660 water-Cherenkov detectors deployed in a triangular grid with a 1500 m spacing that operates at nearly a 100% duty cycle. This surface array is overlooked by a set of 27 fluorescence telescopes comprising the Auger fluorescence detector. These telescopes are situated at four elevated sites atop the Observatory's perimeter, and they operate at a $\sim$15% duty cycle. These two detectors function symbiotically and produce an extremely robust set of hybrid data—events observed by both the FD and SD—that can be used for cross-checks and calibrations. For instance: reconstructing events with solely the

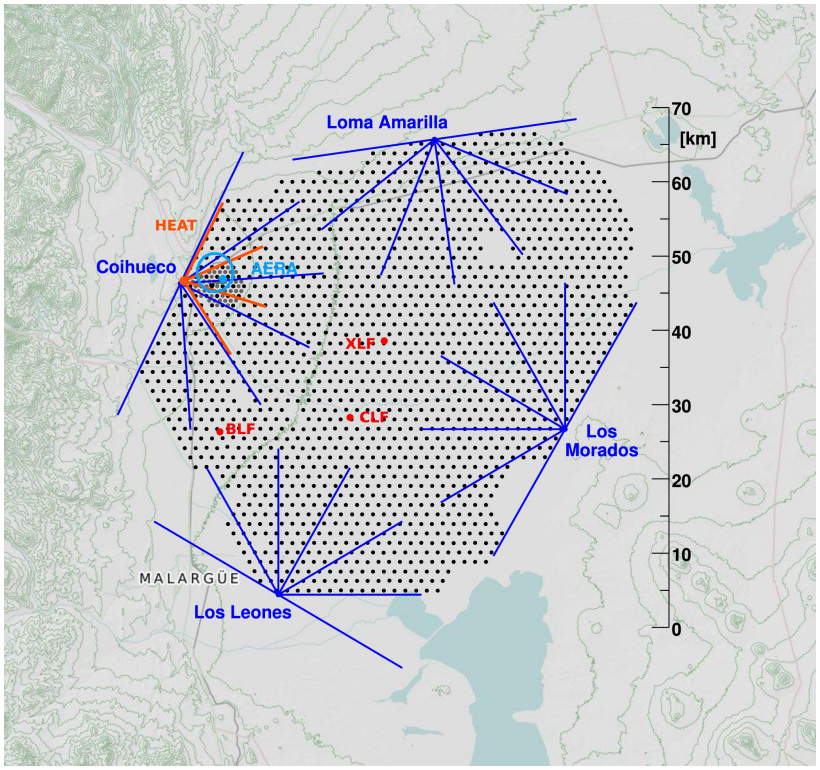

Figure 2.1: Diagram showing the layout of the Pierre Auger Observatory. Each of the dots represents one of the surface detector stations. The four named fluorescence detector stations are named in blue; the lines describe the field-of-view of each telescope. The HEAT telescopes and infill array are shown near the Coihueco FD station.

SD relies on extrapolasting hadronic interaction models to post-LHC thresholds, but this can be alleviated by performing an energy calibration using hybrid events that relies on the FD's more robust calorimetric energy measurement. A diagram showing this hybrid paradigm is shown in Figure 2.2, and more details about this process will be given in Section 2.4.

In this chapter, we will first discuss the hardware of the Observatory in Section 2.1, Section 2.2, and Section 2.3, where we discuss the SD, FD, and atmospheric monitoring equipment. Then we will discuss our analysis and reconstruction methods in Section 2.4. Finally, we will close by outlining the in-progress upgrade to the Pierre Auger Observatory, AugerPrime, in Section 2.5.

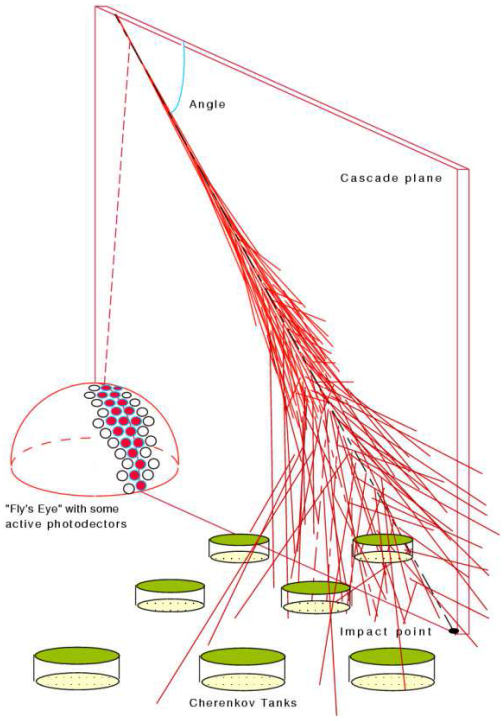

Figure 2.2: Cartoon demonstrating the hybrid detection technique: the SD stations sample charged secondaries at ground level and the FD collects atmospheric fluorescence light.

2.1 The Surface Detector

The SD consists of two distinct arrays. The first is the triangular array of 1660 water-Cherenkov detectors with a 1500 m spacing [78] that spans 3000 km^2 and is fully efficiency above $3{\cdot}10^{18}$ eV. There is also an infill array consisting of 61 stations with a 750 m spacing that is fully-efficient above $3{\cdot}10^{17}$ eV, located at the site of the Coihueco FD sites, part of the Auger Muons and Infill for the Ground Array (AMIGA) project. Though the infill array is much smaller, the significantly-higher flux of UHECRs at these lower energies makes it an effective probe of lower-energic cosmic rays. Both of these arrays are shown in Figure 2.1. A number of grid points also feature two or three stations. These are referred to as "twins" or "triplets," and they are important for understanding uncertainties. Since these tanks are separated by only a few meters (negligible compared to the array spacing), they effectively allow for an independent resampling of the shower at the same location.

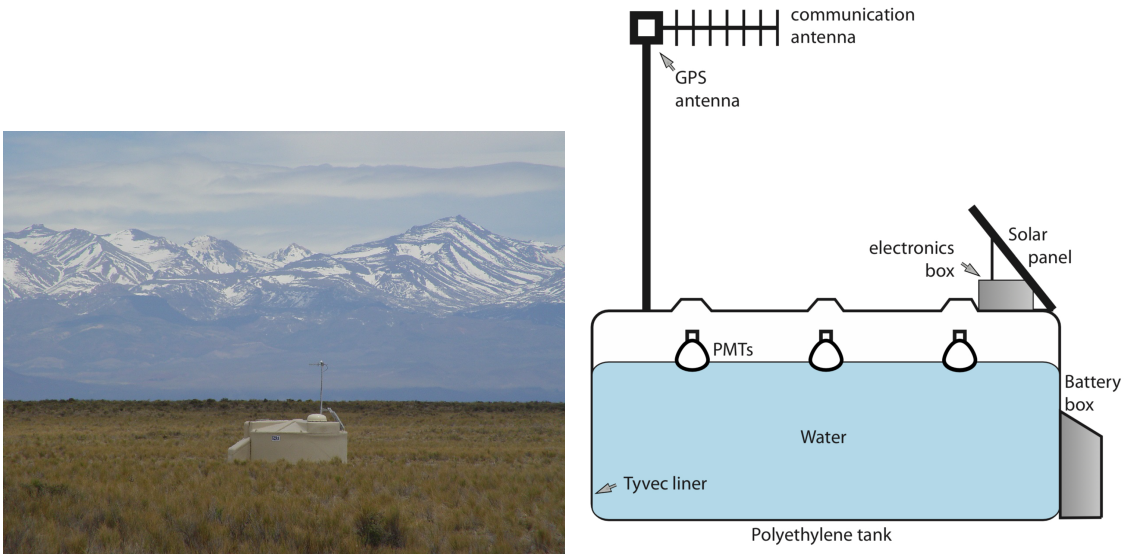

Figure 2.3: Left: One of the 1660 water-Cherenkov tanks of the surface detector. Right: diagram of the SD layout [18].

In this section, I will cover the hardware, trigger, and exposure of the SD.

2.1.1 Hardware

Each SD station station consists of a polyethylene tank (height 1.55 m, diameter 3.6 m), filled to ∼1.2 m with 12,000 liters of ultra-pure water produced by the Observatory at a plant located in Malargüe. This water is contained within a highly-reflective Tyvek liner. Three 9-inch photomultiplier tubes (PMTs) observe the water bulk through clear polyethylene windows. Each station contains a battery that is charged via solar power and a radio transeiver for transmitting trigger information to the Central Data Acquisition Server (CDAS). The signals seen in the SD consist primarily of Cherenkov light produced by ultra-relativistic particles (eg muons) traversing through the water bulk, as well as photons from electromagnetic pair-production and delta rays. Figure 2.3 shows a photograph of an SD tank and a schematic diagram of its major components.

The standard unit of measurement employed by the SD station is the Vertical Equivalent Muon (VEM), defined as the equivalent light produced by a muon vertically traversing the

tank. The energy loss from a muon traversing matter is given by the well-known Bethe-Bloch formula,

$$\left\langle \frac{\mathrm{d}E}{\mathrm{d}X} \right\rangle \propto n \left(\ln \frac{\beta^2}{I \cdot (1-\beta^2)} - \beta^2 \right), \tag{2.1}$$

where n is the electron number density of the medium, β is the relativistic velocity ratio, and I is the mean excitation potential, a characteristic of the medium. This importantly has little functional dependence on the properties of the muon, and hence its net energy deposition depends almost entirely on the path length taken through the medium. The footprint of a vertical relativistic muon is therefore constant regardless of its energy.

Choosing VEM as a standard unit of measure allows us to regularly calibrate the SD based off individual detectors' response to vertical atmospheric muons, standardizing the moment-to-moment performance of the detector. This frees us from long-term performance shifts and allows for detector-level determination of trigger thresholds based on target background frequencies. Each station internally monitors the amplitude and total integrated counts of background muons penetration the tank. Because this rate is extraordinarily high, a distribution of these parameters can be easily obtained and fit to study its statistical properties. An example is shown in Figure 2.4. The distribution of background events contains two peaks: that from the low-energy background of electromagnetic particles (and skimming muons) and that from omnidirectional muons. The ratio of these two peaks is used to determine the detector calibration [79]. A more sophisticated analysis is performed during reconstruction using the muon signals collected immediately prior to the event's detection; these are sent back to the Central Data Acquisition System alongside the rest of the event data prior to reconstruction.

2.1.2 Trigger

The SD uses a hierarchical trigger system consisting of five levels [80], the first two of which (T1 and T2) are constructed at the station level. The Central Data Acquisition System

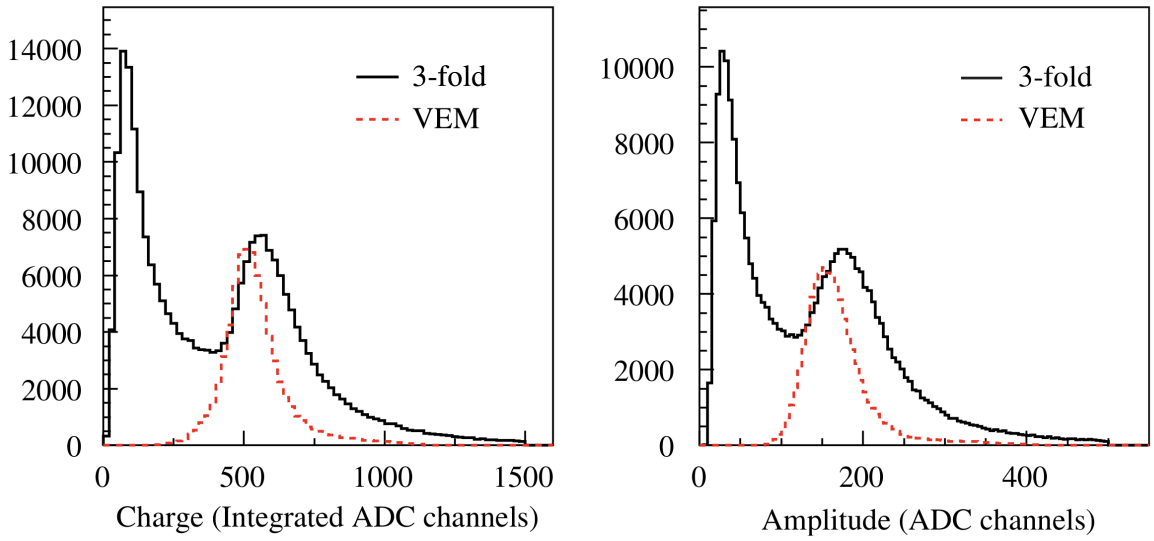

Figure 2.4: Charge and pulse height histograms from an SD stations, triggered by a three-fold coincidence with all PMTs summed. Note the two peaks in the black histogram. The first is a product of low-energy background particles convolved with the trigger. The second peak comes from omnidirectional atmospheric muons. For comparison, the dashed red line is produced by an external muon telescope calibrated to select only vertically-penetrating muons.

(CDAS) constructs T3 triggers from sets of T2 triggers to form science events, and the T4 and T5 triggers are post-processing triggers used for event classification based on the station footprint.

There are four distinct station-level triggers, two of which—the "new triggers"—were first implemented in 2013 to improve the array's sensitivity to lower-energy events that evaded the existing two trigger criteria. Three of these trigger classifications depend on the parameter I_{VEM}, the peak current from the VEM distribution obtained from the calibration procedure described above. The four station-level triggers are summarized in Figure 2.5. They are as follows:

1. Threshold (Th) trigger. This requires a single bin above a set threshold (1.75 and 3.2 I_{VEM} for a T1 and T2, respectively). These triggers have a background rate of 100 Hz for the T1 trigger and 20 Hz for the T2 trigger.

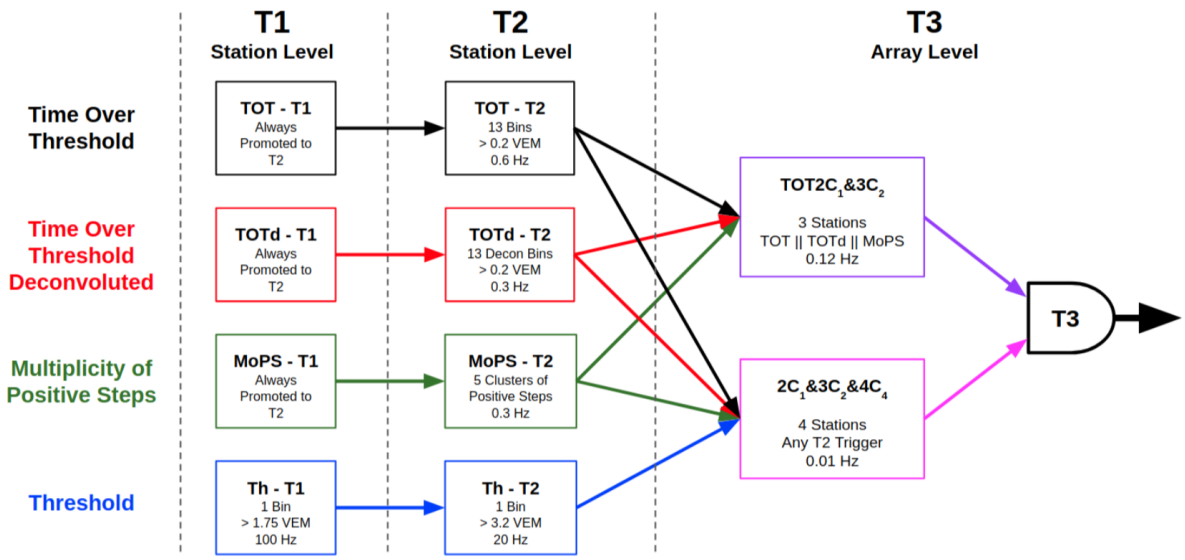

Figure 2.5: Diagram showing the four low-level triggers employed by individual stations of the surface array. These are then used to form the higher-level triggers T3-T5.

2. Time-over-Threshold (ToT) trigger. This requires 13 bins within a 120-bin sliding window above a threshold of 0.2 I_{VEM}. All ToT triggers are classified as T2 triggers.

3. Time-over-threshold de-convolved (ToTd). The first of the new triggers, it applies a transformation to the trace that deconvolves the Cherenkov tail produced by electromagnetic particles. This deconvolution is applied to each individual bin and is dependent only on the decay time and the signal value of the present and previous bin:

$$D_i = \frac{S_i - S_{i-1}e^{-\Delta t/\tau}}{1 - e^{-\Delta t/\tau}}, \tag{2.2}$$

where S_i is the signal in time bin i, Δt is the width of a single time bin (25 ns), and τ is the average Cherenkov light decay time (67 ns). Post-processing, the ToT trigger algorithm is reapplied to the trace. This results in a rate of ∼0.2 Hz.

4. Multiplicity of Positive Steps (MoPS). The second of the new triggers, MoPS abandons the use of an I_{VEM} threshold and instead searches for consecutive steps of

monotonically-increasing signal. A running count is established on the multiplicity m of the number of groups measured in the previous 120 bins. When the multiplicity passes 4, a T2 trigger is formed. The MoPS triggers have a rate of $\sim$0.3 Hz.

The T3 trigger, the array-level trigger, is formed from combinations of T2 triggers. To discuss them, we must first define some terms. Each SD station is surrounded by increasingly-large hexagons of stations, which we call crowns. The first crown, C_1, contains six stations; the second crown, C_2, contains 12; and so on. T3 triggers are built from T1 and T2 triggers laid out in specific crown patterns. There are two such array-level triggers; Figure 2.6 shows the first four crowns of a station and an example of each trigger type.

The first array-level trigger is the three-fold ToTC_1&C_2. It requires at least three ToT-triggered stations (including ToTd or MoPs) in a strict compact configuration: at least three stations within the second crown ($3C_2$) and at least two stations within the first crown ($3C_1$). The left panel of Figure 2.6 shows an example. The second array-level trigger is the four-fold $2C_1$&$3C_2$&$4C_4$. It allows any trigger type (including a Th trigger), but requires at least four stations within four crowns ($4C_4$) and at least there stations within the second crown ($3C_2$, a requirement shared with the ToTC_1&C_2 trigger).

Once a T3 trigger is formed, the SD sends these signals to CDAS for processing. Though T1 triggers are not used in the construction of higher-level triggers, all T1 triggers within 30 μs are sent along with the T2 trigger. This is because stations with small signals can still contribute timing information useful for constraining the shower geometry during reconstruction.

The final triggers levels, T4 and T5, are physics triggers formed offline during reconstruction. T4 triggers are used to reject noise events generated from the T3 trigger. There are two ways to form a T4 trigger: 3ToT and 4C1. The 3ToT discards events that are physically inconsistent with realistic expectations about a shower's footprint in the array. It requires events to have at least three ToT triggers in a compact triangular pattern with at minimum

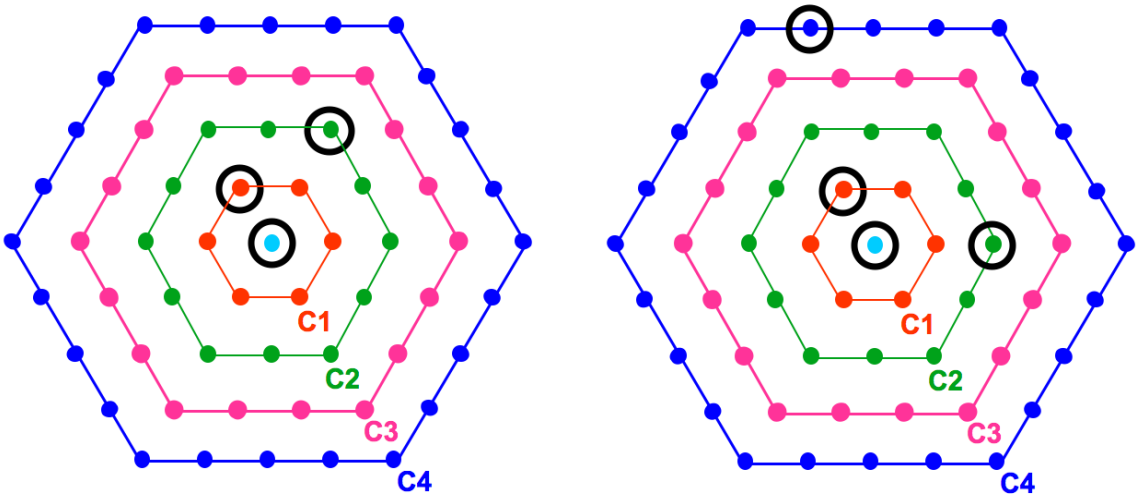

Figure 2.6: Diagram showing the four low-level triggers employed by individual stations of the surface array. These are then used to form the higher-level triggers T3-T5.

two sides equal to the array spacing, as well as requires their trigger times to be consistent a shower traveling at light speed. The 3ToT is the T4 trigger for majority of events with a zenith angle $< 60°$. The second T4 trigger is the 4C1. In parallel to our T3 triggers, it relaxes the trigger type requirements on the 3ToT but requires an additional station. For this trigger, all stations must be contained within a single crown and their trigger times must be consistent with a shower moving at light speed. This is the more common trigger for inclined events (zenith angle $> 60°$).

Finally, the T5 trigger is a fiducial trigger that requires the hottest station to be surrounded by six working stations. It is designed to eliminate edge effects from the array and to handle malfunctioning stations. As the T5 is the most robust trigger the array offers, it is often useful to think of array as a set of N active T5 hexagons. The T5 exposure and aperture can be calculated by tracking the number of active hexagons as a function of time, $N_{\text{cell}}(t)$, a quantity that is monitored by Auger at the second level. It is responsive to mechanical failures (such as communication tower problems, battery problems, PMT failures, etc.) as well as disruptive weather, such as the severe storms we experienced in January 2008.

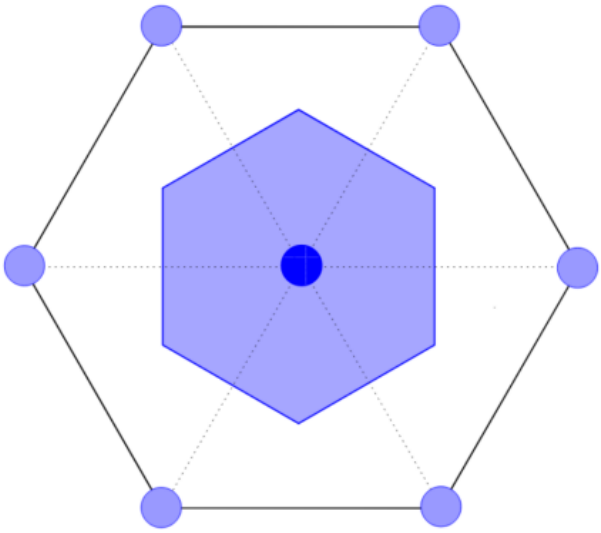

Figure 2.7: Elemental cell of the surface array, used in calculating the T5 exposure.

The elemental hexagon cell, shown in Figure 2.7, is the area in a hexagon of stations that is the closest to the central station. This area spans $1.95\,\mathrm{km}^2$, and the corresponding aperture for showers with zenith angles less than 60° is $a_{\mathrm{cell}} \approx 4.59\,\mathrm{km}^2\,\mathrm{sr}$. The T5 exposure is hence

$$a = \int \mathrm{d}t\, a_{\mathrm{cell}} \cdot N_{\mathrm{cell}}(t). \tag{2.3}$$

2.2 The Fluorescence Detector

The Auger SD is overlooked by a set of 27 fluorescence telescopes located at four sites on the array's perimeter, as shown in Figure 2.1. They are named Los Leones, Coihueco, Loma Amarilla, and Los Morados. Each site consists of a single FD building that contains six telescopes, each of which has a field-of-view of 30° × 30° for a total of 180° of azimuthal coverage. In addition, Coihueco contains the High-Elevation Auger Telescopes (HEAT) extension [81], a set of three telescopes designed to tilt higher in elevation to observe the early-atmospheric development of lower-energy showers.

Figure 2.8: FD site building containing six FD telescopes.

Whereas the SD attempts to reconstruct information about the primary from secondary particles arriving at ground level, the FD directly measures the longitudinal development of the shower. FD telescopes measure the fluorescence light emitted from atmospheric nitrogen, and hence instead of relying on post-LHC extrapolations of hadronic interaction models, they rely on a quantity that may be studied precisely in the laboratory: the fluorescence yield of nitrogen. This best available measurement of the fluorescence yield was performed by the AIRFLY experiment at the University of Chicago [19] [20]; the fluorescence spectrum is shown in Figure 2.9. Because the fraction of energy emitted as fluorescence is well understood, this allows the FD to use the shower's longitudinal profile to obtain a precise calorimetric measurement of the shower's energy.

2.2.1 Hardware

The FD telescopes are housed in a climate-controlled building with six bays, each of which contains a single telescope and its electronics. A shutter opens to a UV bandpass 300-410 nm filter at the entrance window. A diagram of the building's layout is shown in Figure 2.10. Individual telescopes are often referred to as "mirrors," and each is served by its own dedi-

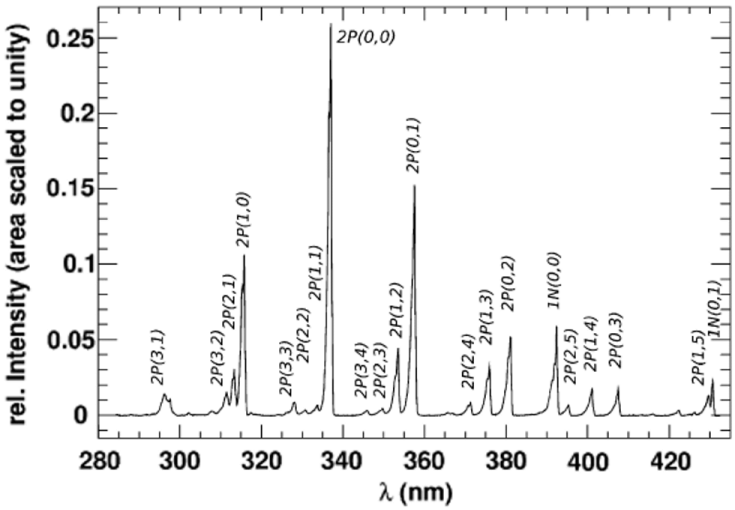

Figure 2.9: The nitrogen fluorescence spectrum as measured by the AIRFLY experiment [19] [20], showing all 21 major transition peaks.

cated "mirror PC." FD sites are often referred to as "eyes," and each contains a single "eye PC" that controls all six mirror PCs. A group of shifters is responsible for operating the FD, performing calibrations, and writing a detailed report at the end of each shift.

The optical system of the telescope consists of the UV filter, a corrector ring for the primary mirror's spherical aberration, a $13\,\mathrm{m}^2$ segmented mirror, and the camera. The camera consists of 440 hexagonal photomultiplier tubes mounted at the focal plane. Each PMT is surrounded with an optical system called a *Mercedes Star* that redirects light from the dead space between pixels, improving the light collection efficiency from 70% to 94 % [82]. The DAQ hardware supplies groups of 10 PMTs with high voltage, low voltage, and signal output. Traces are digitized at 10 MHz (100 ns time bins) and filtered with a 3.4 MHz fourth-order Bessel filter. Two electronics boards provide hardware-level triggers for the first two trigger levels, constructed locally at each mirror PC before being transmitted to the eye PC for further processing. A diagram of the FD's hardware is shown on Figure 2.11.

Telescope absolute calibration is provided by the "drum" [83] [84], a cylindrical apparatus (2.5 m in diameter and 1.4 m long) mounted at the telescope aperture that uniformly illuminates the FD camera with a calibrated 375 nm light source. Reflective surfaces inside

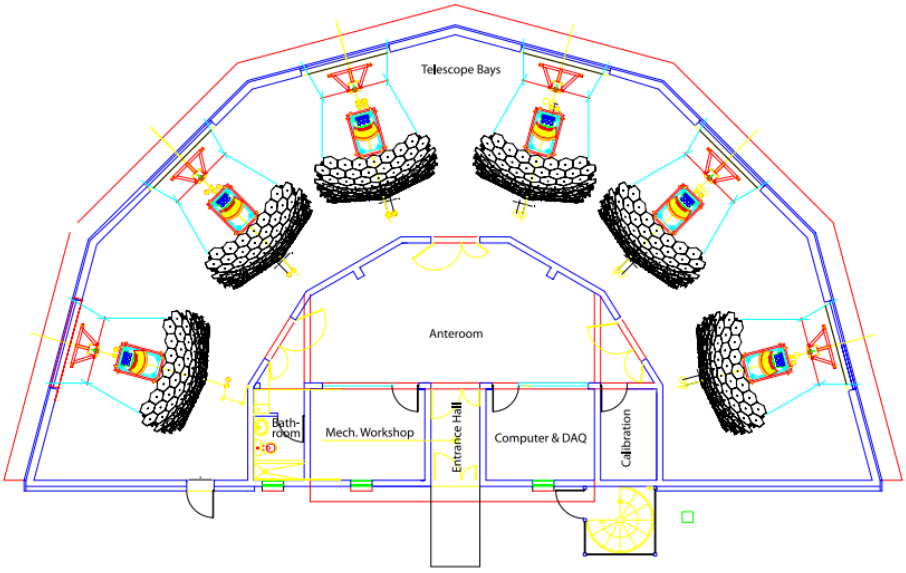

Figure 2.10: Schematic layout of an FD building.

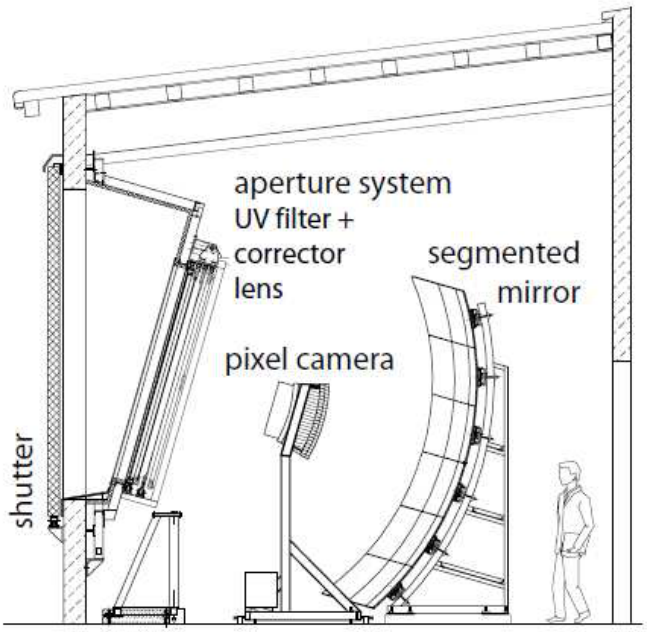

Figure 2.11: The telescope hardware of the FD. The shutter opens and allows light to pass through the UV filter and corrector lens systems. It is then collected by a segmented mirror and directed to the 440-pixel fluorescence detector camera.

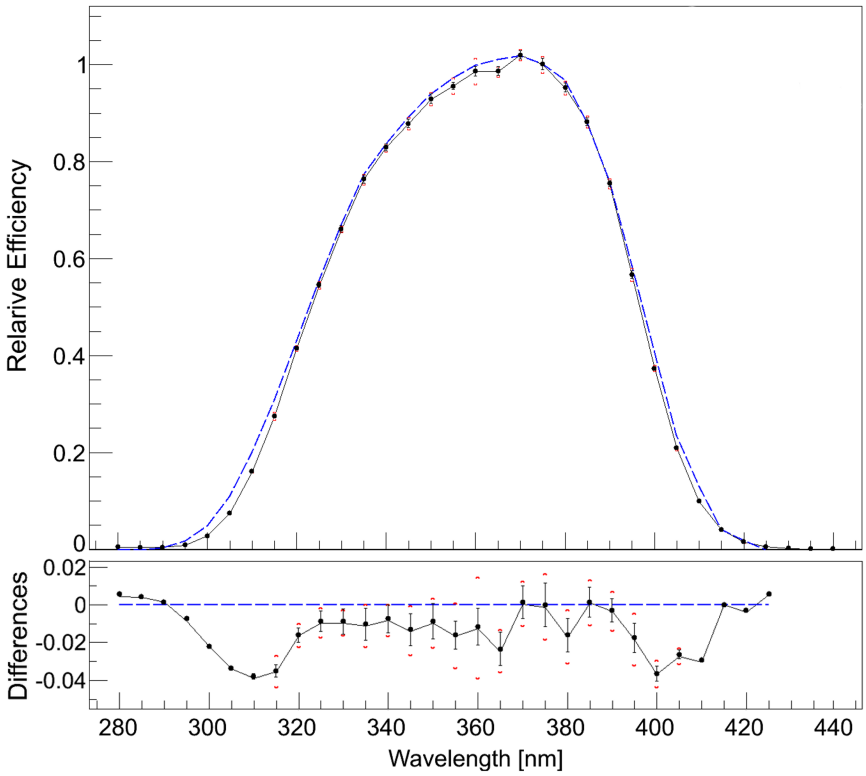

Figure 2.12: Wavelength-dependent relative efficiencies for Los Morados telescopes 4 and 5. Top: the five-point filter curve shown in the dashed line and the monochrometer result shown in solid. Statistical uncertainties are shown in the error bars and the red brackets are systematic uncertainties. Bottom: residuals between these two methods.

the drum funnel the light through a thin sheet of Teflon on its front side. The drum can also provide wavelength-dependent calibrations by replacing the monochromatic light source with a Xenon flasher (an Excelitas PAX-10) capable of emitting five discrete wavelengths. Further refinement of this measurement is provided by a monochromator that allows sampling the entire range of the FD's acceptance over 5 nm intervals. The monochromator system is mounted in a climate-controlled, insulated enclosure to ensure temperature stability throughout the measurement. This work replaced a previous study done using a series of notch filters with a large spectral width. A comparison of these two methods are shown in Figure 2.12.

Relative calibration of the telescope is performed nightly. Before and after each data

acquisition period, three UV flashers (Cal A, B, and C) mounted in three different locations are used to hierarchically assess the telescope's performance [82]: one on the mirror's center (Cal A), one on the camera's sides (Cal B), and one outside the telescope aperture (Cal C). Cal A is a 470 nm flasher that directly illuminates the camera, providing a relative measurement of the PMT gain that is independent of the telescope optics. Cal B is a set of two Xenon lamps that illuminate the mirror, providing a measurement of the combined response of the mirror and the camera. Finally, Cal C's output is diffused towards the UV filter, allowing for a full end-to-end measurement of the telescope's optical properties.

The overall uncertainties in the spectral calibration are less than $\sim 1.5\%$. This uncertainty impacts the energy resolution by approximately 3% and has no impact on $X_{\max}$ reconstruction.

2.2.2 Trigger

The FD trigger consists of four hierarchical steps: the First-Level Trigger (FLT), Second-Level Trigger (SLT), Third-Level Trigger (TLT), and the hybrid trigger (T3). The FLT and SLT are hardware-level triggers implemented by dedicated FPGA-based electronics whose logic is outside the scope of this thesis. For more information, see [82]. The third-level trigger and hybrid trigger are software-level triggers aimed at eliminating noise and fusing lower-level triggers across telescopes and FD sites. Briefly summarized, the four triggers are:

1. **First-level Trigger (FLT):** the pixel-level trigger, formed when the sum of a sliding window exceeds a predetermined threshold. The length of the window varies from 5 to 16 time bins, with the exact number chosen algorithmically to maintain a 100 Hz trigger rate. Once a pixel fires, the electronics extends the pixel trigger for a window of 5 to 30 μs for all pixels to increase the chance of coincidence triggers. The multiplicity (number of simultaneously-triggered pixels within 100 ns) is also tracked and stored for use later in the software-level triggers. These first-level triggers are passed from the

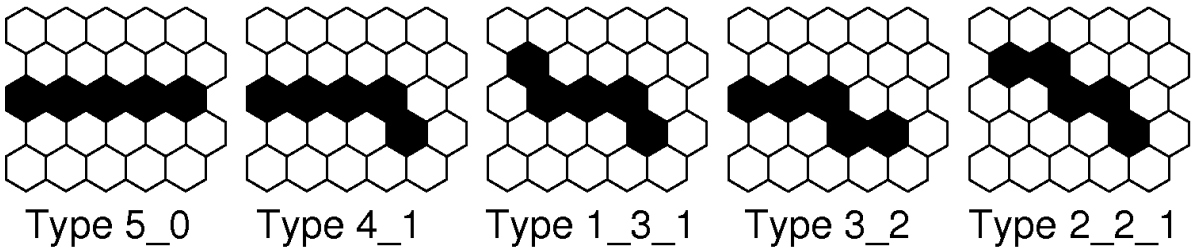

Figure 2.13: Patterns of first-level triggers used in the construction of second-level triggers.

FLT board to the SLT.

2. **Second-level Trigger (SLT):** the pixel pattern trigger, formed when a pattern of FLTs passed from the FLT board matches certain pre-determined templates. Its algorithm x'searches for tracks of at least five FLTs in length using the patterns shown in Figure 2.13 and their reflections and rotations.

3. **Third-level Trigger (TLT):** a software trigger algorithm designed to eliminate noise triggers. Its three specific target backgrounds are lightning events, muons striking the camera, and noise-triggered pixels. Lightning events are extremely bright and the huge number of FLTs they produce can overwhelm the hardware buffers; the pixel multiplicities are used to eliminate lightning events with 99 % effectiveness with thresholds determined from a data-driven study. These lighting cuts also remove noise events with a large number of noise-triggered pixels. Muons and noise-triggered pixels in science effects are filtered primarily by examining spatial information and peak signal times, searching for inconsistencies with the main track.

4. **Hybrid Trigger (T3):** a software trigger that merges events from adjacent telescopes and sends a T3 Hybrid trigger to CDAS in Malargüe. This acts as an external trigger to the surface array and is primarily designed to record SD data for events below the full-efficiency threshold of the array ($3 \cdot 10^{18}$ eV) where the array might not generate an internal trigger of its own. This trigger typically only includes one or two SD stations, but even if insufficient SD information is provided for a full SD reconstruction, the

timing information provided from the SD tanks is extremely effective at constraining the shower geometry.

2.3 Atmospheric Monitoring

Since EAS particles develop and propagate through the atmosphere, understanding its properties is critical for proper reconstruction. This is especially true for the FD: clouds significantly disrupt the scattering of light; weather conditions, including rain and wind, can degrade data quality and damage hardware if shifters do not respond quickly; and atmospheric aerosols dominate the uncertainty of FD measurements. This last point is particularly important since the FD is used for SD energy calibration and hence defines the energy scale of the experiment. The Observatory has developed a robust, sophisticated atmospheric monitoring program comprised of dedicated internal instruments and external tools [85] [86]. These systems contain several redundancies to ensure a robust understanding of the atmosphere.

Each FD building features an infrared (8-14 μm) cloud camera mounted on its roof. The cloud camera produces two outputs: one, an image of the FD field-of-view, taken every five minutes; and two, a full-sky image produced every fifteen minutes. An offline analysis calculates the cloud fraction by utilizing the temperature difference between clouds and the night sky. An example image is shown in Figure 2.14.

The Central Laser Facility [87] is a centrally-located structure containing an upwards-firing 7 mJ ultraviolet laser. It provides a source of calibrated, pulsed light that can be used as a test beam for the observatory for calibration and monitoring purposes. It has been in operation since 2004. In 2008, the eXtreme Laser Facility (XLF) was constructed for the Lomo Amarilla FD site, the farthest from the CLF. It contains the same hardware as the CLF.

Both facilities fire 50 vertical laser shots every 15 minutes that leave tracks in the FD cameras similar to air showers. They are primarily used for inferring properties about the

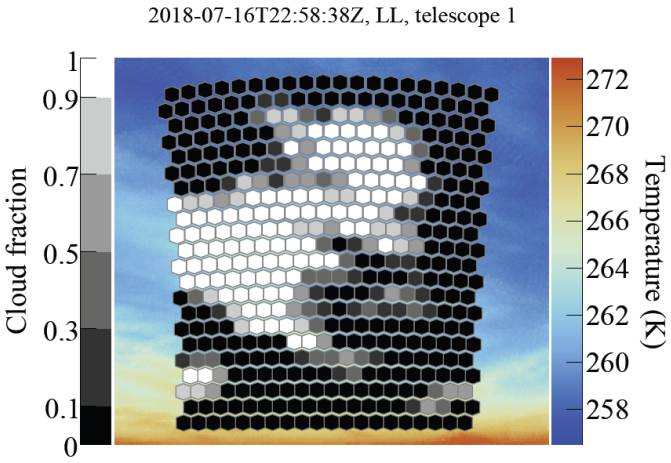

Figure 2.14: Cloud camera image from one FD, showing a cloud in the field-of-view (pixels overlaid).

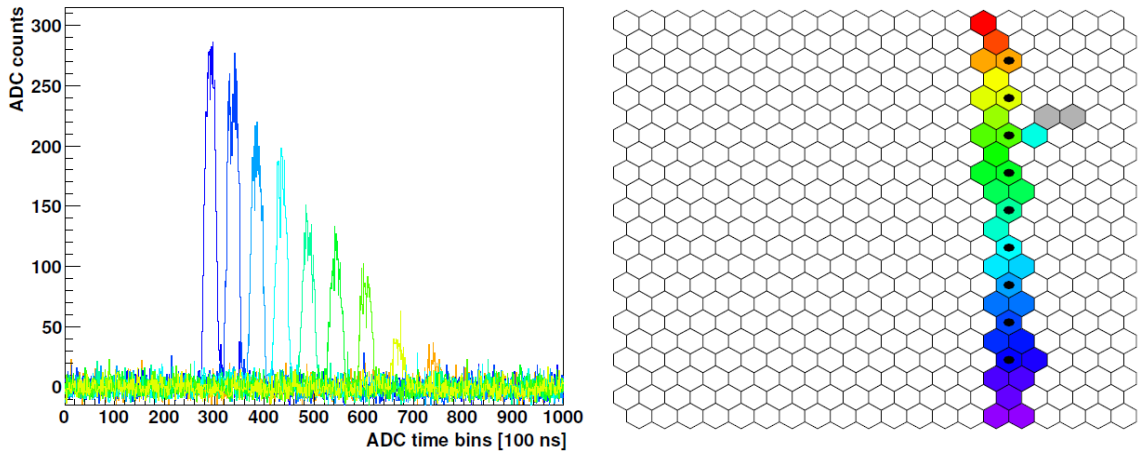

Figure 2.15: A vertical CLF event from the Los Leones FD site, located a distance 26 km from the facility. Left: stacked traces from each of the PMTs marked in color on the right. Right: camera trace; color indicates the trigger time.

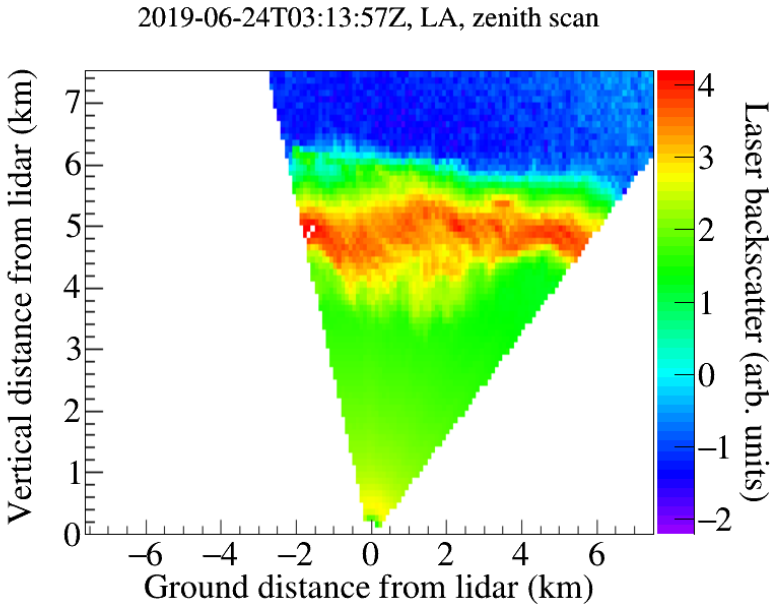

Figure 2.16: FD lidar scan, showing clouds above the FD

aerosols in the atmosphere, one of the most important systematics for the FD analysis. Each year, a reference night is chosen during which the observatory sees the least aerosol burden, and this is assumed to be aerosol free. Comparisons are made offline to this reference night to generate quarter-hourly aerosol reports. This is called the data-normalized method of reconstructing aerosols. Both this method and a simulations-based method, known as the laser simulation analysis, are used to monitor aerosols, and these two independent methods are largely in agreement.

A Raman lidar system was installed in 2013; it makes three measurements of the vertical aerosol profile each night (before, during, and after data acquisition). Each FD site also has a monostatic elastic backscatter lidar that scans for clouds outside the field-of-view every fifteen minutes. The lidar's hardware consists of a 351 nm laser and a three-mirror system. An example lidar image is shown in Figure 2.16.

Finally, the observatory uses two exterior tools. The Geostationary Operational Environmental Satellite (GOES)[88] system is a satellite operated by the United States National Oceanic and Atmospheric Administration that provides its data free to the public. The

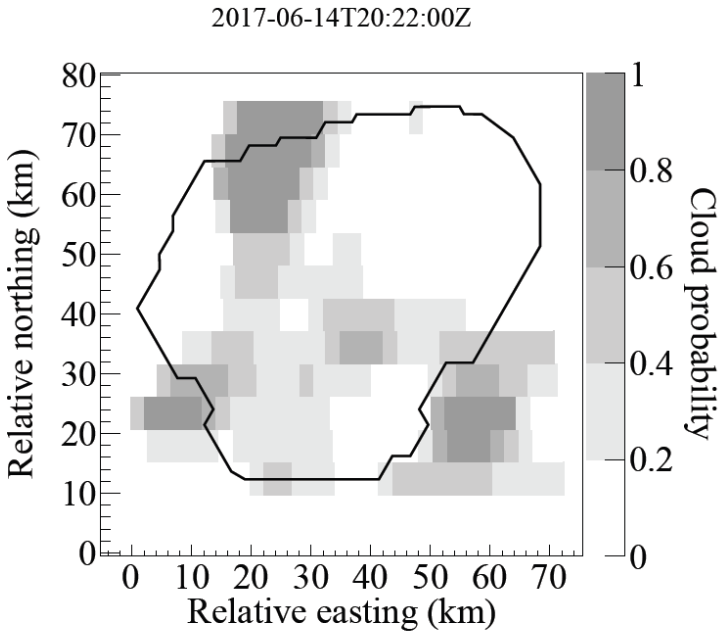

Figure 2.17: Cloud probability map, generated from GOES data.

Observatory processes these data and converts satellite measurements of four infrared bands into cloud probabilities (Figure 2.17). The Observatory also uses the Global Data Assimilation System (GDAS), which provides models of the molecular atmosphere [89]. It uses a combination of meteorological measurements and numerical weather models to generate three-dimensional atmospheric models. Local balloon campaigns have verified the accuracy and reliability of the GDAS analyses.

2.4 Event Reconstruction

This chapter so far has covered only the hardware and trigger of the detector. We now face the monumental task of transforming the data arriving at CDAS from the detectors into scientific measurements. Specifically, we aim to determine the properties of the shower primary: arrival direction, energy, and $X_{\max}$, where possible. This process is called reconstruction.

In this section, I will first cover the software framework used by the Observatory, but

```
<sequenceFile>
<loop numTimes="unbounded">
<module> SimulatedShowerReader </module>
<loop numTimes="10" pushToStack="yes">
<module> EventGenerator </module>
<module> TankSimulator </module>
<module> TriggerSimulator </module>
<module> EventExporter </module>
</loop>
</loop>
</sequenceFile>
```

Figure 2.18: Simplified example in which an XML file sets a sequence of modules to conduct a simulation of the surface array. ¡loop¿ and ¡module¿ tags are interpreted by the run controller, which invokes the modules in the proper sequence. In this example, simulated showers are read from a file, and each shower is thrown onto the array in 10 random position by an EventGenerator. Subsequent modules simulate the response of the surface detectors and trigger, and export the simulated data to file. The pushToStack="yes" attribute instructs the Run Controller to store the event when entering the loop, and restore it to that state when returning back to the beginning of the loop.

first I will discuss the collaboration's software system.

2.4.1 Offline Framework

The Observatory generates a huge amount of data and runs sophisticated analyses that depend on databases generated by the monitoring systems. Further, the detector itself is extremely complicated. To precipitate these tasks, a software system called Offline [90] has been developed. Written in C++ and based on ROOT, it is a modular system configured with XML files. Programs for the Offline framework are written in terms of modules that have full access to the framework's internals. These modules are invoked from a module sequence file. One such example is shown in Figure 2.18. Each module parses its configuration from an associated XML file; although the central configuration system features a default XML configuration for each module, these configurations may be overwritten by the user.

The detector's state is described by read-only data structures, charted in Figure 2.20.

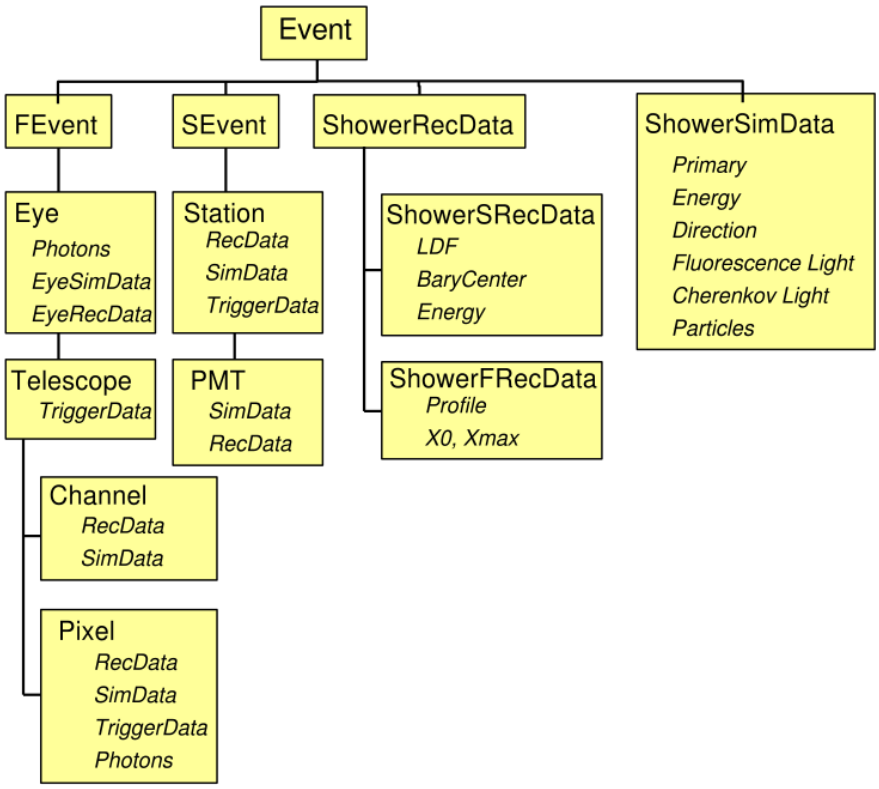

Figure 2.19: Event class structure implemented by the offline framework.

It contains the basic abstractions for all the physical components of the detector, as well as data provided from all the monitoring systems of the array, including temperature and pressure sensors, calibration information, and the physical locations of the tanks.

Science events have their own dedicated class structure, shown in Figure 2.19. Fluorescence detector events and surface detector events, built from the higher-level triggers described in the previous section, contain all the raw data fed into the reconstruction. Each event also has a reconstruction data object that contains the estimated shower parameters. Finally, simulated events also contain an additional class with the input properties of the simulation. These events are stored to disk as ROOT objects, and they are referred to as Advanced Data Summary Tree (ADST) files.

Finally, the Offline software framework includes the event display program whose outputs have been used throughout this thesis. It reads ADST files and displays both the raw data

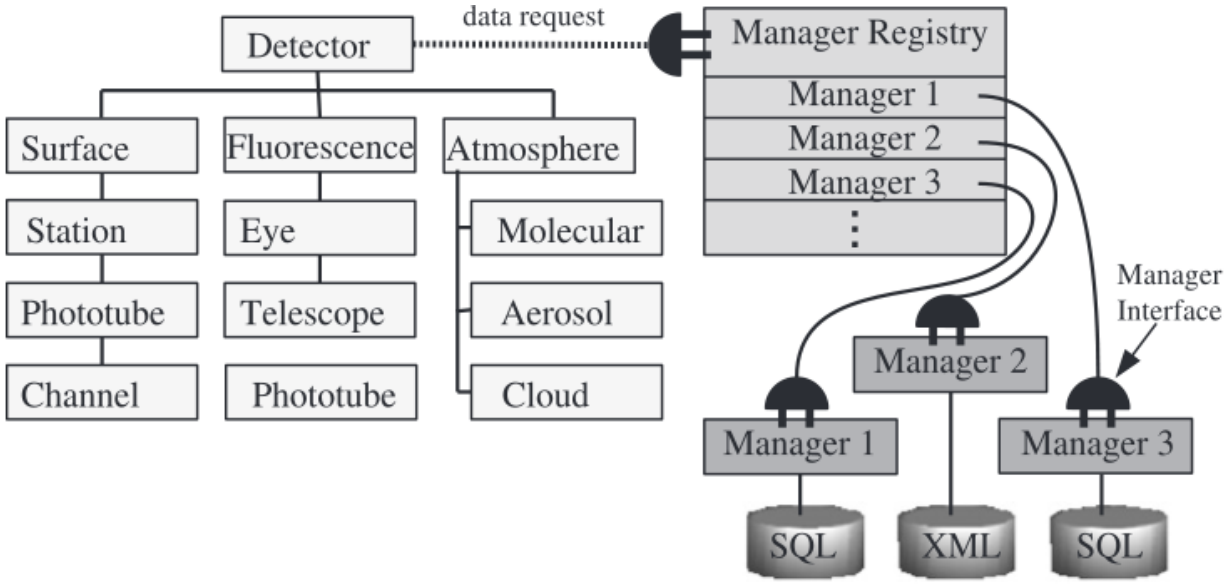

Figure 2.20: Detector class structure implemented by the offline framework.

and information about the reconstruction process.

The following two sections detail the reconstruction tasks of the Observatory. The code for each of these is implemented as module sequences in the Offline program.

2.4.2 SD Reconstruction

The Observatory contains two independent SD reconstruction pipelines: the Herald reconstruction, which is integrated in the older CDAS framework, and the Observer reconstruction, which is integrated through Offline. Since these two algorithms share little code, they have different systematics and hence form important cross-checks with one another. Though they produce similar results, there are some small differences in the exact procedures. Throughout this section, for simplicity's sake, I will focus only on the Observer reconstruction.

The Surface Detector reconstruction consists of five parts:

- extracting the relevant portions of the SD traces and obtaining a first-guess geometry;
- reconstructing the shower geometry using station timing information;

- determining of the "shower size" using the Lateral Distribution Function (LDF) fit;
- normalizing the shower's signal with respect to its zenith angle through the Constant Intensity Cut (CIC) method; and
- calibrating its energy using the hybrid fit.

A schematic of the process described here, illustrated through a readout from the Auger EventBrowser, is shown in Figure 2.21.

We begin by determining the baseline for each trace, analyzing it to extract the relevant portions of the traces from each station, and applying the station calibrations. The full details of this process can be found in [91]. Signal start times provide a first-guess estimate of the beginning of the shower front's impact on the ground; the signal stop time is chosen to incorporate as many secondaries as possible while also minimizing accidentals. The total signal is then calculated by integrating the trace and applying the VEM calibration. This requires a selection of which FADC channel to use.

The Auger SD uses two channels: a high-gain channel used for a majority of measurements and a low-gain channel used when the high-gain channel is saturated. For low-energy showers, this typically occurs in stations that are within 100 m of the shower's core; for high-energy showers, it occurs within 500m̀. Around 10% of low-energy stations feature at least one saturation station, whereas for high-energy showers this number is closer to 50%. In either case, events with more than one saturated station are rare. For stations with extremely high signals, the PMT begins to saturate, and nonlinearity studies may be used to recover signals up to approximately 10^6 VEM with a resolution of $\sim$20% by fitting the non-saturated portions of the trace. The VEM calibration constant $Q_{\text{peak}}^{\text{VEM}}$ is calculated with the high-gain channel; it is applied directly to the high-gain channel and is rescaled by the value of the gain ratio when applied to the low-saturation channel.

After applying an aggressive filter to discard lightning events, the signal-weighted barycen-

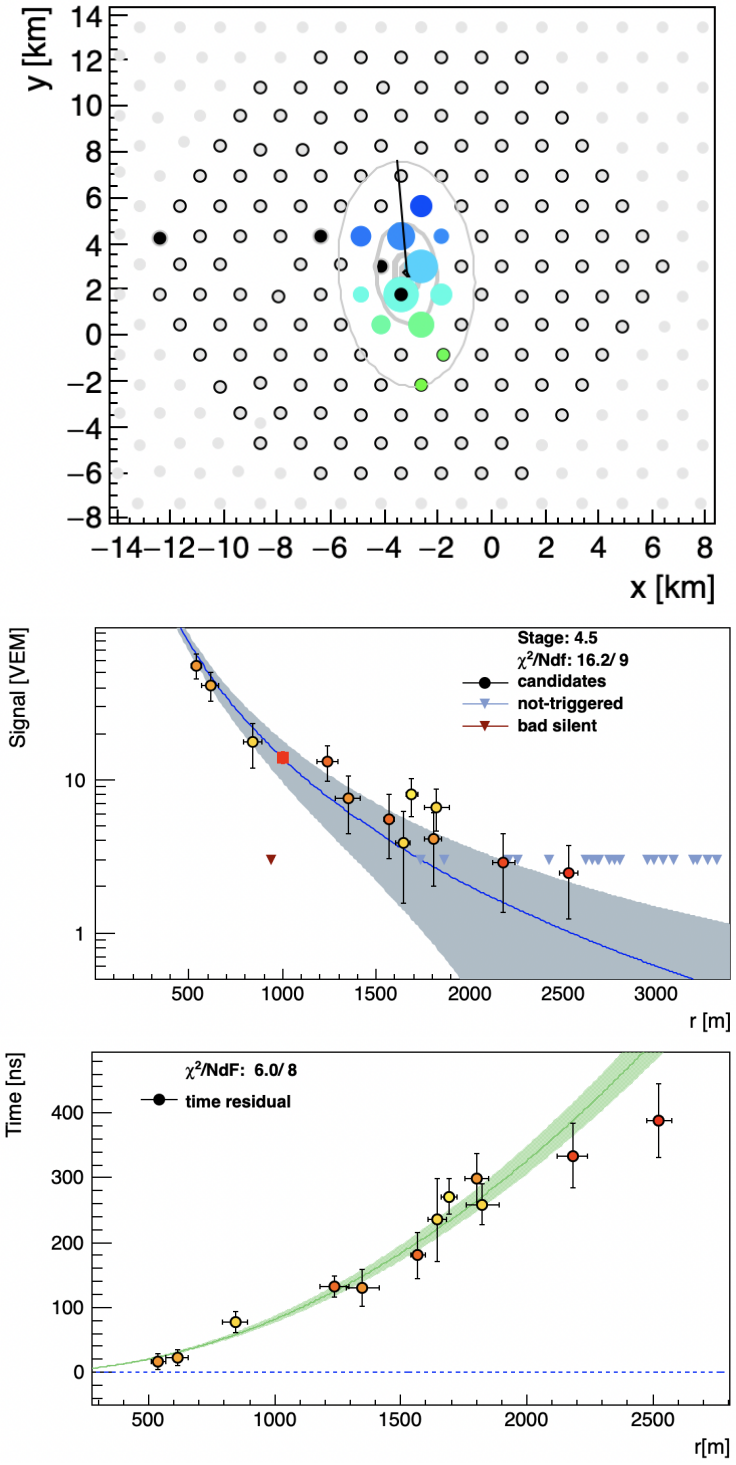

Figure 2.21: Event display for an SD event, showing the array view of triggered stations (top), the lateral distribution function (LDF) fit to obtain the shower energy estimator S_{1000} (middle), and the timing fit to reconstruct the shower axis (bottom).

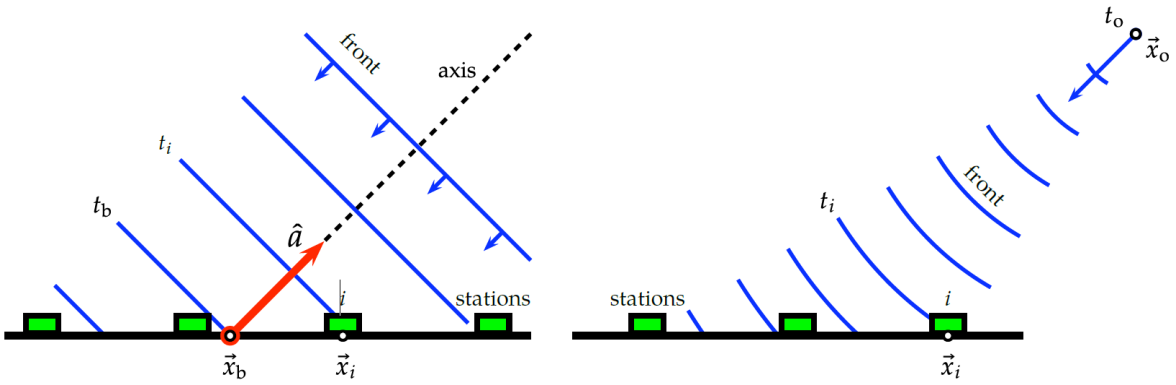

Figure 2.22: Left: schematic of the plane-front approximation, a simplified shower model that does not account for curvature of the shower pancake. Right: schematic of the spherical shower-front development.

ter $\vec{x}_b$ of the event's constituent stations is used to obtain a first-guess reconstruction of the shower's axis direction $\vec{a}$. This guess is obtained by using a simple plane-front approximation that assumes the shower propagates as a plane rather than a sphere, which is more physically accurate and is used in the full reconstruction; see Figure 2.22 for a graphical depiction. The time $t_{\rm sh}(\vec{x})$ that the shower plane passes through an arbitrary point $\vec{x}$ (say, the vector of station positions) is then

$$ct_{\rm sh}(\vec{x}) = ct_b - \vec{a} \cdot (\vec{x} - \vec{x}_b), \tag{2.4}$$

which is solved through the selection of a *seed triangle*. Each station and its two nearest neighbors (passing a station-level trigger) are examined, and the triangle with the greatest total signal is used to solve Equation 2.4. From this we have a first-guess estimate of the shower axis $\vec{a}$ and an estimate of when the shower plane arrives at any arbitrary position. This allows us to reject accidental stations by discarding detectors whose signals begin more than 1 μs prior to the plane's arrival or more than 2 μs after it passes.

Now, the geometrical reconstruction begins. Four parameters are fit: the two directional cosines of the shower axis (u and v), t_c, and the shower front's radius of curvature R_c,

obtained by minimizing the function

$$\chi^2 = \sum_i \frac{(t_i - t_{\rm sh}(\vec{x}_i))}{\sigma_{t_i}^2}, \tag{2.5}$$

where σ_{t_i} is the start time uncertainty

$$\sigma_{t_{\rm start}} = a^2 \left(\frac{2t_{50}}{n}\right) \frac{n-1}{n+1} + b^2. \tag{2.6}$$

Here, t_{50} is the time taken for the trace to reach 50% of its total signal, and n is the effective number of particles. It is equal to $S/\bar{\ell}(\theta)$, where $\bar{\ell}(\theta)$ is the mean track-length of particles intersecting the detector when coming from a zenith angle θ. a and b are parameterized from studies performed with station twins.

The shower-front curvature is approximated as a sphere inflating at the speed of light. It starts at time t_0 from a virtual origin $\vec{x}_0$. The arrival time at point $\vec{x}$ is hence

$$ct_{\rm sh}(\vec{x}) = ct_0 + |\vec{x} - \vec{x}_0|. \tag{2.7}$$

Lower-energy stations typically only feature three or four stations and hence lack sufficient degrees of freedom to explicitly constrain the shower curvature. For events with less than five stations, we approximate the fit using a parameterization obtained from events with more stations.

Next, the shower size is estimated through fitting a Lateral Distribution Function (LDF), a function of core distance S(r) that describes the radial distribution of particles in the shower plane. Understanding the LDF analytically is currently not possible, as it relies on post-LHC extrapolations of accelerator-tuned hadronic interaction models. Instead, it must be fit empirically. Traditionally, functions like log-log parabolas or NKG functions (Nishimura-Kamata-Greisen functions, [92, 93]) have been used. The Observer reconstruction uses a

modified NKG function

$$f_{\mathrm{LFD}}(r) = \left(\frac{r}{r_{\mathrm{opt}}}\right)^{\beta} \left(\frac{r + r_s}{r_{\mathrm{opt}} + r_s}\right)^{\beta+\gamma}, \tag{2.8}$$

where $r_s = 700\,\mathrm{m}$ and the shape parameters β and γ are determined from data and simulations. The measure of shower size is then the signal at a pre-determined distance r_{opt} that minimizes shower-to-shower fluctuations. For the 1500 m spacing of the Auger SD, it has been determined that this distance is 1000 m; hence $S(1000)$ evaluated from the LDF is our measure of shower size.

To fit the LDF, we use the maximum likelihood method to fit the function

$$\ln \mathcal{L} = \sum_i \ln P(S(1000), \vec{x}_c | S_i, \vec{x}_i). \tag{2.9}$$

A detailed description of this likelihood function is beyond the scope of this thesis. The Observer reconstruction decomposes this function into four distinct parts:

- stations with small signals, modeled using Poisson statistics;
- stations with large signals, modeled with a Gaussian distribution;
- stations with unrecoverable saturated signals, treated as lower limits to a Gaussian function; and
- non-triggered stations, modeled with a station trigger probability.

This results in the function

$$\mathcal{L} = \prod_i^{N_{\mathrm{small}}} f_{\mathrm{Poisson}} \prod_i^{N_{\mathrm{large}}} \mathcal{N} \prod_i^{N_{\mathrm{sat}}} F_{\mathrm{sat}} \prod_i^{N_{\mathrm{none}}} F_{\mathrm{No\ trigger}}. \tag{2.10}$$

Once this procedure finishes, we have an estimate of the shower size S(1000), but a number of small corrections must be applied prior to its use as an energy estimator. These

include adjustments for the seasonal and diurnal atmospheric changes as well as for the azimuthally-dependent energy shifts induced by the geomagnetic field. However, even after these corrections, there is still a huge dependence on zenith: a shower arriving vertically will measure a much different S(1000) than the same shower arriving at a more-inclined angle, primarily due to strong attenuation of its electromagnetic component from the additional atmosphere traveled.

To address this, a final correction is applied using the Constant Intensity Cut method. All showers have their shower size estimator S(1000) rescaled to the equivalent size of a shower arriving at the median angle of 38°. This new parameter is called S_{38} and is the SD's best estimator of the shower energy. Although the CIC method relies on the assumption of shower isotropy, the small anisotropies observed in our data do not effect this procedure in practice.

To calculate the CIC, first the data is histogrammed in $\cos^2\theta$ and sorted by S(1000). The S(1000) values are then used as an estimate for the attenuation curve. This is performed for three intensity thresholds: $I_1 = 2.91 \cdot 10^4\,\mathrm{sr}^{-1}$, $I_2 = 4.56 \cdot 10^3\,\mathrm{sr}^{-1}$, and $I_3 = 6.46 \cdot 10^2\,\mathrm{sr}^{-1}$; failing to account for the energy-dependence of the CIC results in inaccuracies of the final reconstruction due to bin migrations. These graphs are then fit with a third-degree polynomial,

$$S(1000) = S_{38}\left(1 + adx + bx^2 + cx^3\right), \tag{2.11}$$

where

$$x = \cos^2\theta - \cos^2 28^\circ. \tag{2.12}$$

The attenuation curves for the CIC are shown in Figure 2.23.

Using hybrid events, S_{38} is then calibrated with the calorimetric FD energy. A number

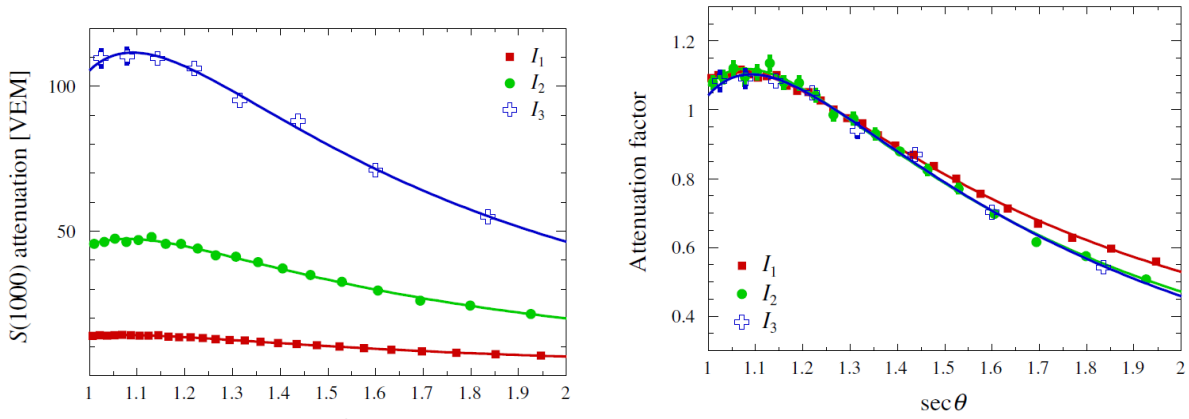

Figure 2.23: Attenuation curves for S(1000) as a function of $\sec\theta$ from the CIC shown a three intensity levels corresponding to $3 \cdot 10^{18}$ eV, $8 \cdot 10^{18}$ eV, and $2 \cdot 10^{19}$ Ev. Left: raw attentuation curves. Right: normalized to 1 at $\theta = 38°$.

of cuts at the FD level (including rigid requirements on the length of the track in the FD camera, the uncertainty of the reconstructed energy, the goodness of fit for the Gaisser-Hillas function fit, and a set of fiducial cuts) are placed to ensure quality of the calibration data. The calibration function

$$E = A(S_{38})^B \tag{2.13}$$

is fit through a maximum likelihood procedure that encapsulates the resolution functions of the FD and SD. The fit is then applied to all SD events to obtain an accurate estimator of the shower energy from S_{38}. The result of this fit is shown in Figure 2.24.

2.4.3 FD Reconstruction

FD reconstruction involves the following steps:

1. determining the shower signal region from the raw PMT pulses;

2. reconstructing the shower axis from the pixel pointing directions;

3. inverting the Cherenkov-fluorescence matrix to build the energy deposition profile; and

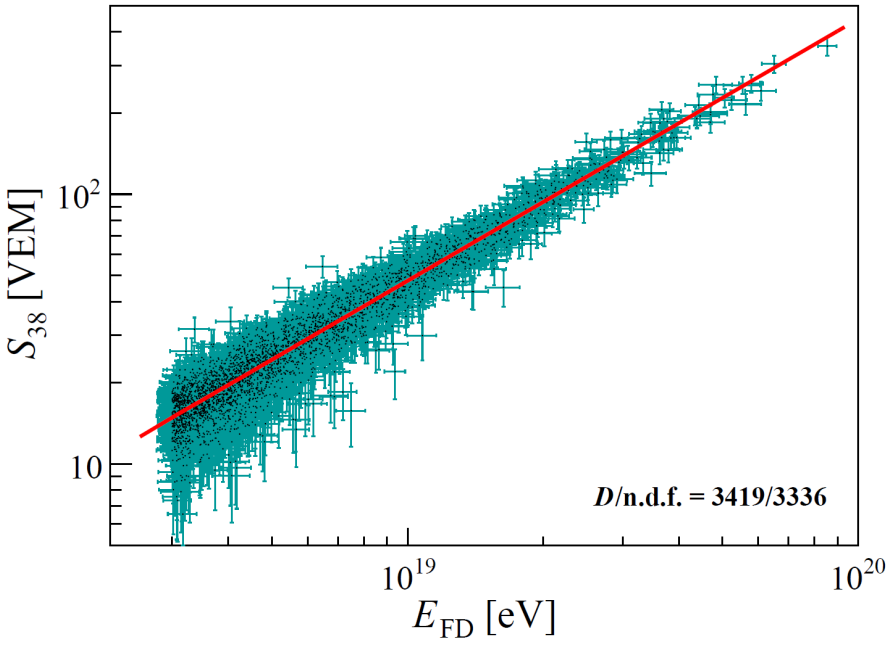

Figure 2.24: Hybrid calibration between the zenith-corrected shower size estimator S_{38} and the calorimetric FD energy, E_{FD}.

4. determining X_{max} from a Gaisser-Hillas function fit to the profile.

Before reconstruction begins, the PMT background is determined and subtracted from the pixel traces. This background consists of two components, added in quadrature: the electronics noise (σ_{elec}) and the night-sky background noise (σ_{nsb}.). Because the PMTs are AC-coupled, it is impossible to determine the absolute NSB; however, the variance of the pedestal from PMT signals can be used as an estimator. Using the known calibration constants of the PMT gain, filter transmissivity, mirror reflectivity, and detection efficiency of the PMTs, this is converted into a photon flux.

The raw PMT pulses provided from the FLT contain a number of time-bins before and after the shower signal itself. The first step in our analysis is extracting the portion of the trace relevant to our analysis. This is performed by the Offline module `FdPulseFinder`; it performs a signal search by use of a sliding window across the trace, finding the stop and

start times $k_{\rm start}$ and $k_{\rm stop}$ that maximize the signal-to-noise ratio

$$S/N = \frac{S_i}{\sigma_i \sqrt{k_{\rm stop} - k_{\rm start}}}. \tag{2.14}$$

After this, each pixel's centroid time is determined for later use.

Next, we reconstruct the shower axis. This analysis is performed in two steps. First, we restruct the shower-detector plane (SDP), the plane containing both the detector and the shower axis. One can think of the SDP as the "plane" seen by the shower's footprint in the FD when viewing the FD pixel display. For this portion of the analysis, only the angular direction of each pixel (p_i) and the total integrated signal (q_i) are used. We find the SDP by minimizing the expression

$$S(p_i, q_i) \equiv= (\Sigma_i q_i)^{-1} \left(\Sigma_i q_i \left[\frac{\frac{\pi}{2} - \arccos\left(\hat{p}_i \cdot \hat{n}_\perp^{\rm SDP}\right)}{\sigma_{\rm SDP}} \right]^2 \right), \tag{2.15}$$

where $\hat{n}_\perp^{\rm SDP}$ is the unit vector normal to the SDP. The parameter $\sigma_{\rm SDP}$ is fixed at a value of 0.35 to allow S to function as a χ^2 function; this value was determined by studying CLF shots where the SDP is known explicitly. Now that we have the shower-detector plane, we must incorporate further information to find the shower axis. The `FdAxisFinder` module does this using the pixel centroid times calculated by `FdPulseFinder`. As is this somewhat complicated geometrically, we'll take some time to define a few parameters:

1. χ, the angle with respect to the horizontal in the SDP; its positive direction is defined by $\vec{n}_\perp^{\rm SDP} \times \hat{z}$, where $\hat{n}_\perp^{\rm SDP}$ is defined as in front of the FD;

2. χ_i, the χ angle for each pixel after projection onto the SDP;

3. χ_0, the shower's χ angle;

4. R_p, the distance-of-closest-approach of the shower to the FD; and

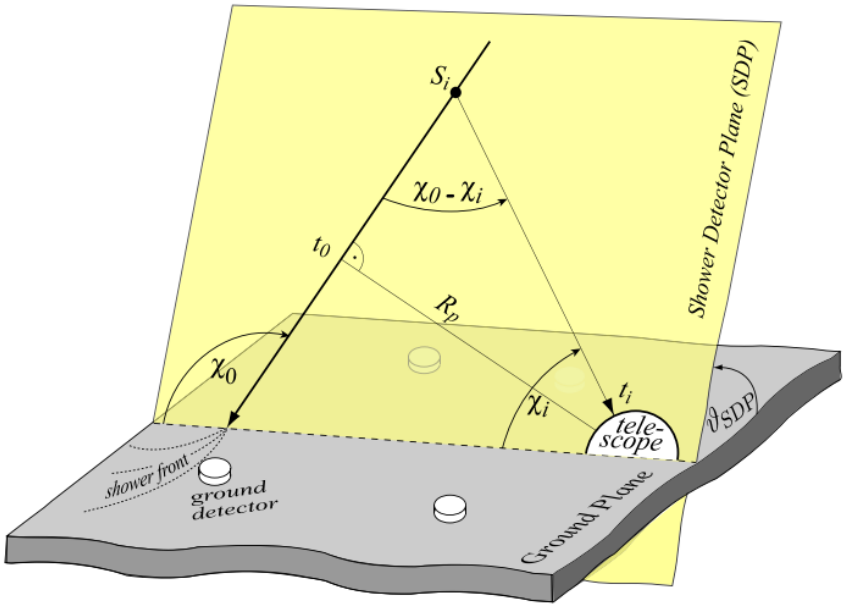

Figure 2.25: Diagram illustrating the geometry of deriving the shower axis from the shower-detector plane from FD observations. See text above for physical explanations of the labeled variables.

5. t_0, the time of closest approach of the shower to the FD.

These last three parameters define the shower geometry and their determination is our primary goal. To better illustrate the geometry of this problem, Figure 2.25 shows a diagram of the problem with all variables labeled [94].

Considering a point S_i along the shower axis, the distance along the axis relative to the shower is

$$dS_i = \frac{R_p}{\tan(\chi_0 - \chi_i)}, \tag{2.16}$$

which yields an arrival time t_{S_i} of

$$t_{S_i} = t_0 - \frac{R_p}{c\tan(\chi_0 - \chi_i)}. \tag{2.17}$$

Considering the propagation time of light to the telescope's aperture, the arrival time at the eye is

$$t(\chi_i) = t_0 + \frac{R_p}{c} \tan\left(\frac{\chi_0 - \chi_i}{2}\right). \tag{2.18}$$

The shower axis parameters χ_0, R_p, and t_0 are determined by minimizing the function

$$\chi^2 = \sum_i \frac{(t_i - t(\chi_i))^2}{\sigma(t_i)^2}, \tag{2.19}$$

where $t(\chi_i)$ is defined in Equation 2.18 above. Because of the geometrical constraints of the problem and the FD's tendency to observe a relatively small portion of the shower's total track, this fit is highly degenerate, particularly between R_p and χ_0. Figure 2.26 illustrates this issue. The problem can be attributed to the typically small variation in $\mathrm{d}\chi/\mathrm{d}t$, which with typical track lengths does not sufficiently constrain the curvature of the function. We will discuss this problem further in our section on the Hybrid reconstruction, but for now it will suffice to note that the inclusion of even a single station into the X fit drastically increases the track length sampled and hence radically reduces the degeneracy of the fit.

Now that the geometry of the shower has been determined, the longitudinal profile can be reconstructed. To understand how we do this, let's consider the physics processes that lead to the shower tracks. As the shower develops longitudinally through the atmosphere, it emits fluorescence and Cherenkov light that scatters to the telescope aperture. A diagram of these processes is shown in Figure 2.27. The physics of these emissions is encapsulated in the construction of a Cherenkov-fluorescence matrix that we must build and invert.

Fluorescence light is emitted isotropically in proportion to the shower's energy deposition.

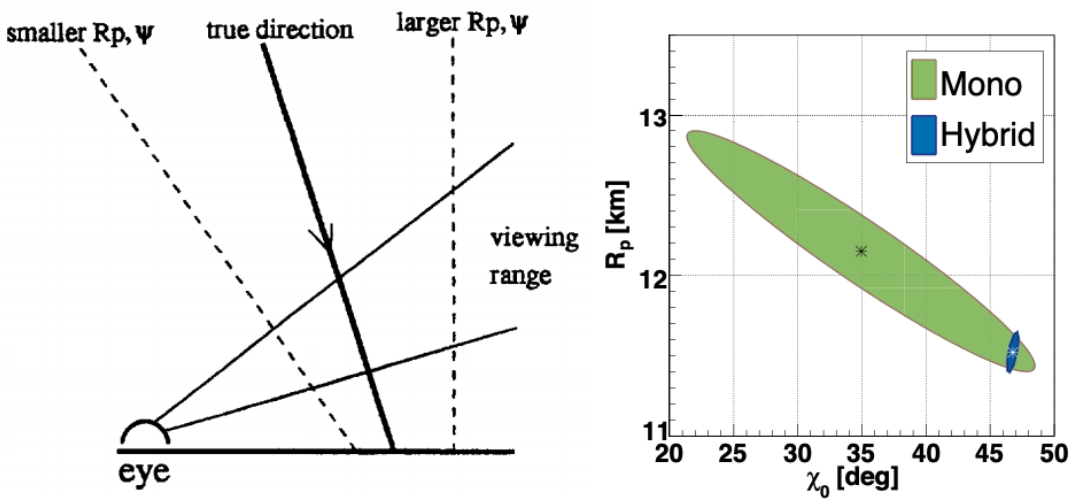

Figure 2.26: Left: illustration of the geometrical degeneracy arising from monocular FD measurements. Right: visualization of the degeneracies of the likelihood fit. The ellipses indicate the uncertainties in the fit for a single event with and without the inclusion of SD data.

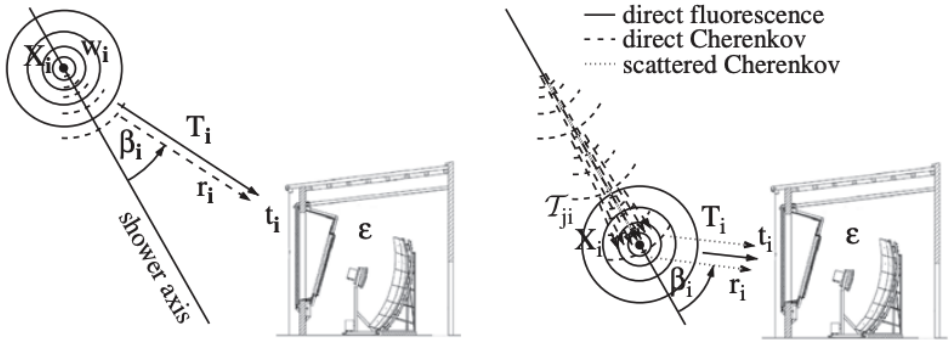

Figure 2.27: The fluorescence and Cherenkov contributions to the signals measured by the FD [21].

At a given slant depth X_i, the number of photons produced in an interval ΔX_i is

$$N_\gamma^{\text{fluor}}(X_i) = \sum_k Y_{ik}^{\text{fluor}} \frac{\mathrm{d}E}{\mathrm{d}X} \Delta X_i, \tag{2.20}$$

where $\mathrm{d}E/\mathrm{d}X$ is the energy deposited per unit depth at X_i and Y_i^f is the fluorescence yield. Because the fluorescence yield is a function of the temperature, pressure, and humidity, here a robust understanding of the atmosphere is helpful. Y_{ik}^f provides light of varying wavelengths, and here we must fold in a number of wavelength-dependent optical properties: the efficiency of the telescope ϵ and the transmittance coefficients for Mie and Rayleigh scattering (which we will collectively refer to as T_{ik}). The light arriving at the diaphragm of the telescope is then

$$y_i^{\text{fluor}} = \frac{\Delta X_i}{4\pi r_i^2} \frac{\mathrm{d}E}{\mathrm{d}X_i} \sum_k \epsilon_k T_{ik} Y_{ik}^{\text{fluor}}. \tag{2.21}$$

Since this quantity is proportional to the atmospheric energy deposition, it is our best estimator of shower energy and is critical to our calorimetric measurement. But the problem is complicated by the addition of Cherenkov light emitted during shower development.

The Cherenkov contribution to the FD signal has two contributions. As the shower develops, Cherenkov light builds into a bright, narrow cone directed along the shower's axis. This beam typically does not impact the FD directly, but scattered light (through Rayleigh scattering and Mie scattering) does. This is the first major contribution to the Cherenkov signals measured at the FD. The other is the potential direct Cherenkov signal from shower particles that acquire a large transverse momentum. The number of Cherenkov photons produced is

$$N_\gamma^{\text{ckov}}(X_i) = \Delta X_i N_i^e \sum_k Y_{ik}^{\text{ckov}}, \tag{2.22}$$

where N_i^e is the number of charged particles under the Cherenkov threshold and Y_{ik}^c is the wavelength-dependent Cherenkov yield. The direct Cherenkov light observed at the detector is

$$Y_i^{\text{ckov, direct}} = \frac{\Delta X_i}{4\pi r_i^2} N_e(X_i) f_d(\beta_i) \sum_k \epsilon_k T_{ik} Y_{ik}^{\text{ckov}}, \tag{2.23}$$

$$= \frac{1}{\alpha_i} \frac{\mathrm{d}E}{\mathrm{d}X} \frac{\Delta X_i}{4\pi r_i^2} N_e(X_i) f_d(\beta_i) \sum_k \epsilon_k T_{ik} Y_{ik}^{\text{ckov}}, \tag{2.24}$$

where $f_d(\beta_i)$ is the fraction of direct light observed at the detector angle β_i. The final equality is a restatement of this quantity in terms of the mean ionization loss rate $\alpha(X_i)$. As the shower develops, the Cherenkov beam builds up from all the previous Cherenkov light emissions attenuated by their transmittance coefficients. The number of photons in the beam at a depth X_i is hence

$$N_\gamma^{\text{beam}}(X_i) = \sum_{j=0}^{i} \Delta X_j N_j^e \sum_k T_{jik} Y_{jk}^{\text{ckov}}, \tag{2.25}$$

but only the scattered fraction $f_s(\beta_i)$ reaches the telescope:

$$y_i^{\text{ckov, scat}} = \frac{f_s(\beta_i)}{4\pi r_i^2} \sum_{j=0}^{i} \Delta X_j N_j^e \sum_k \epsilon_k T_{jik} Y_{jk}^{\text{ckov}} \tag{2.26}$$

$$= \frac{f_s(\beta_i)}{4\pi r_i^2} \sum_{j=0}^{i} \Delta X_j \frac{1}{\alpha_j} \frac{\mathrm{d}E}{\mathrm{d}X_j} \sum_k \epsilon_k T_{jik} Y_{jk}^{\text{ckov}}. \tag{2.27}$$

The total light reaching the detector is then

$$y_i = y_i^{\text{fluor}} + y_f^{\text{ckov, direct}} + y_f^{\text{ckov, scat}}, \tag{2.28}$$

but this is typically expressed as

$$\vec{y} = \mathbf{C}_{ij}\vec{x}, \tag{2.29}$$

where C_{ij} is the (always-invertible) Cherenkov-fluorescence matrix

$$C_{ij} = \begin{cases} 0 & \text{if} < \text{j} \\ c_i^{\text{direct}} + c_{ii}^{\text{scat}} & \text{i} = \text{j} \\ c_{ij}^{\text{scat}} & \text{i} > \text{j} \end{cases}. \tag{2.30}$$

The quantities c_i^d and c_{ij}^s are defined as

$$c_i^{\text{direct}} = \Delta X_i \sum_k \frac{\epsilon_k T_{ik}}{4\pi r_i^2} \left(\frac{f_d(\beta_i)}{\alpha_i} Y_{ik}^C + Y_{ik}^f \right) \tag{2.31}$$

$$c_{ij}^{\text{scat}} = \Delta X_j \sum_k \frac{\epsilon_k T_{ik}}{4\pi r_i^2} \tau_{jik} \frac{f_s(\beta_i)}{\alpha_j} Y_{jk}^C. \tag{2.32}$$

Finally, to determine the calorimetric energy from the reconstructed profile, we perform a maximum likelihood fit to a Gaisser-Hillas function

$$f_{\text{GH}}(\chi) = \left(\frac{\mathrm{d}E}{\mathrm{d}\chi} \right)_{\text{max}} \left(\frac{\chi - \chi_0}{\chi_{\text{max}} - \chi_0} \right)^{(\chi_{\text{max}} - \chi_0)/\lambda} e^{(\chi_{\text{max}} - \chi)/\lambda}, \tag{2.33}$$

where λ and χ_0 are shape parameters. In cases where only a small portion of the shower track has been been observed, there is insufficient information to fit all four parameters of the Gaisser-Hillas function, so these shape parameters are constrained to a small range of typical values. The shower energy can be obtained by integrating this function:

$$E_{\text{cal}} = f_i \int f_{\text{GH}}(X) \mathrm{d}X, \tag{2.34}$$

where f_i is the "invisible energy" lost from neutrinos and high-energy muons that is not deposited into the atmosphere. The invisible energy has been estimated from SD data using hybrid events and it follows the power law

$$E_{\rm invis} = a\left(\frac{E_{\rm cal}}{E}\right)^a. \tag{2.35}$$

In recent years, improvements in this process have been realized by fitting to a slightly-modified GH function [95]

$$f(X) = \left(\frac{{\rm d}E}{{\rm d}X}\right)_{\rm max}\left(1+\frac{R}{L}(X-X_{\rm max}),\right)^{R^{-2}} e^{(X_{\rm max}-X)/RL}, \tag{2.36}$$

where the shape parameters R and L describe the width of the shower and its asymmetry, respectively. These parameters are defined as $R = \sqrt{\lambda/|X_0'|}$ and $L = \sqrt{|X_0'|\lambda}$, where $X_0' = X_0 - X_{\rm max}$ and are uncorrelated with χ_0 and λ.

This standard reconstruction procedure covers the sample of vertical events observed with the SD, which is the dataset used for this thesis, but there are two additional SD datasets generated by the Observatory that I will briefly summarize. The reconstruction for the infill array is similar to what is described here, but it uses $S(750)$ instead of $S(1000)$ as its shower size estimator. Finally, there is a separate reconstruction program for highly-inclined showers ($\theta > 60^\circ$), which are qualitatively different since the electromagnetic component is strongly attenuated in comparison to the muonic one. This reconstruction relies on studies of muon maps derived from simulations [96].

2.4.4 Systematic Uncertainties

The calorimetric $E_{\rm FD}$ determines the observatory's energy scale; understanding the FD's energy resolution is hence critical to our work. It will also be important later as it is the largest systematic uncertainty in the Δ-method (Chapter 3). The contributions to the energy

resolution are broadly split into three categories. I will briefly summarize them here [97]:

- **Atmosphere.** A combination of GDAS measurements and local balloon campaigns reduces our uncertainty from the composition of the molecular atmosphere to approximately 1%. Uncertainties from the two vertical aerosol optical depth measurements performed every quarter-hour through the data-normalized method contribute 1.2%–3.8%. Stereo measurements of showers from multiple FD sites allows us to estimate the uncertainty from the horizontal nonuniformities of aersosols as 1.6%–5%.

- **Calibration and Reconstruction.** The nightly relative calibrations (cal A, B, and C) contribute 1.3%. Long-term studies of the FD's performance yield a 2.5% systematic from drifts on the PMT gains, and systematic differences in telescopes contribute 3.5%. The uncertainties from the reconstruction fits (the geometry fits and the Gaisser-Hillas profile) contribute an additional 2.8%–4.6%, decreasing with energy. Extrapolations of the GH profile contribute an additional 2.2%, estimated through simulations.

- **Invisible energy.** As the invisible energy depends on the primary composition, composition uncertainties and shower-to-shower fluctuations propagate to systematic uncertainties in the energgy. These contribute 1.1%–0.6% and 0.3%–2.4%, respectively, both decreasing with energy.

These are summarized in Table 2.1.

Finally, we can discuss systematic uncertainties on the energy scale. There are six total contributions, most of which we have already briefly touched. I will briefly summarize them here:

- **The Fluoresence Yield.** Since the fluorescent yields are used to calculate the fluorescence light emitted during the shower's development, uncertainties in the fluorescence yield contribute to systematic uncertainties in our measured energy. This contributes 3.6% systematic uncertainty.

FD Energy Resolution	
Aerosol optical depth	1.2%–3.8%
Aerosol horizonal uniformity	1.6%–5%%
Molecular atmosphere	1%
Nightly relative calibrations	1.3%
Time drift of FD energies	2.5%
Mismatches between Telescopes	3.5%
Stat. error from fits	4.6%–2.8%
Profile extrapolation	2.2%
E_{inv} shower-to-shower fluc.	2.4%–0.3%
E_{inv} mass uncertainty	2.4%–0.3%
Total	7.6%–8.6%

Table 2.1: FD energy resolution, split into three sections: atmosphere, detector and reconstruction, and invisible energy. The dashed ranges span from $10^{17.7}$ eV to $10^{19.8}$ eV.

- **Atmosphere.** The fluorescence yield and scattering coefficients depend on properties of the atmosphere, especially its aerosol profile. This contributes 3.4%–6.2%, increasing with energy..

- **FD Calibration.** Uncertainties in the photometric calibration strongly impact the energy. This includes the wavelength-dependence of the telescope efficiency; the nightly relative calibrations with fixed sources A, B, and C; and the uncertainties in the absolute calibration at 375 nm from the drum measurement. This contributes 9.9%.

- **Invisible Energy.** The invisible energy correction applies an overall normalization factor on the Gaisser-Hillas integration and hence uncertainties on this factor translate directly into a systematic uncertainty on the final energy. This contributes 1.5%–3%, decreasing with energy.

- **Energy scale stability.** The stability of the correlation between E_{FD} and S_{38} provides an estimate of the stability of our energy scale over time. This contributes 5%.

The systematic uncertainties are tabulated in Table 2.1.

Energy Scale Systematic Uncertainty	
Fluorescence Yield	3.6%
Atmosphere	3.4%–6.2%
FD calibration	9.9%
FD profile reconstruction	6.5%–5.6%
Invisible energy	3%–1.5%
Energy scale stability	5%
Total	14%

Table 2.2: Systematic uncertainties in the energy scale. The ranges indicated with dashes begin at $3 \cdot 10^{18}$ eV and extend to the highest energies.

2.4.5 Hybrid Reconstruction

The hybrid reconstruction is primarily based on the FD reconstruction, but includes additional timing information provided from SD stations. Because a T3 FD trigger also sends an external trigger to the surface array, there is no reliance on meeting the strict trigger requirements for SD T5 events. The χ^2 function for the χ-angle fit becomes

$$\chi^2 = \sum_i \left(\frac{(t_i - t(\chi_i))^2}{\sigma(t_i)^2} + \frac{(t_{SD} - t(\chi_{SD}))^2}{\sigma(t_{SD})^2} \right) \tag{2.37}$$

. The timing information provided from SD stations, even as little as a single one, is extremely effective at eliminating degeneracies in the χ fit; see Figure 2.28 for an example showing the enormous impact of including SD stations into the χ fit.

2.5 AugerPrime

The Pierre Auger Observatory is currently undergoing a major upgrade called AugerPrime [98] that is designed to

1. understand the origin of flux suppression at higher energies by differentiating between source depletion and propagation effects;

2. examine the composition at the highest energies and investigate the existence of a

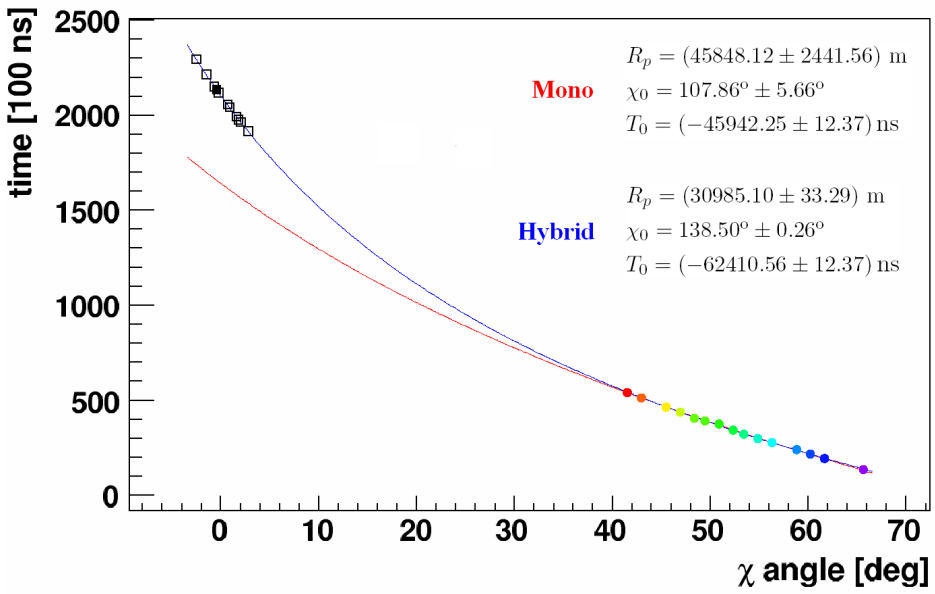

Figure 2.28: χ-angle fit for the shower axis reconstruction with and without including SD stations into the fit. Because the FD samples only a small portion of the shower track, it is ineffective at adequately sampling the curvature of this function to constrain the fit and introduces significant degeneracies. Inclusion of SD timing information to the fit significantly alleviates this problem.

proton fraction, which is important for future-generation cosmic ray observatories; and

3. elucidate hadronic interactions and muon production at the energy ranges that are inaccessible at current man-made accelerators.

There are six distinct parts to this upgrade:

- **SD Scintillator Detectors.** Each tank will be affixed with a scintillator (Surface Scintillator Detector, SSD) that compliments its tank measurements. Because scintillator detectors and Cherenkov tanks have different responses to the electromagnetic and muonic components of the shower, this addition will allow more sophisticated composition studies by providing event-by-event composition information. The SSD unit will consist of two scintillators, each $3.8\,\mathrm{m}^2$.

- **Increased SD dynamic range.** As discussed earlier in the text, SD signals experience saturation close to the core. A small fourth PMT (1" Hamamatsu R8619) will be

inserted into each SD tank to alleviate this problem and match the dynamic range of the WCD to the scintillator. This will allow for increased resolution in the sample of events were saturation recovery techniques are currently employed and allow low-gain saturated events to be used in the reconstruction. The planned ratio of gain between this new PMT and the existing ones is a 1/32. Its small dimensions complicate calibration using muons, but the signal ratios in showers may be used for on-the-fly calibration.

- **Upgraded SD electronics.** The Upgraded Unified Board (UUB) is a new board design implementing upgraded SD electronics capable of handling the burden of an additional PMT and the SSD. It digitizes signals at a rate of 120 MHz, a three-fold improvement in our current timing resolution. A more-powerful station-level processor and FPGA allow for the implementation of new triggers that include SSD triggers. It will also handle the calibration of the SSD, which is based on minimum-ionizing particles signals.

- **Underground AMIGA Detectors.** As part of the Auger Muons and Infill for the Ground Array (AMIGA) project [99], underground detectors will be installed beneath the 61 water-Cherenkov detectors of the infill array. Burying the detectors allows for complete shielding from the electromagnetic component of the shower from the earth, allowing a more precise study of the shower's muonic component. Each detector will include three scintillator modules 10 m^2 in area buried 2.3 m underground.

- **Higher FD duty cycle.** The FD currently operates only on clear moonless nights. Specifically, the sun must be 18° below the horizon and the moon must be below the horizon for 3 hours, constraints that limit the FD duty cycle to ∼15 %. AugerPrime proposes to increase this to ∼29 % by reducing the PMT supply voltage by a factor of ten. This will provide 40 % more events above 19.5 EeV, at the cost of losing some

lower-energy showers in the field-of-view.

- **Radio Upgrade.** Radio detection of UHECRs has been tested at Auger since 2011 with the Auger Engineering Radio Array (AERA) [100], which consists of 153 radio stations covering a $17\,\mathrm{km}^2$ area. This technique targets highly-inclined showers and relies on radio emission from interactions between shower particles and the geomagnetic field. The radio upgrade involves affixing a radio antenna to every SD station, which will make the Observatory the largest UHECR radio detector [101].

Chapter 3

An Updated Surface Detector Composition Study using the Delta Method

Although FD measurements are the gold standard for composition studies since they allow for direct observation of the composition-sensitive depth of maximum development $X_{\max}$ (see Section 1.4.3), the possibility of using the larger SD dataset for mass composition is enticing. In this section, we will discuss using the Δ method for this task.

The Δ method exploits the composition-sensitivity of signal risetimes in the SD's water-Cherenkov tanks. This method begins with the calculation of the station-level parameter Δ,

$$\Delta = \frac{t_{1/2} - t_{\text{bench}}}{\sigma_{RT}}, \tag{3.1}$$

where $t_{1/2}$ is the station risetime (the time taken to rise from 10% to 50% of the total signal, in nanoseconds), t_{bench} is the benchmark risetime (a data-derived function parameterizing the average behavior of the risetime), and σ_{RT} is the risetime uncertainty. A schematic is

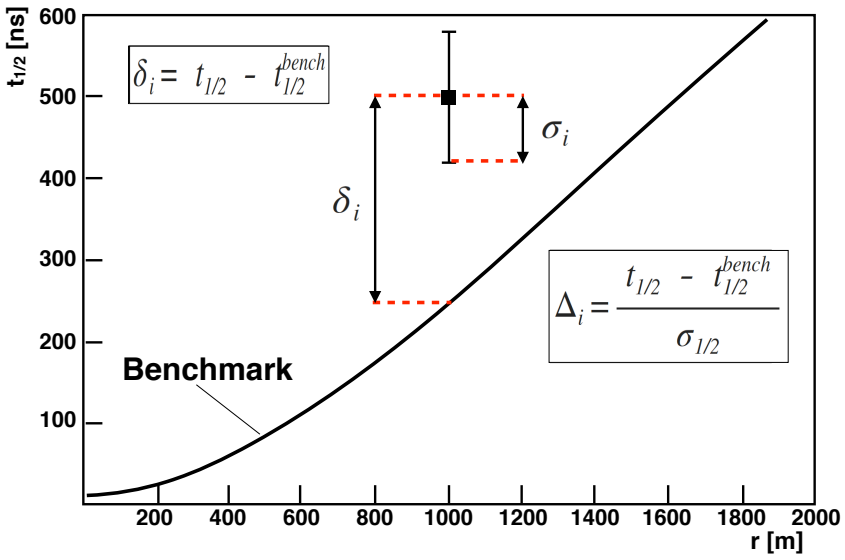

Figure 3.1: Schematic demonstrating the method for calculating Δ from the risetime, benchmark function, and risetime uncertainty.

shown in Figure 3.1. The composition sensitivity of Delta has been extensively demonstrated in the past through both simulation studies and empirical studies [15, 102]. Once the Δ measurement is obtained, a cross-calibration can be performed with the Golden Hybrid data between Δ_S (the average Δ for each shower) and the FD-measured $X_{\max}$, which permits the calculation of $X_{\max}^{\Delta}$, an SD-level composition measurement. Alternatively, Δ by itself can be used for composition studies. Previous publications using this method have demonstrated its feasibility and robustness [15, 102]. The purpose of the work presented in this thesis is to update this work to include the Obseratory's full modern dataset and improve our understanding of its systematics.

This chapter will begin by discussing the risetime's sensitivity to composition, outlining its calculation, motivating the Δ technique, and presenting our data selection. We will then use these data to produce several parameterizations essential to this method. We will close by applying this technique to our data and examining its systematic uncertainties.

3.1 Composition-Sensitivity of the Risetime

The SD reconstruction algorithms make use of the centroid time and total signal of SD traces. There is a third parameter that encodes important information about the shower: the temporal spread of arriving particles. An effective way of examining this quantity is the risetime of the traces. For our studies, we use the time taken to rise from 10% of the total signal to 50%. This allows us to ignore trailing effects from the beginning and end of the trace and focus primarily on the signal's muonic component.

The signal risetime is influenced by geometrical factors and shower properties. It is sensitive also to the ratio of the muonic and electromagnetic components of the shower, since the light-speed muonic component tends to arrive before the electromagnetic one (which suffers from scattering and attentuation in the atmosphere). Detector risetimes are a function of several variables: distance to the shower core, azimuth angle ζ, zenith, composition, and energy. I will briefly discuss the mechanisms for each:

1. **Distance.** Muons arriving from a shower developing farther away from a given station must travel greater distances to reach the detector, and their signals will thus be more temporally spread (see Figure 3.4). An example of this dependence, over a narrow bin of zenith angle and shower energy, is shown in Figure 3.2.

2. **Zenith.** Showers at higher elevations have their electromagnetic components more sharply attenuated by the atmosphere. Further, a 'beam' of light-speed muons builds along the shower axis that traverses more parallel to the array spacing, meaning risetimes become much quicker as zenith rises, and hence more difficult to resolve with the time resolution of the SD FADC. An example of this dependence, over a narrow range of shower energy and core distance, is shown in Figure 3.3.

3. **Azimuth angle ζ.** This is the local azimuthal angle relative to the direction antiparallel to the shower's travel (ie its shadow), not the absolute azimuthal angle in

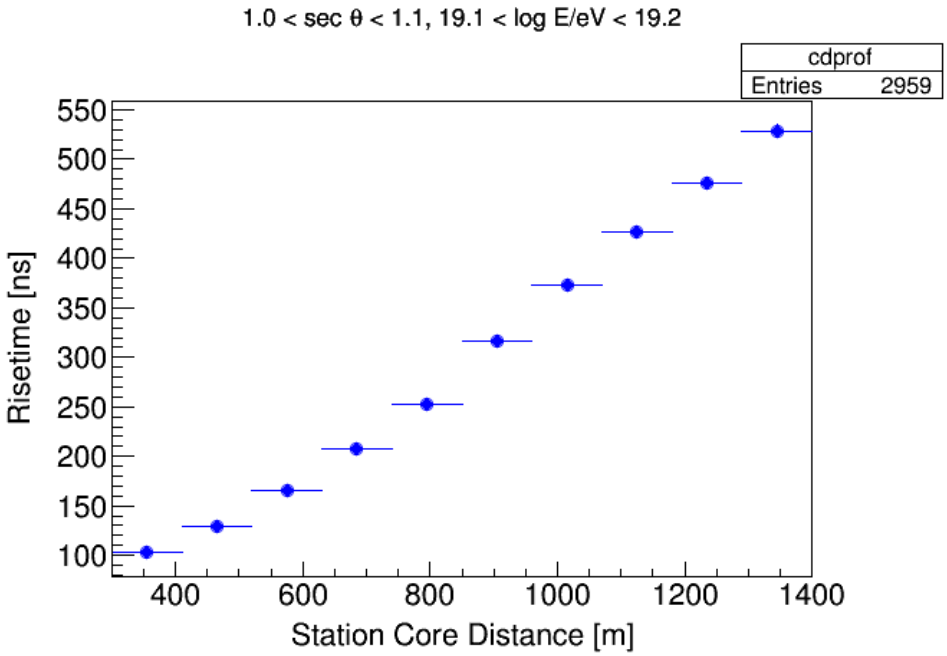

Figure 3.2: Distance dependence of the risetime from a narrow bin of zenith angle and shower energy.

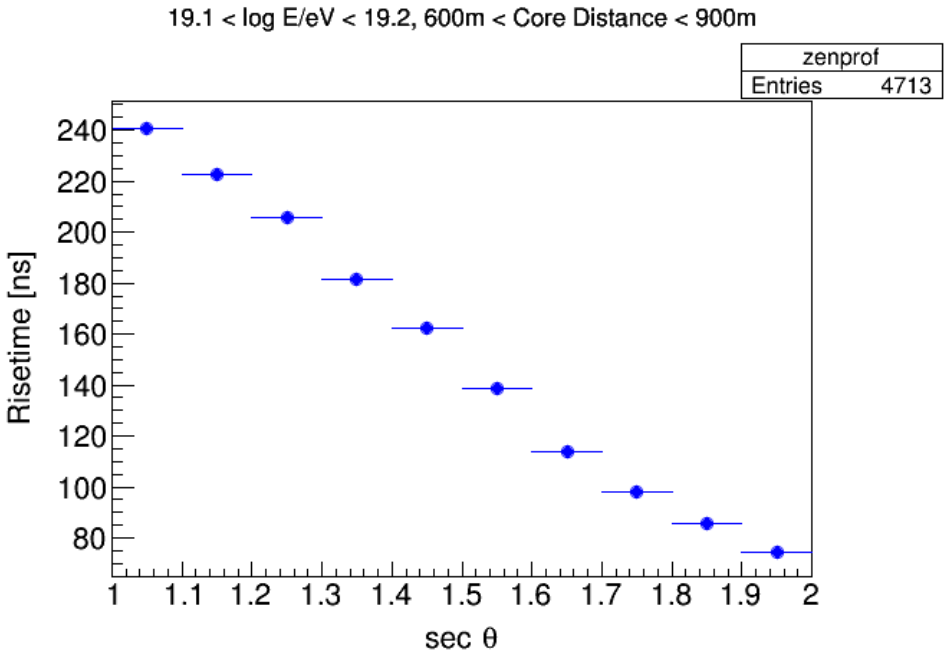

Figure 3.3: Distance dependence of the risetime from a narrow bin of zenith angle and shower energy.

the array. Azimuthal asymmetries emerge in the risetime footprint of showers due to two effects: the early-late effect, whereby the later-arriving sections of the shower have experienced a significantly-higher attenuation of their electromagnetic component; and complicated geometrical effects on the angular distribution of muons. This results in a sinusoidal dependence of the risetime with station ζ angle. This will be discussed in more detail in Section 3.4.2.

4. **Composition.** Showers that reach maximum development at different depths will have differing levels of electromagnetic attentuation and different arrival distributions of muons, due to geometrical effects resulting from their production depth. Heavier primary particles tend to produce slower risetimes. This is illustrated in Figure 3.5.

5. **Energy.** The energy of a shower affects its depth of first interaction and hence its X_{max}. Risetimes for more energetic showers will hence be slower.

To study mass composition with the risetime, we must understand the risetime's dependence on the above qualities and control for them. The azimuthal dependence can be corrected by parameterizing the nonuniformity as a function of station core distance and shower zenith angle. Risetimes for individual stations can then be azimuthally corrected. The distance and zenith dependence of the risetime will be parameterized by deriving a data-driven benchmark function that describes the risetime's average performance over the studied ranges. This leaves only the composition and energy dependence, from which we can study the elongation rate. To understand the significance of the observed deviations from the benchmark function, we must also understand the risetime's uncertainty. One of the major tasks of this thesis is deriving these three new parameterizations: the azimuthal correction, the risetime uncertainty, and the benchmark function, and this is the subject of Section 3.4. But first, we will discuss how to calculate the risetime from the SD traces and describe our data selection process.

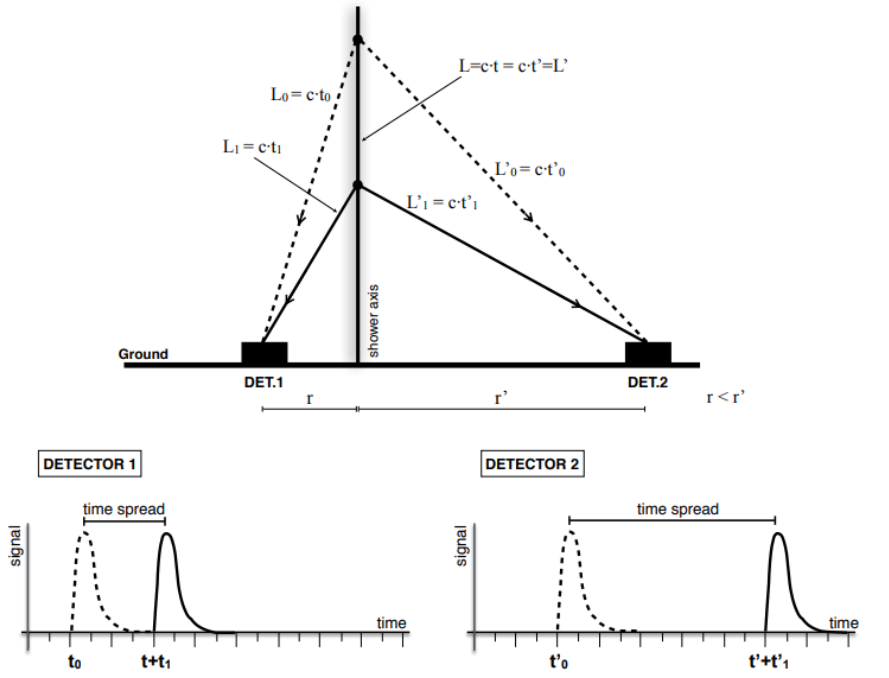

Figure 3.4: Schematic diagram illustrating the dependence of the risetime on core distance [15].

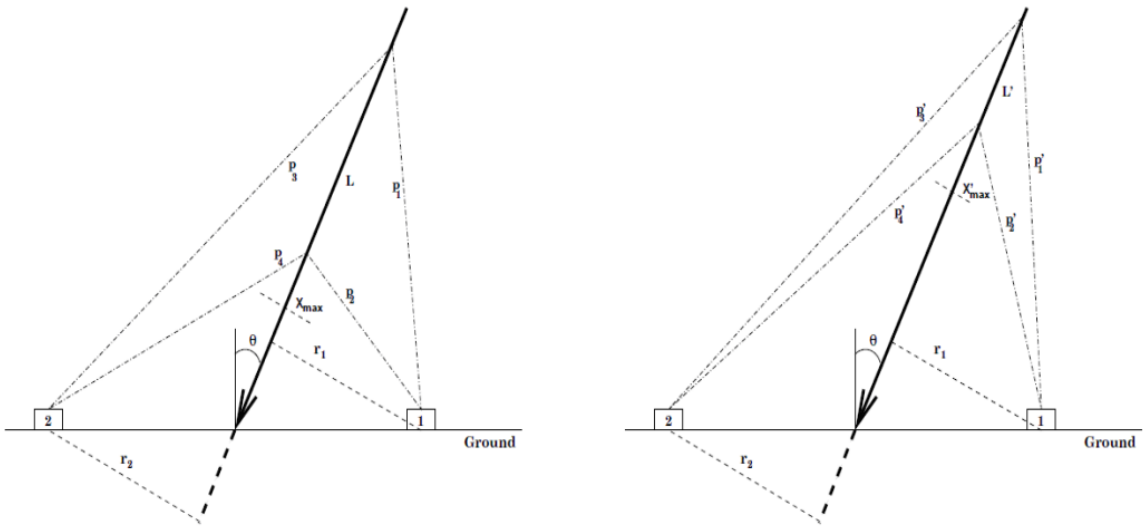

Figure 3.5: Schematic diagram illustrating the dependence of the risetime on depth of maximum development $X_{\max}$ [22].

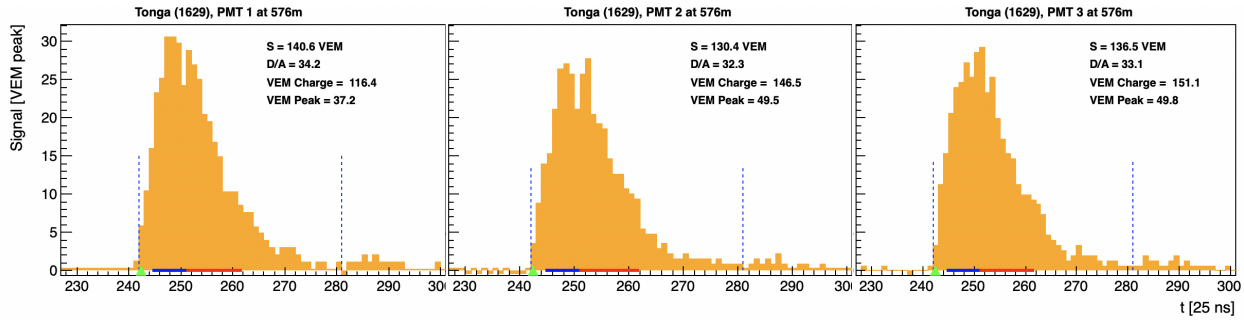

Figure 3.6: Event display showing the three SD traces comprising the signal from one tank of an event.

3.2 Risetime Calculation

Calculating $t_{1/2}$ is straightforward. First, the start and stop times must be accurately deduced. This is performed adequately by the Offline reconstruction algorithms, but there is one additional complication that will be discussed in more detail in Section 3.3. Next, the total signal in the trace is calculated. Then an algorithm iterates over the trace and tracks the running total signal. The bins where this total exceeds 10% and 50% are noted, and this time difference is saved as the risetime.

It is important to remember from Section 2.1 that SD stations have three PMTs (see Figure 3.6. Following some minor processing of the trace (as we will detail shortly), the risetime must be calculated individually for each PMT. The risetime of the station is then the average of the risetimes from the active PMTs in the tank. An example of this calculation is shown in Figure 3.7.

3.2.1 Direct Light Correction

In a small number of traces, sharp peaks (typically 2-3 time bins in width) are observed in single PMTs. These are from spatially-constrained physics processes that produce large signals. For example: electron backscatters, direct Cherenkov light production inside the PMT glass, and direct light from electron Cherenkov cones resulting from muon decays.

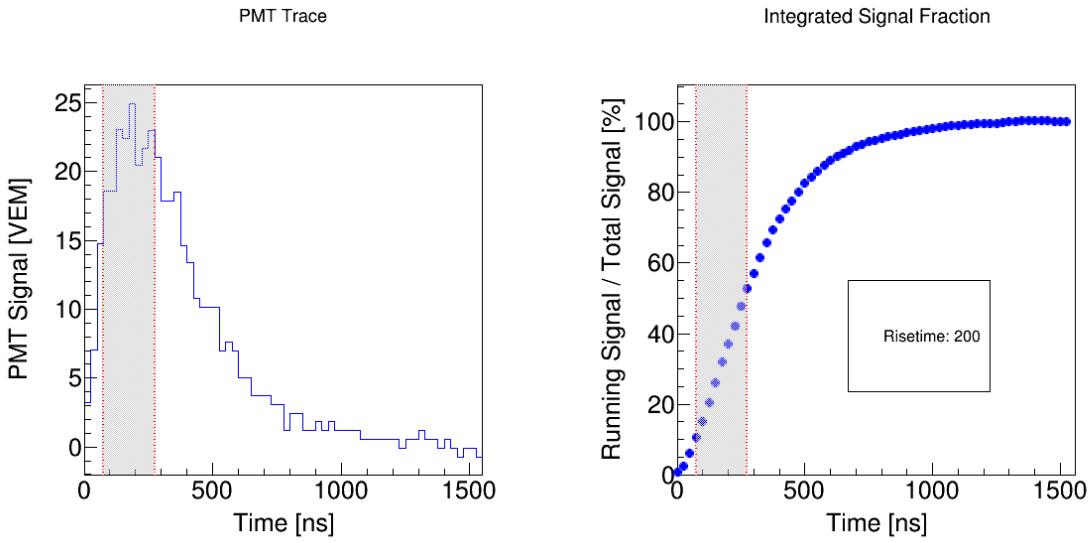

Figure 3.7: Example risetimes calculation from an SD PMT. Left: raw trace from the PMT. Right: fractional integrated signal over the trace. In both cases, the region highlighted in gray is the PMT's risetime.

This is hence called the direct light effect, and traces are processed to remove these abrupt spikes from individual PMTs.

The direct light correction begins by examining the bin-by-bin statistics of the three PMTs. For each bin, the mean and RMS of the signal value is calculated, and if one bin is significantly outside a tolerance threshold, it is replaced with the average of the other two bins. The purpose of this correction is to eliminate inflated risetimes from these spurious signals located on the trace's tail. This has been shown to impact the mean signals from the PMTs by less than 1%.

An example of this correction being applied is shown in Figure 3.8. In this trace, the correction algorithm found a large direct light signal around the 450 ns mark. The trace is shown both before and after the direct light correction is applied, and in this case, the risetime was unchanged.

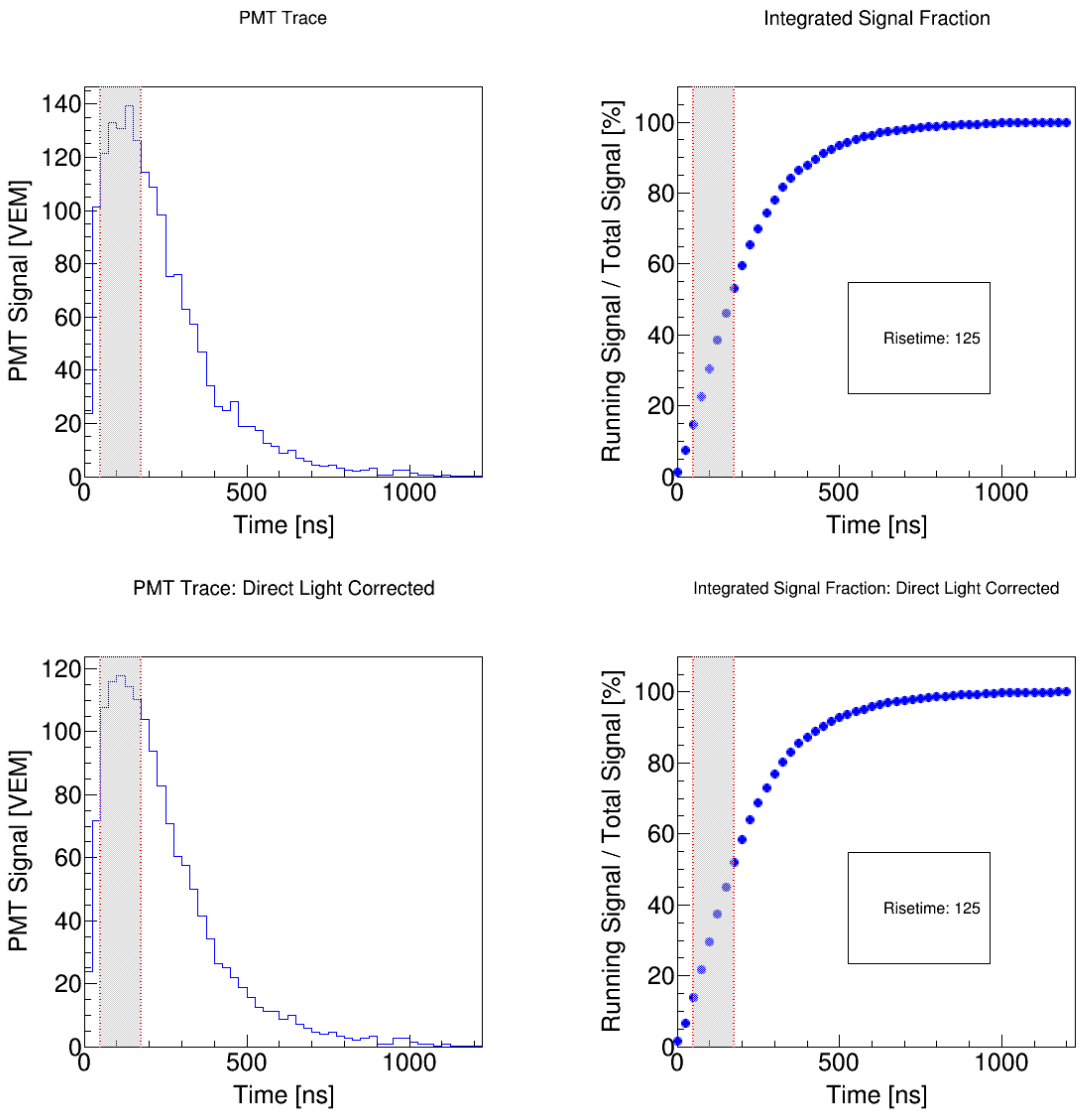

Figure 3.8: Top: trace and risetime calculation for a PMT signal with direct light (at $\sim 450\,\text{ns}$). Bottom: the same trace and risetime calculation after the direct light correction. In this case the correction did not change the risetime.

3.2.2 Deconvolution

The signals seen in the PMT are convolved with the detector response, producing an artificial lengthening of the signal. This results in larger risetimes. This is mainly attributed to particle reflections in the Tyvek tank liner.

This property of the detector is called the Single Particle Response (SPR), the response of the detector to a single particle (represented by a delta function), which has been measured experimentally using background muons. This effect is

$$F(t) = A\left(\exp\left(-t/67\right) - \exp\left(-t/13\right)\right), \tag{3.2}$$

where A is a normalization factor and the numbers 67 and 13 are the rise and fall times of the muon signal. It has been determined in previous works that deconvolution of station risetimes is not stable due to its extreme sensitivity to small negative signals, and hence this deconvolution is no longer used in our risetime studies. Because the Δ is data normalized, this does not affect the quality of our results.

3.3 Data Selection

We begin by selecting the subset of data for the risetime calculation. The standard ADST reconstruction is insufficient for the Delta method. In the standard Auger dataset, there is a large sample of events with anomalous risetimes, stemming from a problem in the analysis of high-gain FADC traces. These traces have their baselines overestimated and their stop times miscalculated. Since the PMTs are AC coupled, this leads to bins with negative signals that are problematic for the risetime calculation.

An algorithm by Ronald Ruijn recalculates the baselines, start times, and stop times for these traces to eliminate the negative signal problem. This is a necessary step in this analysis; however, this algorithm is not implemented by default in the Offline reconstruction,

```
<SdCalibrator>
<treatHGLGEqualInSignalSearch/>
<applyBackwardFlatPieceCheck/>
<decreaseLGFlatPieceTolerance/>
<alwaysCalculateSignalStartTimeFromHighGain/>
</SdCalibrator>
```

Figure 3.9: Configuration parameters for the SdCalibrator module to enable Ronald's correction.

and so the dataset will exhibit reconstruction differences from this correction. The Offline configuration file for the `SdCalibrator` module that enables Ronald's correction is shown in Figure 3.9. To test these differences, we took events with the same SDID from both datasets and compared the reconstruction using basic event properties, such as zenith and energy. On average, the zenith angle of events changed by about $0.03^\circ \pm 0.5$, but around 20 events have a change in zenith angle of above 20°, with a few as high as 50°, hinting that perhaps there is some issue with timing information with these events. Energy differed on average by $\sim 10^{16} \pm 3 \cdot 10^{17}$). Both of these shifts are on average well within the resolution of the detector.

3.3.1 Event- and Station-Level Cuts

The base dataset is reconstructed with Offline v3r99p2a (ICRC2019), modified with Ronald's correction for the negative signal problem. The reconstruction was performed on the University of Chicago's Midway Cluster, using automation scripts written by the author. From this, we apply several cuts to obtain the science data. These are performed both at the event and the station level.

The event-level cuts, are as follows:

1. log(E) > 18.5 (full efficiency of the SD)

2. Zenith angle $< 60^\circ$ (zenith range of the standard reconstruction)

3. No Bad Periods

4. No Lightning Events.

These are standard event-level cuts applied to most analyses using the SD data.

The station-level cuts are more specific to our analysis. They are:

1. Total signal $> 5\,\mathrm{VEM}$

2. Risetime $> 40\,\mathrm{ns}$

3. Core-Distance Cuts

4. Removal of Bad PMTs.

These station-level cuts merit some discussion. The minimum on the risetimes is imposed for two reasons. One is to restrict our analysis to the regime where the 25 ns resolution of the FADC traces can feasibly resolve risetimes. The second is that because of the method we use for azimuthal correction (see Section 3.4.2), post-correction risetimes below 40 ns are considered unphysical. The signal-level cuts are intended to remove stations for which small local Poisson fluctuations dominate the station signals.

The cuts on core-distance are more subtle. If insufficient particles arrive at a detector to adequately sample the distribution of arrival times, $t_{1/2}$ becomes ill-defined. We want to select only the range of core distances where we have unbiased values of $t_{1/2}$. This can be studied by examining the quantity $t_{1/2}/r$. Restricting our analysis to the regime where this quantity is linear ensures that the risetimes are well-defined. Because the shower size grows with energy, this core distance threshold is expected to have some energy dependence. A few example plots examining this quantity are shown in Figure 3.10. The cuts used are:

$$300\,\mathrm{m} < r < 1400\,\mathrm{m}, \qquad \log E < 19.5 \tag{3.3}$$

$$300\,\mathrm{m} < r < 2000\,\mathrm{m}, \qquad \log E > 19.5 \tag{3.4}$$

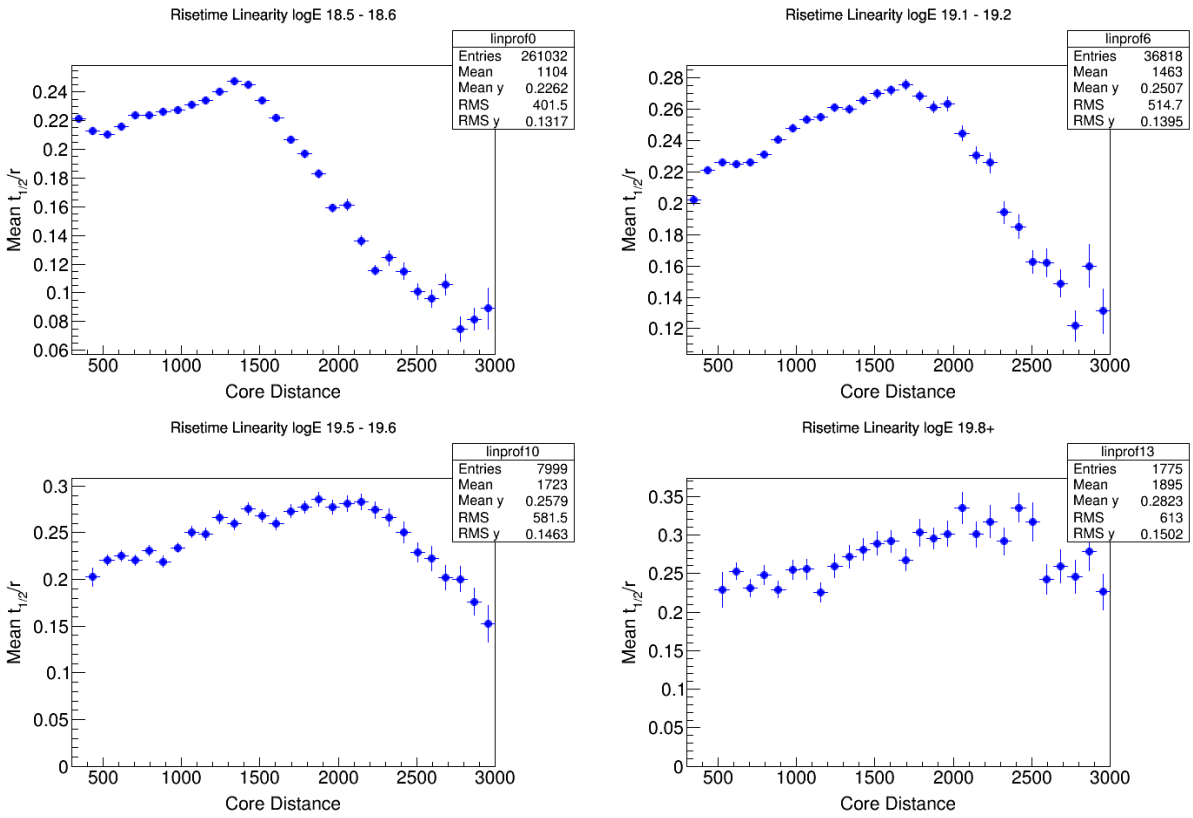

Figure 3.10: Linearity of risetime over core distance as a function of core distance.

Finally, it has been shown that events with a higher number of stations are correlated more strongly with $X_{\max}$ and are hence more composition sensitive, so we keep only events with at least three passing stations. These station-level cuts result in the removal of $\sim 14\%$ of the data.

Our final dataset includes 602531 stations from 153884 SD events.

3.4 Updated Parameterizations

To see the dependencies in calculating Δ, we can rewrite Equation 3.1 as

$$\Delta = \frac{t_{1/2}^{\text{corr}}(t_{1/2}, \zeta, \theta, r) - t_{\text{bench}}(\sec\theta, r)}{\sigma_{RT}(r, S, \sec\theta)}, \tag{3.5}$$

where S is the average measured tank signal in VEM and r is the shower-transverse-plane (STP) distance of the tank in meters. Our task is now to obtain parameterizations for the azimuthal correction $t_{1/2}^{\mathrm{corr}}$, the benchmark function t_{bench}, and the risetime uncertainty σ_{RT}.

3.4.1 Uncertainty Calculation

A new parameterization of the risetime uncertainty is essential, because prior to this work, studies on risetimes from events with $\sec\theta > 1.45$ have relied on extrapolations of an older uncertainty parameterization that does not accurately describe its behavior at higher energies.

To calculate the risetime uncertainty, we use twins and pairs. Twins (sets of stations placed within a few meters) are more robust, as they allow multiple measurements at a single core distance, but these stations are few in number. Pairs (sets of stations in close proximity of core distance) must be azimuthally corrected for different levels of shower attenuation. Further, for geometric reasons, no pairs exist below $\approx r = 750\,\mathrm{m}$, necessitating the inclusion of twins. It has previously been shown that both datasets provide compatible results within their common ranges, so we combine both twins and pairs into a single sample to study the uncertainty. Because the number of available twins and pairs has expanded significantly since the original Δ study, it is no longer necessary to join the 1500 m dataset with the 750 m one to obtain a full uncertainty parameterization.

At the station level, the uncertainty is $\propto 1/\sqrt{S}$, a reflection of the Poisson statistics associated with counting particle number. This adds in quadrature with the small uncertainty associated with the discrete binning of signals in the SD, leading to

$$\sigma_{1/2} = \sqrt{\left(\frac{J(r,\theta)}{\sqrt{S}} + \left(\sqrt{2}\frac{25}{\sqrt{12}}\right)\right)}, \tag{3.6}$$

where $J(r,\theta)$ is the uncertainty parameterization over zenith angle and core distance we are

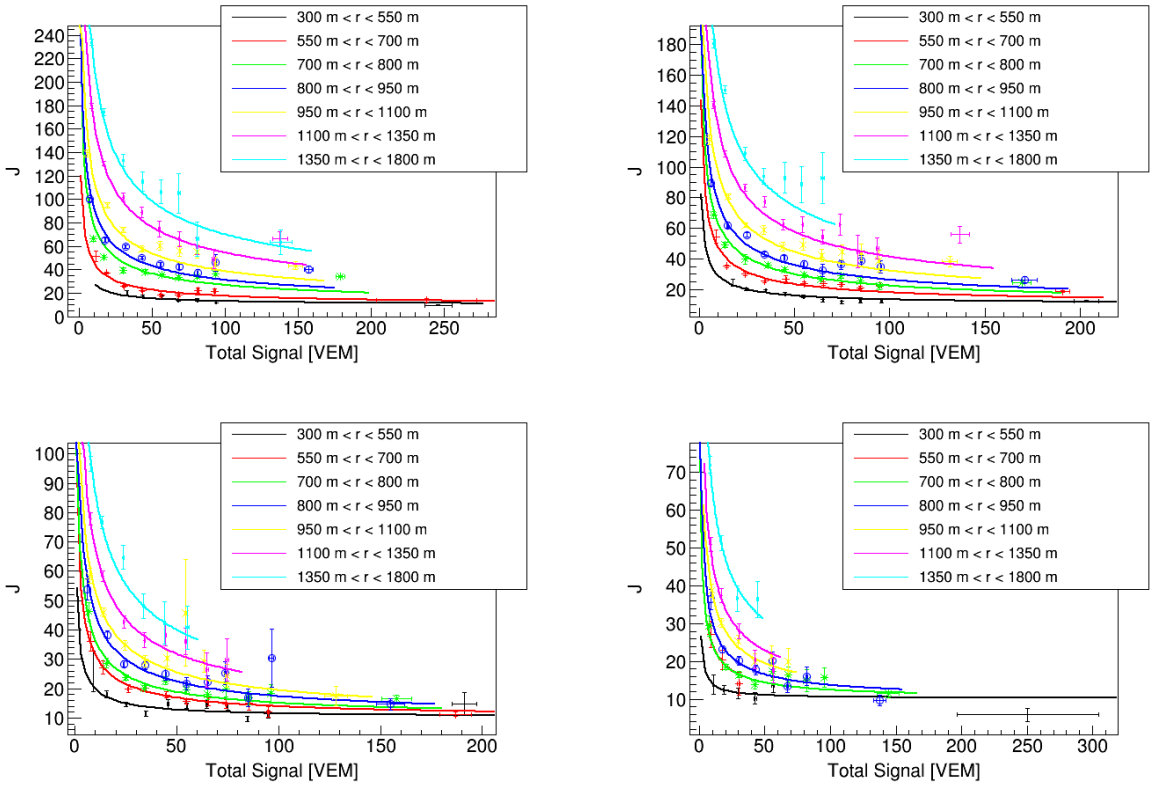

Figure 3.11: Uncertainty fits for four bins of the zenith angle.

attempting to derive.

The data is split and binned in three dimensions: station signal, core distance, and zenith angle. We first fit $J(r, \theta)$ to each bin in core-distance, from which we find a linear dependence in r; the coefficients of this linear relationship are polynomials $\sec\theta$, so in total

$$J(r, \theta) = p_0(\theta) + p_1(\theta) \cdot r. \tag{3.7}$$

Shown in Figure 3.11 are some example uncertainty fits performed at the station-level for two ranges of core distance. From each of these fits we obtain a value of $J(r, \theta)$, an input for the core-distance fit. The result of the core-distance fit is shown in Figure 3.12.

Although the previous uncertainty parameterization [22] found p_0 and p_1 behaved linearly as a function of $\sec\theta$, we discovered that at higher zenith angles, curvature appears at its

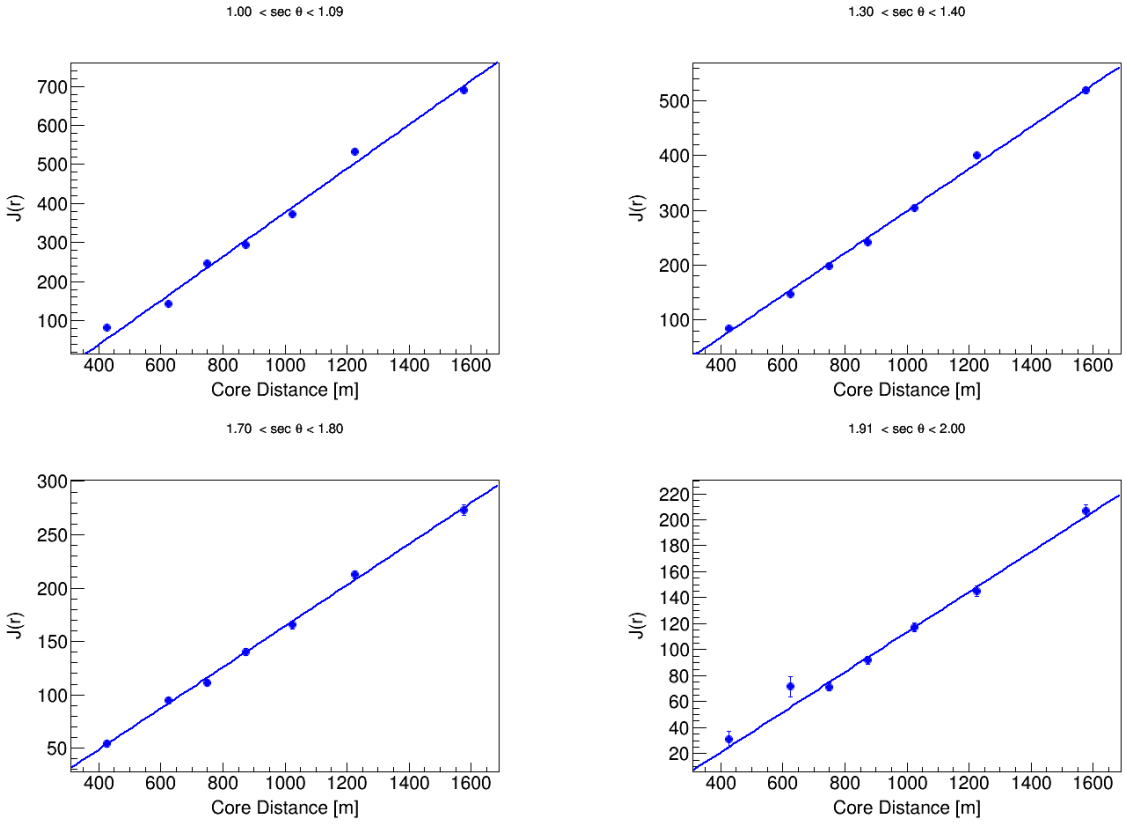

Figure 3.12: The linear core-distance fits parameterizing the parameter J obtained from the signal fits in Figure 3.11.

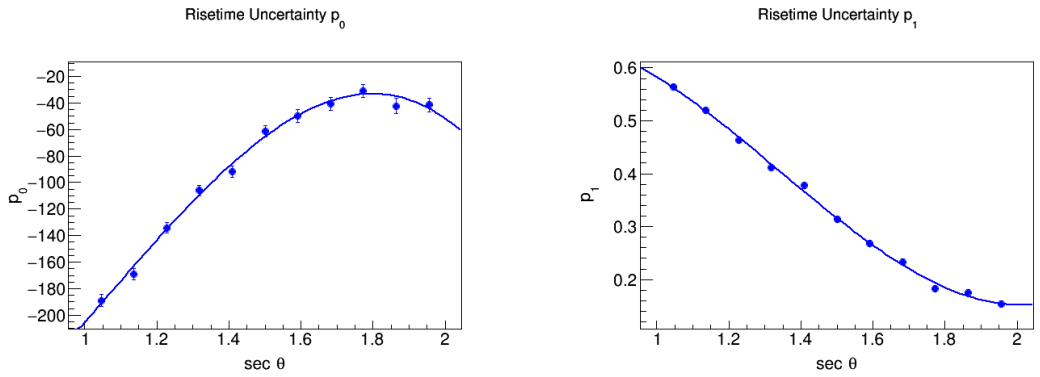

Figure 3.13: The fit over zenith angle to obtain the final parameterization of the uncertainty. The left figure shows parameter p_0, and the right shows parameter p_1.

Parameter	Value
a_0	-482.147
a_1	109.002
a_2	299.497
a_3	-123.727
b_0	0.0984858
b_1	1.69652
b_2	-1.64451
b_3	0.405379

Table 3.1: Parameters for the new risetime uncertainty fit.

upper range, necessitating the use of a higher-order polynomial fit; see Figure 3.13. We chose a third-degree polynomial for this fit.

The difference between the new and former uncertainty parameterization occurs primarily at high zenith angles ($\sec\theta > 1.7$) where curvature emerges. Figure 3.14 shows a comparison between the uncertainty of stations from the science data in these two ranges. Note the absolute offset at the highest zenith angles, indicative of the previous parameterization's failure to account for this curvature. The overall impact of this change is small, resulting in a $\sim$2% RMS change in the value of Δ. A table of the parameters of this fit is shown in Table 3.1.

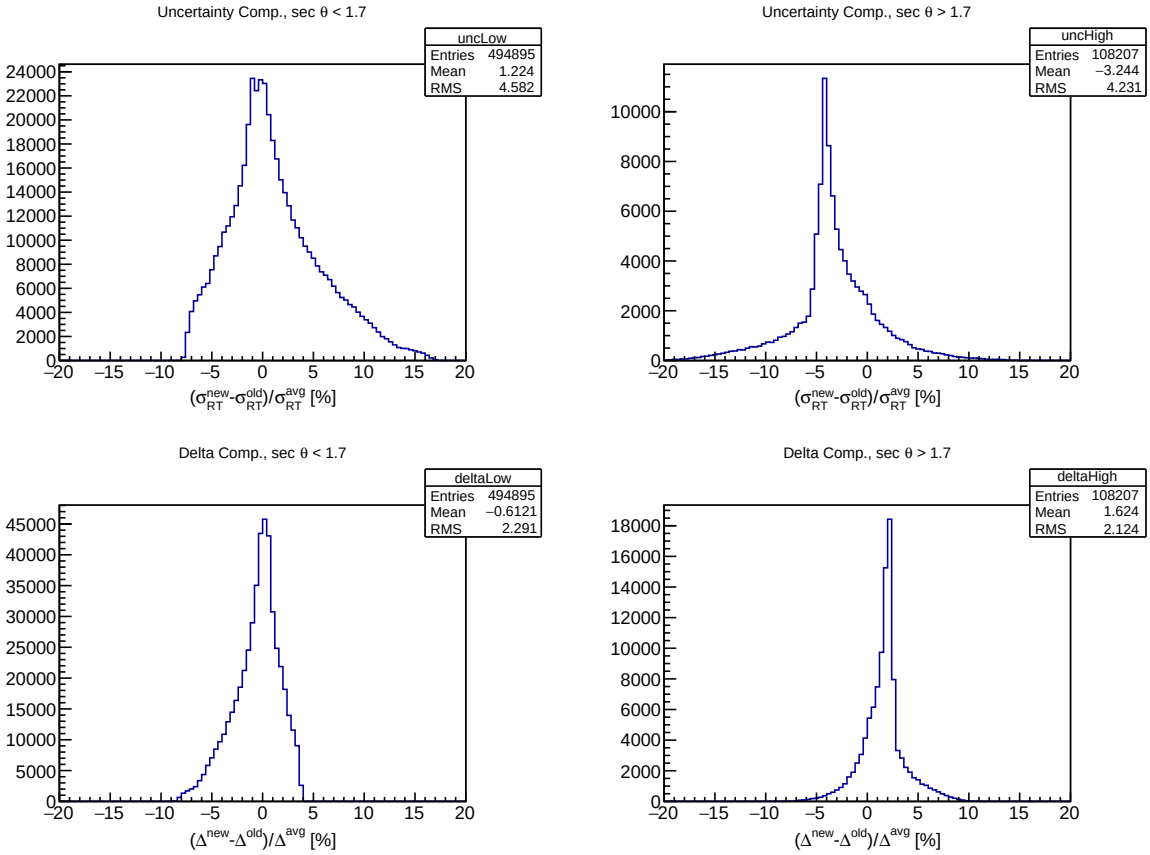

Figure 3.14: Comparison between the new and old uncertainty parameterizations in two ranges of zenith angle across the science data.

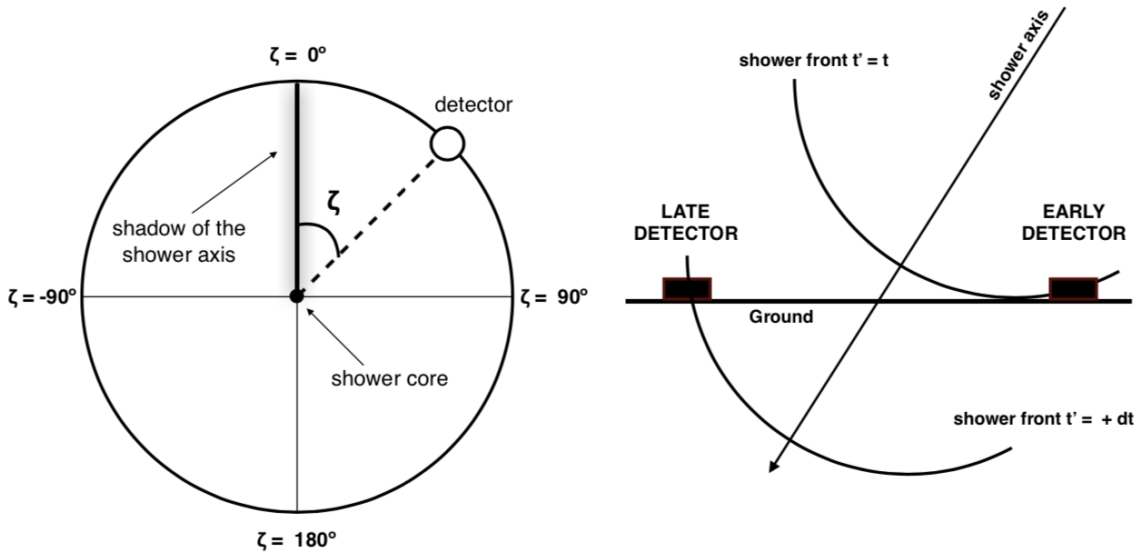

Figure 3.15: Left: definition of the angle ζ with respect to the shower axis. Right: schematic representation of the early-late effect.

3.4.2 Azimuthal Correction

When a shower arrives at a zenith angle $\theta > 0$, azimuthal asymmetries result at the ground level from two sources. The first is the early-late effect: particles arriving on the shower's "early" side propagate through significantly less atmosphere than those arriving on its "late" side, resulting in strong attenuation of the shower's electromagnetic component. The second is due to geometrical effects and primarily affects the angular distribution of muons, resulting in more muons at the late detectors. In order to use station risetimes as composition-sensitive variables, these nonuniformities must be corrected.

A schematic of the problem is shown in Figure 3.15. The risetime asymmetry is defined in terms of the angle ζ from the shower axis shadow. The "early" part of the shower is hence $\zeta = 0°$, and the "late" part is $\zeta = 180°$. Each detector measuring the event can be expressed in a local coordinate system consisting of its ζ angle and its distance to the shower core.

Our task is now to construct a data-driven parameterization of this azimuthal asymmetry.

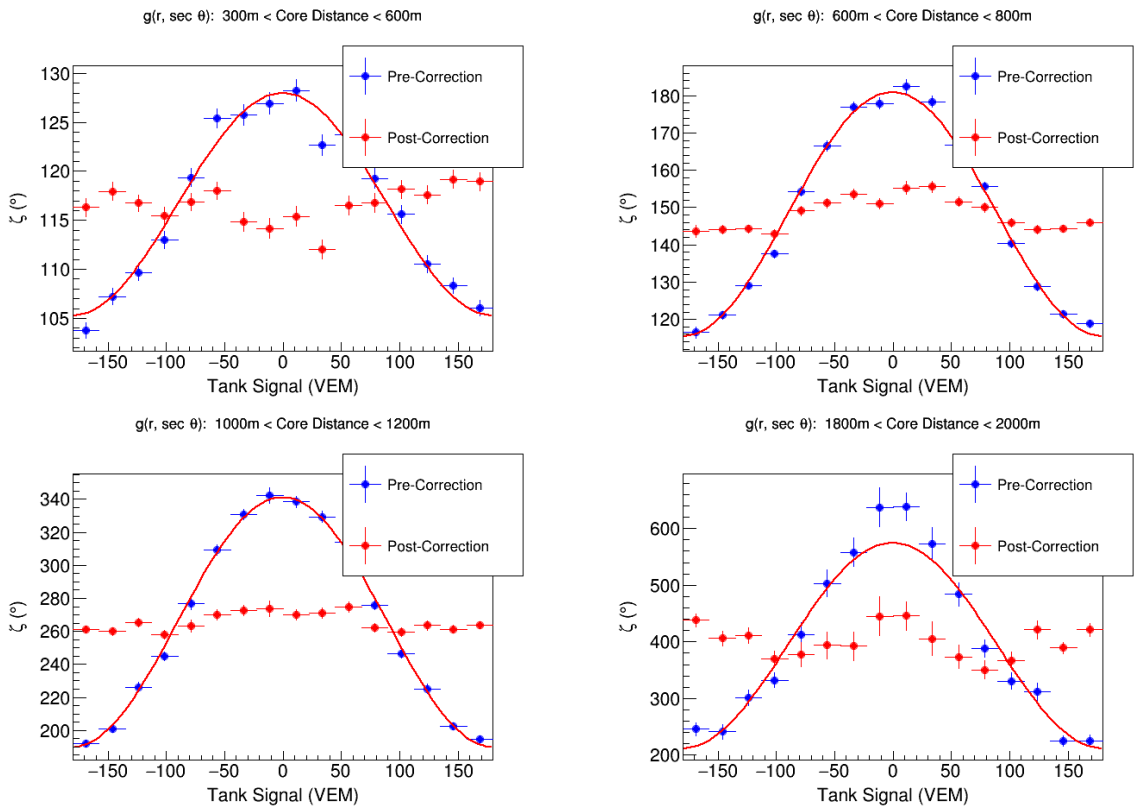

Figure 3.16: Sinusoidal fits from the four of the azimuthal correction bins, showing the dependence of the risetime on ζ with and without the correction. See Equation 3.8.

This asymmetry can in general be described by a cosine function,

$$t_{1/2}(\zeta) = f + g(r, \sec\theta)\cos(\zeta), \tag{3.8}$$

the amplitude of which $g(r, \sec\theta)$ is dependent upon the station core distance r (in meters) and the incident shower zenith angle. To understand the behavior of this function, we bin the data in both dimensions and parameterize the behavior of g. For each bin, we fit the simple cosine function

$$t_{1/2}(\zeta) = a + b\cos\zeta. \tag{3.9}$$

A few examples of this fit are shown in Figure 3.16. Once this multi-dimensional space is

Parameter	Value
m_0	-0.00127155
m_1	0.00263646
m_2	-0.00169657
m_3	0.00350688
n_0	78.6158
n_1	-225.949
n_2	193.301
n_3	-50.023

Table 3.2: Parameters of the new risetime azimuthal correction.

fit with these sinusoidal functions, we step along slices of it and attempt to parameterize its behavior. In each bin i of $\sec\theta$, we find $g(r, \sec\theta_i)$ can be well-described by the power-law function

$$g(r, \sec\theta_i) = n + mr^2. \tag{3.10}$$

Examining the behavior of n and m as a function of $\sec\theta$, we find that a new function is needed to accurately describe the behavior. Previous studies have used a simple fit $\propto r^2$, tracking the evolution of its coefficient as a function of $\sec\theta$; however, we find the function $n+mr^2$ better describes the data, and we will examine the zenith-dependence of both n and m (see Figure 3.17). In total, then, we have

$$g(r, \sec\theta) = \left(N(\sec\theta) + M(\sec\theta)r^2\right), \tag{3.11}$$

and the final risetime correction is then

$$t_{1/2}^{\text{corr}} = t_{1/2} - \left(N(\sec\theta) + M(\sec\theta)r^2\right)\cos\zeta. \tag{3.12}$$

The final fits for these parameters are shown in Figure 3.18, and the parameters are listed in Table 3.2.

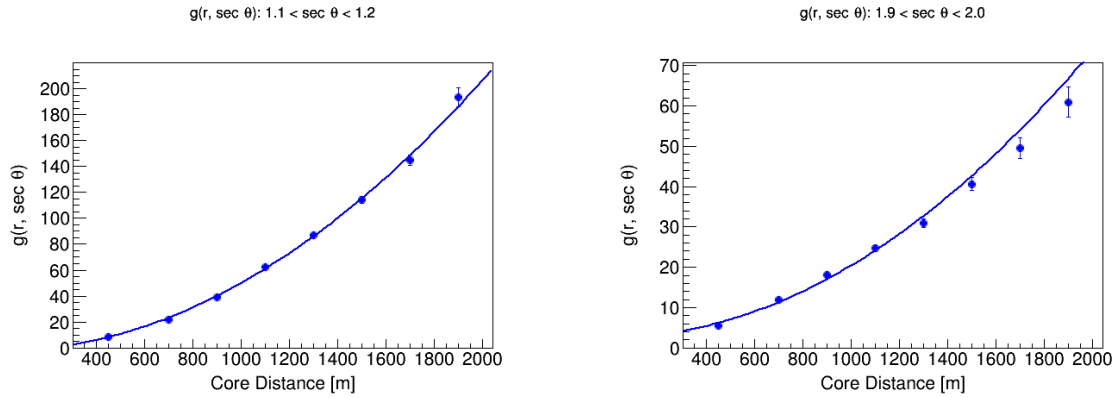

Figure 3.17: Dependence of n and m as a function of core distance for bins of fixed zenith. See Equation 3.10.

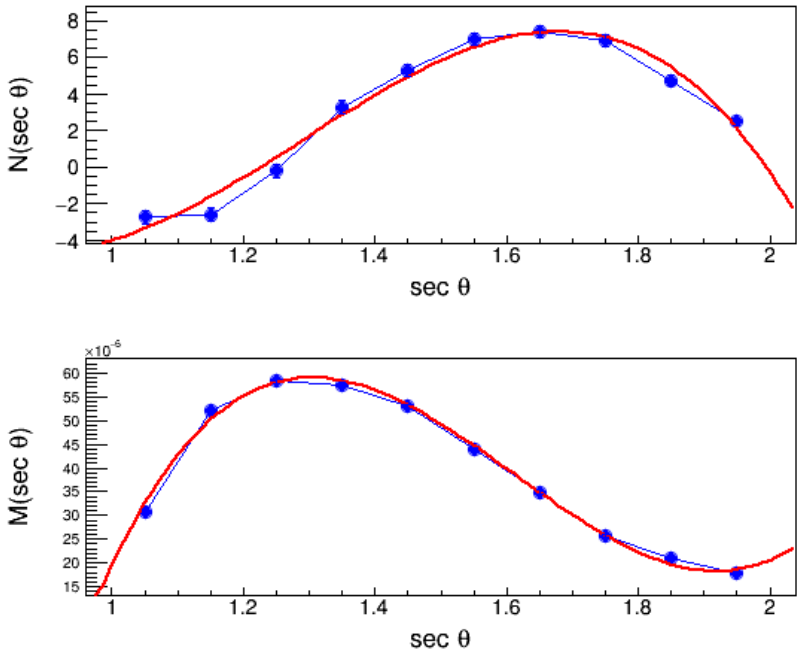

Figure 3.18: Fits of the parameters n and m that describes the azimuthal correction for the station risetimes. These are $N(\sec\theta)$ and $M(\sec\theta)$ from Equation 3.12.

3.4.3 Benchmark Function

Before we calculate the benchmark function, we must split the data in two parts. As covered in Section 2.1, the SD data comes from two different channels: the high-gain channel and the low-gain channel. The low-gain channel is used when the high-gain channel is saturated, and the ratio of their gains is 1/32. However, there is a small but consistent ($\sim 7\,\mathrm{ns}$) systematic difference in the risetimes between the two channels. Because of this, the two datasets must be separated and a benchmark function must be calculated for each.

First, we select a benchmark energy bin, motivated by obtaining a balance of saturated and non-saturated signals in both samples across the relevant ranges of core distance. Because stations near the core are more likely to be saturated, this ratio evolves as a function of core-distance and energy. A few examples of this behavior are shown in Figure 3.19. We select the energy bin $19.1 < \log E < 19.2$ for our benchmark function.

First we isolate only the events inside the benchmark energy bin. We then split the data into bins of $\sec\theta$. The benchmark function for high-gain saturated detectors is given by:

$$t_{1/2}^{\mathrm{sat}} = 40 + \sqrt{A_{\mathrm{sat}}(\theta)^2 + B_{\mathrm{sat}}(\theta) r^2} - A_{\mathrm{sat}}(\theta), \tag{3.13}$$

where r is the core distance. For the non-saturated detectors, we keep the same parameters A_{sat} and B_{sat} (fixing them in the fit) and fit the correction factor $N(\theta)$:

$$t_{1/2}^{\text{non-sat}} = 40 + N(\theta)\sqrt{A_{\mathrm{sat}}(\theta)^2 + B_{\mathrm{sat}}(\theta) r^2} - A_{\mathrm{sat}}(\theta). \tag{3.14}$$

This fit is performed for each $\sec\theta$ bin. A few example fits are shown in Figure 3.20. Next, we parameterize the behavior of A_{sat}, B_{sat}, and N over $\sec\theta$. This fit is split into two stages, one below $\sec\theta = 1.45$ and one that extends up to $\sec\theta = 2$. We use the following

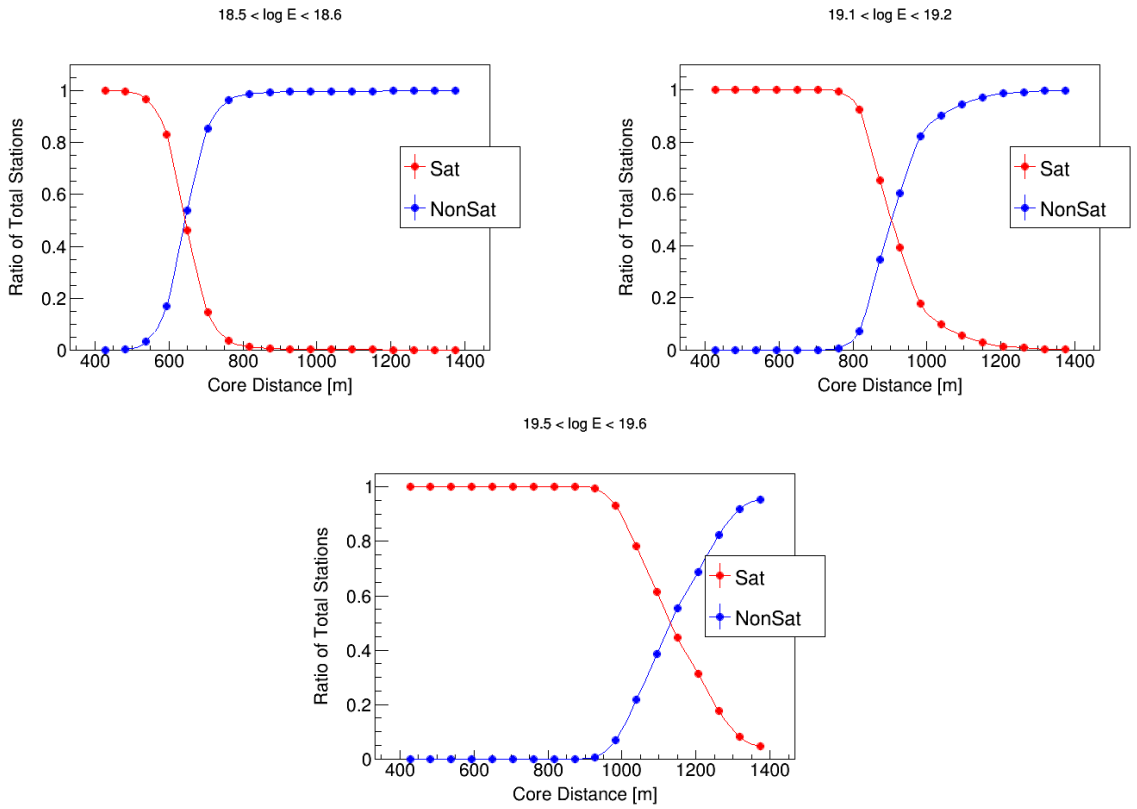

Figure 3.19: Ratios of saturated and non-saturated stations calculated across three energy ranges. The $19.1 < \log E < 19.2$ bin was selected as the benchmark bin since it achieves a balance of both.

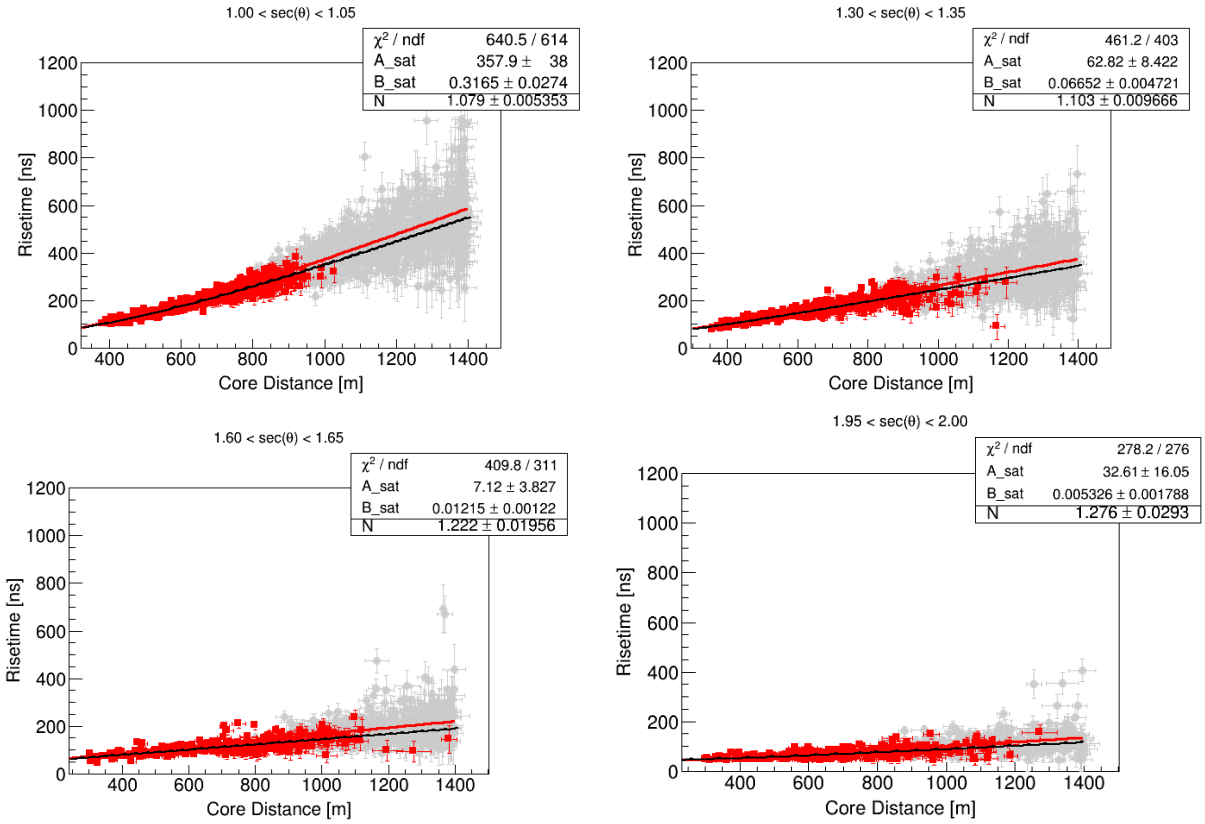

Figure 3.20: Benchmark fits for four bins of $\sec\theta$.

fit functions for the parameterization:

$$A_{\text{sat}}^{\text{low}} = a_0 + a_1(\sec\theta)^{-4}, \qquad A_{\text{sat}}^{\text{high}} = a_2 + a_3(\sec\theta)^{-4} \tag{3.15}$$

$$B_{\text{sat}}^{\text{low}} = b_0 + b_1(\sec\theta)^{-4}, \qquad B_{\text{sat}}^{\text{high}} = b_2 + b_3(\sec\theta)^{-4} \tag{3.16}$$

$$N^{\text{low}} = n_0, \qquad N^{\text{high}} = n_1 + n_2\sec\theta. \tag{3.17}$$

The resulting parameters a_n, b_n, and N_n define the benchmark function (Figure 3.21), and the fit results are tabulated in Table 3.3. Because of the discrepancy in the final two bins, we have excluded them from the analysis. This qualitatively-different behavior in the final two bins is a reflection of the SD FADC's time resolution failing to resolve these faster signals. It is possible to include these final two bins by instead calculating a benchmark function using a linear interpolation between each individual data point of the benchmark

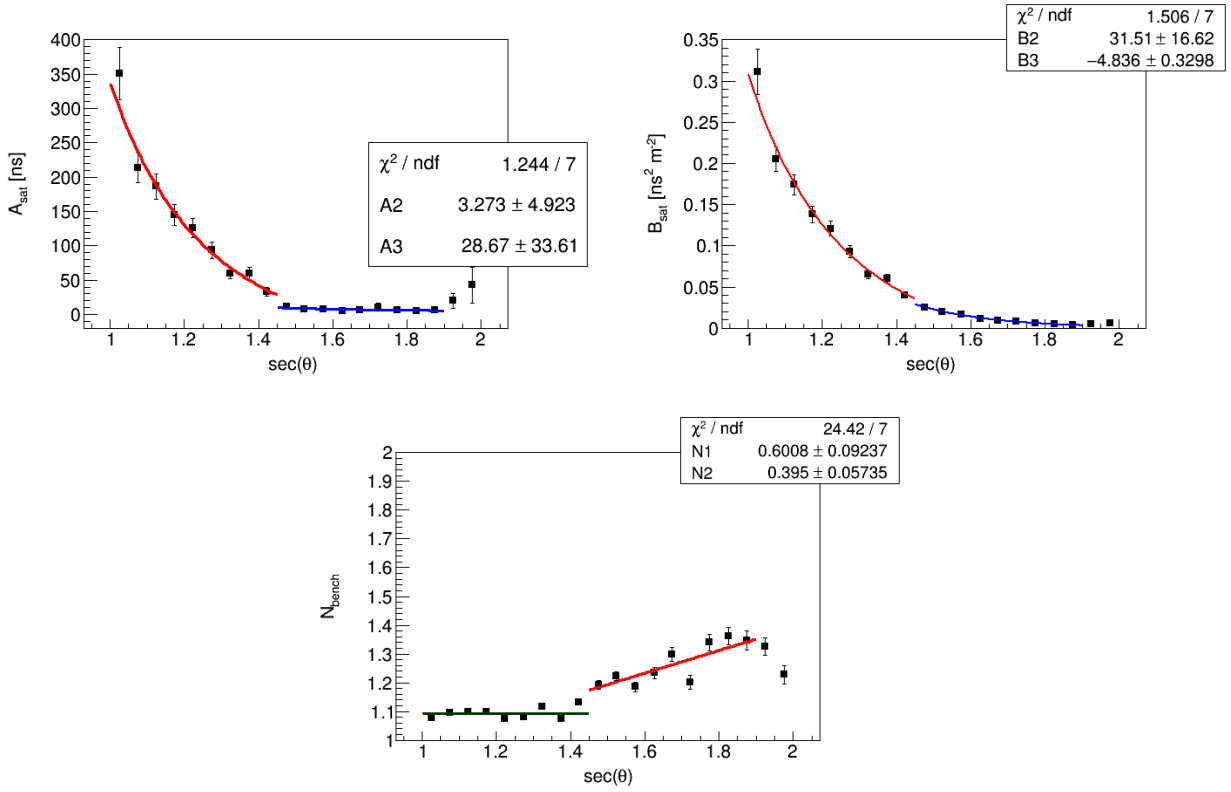

Figure 3.21: Benchmark parameter fits for A, B, and N for the new dataset. A is shown on the top left, B on the top right, and N on the bottom. The final two bins ($1.90 < \sec\theta < 2.00$) are excluded from the fit due to their significant break in behavior.

function. This is an attractive possibility because it further expands the sky coverage and statistics of the analysis, but the work presented in this thesis will focus on this fitting method. We will note, however, that a cross-check has been performed using the linear interpolation method and it found no significant difference in final results.

3.5 Application to the Data

Now that we have calculated the station risetimes, corrected them for azimuthal asymmetry, and parameterized the necessary functions to calculate Δ, we can apply our work to the data.

Parameter	Value
a_0	-66.5887
a_1	416.891
a_2	2.77961
a_3	34.0025
b_0	-0.0484237
b_1	0.0367379
b_2	31.8829
b_3	-4.83497
n_0	1.0887
n_1	0.586086
n_2	0.397275

Table 3.3: Parameters of the risetime benchmark function fit.

3.5.1 Delta Calculation

First, we calculate the Delta parameter at the station-level. Again, we wish to only keep events with at least three stations measuring a value of Δ. We then calculate the average Δ for each shower, Δ_S:

$$\Delta_S = \frac{1}{N_{\text{stations}}} \sum_{i}^{N_{\text{stations}}} \Delta_i \tag{3.18}$$

Δ_i is defined as a pull distribution, and Δ_S is the sum of several pulls, normalized by the number of stations performing the measurement. Hence we expected σ_{Δ_S} to decrease as we add stations. Although there is a small contribution to the uncertainty of Δ_S from the parameteriations used to calculate the Δ_i, this contribution is tiny. Straightforward error propagation reveals our expression for the uncertainty in Δ_S:

$$\sigma_{\Delta_S} = \frac{1}{\sqrt{N}}. \tag{3.19}$$

Now we have all the tools we need for this analysis. The overall distribution of Δ_S is shown in Figure 3.22. Before we present our results as an elongation rate, we will first

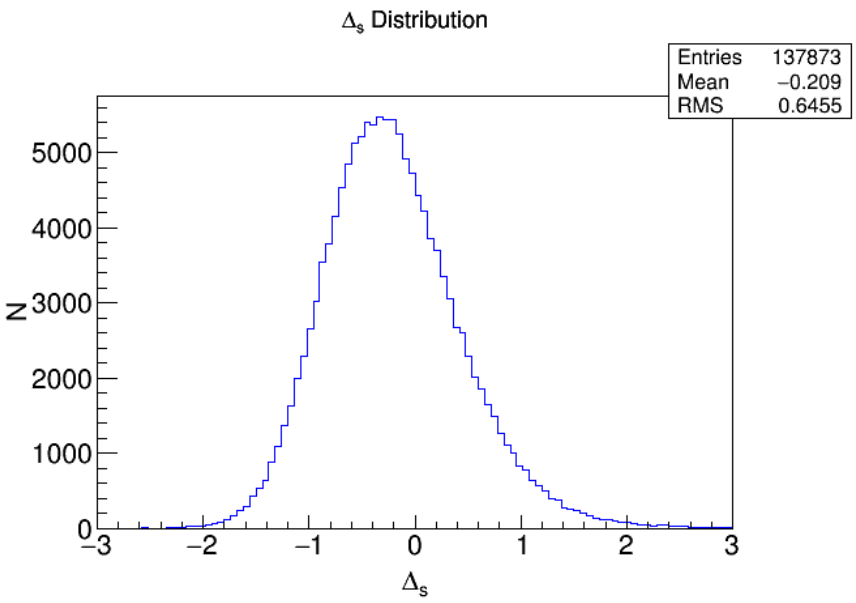

Figure 3.22: Histogram of Δ_S.

examine the systematic uncertainties in this dataset.

3.5.2 Systematic Uncertainties

This measurement has six sources of systematic uncertainty. The dominant uncertainty is that of the FD energy calibration. One systematic emerges from the analysis chain: specifically, the benchmark function fit. Four other contributions come from the detector and the data: the SD aging, the seasonal fluctuations, the diurnal fluctuations, and the $\sec\theta$ dependence of Δ_S (see Figure 3.23). The aging effects result from deterioration of the detector throughout the observatory's more than a decade of continuous operation, including the electronics and the water quality. The diurnal and seasonal effects are similar because they reflect periodic atmospheric changes due to temperature and pressure cycles throughout the day and year, respectively. The dependence on $\sec\theta$ is an artifact of the benchmark method used in this study, and a reflection of the fact that the data does not perfectly follow its $\sec\theta$ dependence. This is particularly noticeable around the break between the two fits at $\sec\theta = 1.45$, and in the monotonic increase in Δ_S.

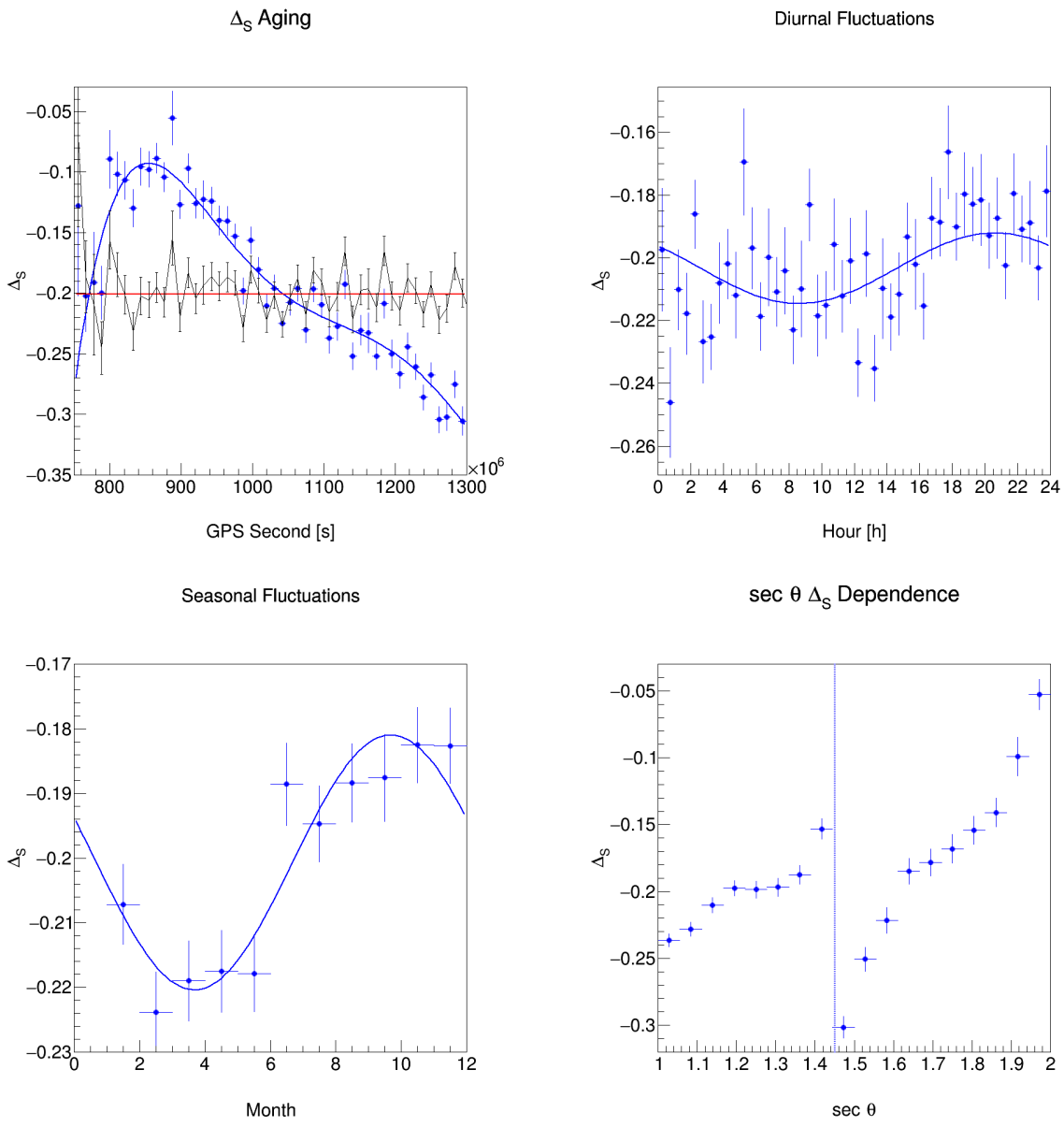

Figure 3.23: Various systematic uncertainties of Δ_S. Top left: aging, with the age-corrected data shown in black; top right: diurnal fluctuations; bottom left: seasonal fluctuations; and bottom right: $\sec\theta$ dependence.

Of these, the two largest are aging and the $\sec\theta$ dependence. It is possible to produce an age-corrected dataset that subtracts the observed time dependence. This is shown in black on the aging plot. Our presented work here does not include an age correction, though we note it does not change the final result, since it effectively averages out in each bin of the elongation rate.

The $\sec\theta$ dependence contains important implications for composition anisotropy studies using Δ_S, where systematics that vary with arrival direction can induce spurious signals. The change in benchmark parameterizations results in a discontinuity at $\sec\theta = 1.45$ (see Figure 3.23, lower right), and we observe a nearly monotonic increase in $X^{\Delta}_{\rm max}$ over both fit regimes. It is possible this trend reflects nonuniformities in the data, although $X_{\rm max}$ itself is relatively flat over $\sec\theta$, varying by only a few $\mathrm{g\,cm^{-2}}$.

To evaluate the impact of the benchmark fit uncertainty, we performed a bootstrapping procedure on the benchmark fit for A, B, and N. Probability distribution functions for each of the parameters were constructed from their fit uncertainties, and Δ was recomputed across the data using 2000 samples from these distributions. This approach is conservative since it neglects the existences of correlations between the fit parameters. These uncertainties were propagated through the entire analysis chain, where the uncertainty was evaluated on a bin-by-bin basis in the construction of the elongation rate. The uncertainty varies bin-by-bin from 0.003 to 0.004. This effect is so small as to be completely negligible (see Figure 3.24).

Figure 3.4 summarizes all systematics. We find a total systematic uncertainy on Δ_s of ≈ 0.15 . Since many of these effects average out in aggregate, we consider this a conservative estimate when applied to the elongation rate.

3.5.3 The Δ Elongation Rate

The final elongation rate plot calculated with Δ_S, including all the systematic uncertainties, is shown in Figure 3.25. As a cross-check of our method, we repeated the data selection

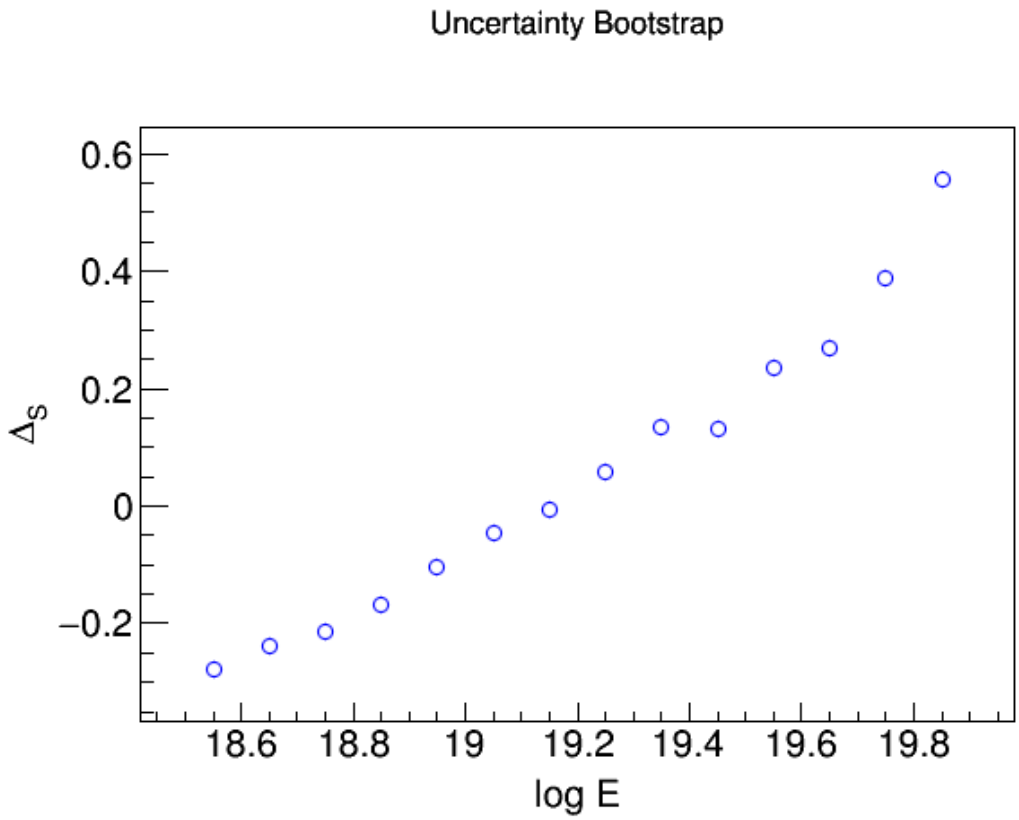

Figure 3.24: Bootstrap study performed on the analysis chain, using 2000 samples. Δ is recalculated over the dataset using a new benchmark parameterization generated from the fit's uncertainties. The points are the means of the resulting elongation rates generated with these artificial samples, and the error bars (drawn, but too small to be visible) are the standard deviations.

Effect	Uncertainty Contribution
Aging	0.1
Diurnal Effect	0.01
Seasonal Effect	0.03
$\sec\theta$ Dependence	0.06
Benchmark Fit	$\approx$ 0.003-0.004 (by bin)
FD Systematic Uncertainty	0.1
Total	$\approx$ 0.15

Table 3.4: Systematic uncertainties for the Δ_S study.

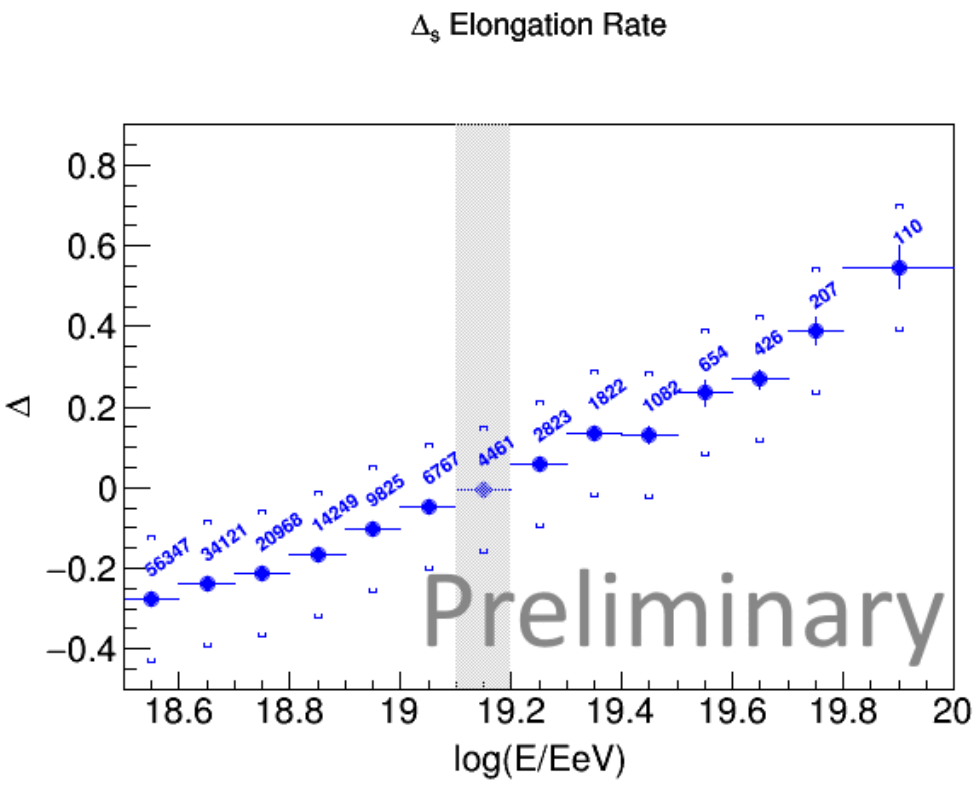

Figure 3.25: Elongation rate of Δ_S. The benchmark bin is hightlighted in gray. Higher values of Δ correspond to lighter composition.

used in [15] and compared our results with those from that paper. This exercise is shown in Figure 3.26.

3.5.4 Golden Calibration

Now that we have Δ_S, we can translate this into a calculation of $X^{\Delta}_{\rm max}$ by fitting the correlation between Δ_S and $X_{\rm max}$ for Golden Hybrid events.

Golden Hybrid events are the highest-quality hybrid events measured by the Observatory. As we saw in Section 2.4, a T3 trigger from the FD sends an external trigger to the surface detector. Because degeneracies in the hybrid χ fit improve drastically upon inclusion of a single SD tank, it is advantageous to include any available SD data with a T3 FD event. However, since we are correlating observables that are measured independently by the SD

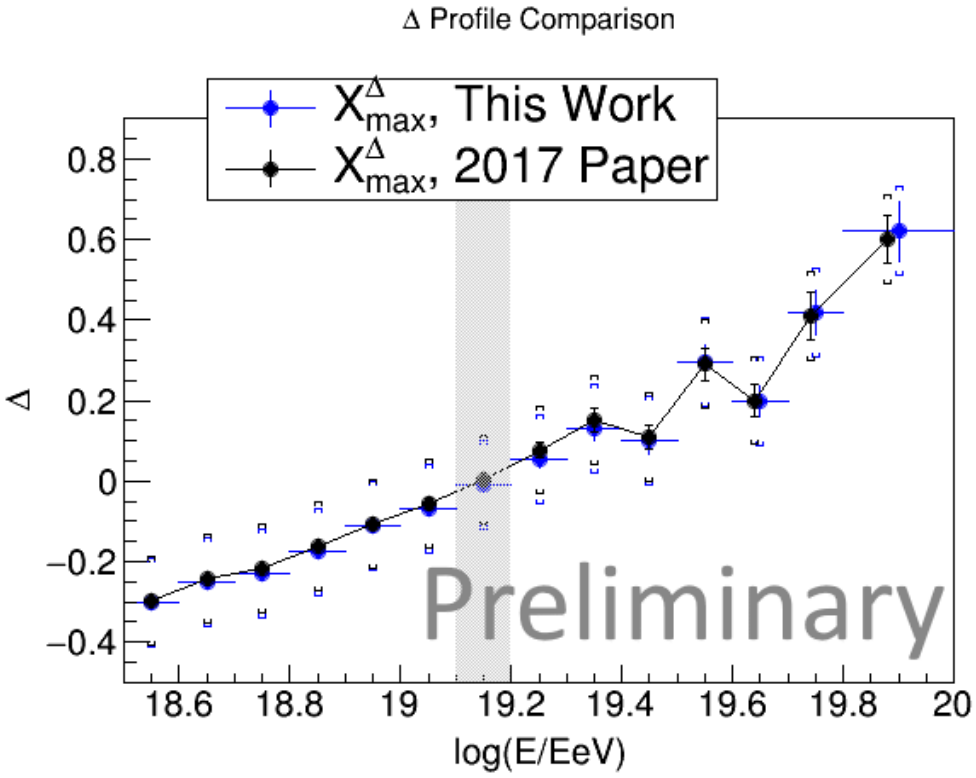

Figure 3.26: Consistency check with the published results from [15], restricting our data to the ranges of parameters explored in that study.

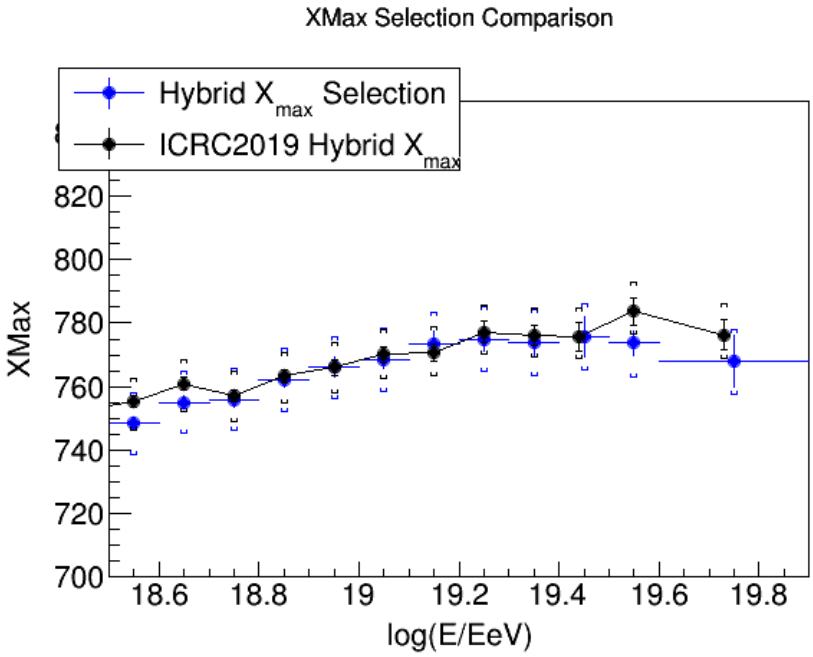

Figure 3.27: The elongation rate as calculated from our selection of Golden Hybrid events used to calibrate the $X^{\Delta}_{\mathrm{max}}$ measurement. The discrepency in the first two bins come from downwards bin migrations due to the energy cuts.

and FD, we want the set of hybrid events that can be independently reconstructed by both. These are the Golden Hybrid events.

We first extract all FD events from the ICRC2019 FD dataset [14] and ID-match them with our Δ_S data. We keep only 6T5 SD events with at least three stations, and we cut independently on both $\log(E_{\mathrm{FD}}) > 18.5$ and $\log(E_{\mathrm{SD}}) > 18.5$. 2561 Golden Hybrid events met these cuts. The elongation rate of our selected sample is shown in Figure 3.27. The deviation in the first two bins is a byproduct of the cut on E_{SD} and does not significantly impact our results. Our model for the correlation is

$$X^{\Delta}_{\mathrm{max}} = a + b \cdot \Delta_S + c \cdot (\log_{10} E - 18.5)\,, \tag{3.20}$$

where the energy offset serves to reduce the degeneracy between parameters a and c. We perform this fit using Bayesian inference, which allows us to more precisely understand the

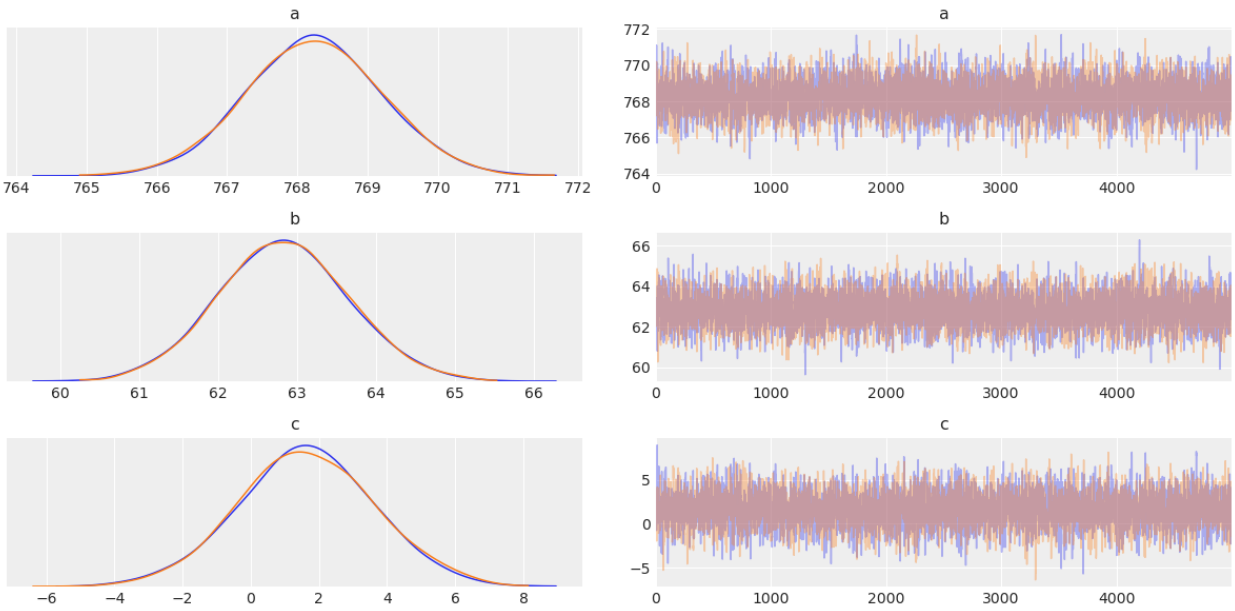

Figure 3.28: Posterior distributions for the calibration parameters obtained using Bayesian inference.

uncertainties in the final fit. The posterior distributions are shown in Figure 3.28, and our selected parameter values are obtained with maximum a posteriori (MAP) estimation. Gaussian priors were chosen centered around a by-eye first guess. Although it is not possible to easily visualize the resulting fit, a two-dimensional slice of it is shown in Figure 3.29.

To test the efficacy of the fit, we evaluated the mean difference between X_{max} and $X_{\mathrm{max}}^{\Delta}$ for all hybrid events (see Figure 3.30), finding consistency with zero. We note the existence of an absolute offset between this data and previous published results, which showed a mean deviation of $\approx 4 \pm 2\,\mathrm{g\ cm^{-2}}$; we attribute this to a difference in the fitting procedure. Including higher-order terms in Δ_S or $\log_{10} E$ does not significantly impact the final result.

We can see that $X_{\mathrm{max}}^{\Delta}$ is overestimated at the highest energies compared to X_{max} in hybrid events. This is likely due to lower-energy events dominating the fit and is seen consistently through various fitting techniques. The handling of this phenomenon must be deliberated by the collaboration.

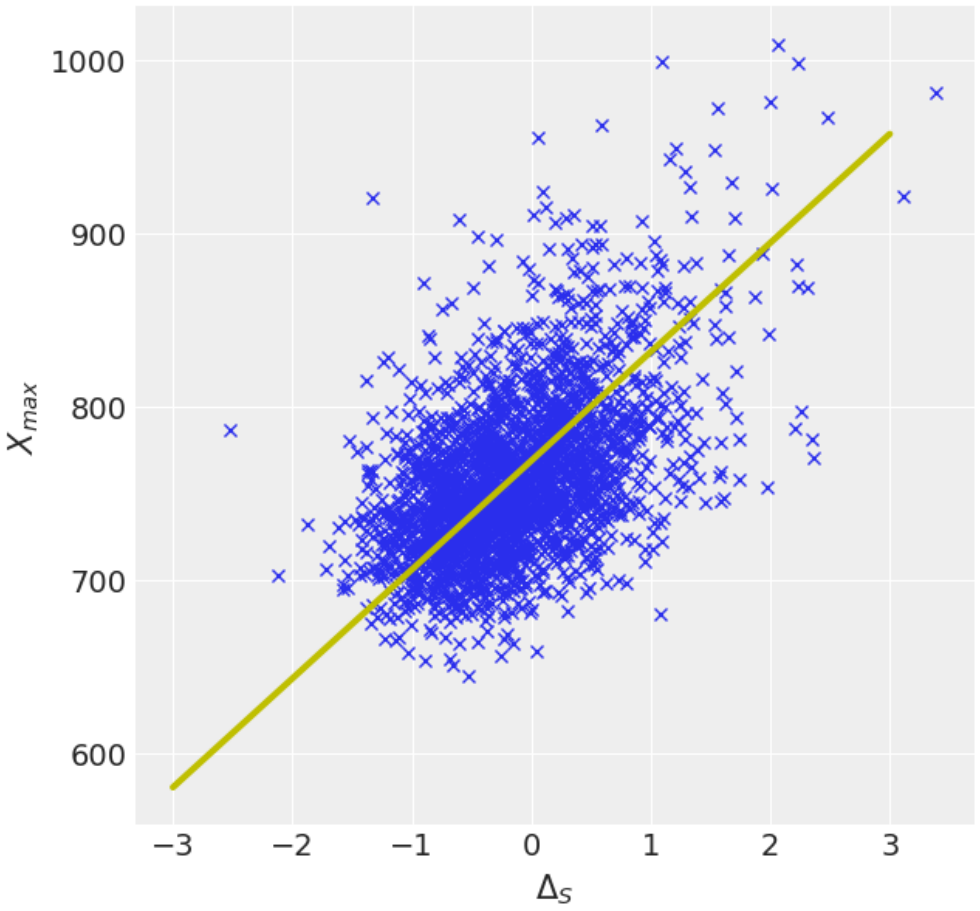

Figure 3.29: A two-dimensional slice of the golden hybrid calibration fit, showing in yellow the correlation between $X^{\Delta}_{\max}$ and $X_{\max}$.

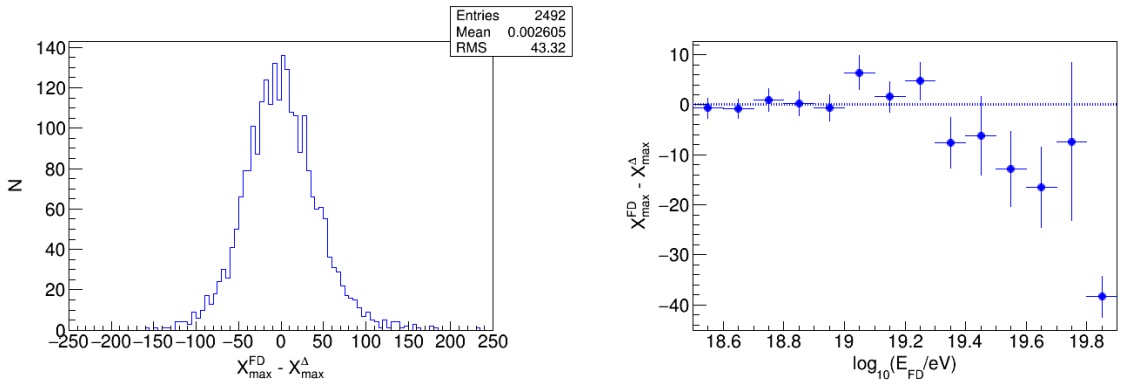

Figure 3.30: Left: Average difference between $X_{\max}$ and our calculated $X^{\Delta}_{\max}$ from the hybrid fit. The mean difference is approximately zero, confirming the efficacy of the fit. Right: Average difference between $X_{\max}$ and our calculated $X^{\Delta}_{\max}$ from the hybrid fit, now shown as a profile over $\log_{10}(E/\mathrm{eV})$. Note the tendency at higher energies to overestimate $X_{\max}$ with the SD.

3.5.5 Systematic Uncertainties

The systematic uncertainties here are similar to those discussed for the raw Δ_S measurement. One additional systematic emerges from the hybrid calibration, obtained by sampling from the posterior distributions and recalculating each $X^{\Delta}_{\max}$ with the resampled parameterization. For each $X^{\Delta}_{\max}$, a distribution of values is hence produced, and the standard deviation of this distribution is calculated. The result of this study is shown in Figure 3.31. The mean of this distribution is $0.7\,\mathrm{g\,cm^2}$, which taken for this uncertainty.

All the systematics studied previously for Δ_S apply here: the diurnal effect, the seasonal fluctuations, aging, and the $\sec\theta$ dependence. These are all shown in Figure 3.33.

The bootstrapping procedure used to characterize the uncertainty from the benchmark function has been extended. From the Δ_S bootstrap study, 2000 artificial datasets were produced by recalculating Δ from resamples of the benchmark parameters. This study is extended by including a hybrid calibration fit into each realization. The results are then propagated through to the final elongation rate, where the systematic uncertainty is computed on a bin-by-bin basis. We found that it varied between $\sim 2.5 - 4\,\mathrm{g\,cm^2}$. The results

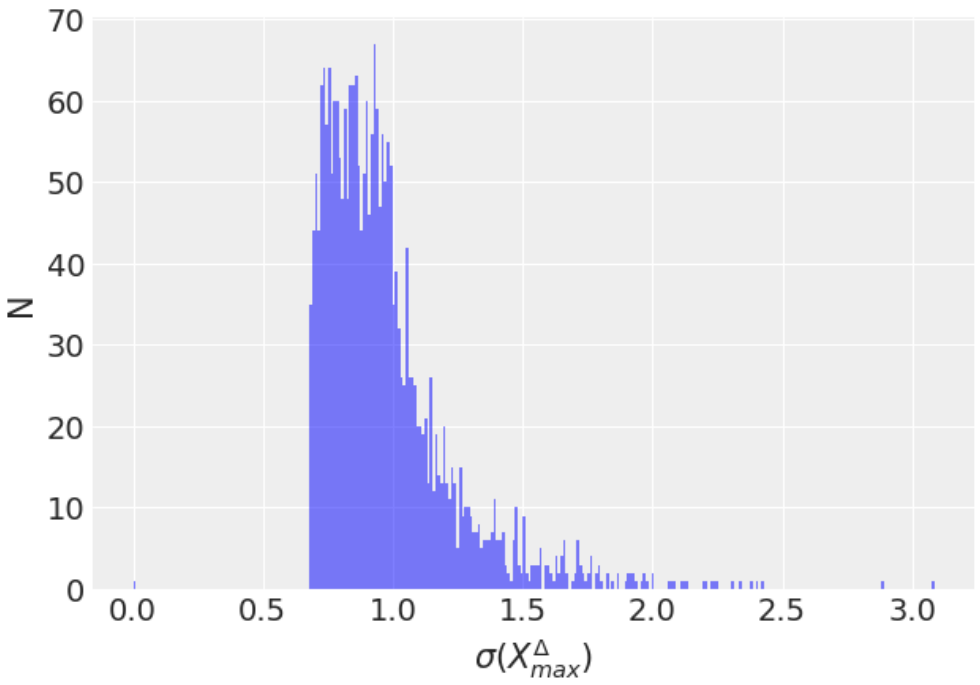

Figure 3.31: Study on the uncertainty on $X^{\Delta}_{\rm max}$ from resampling the posterior distribution from the hybrid calibration. See text for additional details.

of this study are shown in Figure 3.32.

The systematic uncertainties for the $X^{\Delta}_{\rm max}$ study are summarized in Figure 3.5, and they sum to $\sim 11\,{\rm g\,cm^{-2}}$. It is important to understand that many of these numbers are conservative upper bounds when applied to the elongation rate, since they tend to cancel in aggregate. However, this does not factor in the bias discovered at the highest-energies in the previous subsection.

3.5.6 The $X^{\Delta}_{\rm max}$ Elongation Rate

Presenting our results naively would fail to account for the fact that the FD and SD have systmatic offsets in their energy measurements. The energy shift is $\sim 2\%$ on average, but the large RMS means bin-to-bin migrations will significantly impact the result if this difference is not corrected. Further, this effect has a dependence on $X^{\Delta}_{\rm max}$. To make direct comparisons between our method and that using $X_{\rm max}$ from the FD, we must first build a common energy

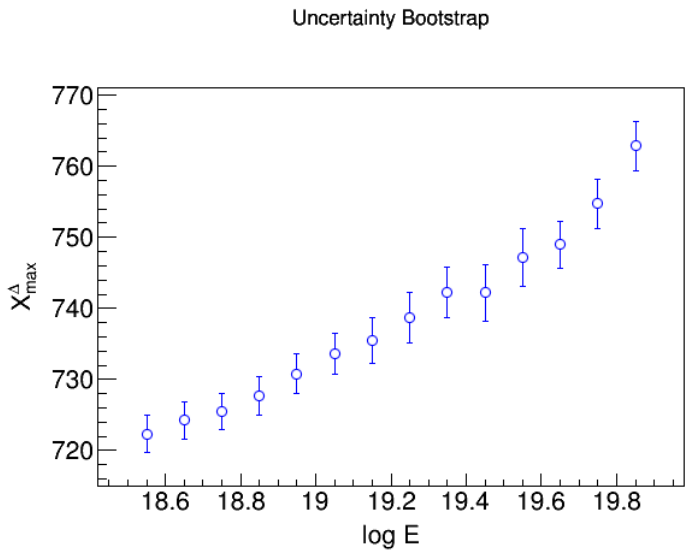

Figure 3.32: Bootstrap study performed on the analysis chain, using 2000 samples. Each sample consists of a new resampled benchmark parameterization and a new hybrid calibration fit. The points are the means of the final distributions and the error bars are their standard deviations.

Effect	Uncertainty Contribution ($\mathrm{g\,cm^{-2}}$)
Aging	3
Diurnal Effect	0.5
Seasonal Effect	1
$\sec\theta$ Dependence	4.5
Benchmark Fit	$\approx$ 2.5-4
FD Systematic Uncertainty	8.5
Total	$\approx$ 11

Table 3.5: Systematic uncertainties for the $X^{\Delta}_{\mathrm{max}}$ study.

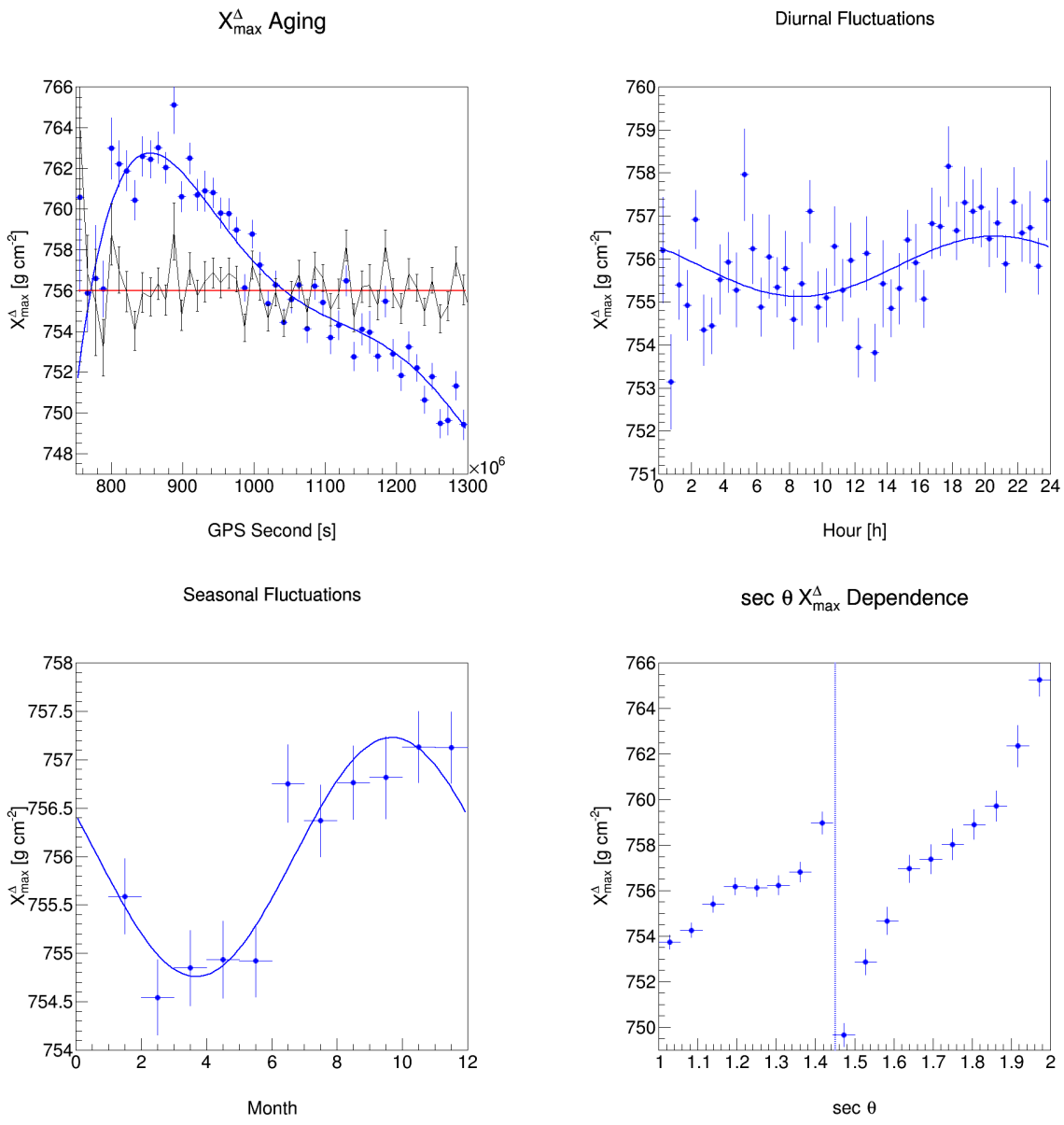

Figure 3.33: Various systematic uncertainties. Top left: aging, with the age-corrected data in black; top right: diurnal fluctuations; bottom left: seasonal fluctuations; and bottom right: $\sec\theta$ dependence.

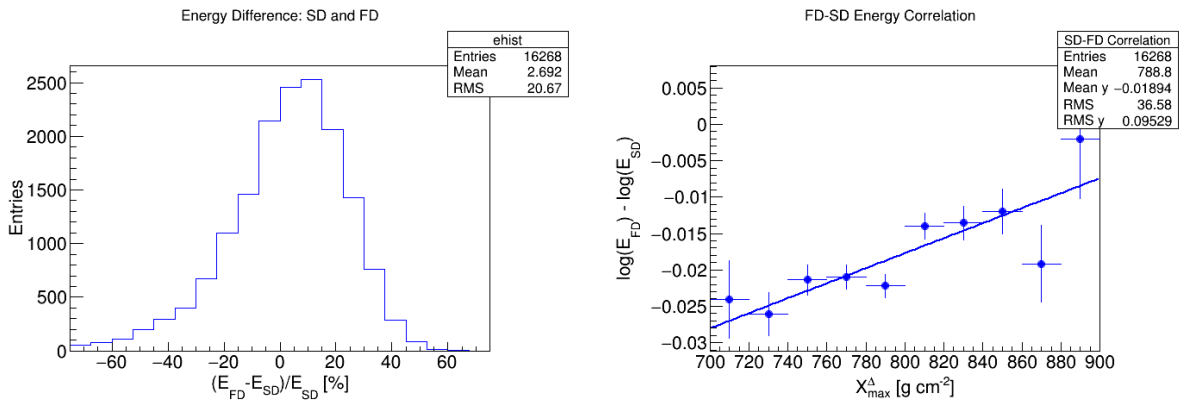

Figure 3.34: Left: energy difference between the SD and FD's measurements for our hybrid event selection. Right: profile showing the energy difference as a function of $X^{\Delta}_{\mathrm{max}}$.

scale. We can do this by parameterizing the energy difference and correcting for it in our data. Figure 3.34 shows this process. The energy difference has a dependence on $X^{\Delta}_{\mathrm{max}}$. For our sample of Golden Hybrid events, we fit the correlation between the SD and FD energies, and in producing our elongation rate measurement with $X^{\Delta}_{\mathrm{max}}$, we first energy-correct the data as follows:

$$\log_{10}(E_{\mathrm{corr}}/\mathrm{eV}) = \log_{10}(E_{\mathrm{SD}}/\mathrm{eV}) + p_0 + p_1 X^{\Delta}_{\mathrm{max}}, \tag{3.21}$$

where $p_0 = 0.191394$ and $p_1 = 0.00024698$.

Figure 3.35 shows our final result. Although the FD measurement and the SD measurement generally agree despite the systematics and significant differences in the data selection, we note the divergence seen at higher energies where this technique shows hints of lighter composition. This result is the highest-statistics composition study ever performed in UHECR physics. Expanding the scope of composition analyses unlocks the possibility of new mass composition studies that combine the discriminating power of both arrival directions and mass to perform novel studies of UHECR sources, and the extension of robust physics to higher zenith angles is essential for increasing sky coverage for this emerging field.

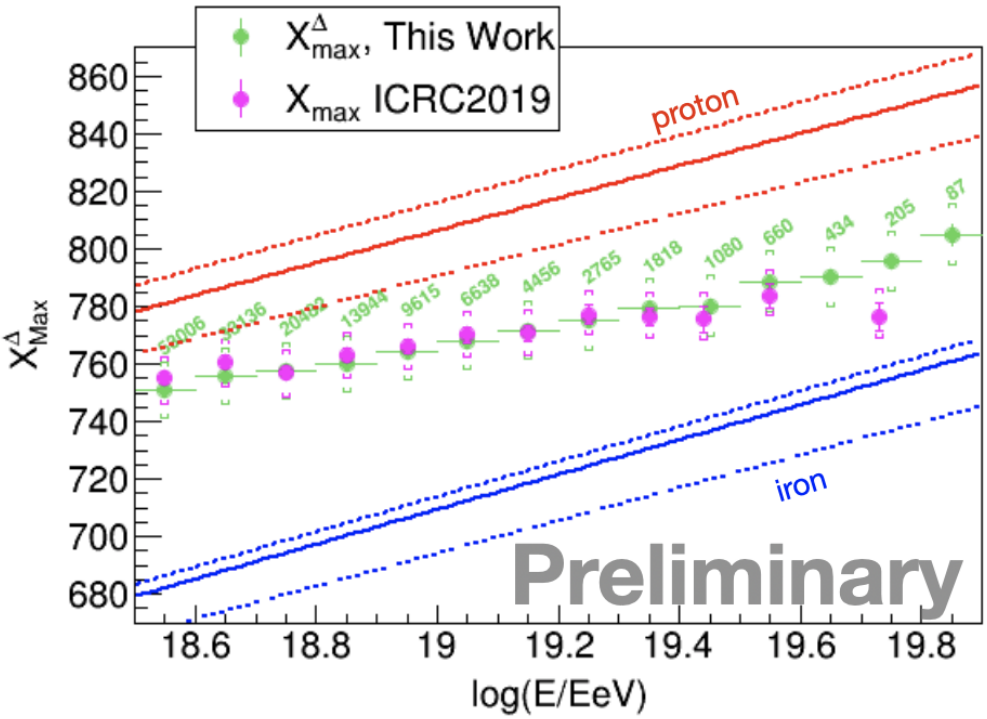

Figure 3.35: Final elongation rate plot. For comparison, the ICRC2019 X_{max} hybrid measurement from [23] is also shown. The lines represent elongation rates calculated with different hadronic interaction models. These results show hints of lighter composition at higher energies.

Chapter 4

The Fluorescence detector Array of Single-pixel Telescopes (FAST) Project

While discoveries made over the past decade have transformed our understanding of ultra-high energy cosmic rays (UHECRs) and their sources, their nature and origin remain a mystery. Because of the exceptionally low UHECR flux at the highest energies (less than one per square kilometer per century at the highest energies), it is necessary to instrument a huge area in order to collect a suitably large dataset for meaningful statistical analysis. There is therefore a strong motivation to develop detectors that are low-cost, robust, and autonomous, which can be deployed in large ground arrays to directly measure the energy and mass composition of the highest energy cosmic rays.

The largest present-day cosmic ray experiments are hybrid detectors that employ a combination of two techniques: surface detection (sampling the lateral distribution of secondary EAS particles at ground level) and fluorescence detection (observing the faint isotropically-emitted ultraviolet light produced during the de-excitation of atmospheric nitrogen). The

Telescope Array experiment [103], spanning 700 km^2 in the desert of Utah, USA, and the Pierre Auger Observatory [63], spanning 3000 km^2 in the province of Mendoza, Argentina, both instrument a very large area with a grid of surface detector stations overlooked by a set of fluorescence telescopes. Surface detectors feature an exceptionally high duty cycle ($\sim 100\%$) and excel in providing information about the lateral distribution of particles in the EAS at ground level [78, 104]. Fluorescence detectors provide a calorimetric measurement of a shower's energy by collecting fluorescence light emitted during its longitudinal development. This method does not depend on extrapolation of accelerator-tuned hadronic interaction models to higher energies and is therefore a more accurate estimator of the shower energy. Observing a shower's development directly also provides another distinct advantage: observation of the depth of maximum development (X_{max}), a parameter indicative of the primary particle's mass. In spite of these benefits, fluorescence detectors suffer from a significantly lower duty cycle ($\sim 15\%$) and reduced directional coverage [82, 105]. Using a sample of showers detected in coincidence with both a surface and fluorescence detector, the calorimetric measurement of the shower energy provided by the fluorescence detector can be used to calibrate the energy scale of the surface detector using a suitable measured observable. This method of hybrid detection is employed by both the Auger and TA collaborations to calibrate the energy measured by the high duty cycle surface array.

Recent years have seen significant progress in the field, with advances in analysis and increased exposures enabling the UHECR energy spectrum, composition, and anisotropies to be measured with increased resolution above 0.1 EeV [106]. Both TA and Auger have measured the energy spectrum up to 100 EeV, with clear indications of a break at around 5 EeV (the ankle), and a flux suppression above 50 EeV often attributed to energy loss through interactions with blue-shifted (in the centre of mass of the CR particle) cosmic microwave and infrared background photons through the GZK process [65, 66]. Measurements of the elongation rate (X_{max} as a function of energy) by both experiments indicate a predomi-

nantly light composition around the ankle, while above 10 EeV Auger shows a decrease in the growth of $X_{\max}$ with energy, as well as a decrease in RMS($X_{\max}$), indicating a gradual increase in the average cosmic ray mass. Recent results have provided increasing motivation to probe the energy range above 100 EeV, such as the Auger surface detector's hints at a lighter composition above 30 EeV [107]. Below the ankle both TA and Auger measure arrival directions that are highly isotropic, with warm- and hot-spots appearing at higher energies due to the smearing of point sources by both Galactic and extragalactic magnetic fields. TA has recorded an excess above isotropic background expectations above 57 EeV [11], while a blind search using a combination of both Auger and TA data shows an excess above this energy in a 20° search window with a 2.2σ post-trial significance [108]. In 2017 Auger reported on a large-scale dipole above 8 EeV with a 5.2σ significance, pointing 125° away from the galactic center, suggesting an extragalactic origin for the highest energy particles [67, 68]. To further advance and establish the field of charge particle astronomy, the next generation of ground-based UHECR detectors will require an unprecedented aperture, which is larger by an order of magnitude; mass composition sensitivity above 100 EeV; and energy, $X_{\max}$, and angular resolutions that are comparable to those of current-generation experiments.

The Fluorescence detector Array of Single-pixel Telescopes (FAST) [109] is an R&D project aimed at developing a next-generation cosmic ray detector. It is a low-cost fluorescence telescope sensitive to UHECRs with energies greater than 30 EeV. The main features of its design are a portable, compact mechanical structure and a camera consisting of four 200 mm diameter PMTs, in contrast to the expensive, highly-pixelated cameras used by both Auger and TA. The optical and mechanical design of the FAST prototype telescopes are further described in Section 4.1. With traditional fluorescence cameras, each pixel provides a single point of angularly-resolved timing information that can be used to constrain the shower axis. First, the shower-detector plane is determined using the angular direction and total signal of the pixels. Pixel timing is then used to determine the axis. Inverting the

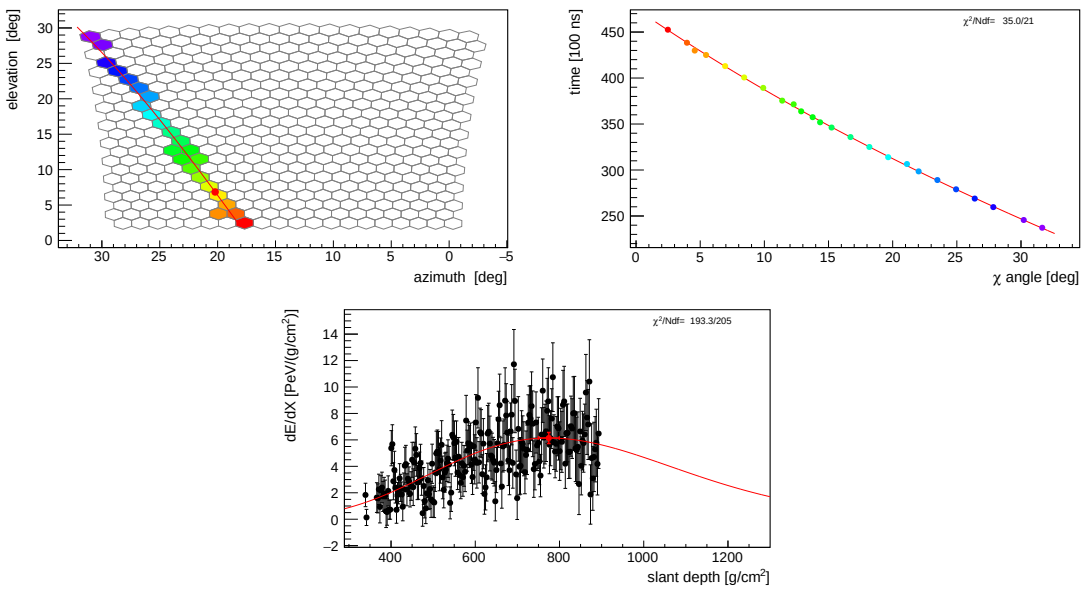

Figure 4.1: An example event viewed by the Auger FD demonstrating its more traditional process. Top left: the shower path through the FD camera, with pixels color-coded by trigger time. Top right: the curvature of the shower obtained by fitting the timing information obtained from the PMT readouts. Bottom: a Gaisser-Hilas fit to the energy deposition profile obtained from the traces. It provides an estimate of the shower energy and $X_{\max}$. FAST abandons this paradigm in favor of a coarser camera that employs a novel top-down reconstruction algorithm.

Cherenkov-fluoresence matrix obtained from the pixel signals allows a full reconstruction of the shower energy deposition profile as a function of slant depth, and a Gaisser-Hillas fit provides the depth of maximum development $X_{\max}$. Through this method, a monocular reconstruction with a single FD eye is possible. An example of an event detected by the Auger FD and the accompanying timing fit is shown in Figure 4.1. of the shower are taken to be those of the best-fit simulation. An example of a UHECR detection by a hypothetical FAST array, reconstructed in this method, is shown in Figure 4.2, for comparison with its more traditional counterpart.

The final design goal of FAST is a triangle grid of FD stations, the prototypical design of which is demonstrated in Figure 4.3. Taking each FAST telescope to cover a 30 field-of-view (the same as existing experiments like Auger), twelve telescopes in a single station can attain 360° coverage, and since we are specifically targeting the highest-energy events (those which

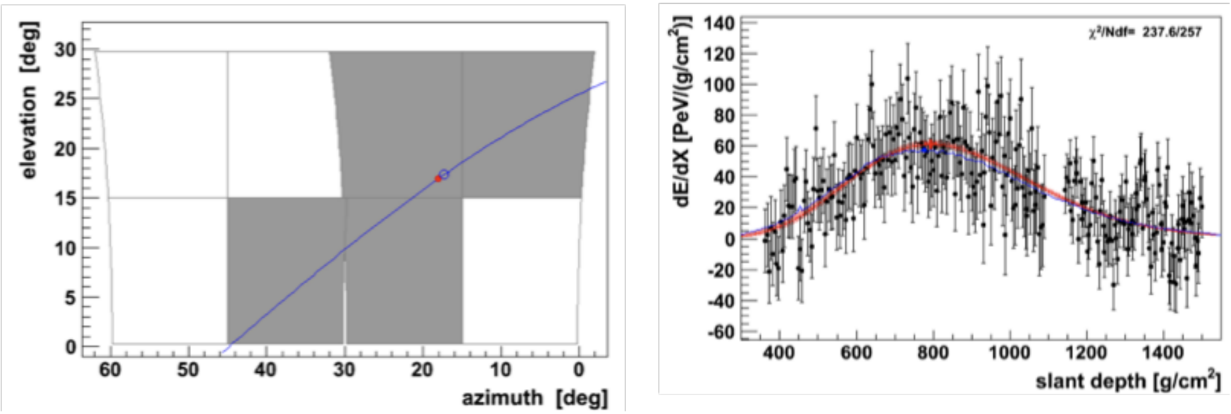

Figure 4.2: An example event viewed by a pair of simulated FAST telescopes, demonstrating its use of a coarsely-pixelated camera that fits the shower profile with individual time bins of the trace. There is insufficient timing information to constrain the shower geometry as in the more traditional FD method shown in Figure 4.1.

produce the brightest signals), each station can cover a substantial physical area.

Beginning in 2014, a number of tests and prototypes validating the FAST design have been constructed. The first experimental test of the FAST concept was performed in 2014, a single-pixel test with the JEM-EUSO optics at the Black Rock Mesa FD site of the Telescope Array experiment. This verified the capability of using large PMTs to observe the night sky as UHECR detectors. This initial test will be described in Section 4.5.1. In parallel with this test, a prototype design for the full FAST telescope system was being evaluated. Beginning in 2016, a series of three full FAST prototypes (FAST@TA) were constructed at the same site with a shared field-of-view with the Black Rock Mesa FD. These served as our first robust test of FAST telescope design, and these prototypes have been in operation since their commissioning in 2016, 2017, and 2018. Section 4.5.2 discusses these three telescopes. Following the success of FAST@TA, a FAST prototype was also constructed at the Pierre Auger Observatory site at the Los Leones FD site (FAST@AUGER). This prototype is discussed in 4.5.3. Our next major milestone will be the first test of an independent, free-standing FAST telescope with our new FPGA-based data acquisition electronics, which will enable us to test stereo observation of showers.

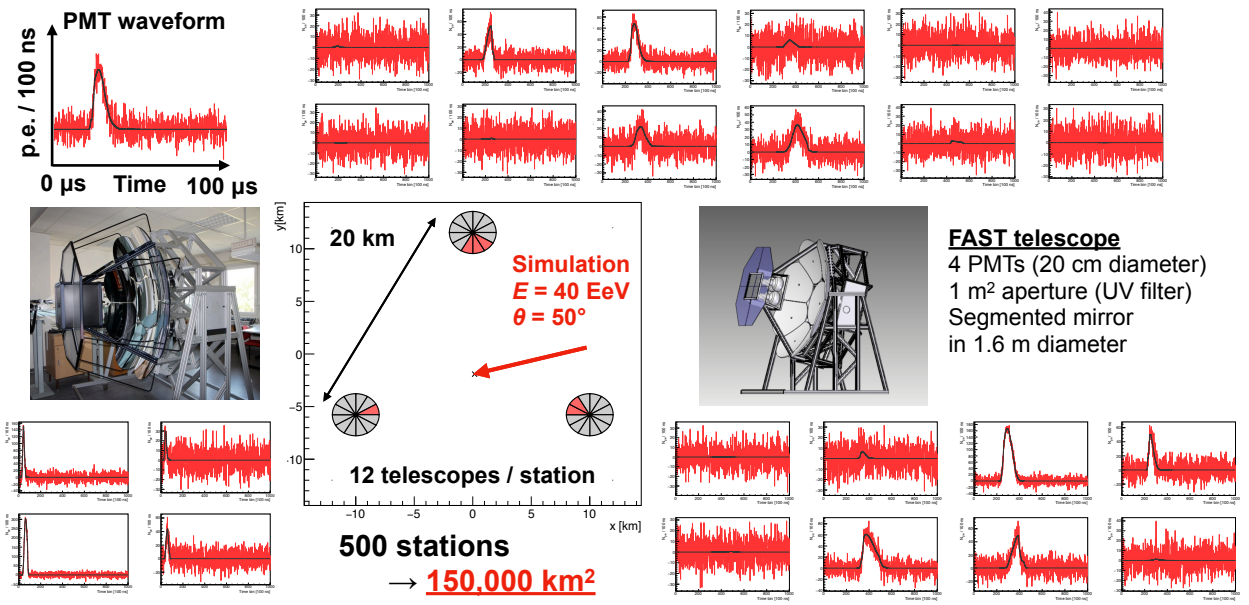

Figure 4.3: Schematic of how a future FAST array would operate. A simulated shower is thrown onto a triangular grid of FAST stations, each covering 360° with 12 telescopes (see Section 4.1. This shower is measured in three-fold coincidence from three FAST stations, consisting of traces from six telescopes. Our novel top-down reconstruction technique is applied to determine the shower energy and geometry (see Section 4.6.3; the black lines describe the best-fit template provided by the reconstruction algorithm.

4.1 Telescope Design

The full-sized FAST prototypes use a lensless Schmidt-type optical design. In a typical Schmidt telescope, a corrector plate is placed at the entrance aperture (located at the mirror's radius of curvature at a distance of twice the focal length) to control the off-axis aberrations (coma and astigmatism). Because of the FAST camera's coarse granularity, strict requirements on the size and shape of the point-spread function (PSF) can be relaxed. In the interest of cost, we have hence chosen to forego the corrector plate, use a smaller mirror, and employ a shorter distance between the mirror and the camera relative to a regular Schmidt telescope, with the entrance aperture located closer to the focal surface. Additional details about the optical and mechanical design of the telesopes can be found in [110].

The dimensions of the FAST prototype telescope are shown in Figure 4.4b. An octagonal aperture of height 1.24 m is located at a distance of 1 m from a 1.6 m diameter segmented spherical mirror (radius of curvature ~ 1.38 m). This design meets the FAST specifications for an effective collecting area of $1\,\mathrm{m}^2$ after accounting for the camera shadow and a field-of-view of $30^\circ \times 30^\circ$.

FAST's central circular mirror and 8 side mirrors, or "petals", are produced by the Joint Laboratory of Optics of the Palacky University and the Institute of Physics of the Academy of Sciences of the Czech Republic from a borosilicate glass substrate. The reflective surface consists of several vacuum coated Al and SiO_2 layers, offering a relatively constant reflectivity over the fluorescence wavelength band between 300 nm and 420 nm, as shown in Figure 4.5.

To reduce exposure to night-sky background, a UV filter (ZWB3 by Shijiazhuang Zeyuan Optics) is placed at the aperture to block light above 400 nm. Its spectral transmission is shown in Figure 4.5. To fit the octagonal aperture, the filter is constructed from several smaller segments. These individual segments are tessellated using brass "U" and "H" profiles, resulting in an aperture of area $1\,\mathrm{m}^2$.

The telescope's mechanical support structure, shown in Figure 4.4a, is based on commercially-

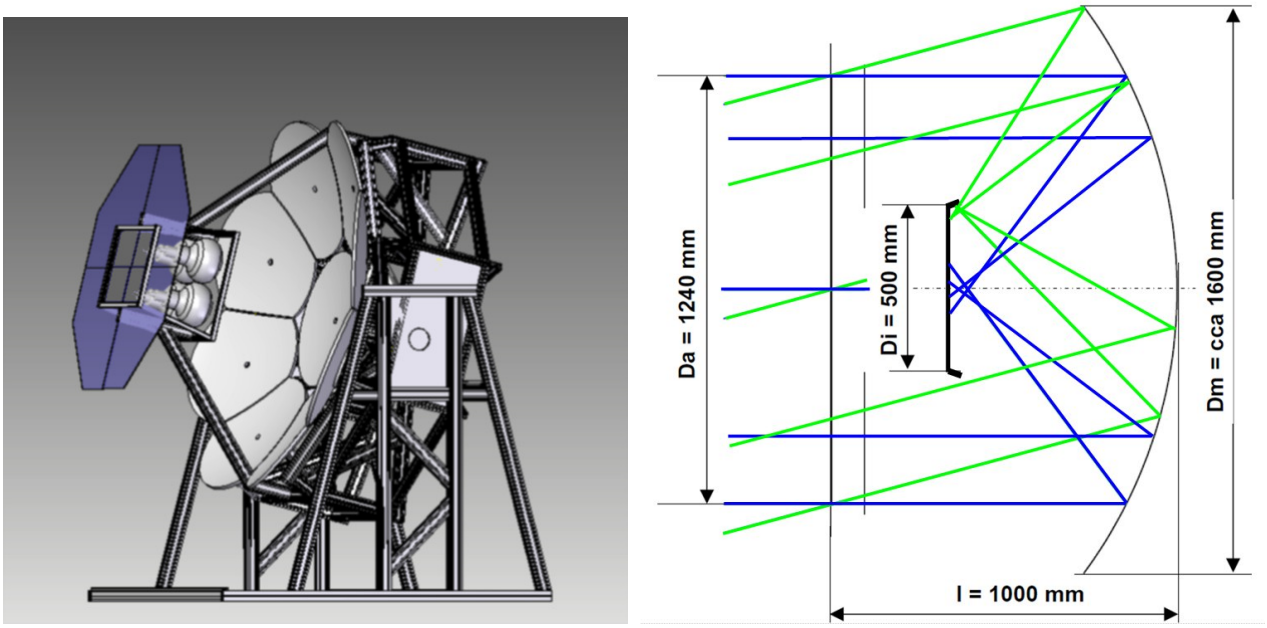

(a) The telescope frame, showing four PMTs at the focus of a 1.6 m diameter segmented mirror. The support structure is made from aluminium profiles. The UV filter can be seen attached to the periphery of the camera box. Not shown is the protective shroud around the body of the telescope, or the side mirrors.

(b) The dimensions of the FAST prototype telescope's optical system. D_{a} is the diameter of the telescope aperture, D_{i} is the side length of the square camera box, D_{m} is the diameter of the primary mirror, and l is the mirror-aperture distance.

Figure 4.4: The mechanical and optical design of the full-scale FAST prototype telescopes.

available modular aluminum profiles. They provide an stable and rigid platform to mount the FAST optical system. Their light weight allows for easy packaging and transportation, while their modular design makes assembly straightforward, requiring only a small team. The mechanics consists of a primary mirror stand mounted with a single degree of freedom to facilitate adjustment of the telescope's elevation in discrete steps, to 0°, 15°, 30° and 45°. The square camera box (side length 500 mm), which holds four 200 mm PMTs, is mounted on a support structure connected to the perimeter of the mirror dish which also holds the octagonal filter aperture. Surrounding the camera box are four flat side mirrors (area $\sim 66\,\mathrm{cm}^2$ mounted at $\sim 80°$ to the camera surface) designed to reflect light lost due to the enlarged spot size at the camera edges back into the PMTs. The mirror stand contains

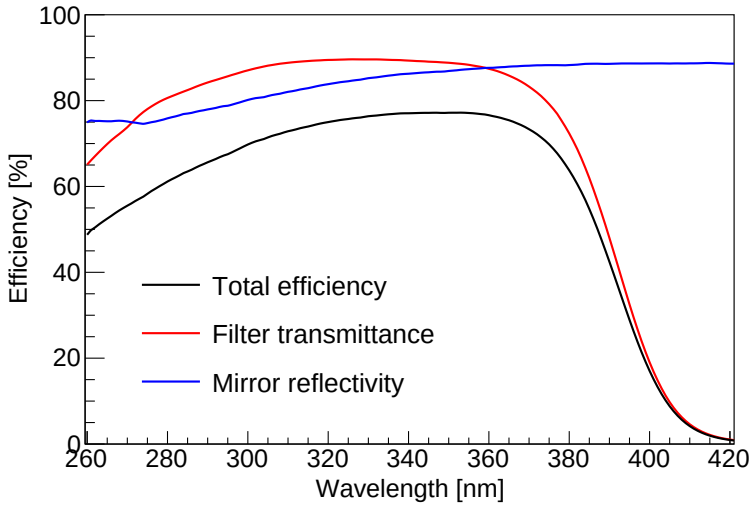

Figure 4.5: Spectral efficiency of the FAST prototype mirror and UV filter over the fluorescence wavelength range.

9 mirror mounts, each with 2 degrees of freedom to allow for mirror segment alignment. The mechanical construction is covered with a shroud to both protect the optical system from the surrounding environment and operate as a field stop to restrict light from outside the field of view.

This general telescope design has been tested throughout the construction and operation of several physical prototypes through remote observation, and we have encountered no major issues. This is important because a future FAST array would require stations placed at vast distances across which physical maintenance would be unfeasible. Throughout the prototyping process, some minor improvements in its design have been made, including a reduction of its overall physical size and weight, while maintaining its target scientific specifications. The physical size of the camerabox has also been reduced to lessen the impact of its shadow.

4.2 Optical Performance

The top row of Figure 4.6 shows the results of a ray-tracing simulation of collimated optical beams at various angles of incidence (on-axis, 7°, and 11°) to the telescope aperture performed with the Zemax software package [1], with the 200 mm scale representing the diameter of the PMTs installed in a custom-built box close to the telescope's focal surface. The "star" shape of the optical spot is a result of the octagonal aperture dimensions. In order to minimize the dead space between PMTs, the image plane is moved 25 mm closer to the mirror (relative to the focal surface) in the prototype design. This serves to eliminate a complete loss of signal for on-axis optical beams where light is focused towards the central point between all four PMTs, by enlarging the optical spot. Some of this signal loss is also mitigated in the prototype design by applying a Tyvec diffusing material to the surface of the camera box between the PMTs.

The lower row of Figure 4.6 shows the results of an *in-situ* measurement of the optical point spread function of one of the three prototype telescopes installed at the Telescope Array experiment (see Section 4.5.2). These measurements were made using a point-like light source located at a distance of $\sim$ 150 m from the telescope, imaged on a flat screen mounted to the front of the camera box. These measurements show good agreement with simulations, verifying not only the performance of the optical system (and the applicability of simulations in assessing its performance), but also the directional alignment of the telescope. The finer structure present in the measured point spread functions is due to the presence of a low chain-link fence between the light source and the telescope.

Figure 4.7 shows the results of a full wavelength-independent ray-tracing simulation of the FAST prototype optical system produced using the Zemax software, where the axes represent the angular distance of a collimated beam to the optical axis of the telescope. The simulation model includes a mirror with a realistic surface shape and spectral reflectance

1. https://www.zemax.com

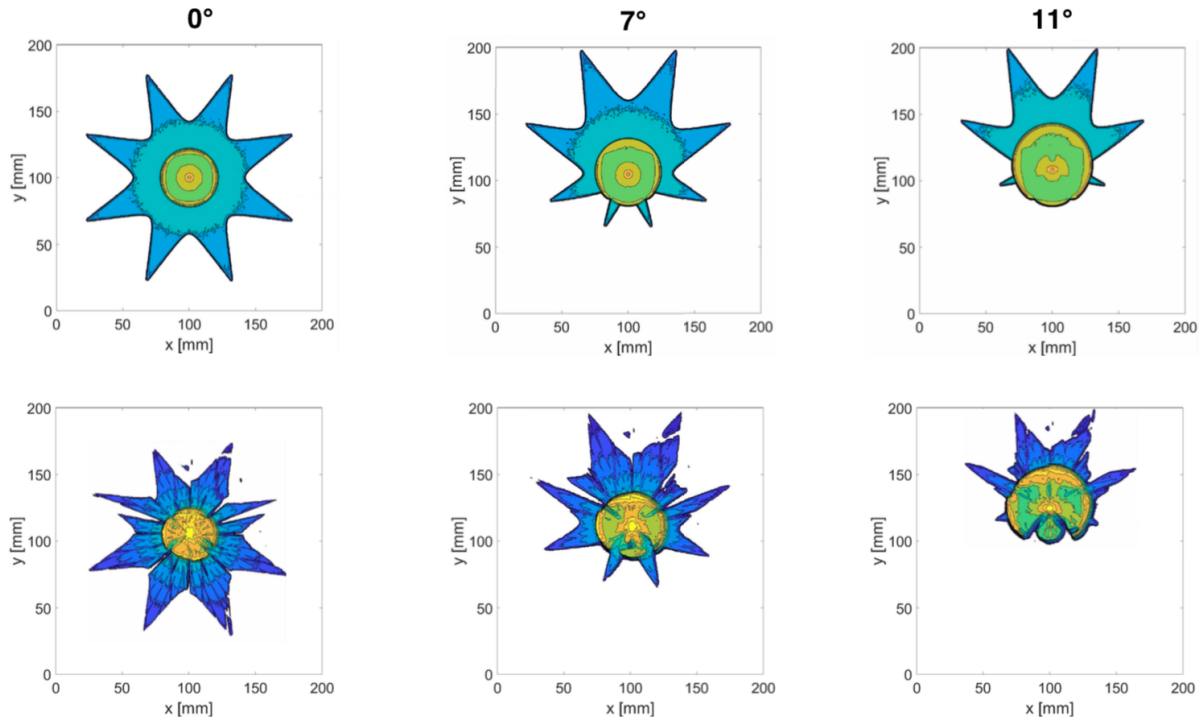

Figure 4.6: The simulated point spread function (top) for on-axis, 7°, and 11° incidence angles and the true point spread function of a FAST prototype telescope (bottom) measured *in-situ* at the installation site.

(taken from measurements), a complete description of the telescope structure, including the aperture with the filter support structure, the camera box containing the four 200 mm PMTs, the diffuser attached to the dead space between PMTs, and the four small side mirrors attached to the periphery of the camera. The analysis includes the Fresnel losses on the glass surface of the PMTs. These losses significantly influence the simulation results due to the high incidence angles of light on the hemispherical photocathode surfaces. In addition, the spatially-dependent collection efficiency of the PMTs is taken into account using measurements made using a dedicated set-up at Chiba University [111]. This non-uniform collection efficiency across the PMT photocathode arises due to the distance between the photocathode and the first dynode within large-format PMTs, and manifests itself primarily as a "cold spot" of $\sim 25\%$ lower efficiency diametrically opposite the first dynode. Note that this non-uniformity factor is included in the simulation.

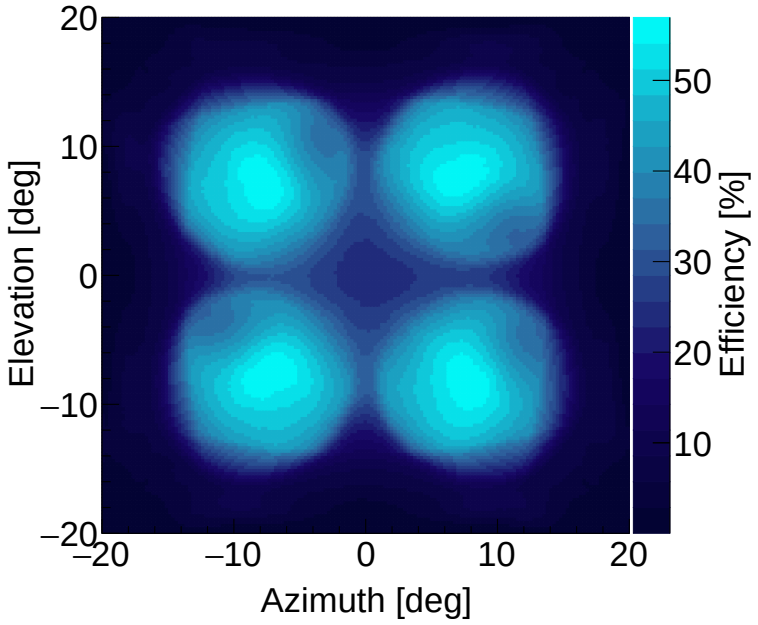

Figure 4.7: Directional efficiency of the FAST prototype design. See text for details.

4.3 Electronics Chain

The FAST camera and electronics chain is comprised entirely of commercially-available components. The camera comprises four AC-coupled 200 mm PMTs (mod. R5912-03, Hamamatsu). Each one has ten dynode stages and a maximum operating voltage of $\sim 2600\,\mathrm{V}$, with active bases (mod. E7694-01, Hamamatsu) arranged in a 2×2 matrix, and covering a $\sim 30^\circ \times 30^\circ$ field of view (see Figure 4.5).

All PMTs were tested in the laboratory at the University of Chicago, where their detection efficiency and differential linearity were measured, and their nominal operating voltages were determined (typically $\sim 900\,\mathrm{V}$ with a positive polarity for a target gain of 5×10^4). The calibration procedure was almost entirely automated, requiring only that an operator successively install each PMT in the light-tight test box, and ensuring reproducible test conditions for the measurement of each of the PMTs. This calibration process is described

in more detail in Section 4.4.

A NIM-mounted module (mod. N1470, CAEN) provides high voltage to the four PMTs. The PMT signals are routed through a 15 MHz low-pass filter (mod. CLPFL-0015, Crystek) to remove high-frequency noise, before being amplified by a factor of 50 using a fast amplifier (mod. 777, Phillips Scientific). The resultant amplified signal is digitized at 50 MSamples/s using a 16-channel, 14-bit FADC (mod. SIS3316, Struck Innovative Systeme) hosted in a portable VME crate along with a GPS module (mod. GPS2092, Hytec) providing event time stamps, and a single-board PC (mod. V97865, GE Intelligent platforms) running the DAQ software. Triggers can be provided to the FADC either externally via a NIM pulse input, or internally via a high-threshold internal trigger implemented in the DAQ software as a trapezoidal finite impulse response (FIR) filer. A schematic of the FAST back-end and data acquisition electronics for a single PMT is shown in Figure 4.8.

The total cost of a single FAST telescope as of the FAST@TA experiment, including the optical system, mechanical structure, and the electronics and data acquisition system is ∼$25k US. The commercial electronics systems comprise a significant portion of this cost. The development of our future FPGA-based data acquisition electronics will greatly reduce this expense.

4.4 PMT Calibration

FAST PMTs are handmade in batches, and their gain characteristics vary both individually and by series. Each PMT must be measured individually so that we can verify its properties match that of its data sheet specifications (Figure 4.9), and so that we can obtain its operational voltage for its target gain of $2 \cdot 10^5$.

Our calibration procedure involves measuring the single photoelectron response, gain as a function of high voltage, detection efficiency, stability, and differential nonlinearity. The gain and single-photoelectron measurements are essential and much be performed for each

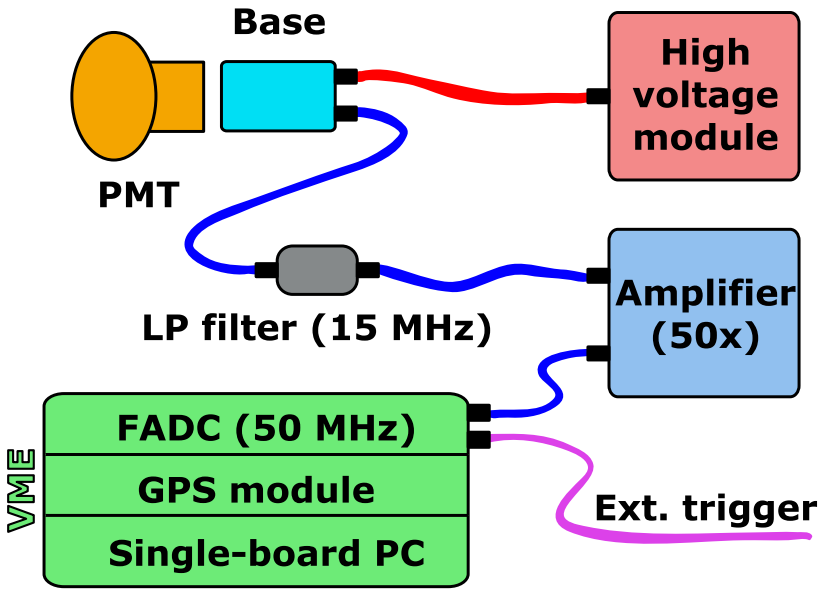

Figure 4.8: Schematic showing the FAST electronics chain for a single PMT.

individual PMT to obtain the operational high voltage. The final tabulated calibration data for the FAST@TA experiment is shown in Table 4.11.

4.4.1 Single-photoelectron

We begin by measuring the PMTs single-electron response at maximum supply voltage. As this measurement sets the scale for several future measurements (including the absolute calibration for the gain measurement and the discriminator threshold for the detection efficiency measurement), obtaining an accurate assessment of the single-photoelectron response is extremely important.

We begin by affixing a small LED to a spot on the PMTs surface and pulse it with a small AC current. In coincidence, a NIM pulse is sent to the FADC as an external trigger to capture the PMTs response to each LED pulse. The PMT signal is amplified so that individual photoelectrons are visible on the oscilloscope. The PMT voltage is carefully tuned (by observing single captures on the oscilloscope) to assure that zero-photoelectron and single-photoelectron events dominate the spectrum.

CHARACTERISTICS (at 25 deg. C)

Parameter		Min.	Typ.	Max.	Unit
Cathode Sensitivity	Luminous (2856 K)	-	70	-	uA/lm
	Radiant at 420 nm	-	72	-	mA/W
	Blue Sensitivity Index (CS 5-58)	-	9	-	-
	Quantum Efficiency at 390 nm	-	22	-	%
Anode Sensitivity	Luminous (2856 K)	-	14	-	A/lm
	Radiant at 420 nm	-	1.4×10^4	-	A/W
Supply Voltage for Gain of 2×10^5		-	1500	-	V
Supply Voltage for Gain of 1×10^6		-	2000	-	V
Anode Dark Current (after 30 min. storage in darkness)		-	2	20	nA
Dark Count (after 15 hrs. storage in darkness) *2, *4		-	4000	-	s^{-1}
Time Response *2	Anode Pulse Rise Time	-	2.4	-	ns
	Electron Transit Time	-	42	-	ns
	Transit Time Spread (FWHM) *3,*4	-	2.5	-	ns
P/V (Peak to Valley) Ratio *2, *3, *4		-	2.2	-	-
Pulse Linearity at +/-5% deviation *1		-	50	-	mA

Figure 4.9: Table provided by Hamamatsu giving the typical design specifications of the PMTs. However, because the PMTs are made by hand in batches, their properties often differ from these stated characteristics and must be individualled measured in the laboratory to verify their functioning and obtain their operational high voltage.

We use a long integration time to collect a large sample of events, isolate the signal region, and compute the spectrum of integrated counts. At this point, an assessment is made on the quality of the measurement. If the voltage is tuned too low, then few single photoelectron events are visible. If the voltage is tuned too high, our sample is contaminated by events with multiple photoelectron peaks.

Once we obtain a clear peak, we fit a Gaussian to this distribution and obtain its mean, $\mu_{1\mathrm{pe}}$, which is used to infer the single photoelectron gain

$$G_{1\mathrm{pe}} = \frac{\epsilon}{e}\mu_{1\mathrm{pe}}, \tag{4.1}$$

where ϵ is the measured conversion between counts and charge for a given setting of the FADC amplifier and e is the elementary charge.

The ratio between the single-photoelectron peak and the gap region between it and the pedestal is the peak-to-valley ratio (P:V ratio), which is an indicator of the quality of the PMT signal. For each PMT, this value is also recorded. The datasheet specifies a typical

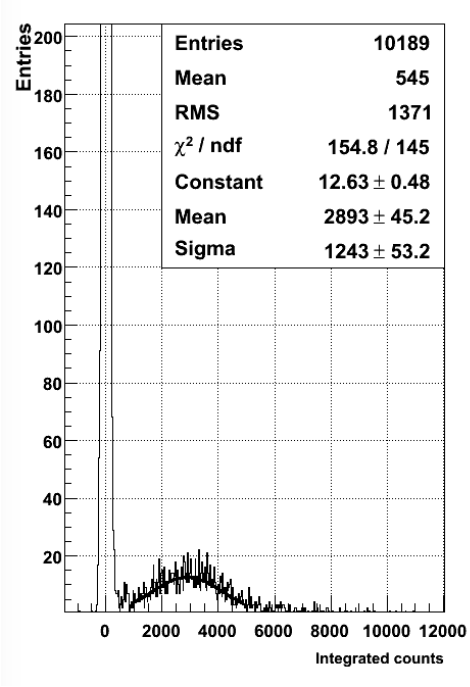

Figure 4.10: A single-photoelectron measurement for the ZS0018 PMT, showing a histogram of the total integrated counts over the selected signal region. Centered around zero is the pedestal region, reflecting zero-photoelectron events. A gaussian is fit to the single-photoelectron peak immediately following.

expected P:V ratio of ∼2.8 and a minimum of 1.5. We found no studied functional PMTs with a P:V ratio below ∼2.1.

	PMT	Max. Gain (10^6)	HV for Nominal Gain		P:V Ratio	DE at 390 nm
			$5 \cdot 10^4$	$2 \cdot 10^5$	$3 \cdot 10^6$	
Batch 1	ZS0018	7.79	871	1116	1972	2.7	18.3
	ZS0020	7.79	861	1114	1971	4	20.5
	ZS0022	5.55	944	1204	2146	2.4	21.0
	ZS0024	11.06	824	1061	1824	2.3	19.8
	ZS0025	11.80	827	1030	1769	2.5	19.1
	Mean	8.79 ± 2.5841	865.4	1105	1936.4	2.78 ± 0.70	19.74 ± 1.08
Batch 2	ZT0151	3.31	1017	1317	2437	2.5	20.9
	ZT0152	4.07	984	1268	2313	2.3	21.8
	ZT0153	4.10	974	1256	2308	2.20	21.5
	ZT0154	-	-	-	-	-	-
	ZT0155	4.09	969	1238	2303	2.6	22.3
	ZT0156	3.49	1053	1343	2410	2.4	22.2
	ZT0157	3.9	1019	1308	2343	2.1	21.7
	ZT0158	3.82	995	1281	2350	2.9	25.5
	Mean	3.82 ± 0.31	1002	1287	2352	2.43 ± 0.27	22.3 ± 1.5

Figure 4.11: Final tabulated calibration data of the PMTs used for FAST@TA, as measured in the laboratory at the University of Chicago.

4.4.2 Gain

Characterizing the gain as a function of high voltage is critical to determining our operational voltage for both the FAST experiment and for other calibration measurements, which are performed at predetermined gain levels given by the manufacturer.

Immediately prior to performing this measurement, the PMT's single-photoelectron response must be measured. A recent $G_{1\mathrm{pe}}$ is vital to the accuracy of this measurement and should be considered the first step of this task. Once this is obtained, we remove the amplifier and increase the LED voltage until each flash generates $\gg 1$ photoelectrons. The supply voltage is left unchanged at 2500 V. We then measure the value μ_{2500}, the mean of the multiple-photoelectron distribution at 2500 volts. From this we can solve for the average number of photoelectrons:

$$n_{\mathrm{pe}} = \frac{\mu_{2500}}{\mu_{1\mathrm{pe}}}, \tag{4.2}$$

Since we do not change the LED voltage, the number of photoelectrons should be constant, provided the experiment begins after a sufficient warm-up period for the LED is allowed. We then step the voltage from 2500 V to 600 V in increments of 100 V. At each voltage V, we calculate the gain as

$$G_V = \frac{\epsilon}{e n_{\mathrm{pe}}} \mu_V. \tag{4.3}$$

The errors are then

$$\Delta G = \sqrt{\left(\frac{\Delta\mu_{1\mathrm{pe}}}{\mu_{1\mathrm{pe}}}\right)^2 + \left(\frac{\Delta\mu_{\mathrm{max}}}{\mu_{\mathrm{max}}}\right)^2 + \left(\frac{\Delta\mu}{\mu}\right)^2}. \tag{4.4}$$

Once all measurements have been attained, a power law is fit to the gain to produce the final gain curve. An example gain curve for the PMT ZT0152 is shown in Figure 4.12.

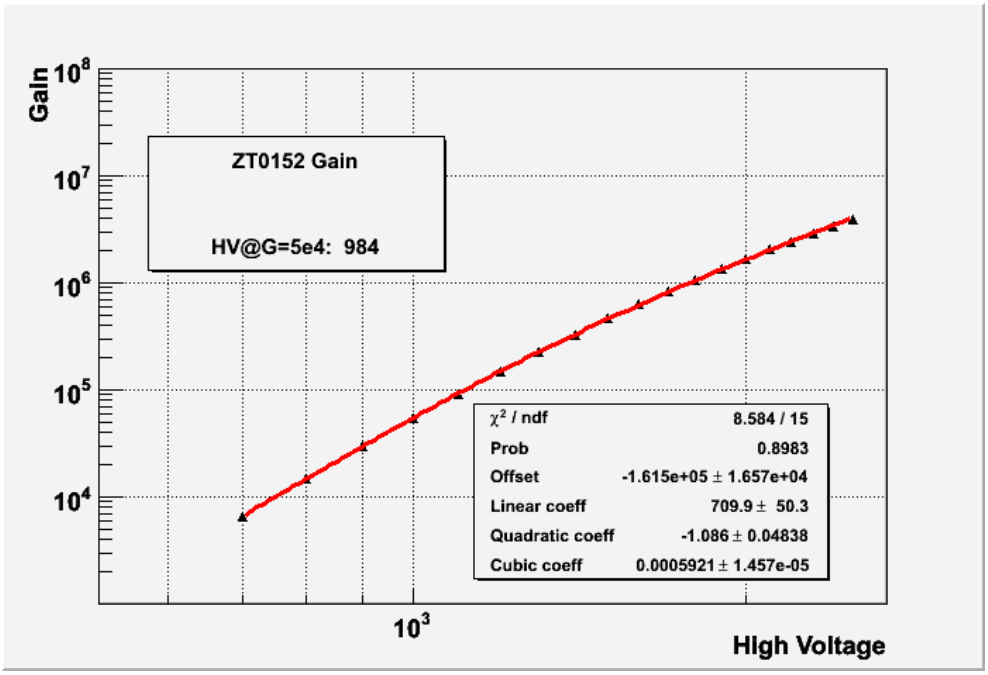

Figure 4.12: Gain curve for the PMT ZT0152 obtained through our automated laboratory calibration procedure. A polynomial power law was fit to the data to obtain the operational high voltage for a gain of $5 \cdot 10^4$. In this case, this was found to be 984 V.

Most of this measurement has been automated. A USB connection to the CAEN HV module sends commands to increment the voltage in steps of 100 V. The voltage is monitored and once the target has been reached, the program pauses for several minutes to let the system stabilize. Then a readout is performed to obtain the multi-photoelectron spectrum at that level. Because the gain evolves over several orders of magnitude throughout the course of this measurement, the magnitude of the output signal will diminish enough that noise begins to dominate the measurement. At this stage, the amplifier setting on FADC must be adjusted. This is performed by simply running a different readout program once the voltage lowers to around 1000 V, and this is handled automatically by the measurement program.

This program outputs all data files to a single folder, which is then used as the input for the analysis program that produces the final gain curves for the PMT. No manual fitting of the spectra is necessary.

4.4.3 Detection Efficiency

The detection efficiency of the PMT is a wavelength-dependent function that incorporates two physical phenomenon: (1) the quantum efficiency, or the probability that an incident photon will generate a photoelectron at the photocathode; and (2) the collection efficiency, the probability that a photoelectron reaches the first dynode and begins the multiplication stage. Like the gain measurement, this measurement begins by collecting a single-photoelectron measurement. It is vital to the later steps of this analysis. To measure the detection efficiency, we use the setup shown in Figure 4.13. A monochromator selects wavelengths from a broad-spectrum deuterium lamp. Its output is fed into an integrating sphere with a NIST-calibrated photodiode that provides absolute calibration for the incident light through a powermeter readout. Single photoelectrons are injected into the PMT through the collimator output of the integrating sphere.

The single-photoelectron measurement is used to tune the threshold for a discriminator module. The discriminator outputs pulses to a scaler that counts the number of photoelectrons observed at the dynode. We hence obtain a ratio of injected photons incident on the PMT from the integrating sphere to the number of photoelectrons measured by the discriminator-scaler setup. The detection efficiency ϵ is hence calculated from the powermeter reading, P, and the integrated time of each measurement, t, as

$$\epsilon = \frac{n_{\text{pe, anode}}}{n_{\gamma,\text{photocathode}}} = \frac{n_{\text{pe}} hc}{Pt\lambda\alpha} \tag{4.5}$$

An example measured detection efficiency is shown in Figure 4.14. We note an excess around 200 nm and 350 nm which we attribute to imperfections in the monochromator or stray light, but overall find consistency with the quoted efficiencies on the Hamamatsu data sheet.

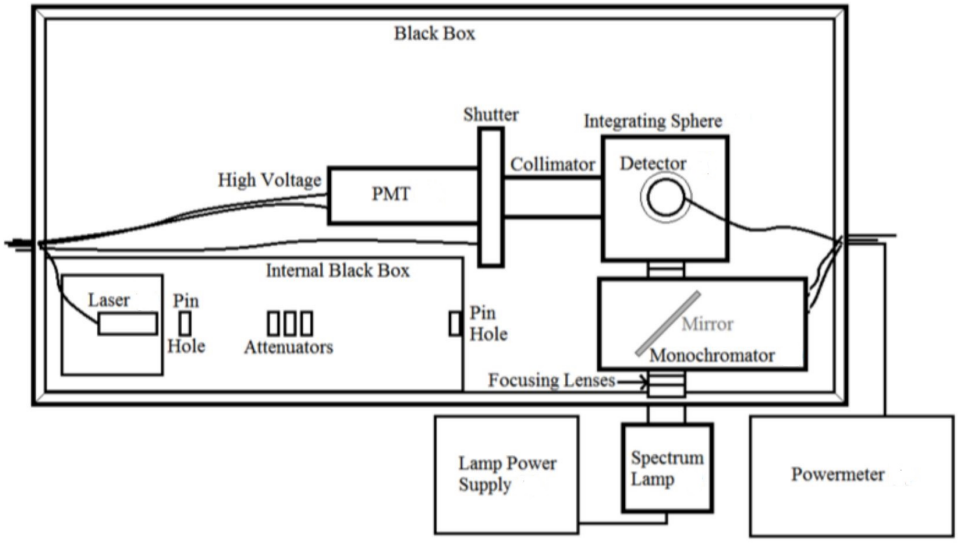

Figure 4.13: Experimental setup of the black box used for PMT tests.

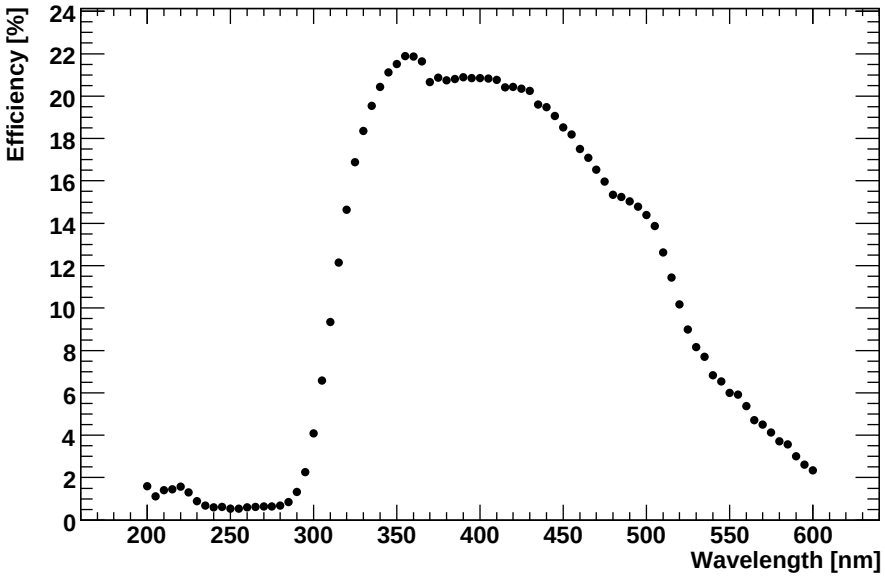

Figure 4.14: Measured detection efficiency for the PMT ZT0151. Note the excesses at approximately 250 nm and 350 nm likely caused by light leakage.

4.4.4 Differential Nonlinearity

For each photomultiplier, we measured the differential nonlinearity as a function of anode current at a nominal gain of $2 \cdot 10^5$. Because the two LEDs used for this measurement have different electrical responses, we began by selecting parameters on the function generator to produce approximately identical signals on the anode. We used pulse widths of 300 and 380 ns for each PMT and adjusted the LED voltage to give the desired peak height. We found that using a delay of approximately 74 nanoseconds combined the two pulses, hence we took measurements at each voltage with a delay of 1.074 microseconds and 74 nanoseconds. We pulsed the LEDs at a rate of 5kHz. Too high of a pulse rate results in deterioration of the electric field between the last two dynodes due to accumulation of space charge.

Because the high-frequency response of the PMTs is not a major concern of our operations (given our trigger frequency maxes out around $\sim$10 Hz during CLF runs), and because this measurement is particularly difficult to automate, we elected to forego this measurement in later batches.

4.4.5 Gain Stability

Another important characteristic to understand is the stability and performance of gain as a function of time since the PMT high voltage is switched on. To avoid contamination from this systematic on our scientific results, the detector start-up process must begin sufficiently in advance of the data acquisition period.

There are two main methods to test this. The first is by applying a fixed LED signal to the PMT over a long period of time and observing the difference in the integrated counts of the anode signal. This suffers from a few additional problems, namely the dependence on the warm-up of the LED and function generator that are used as inputs. The second method is by using a YAP pulser. This is a small fixed light source consisting of a $YAIO_3$:Ce scintillator crystal excited with a 50 Bq ^{2}41Americium source. Because this depends only

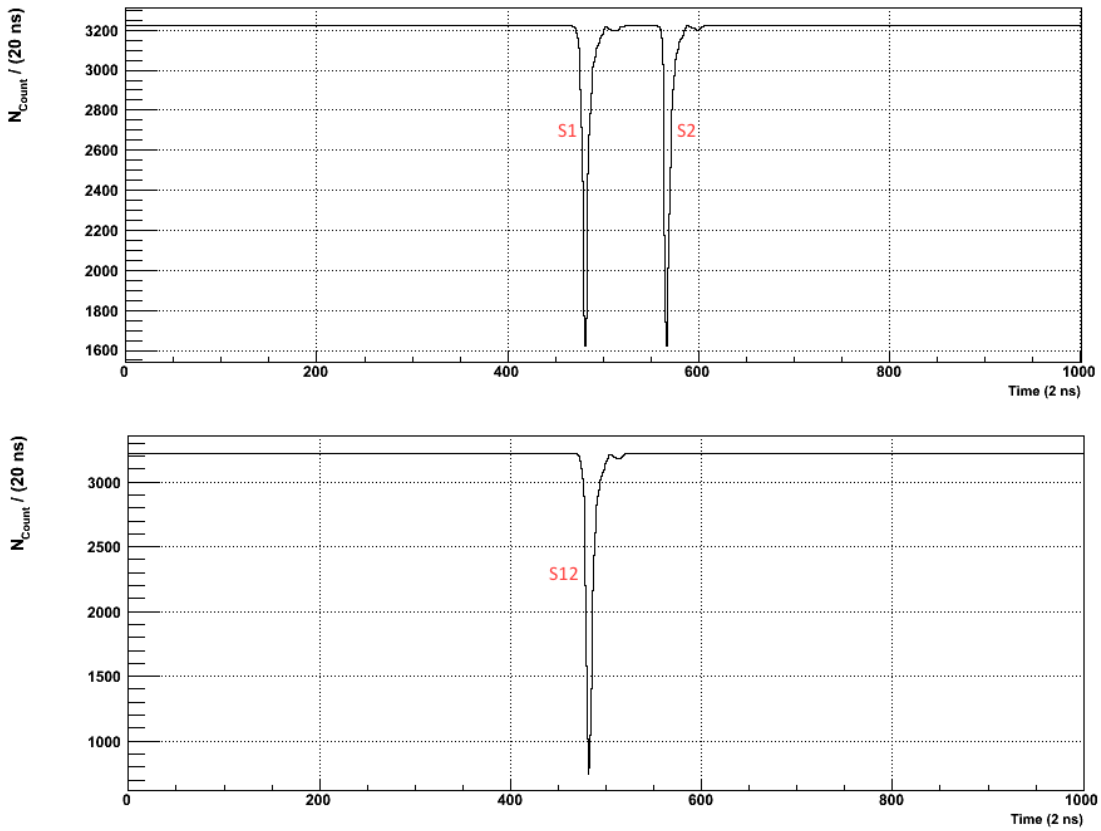

Figure 4.15: Setup for the differential nonlinearity measurement of FAST PMTs. Top: two identical pulses, S1 and S2, are sent to the PMT separated by a small delay and their total combined signal $S_1 + S_2$ is calculated. Bottom: the delay is removed and the total signal S_{12} is calculated and compared to $S_1 + S_2$.

on the scintillator emission and the energy emitted by the radioactive source, this is free of all systematics associated with unstable inputs. Hence this can be used to monitor the PMT's gain very effectively. A downside of this is the scarcity and expense of these YAP pulsers: these were produced only in limited quantities and only a finite number currently exist. They are hence hugely expensive, and it is impossible to monitor every PMT deployed in the field with a YAP pulser.

Experiment	Tel. Aperture (m^2)	Pixel Opening Angle ($^\circ$)
Auger	13	1.5
Telescope Array	7	1
FAST	1	15

Table 4.1: Comparison of the telescope aperture and pixel opening angle between FAST and themajor current-generation UHECR observatories.

4.5 The FAST Prototypes

Beginning in 2014, we underwent several tests of the FAST design. Since PMTs of this size had never been used for UHECR research before, we had a number of concerns to address, the largest of which is stable long-term operation and UHECR detection under the high night-sky background (NSB) a FAST pixel encloses. The average photocathode current produced by the NSB is proportional to $A\Delta\Omega$, where A is the aperture and $\Delta\Omega$ is the enclosed solid angle of the pixel. In addition, the signal-to-noise ratio is proportional to $\sqrt{A/\Delta\Omega}$. Table 4.1 summarizes a comparison of these quantities among current-generation major observatories. Because the aperture of FAST is significantly lower and its pixel opening angles significantly higher than that of contemporary experiments, there are some concerns about both the PMT gain and the practical detection of UHECR events under these high-background conditions. To address these concerns, our first test of the FAST concept was a short-term experiment with a single PMT aimed at demonstrating the feasibility of such large pixels as UHECR detectors. The details of this first test (which took place in 2014 at the Telescope Array Black Rock Mesa FD site) are shown in Section 4.5.1.

In parallel to this first test, we developed the full optical and mechanical designs of the FAST telescopes, discussed previously in Sections 4.1 and 4.2. Plans solidified to construct full-scale FAST prototypes at both the TA and Pierre Auger sites. There are numerous advantages to prototyping at the sites of existing experiments. The first is the utility of capitalizing on existing infrastructure. FD sites provide simple benefits like power, Internet connection, and a location relatively free of light pollution, but most importantly, we gain

access to a huge number of tools by constructing our prototypes to share fields-of-view with existing FD telescopes. Gaining access to the results of the robust reconstruction provided by these hybrid detectors provides us with important tools to cross-check and verify our own observations. Furthermore, by triggering externally off an existing telescope, we gain an important understanding of which events are detectable given our different systematics. Both sites also have central laser facilities consisting of a 355 nm UV laser that fires periodically throughout the night that will be useful for FAST commissioning and monitoring purposes. Finally, deploying a single consistent instrument (ie a FAST telescope) at these two different sites will allow us to make measurements that are largely independent of those made from current FDs (aside from the geometry provided by the surface detectors), and will allow us to explore cross-checks between these two experiments.

Constructing and operating these prototypes long-term provides an invaluable test of the FAST concept. With the goal of a future super-array in mind, it is important to understand how effectively these stations can be operated independently. This includes reliance on on-site staff for intervention in shifts or regular maintenance, both of which would be unfeasible in a future FAST array. Importantly, these prototypes allow us to assess the performance of the instrument over a period of several years, including large seasonal temperature variations and degradation of the optical components due to wear and accumulation of dust. If the FAST mirrors degrade quickly enough to require regular cleanings, for instance, a large-scale array would be impossible. Finally, these prototypes allow us to understand the quality of data collected with FAST and test our developing analysis methods.

Following the success of the single-pixel experiment, we began constructing full-scale FAST prototypes for long-term remote operations. We constructed and commissioned these detectors on-site in 2016, 2017, and 2018, and they have all been in steady remote operation since. We also built a rigorous remote atmospheric monitoring system. Over the course of these years, we have collected a sizeable sample of UHECR data, which we have used as a

first test of our developing analysis tools. Section 4.5.2 describes the construction and results of these prototypes.

Our next milestone is the deployment and construction of an independent FAST telescope with no dependency on existing infrastructure. This involves abandoning the electronics systems discussed in Section 4.3 in favor of an FPGA-based low-power data acquisition system powered by solar and the development of FAST internal trigger. Our projected test site for this next milestone is the Auger experiment, where in 2019 we constructed a single FAST telescope at the Los Leones FD site and began testing our internal trigger. We plan for an independent FAST station several kilometers from this site to test stereo observation of UHECRs. Section 4.5.3 describes developments on this next milestone.

4.5.1 Single-Pixel Test

The first test of the FAST design was in 2014, when a single PMT at the focus of a Fresnel lens was used to demonstrate the feasability of using a large-pixel camera to observe UHECRS and ultraviolet laser shots. For this test, we capitalized on the similarity between the FAST design and the JEM-EUSO prototype telescope (EUSO-TA) optics. With a light-collecting area of $\approx 1\,\mathrm{m}^2$ and a circular field of view with a 7° radius, it functions as a remarkably effective testbed for FAST. This prototype was housed at the Black Rock Mesa site of the TA experiment. The EUSO-TA optics consist of two 1 m^2 Fresnel lenses shielded by a UV-transparent acrylic plate at the diaphragm. Shown in Figure 4.16 are the EUSO-TA telescope design and a picture of the FAST test apparatus using these optics.

During this test, we monitored the NSB and tested the stability of the PMT gain. Figure 4.17 shows our background current before and after opening the telescope shutter. We determined the RMS fluctuations in the NSB to be approximately 11 photoelectrons per 100 ns. We observed no sudden spikes in the background suggesting contamination with bright starlight. In addition, we determined the stability of the gain over a full night of

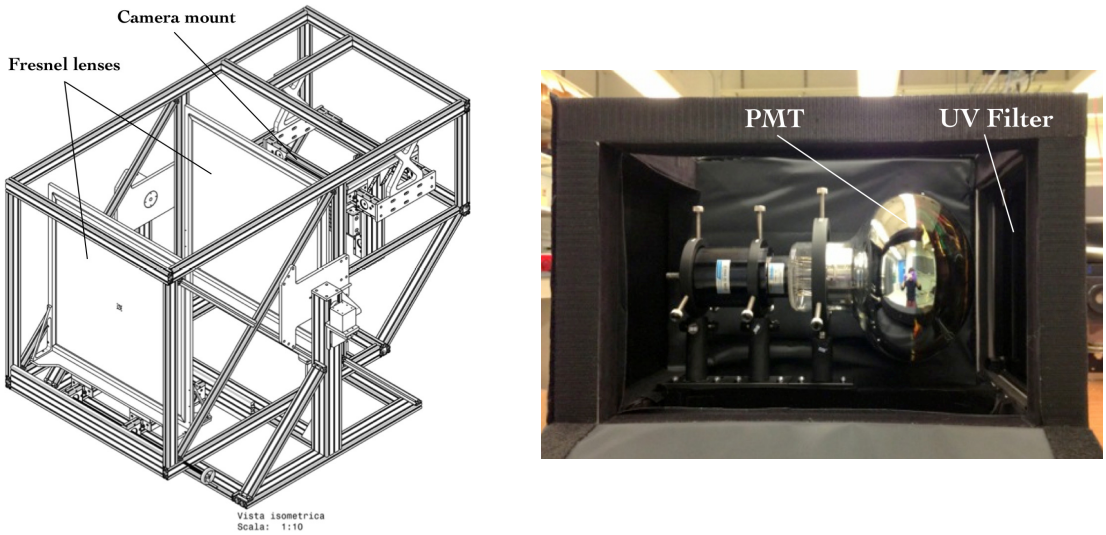

Figure 4.16: Left: JEM-EUSO prototype telescope optics, used for the single-pixel FAST test. Right: a photo of the single-pixel test using the JEM-EUSO optics.

operation by attaching a YAP pulser to the PMT and observing the evolution of the YAP signal (a fixed optical source) thoughout the night; our results showed a variance of only about 7%, which can be explained readily by the temperature dependence of the setup, about 1% per degree Celius, since the PMT housing for this test is not climate controlled. Figure 4.18 shows the stability of both the background photocathode current from the NSB and the total integrated YAP pulse counts (see Figure 4.19 for an example) over the course of a single night of data acquisition. The electronics for this first test is a simplified version of the final electronics setup used for the FAST prototypes. A diagram of the DAQ electronics is shown in Figure 4.20.

We also tested this setup's capability as an UHECR detector in three important ways. The first is by observation of the TA Central Laser Facility (CLF). Located ∼21 km from our site, the CLF is a 355 nm laser equivalent to approximately a 15 EeV shower. It fires 300 vertical shots every half-hour during TA operations. These laser shots are used for monitoring and calibration of the TA FDs, and since they run every night, as long as the CLF beam is in our field of view, detections are guaranteed, whereas it is possible to have data

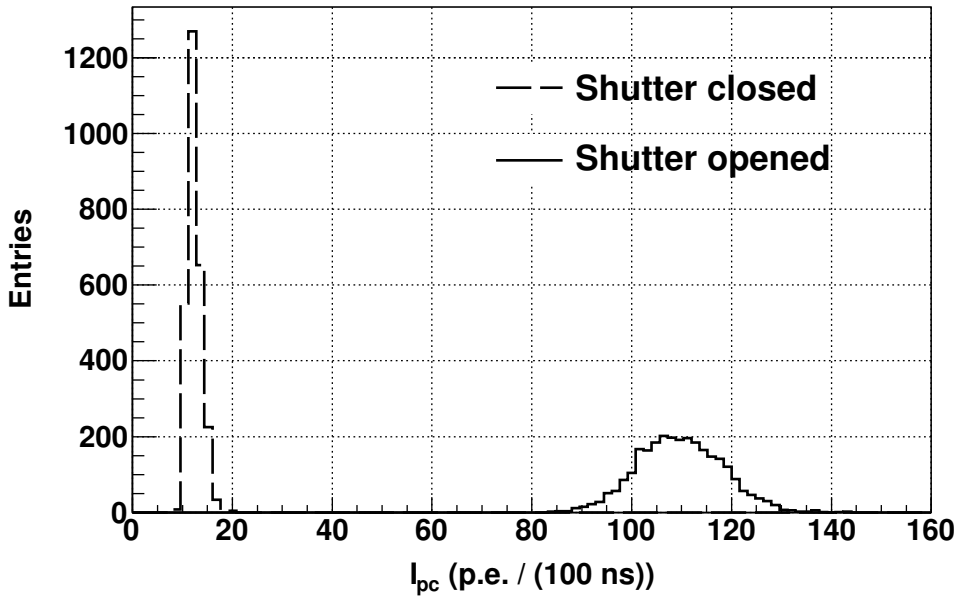

Figure 4.17: Observed night-sky-background by the FAST single-pixel prototype before and after opening the shutter.

acquisition runs where no UHECR events are observed. While it traverses the atmosphere, the laser light side-scatters on air molecules and aerosol particles into the FD field of view, producing signals similar to a UHECR shower. Since these artifical showers move upwards instead of downwards, their time profile in the detector makes distinguishing these events straightforward.

Because of the lower signal-to-noise of the single-pixel FAST test, individual CLF signals were expected to be attenuated beyond the level of detectability. However, by stacking and averaging all of the 300 CLF shots in a single firing window, we were able to observe a clear signal. Figure 4.21 shows an example of one such observation, averaging over many laser shots. The average signal amplitude was found to be approximately 7 p.e./100 ns, which is indeed smaller than our average photocathode current from the NBS ($\sim$11 p.e./100 ns).

The second method is by use of a Portable UV Laser System (PLS) [112], which can be deployed at various locations across the TA site. We observed PLS shots from approximately 6 km from our telescope, compared to the CLF's distance of 21 km. The PLS laser energy is

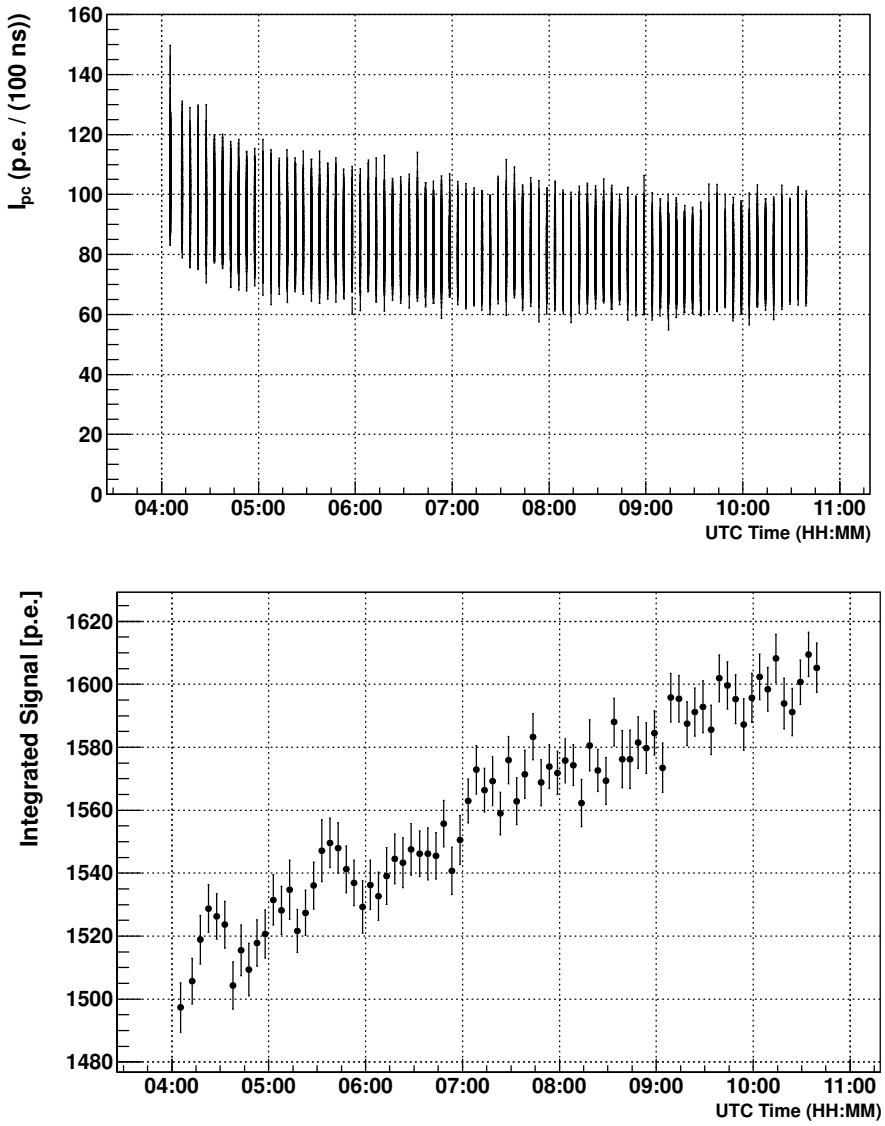

Figure 4.18: Top: Evolution of the photocathode current during a seven-hour data acquisition period. Bottom: Evolution of the YAP signal during the same seven-hour data acquisition period.

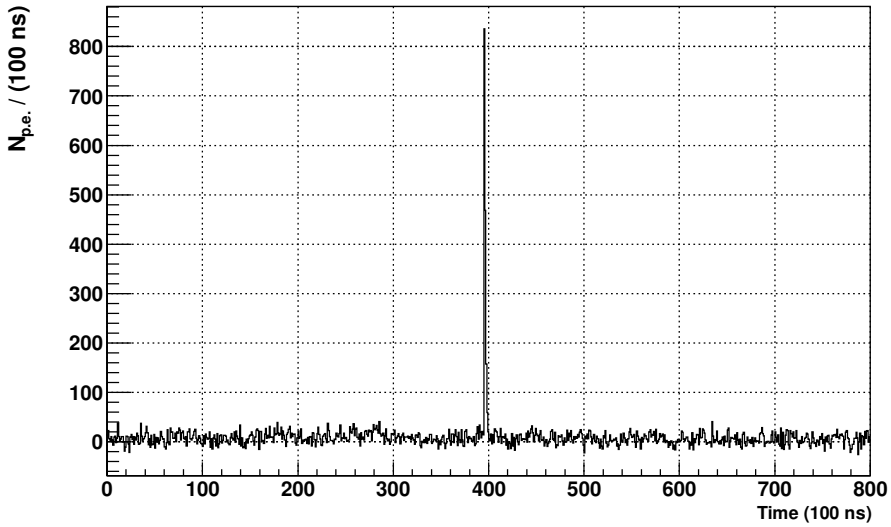

Figure 4.19: An example signal collected from an internally-triggered YAP pulse on a FAST PMT. Since the YAP pulser is a stable optical source, it can be used to monitor stability of the PMT gain.

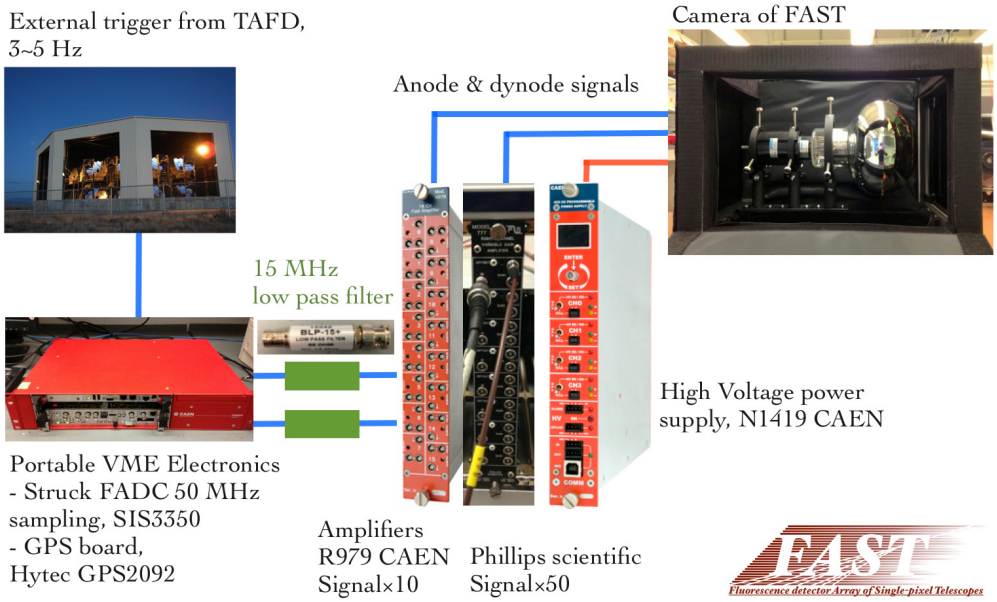

Figure 4.20: Diagram showing the FAST electronics chain for the single-pixel test, a simpler version of the final DAQ electronics for the FAST prototypes.

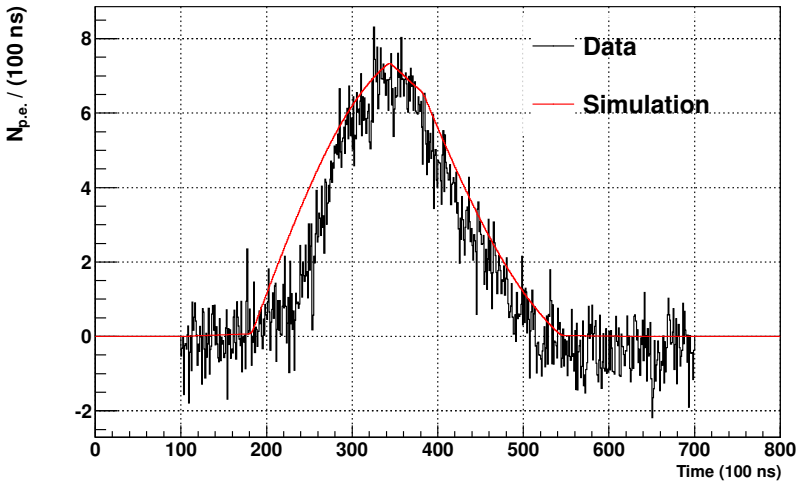

Figure 4.21: A laser signal from the TA Central Laser Facility seen by the FAST single-pixel test using the JEM-EUSO optics. Shown in red is a simple simulation.

identical to that of the CLF (2.2 mJ, $\sim 10^{19.2}$ eV equivalent). Since it has the same energy but fires from a significantly closer distance, its signal-to-noise in the FAST testbed is much higher. An example of a portable laser detection is shown in Figure 4.22; its peak amplitude of approximately 350 p.e./100 ns is well above the NSB, and single shots can be easily resolved at 100% efficiency.

We used these data to calibrate the relative timing between FAST and the TA FD by comparing the GPS timing recorded by the two detectors for the same laser shot. We expected an offset, since the external trigger to the FAST DAQ required not only physical travel time through a long cable but also processing time in the TA trigger board. The distribution of timing differences between the FAST and TA fluorescence detector GPS timings is shown in Figure 4.23. We measured an offset of 20.86 μs, attributed to the TA trigger processing time. The RMS of $\sim$100 ns is consistent with the GPS resolution and adequate for the purpose of the FAST prototype test. A proper understanding of this temporal offset between triggers was important for matching UHECR shower signals observed with FAST to known reconstructed events from the TA FD, an essential test of our capacity for UHECR detection.

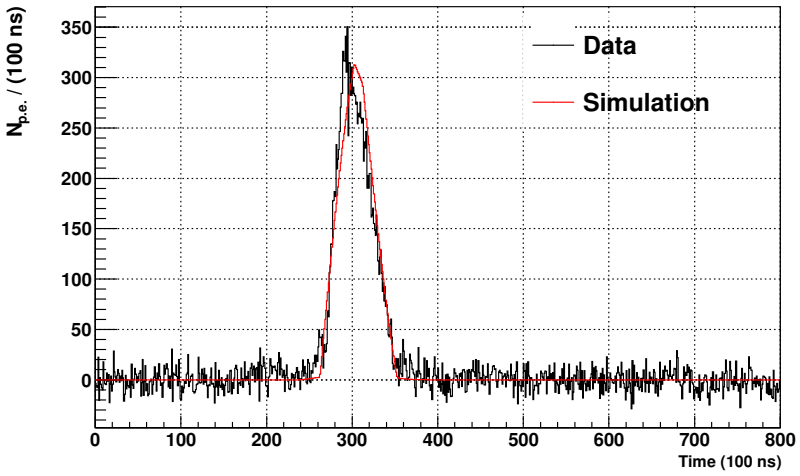

Figure 4.22: A laser signal from the Portable UV Laser System, seen from a distance of approximately 6 km. Shown in red is a simple simulation.

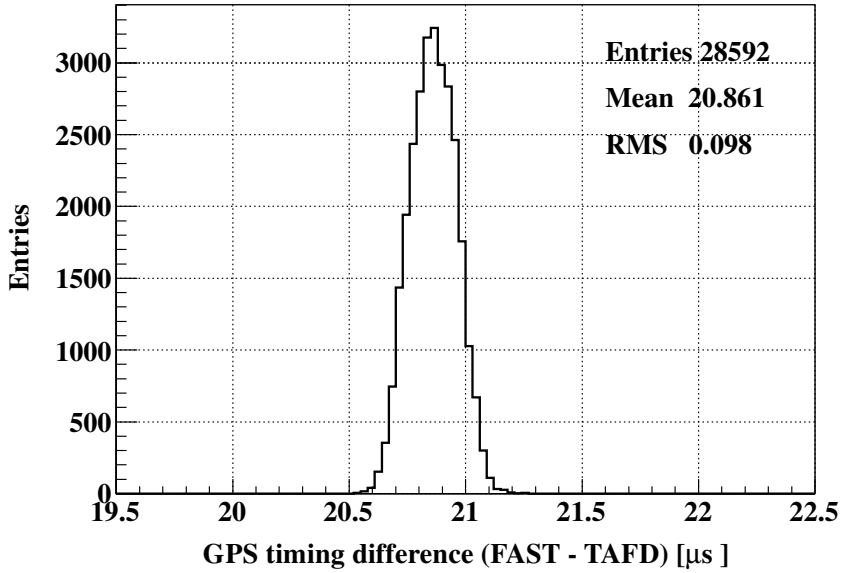

Figure 4.23: Difference between the TA FD and the FAST prototype GPS time for laser shots. This difference is due to the trigger processing time and signal travel time between the TA FD and FAST and is used to understand the timing offset between TA and FAST for matching UHECR events.

We performed a simulation of the FAST prototype's response to laser shots to compare with the PLS and CLF data. For this purpose, the efficiency of the EUSA-TA telescope as a function of angle was obtained from a ray-tracing simulation of the Fresnel lenses (Figure 4.24). This efficiency is defined as the ratio between the number of photons arriving at the camera to the number of photons injected at the aperture; it is calculated as a function of the injection angle relative to the optical axis. This simulation includes the wavelength-dependent quantum efficiency of the FAST PMT (measured as described in Section 4.4). This does not, however, account for the full azimuthal variance of the PMT's detection efficiency to account for variations in the electric field due to the positions of the dynode structure. These simulated signals are overlayed in red in Figures 4.21 and 4.22. As the laser energy of the PLS is not monitored and logged (to account for fluctuations due to temperature, etc.), the simulated signal was rescaled by $\sim$30% to match the meaesured signal. Since the CLF is continuously monitored, we were able to accurately simulate its firing energy and did not need to perform any rescaling. Overall, there is good agreement between the simulations and our observations, and any differences in the signal shape can be explained by uncertainties in the optical efficiency (as the ray-tracing model assumes perfect Fresnel lenses), in the alignment of the TA-EUSO telescope and the FAST camera position, and in the assumed atmospheric attenuation.

The third and final method is by actual detection of UHECR showers. Though FAST is designed with UHECR events at the highest energies in mind, detection of highly-energetic showers ($>10^{19}$ eV) in our limited running time was extremely unlikely. However, we could still test the FAST design by observing lower-energy showers closer to our prototype. Lower-energy Cherenkov events with their emissions cones directed towards our aperture were also likely targets. To verify the validity of our observations, we performed a search driven by well-reconstructed events supplied from the TA FD (with which we shared a field-of-view and an external trigger). This allowed us to carefully verify the validity of each significant

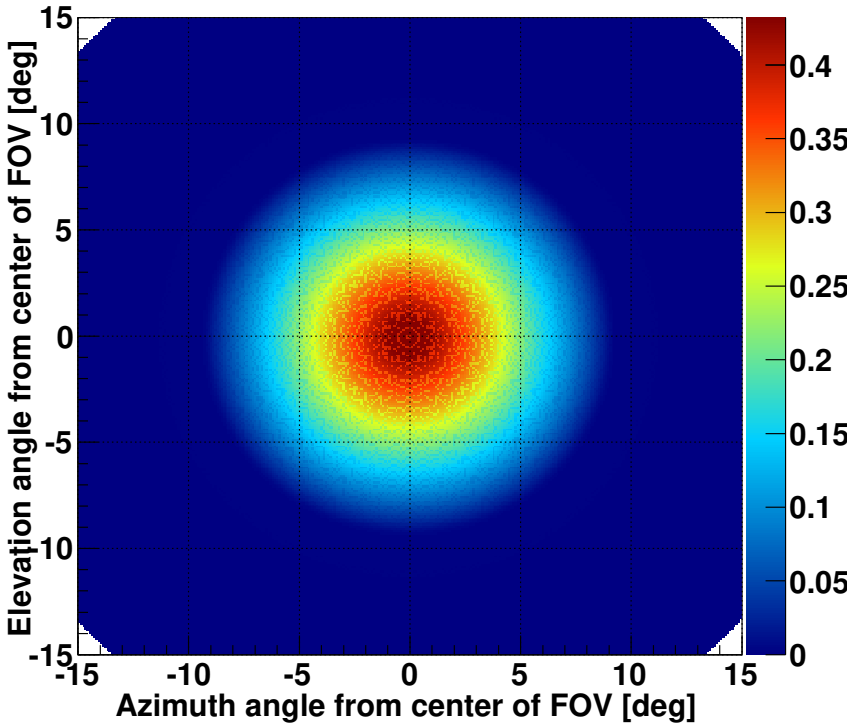

Figure 4.24: Efficiency of the FAST single-pixel test's optics as a function of the angle to the optical axis, obtained with a ray tracing simulation of the telesope's Fresnel lenses.

detection that we made.

First we selected TA FD events with a reconstructed shower geometry passing through the field-of-view of the FAST prototype. We also searched through our FAST data and selected events that have traces reporting a highly-significant detection, which we defined as containing a 5σ signal-to-noise ratio as calculated from the pedestal of each individual trace (the first 10 mus) over a $70\,\mu$s time interval positioned in the trace according to the time offset measured with the PLS study. By matching between these datasets, we found 16 shower candidates in the 83-hour dataset, with an estimated background of less than a single event. This background was estimated by applying this same matching technique to FAST traces recorded in coincidence with showers that fell outside the FAST field-of-view. An example event is shown in Figure 4.25, showing both the reconstructed TA geometry from the collaborations event display and the accompanying trace seen by FAST.

Because we have access to full TA reconstructions for these events, we can also draw some further conclusions about FAST. First, we can use a simple s Figure 4.26 shows our observed correlation between impact parameter and energy based on our small dataset and provides a rough estimate for our maximum detectable distance as a function of energy, $r_{\rm det}$. When extrapolated to an energy of 10^{19}, we obtain a maximum detectable distance of approximately 15 km.

Given the limited field-of-view of the single-pixel test, only a small portion of the shower development is visible; hence most of these events have their depth of maximum development $X_{\rm max}$ located well outside our field-of-view. Because of this, a robust Gaisser-Hillas fit to the shower profiles is generally unfeasible. However, a comparison between our observations and simulated shower profiles generated from the geometry provided by the TA FD can provide an important cross-check on our results. For each shower candidate, we generated a shower with the same energy, direction, and core distance and estimated the corresponding signal in FAST. The same simulation of the optics, atmospheric attenuation, and quantum

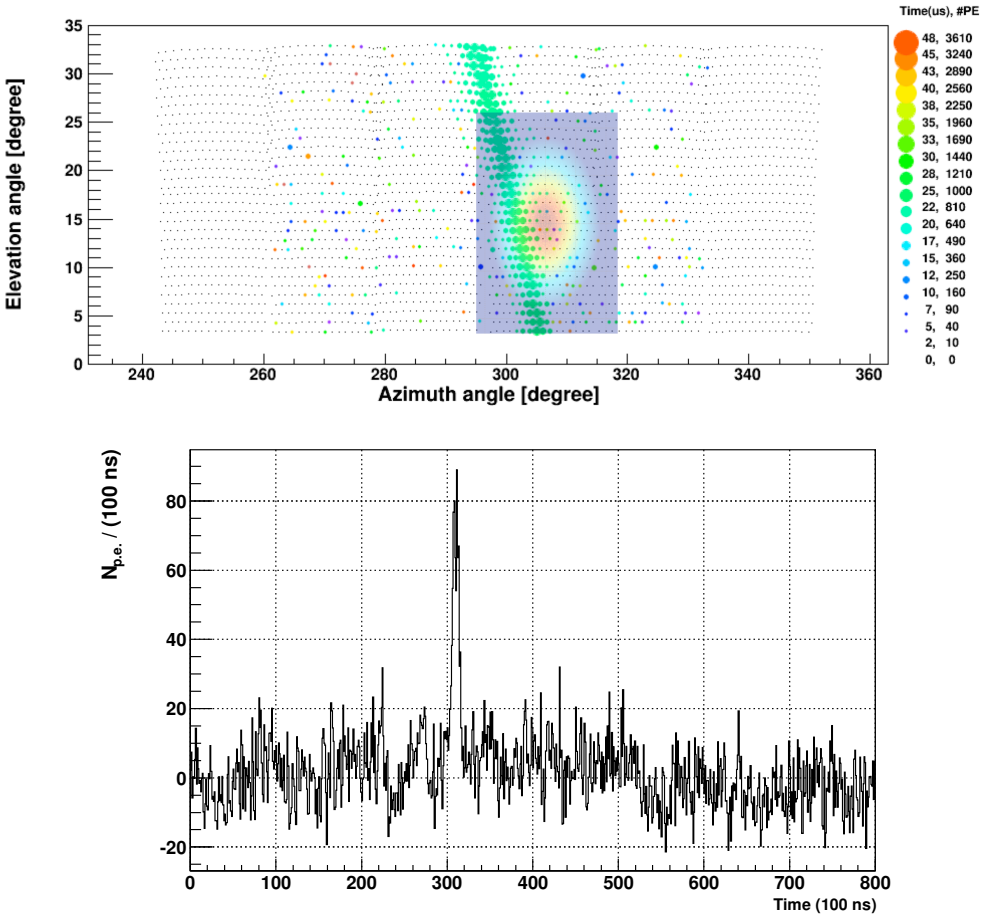

Figure 4.25: Top: TA FD event display showing the geometry of a 10^{18} EeV shower that fell into our FAST field-of-view, indicated on the figure by the overlay of our optical efficiency. Bottom: The observed trace for this 10^{18} EeV shower as seen by the FAST prototype.

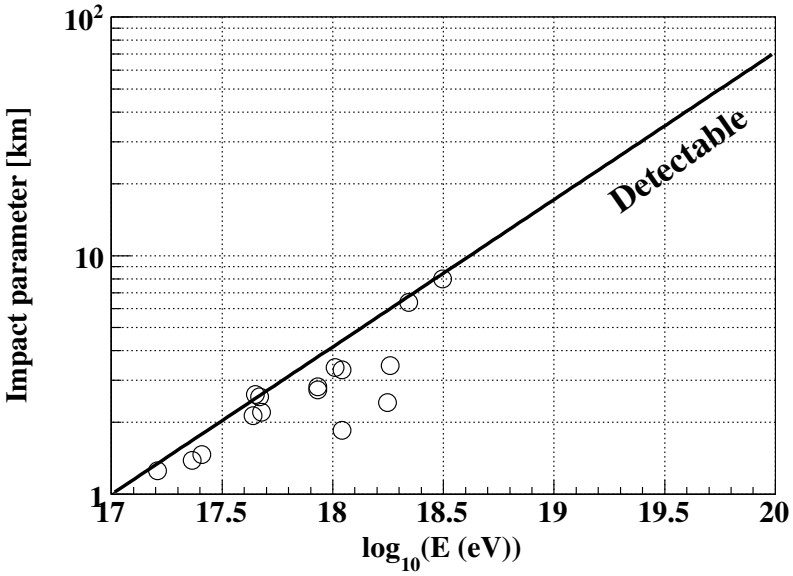

Figure 4.26: Correlation between impact parameter and energy of the 16 shower candidates observed by the FAST prototype, both estimates provided by the TA reconstruction. The line provides a rough estimate of our maximal detectable distance as a function of energy based on our small sample of data.

efficiency was used as with the laser simulations. A comparison between the measured and simulated signals for two showers is shown in Figure 4.27. The amplitude and shape of these simulated pulses are in good agreement of our observations with no rescaling to account for our systematic uncertainties.

Concurrent to this work, development was underway for full-scale FAST telescope prototypes. The successful observation of ultraviolet lasers and UHECR events with this first single-pixel test provided sufficient validation of the FAST concept to advance the project and pursue the construction of these full-scale prototype telescopes at the Black Rock Mesa site.

4.5.2 FAST at TA

Following the single-pixel test in 2015, in the next three years we installed a series of full-scale FAST prototypes at the Black Rock Mesa site. The first prototype was installed and

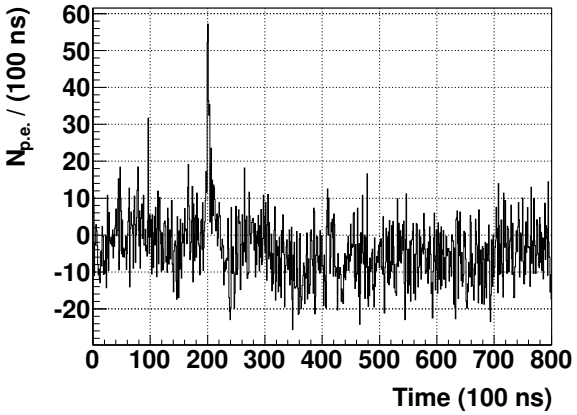

(a) Data: $E_{\rm rec} = 10^{17.2}$ eV

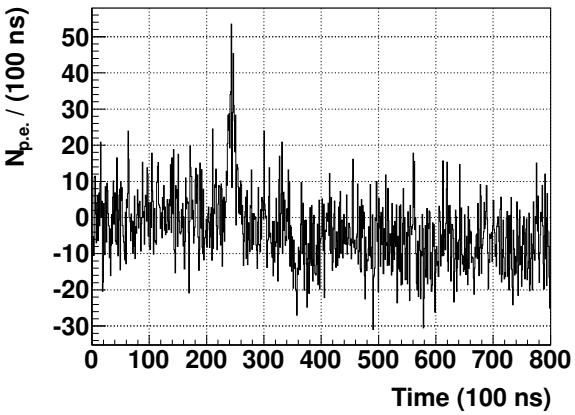

(b) Data: $E_{\rm rec} = 10^{18.0}$ eV

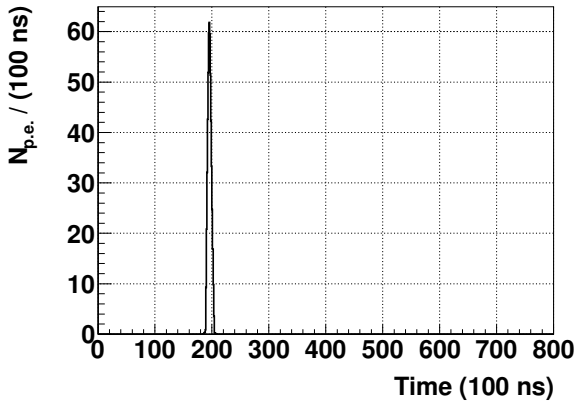

(c) Simulation: $E_{\rm sim} = 10^{17.2}$ eV

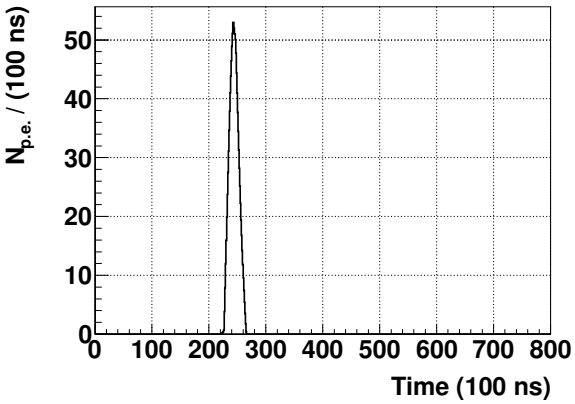

(d) Simulation: $E_{\rm sim} = 10^{18.0}$ eV

Figure 4.27: (a) and (b): FADC signals recorded for two shower candidates; (c) and (d): corresponding simulated signals, generated from the reconstruction provided by TA.

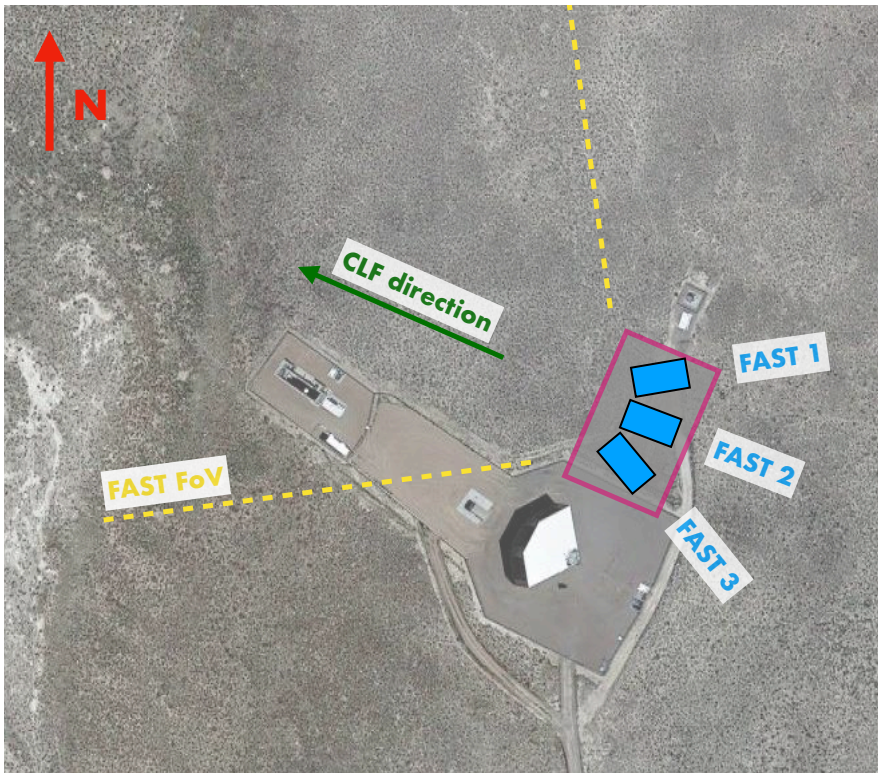

Figure 4.28: Location and field-of-view (FoV) of the three FAST prototype telescopes installed at the Black Rock Mesa site of the Telescope Array Experiment. The TA fluorescence detector is located south-west of the FAST installation. The central laser facility (CLF) is located $\sim 21\,\mathrm{km}$ away from the BRM site in the indicated direction and is within the FoV of FAST 2.

commissioned in October 2016, and after its successful deployment, two additional telescopes followed in September of 2017 and 2018. We constructed a large concrete pad in 2016 on which to house the trio of detectors and explored various designs for buildings to house the telescopes, whose designs also evolved over the course of this R&D experiment. An aerial drone photo of our detector layout, showing all three FAST buildings and the TA FD building, is shown in Figure 4.28. Figure 4.29 shows a group photo of our commissioning team plus the final three assembled prototypes in their housings. Figure 4.30 details the numbering and layout scheme of our telescopes and DAQ channels, as well as shows the physical orientation of the telescopes in both sky view and telescope view.

Figure 4.29: The three FAST prototype telescopes installed at the Black Rock Mesa site of the Telescope Array experiment in central Utah, USA. The FAST All-Sky Camera (FASCam) and Sky Quality Monitor (SQM) can be seen attached to the roof of the central building.

Operations

FAST is operated remotely with no on-site staff. It runs on clear, moonless nights when the TA FD is operational and is externally triggered from the Black Rock Mesa FD. The startup procedure is initiated from a Raspberry Pi computer connected to the DAQ system. This process is fully automated through a series of scripts. Wake-up commands are sent to the NIM and VME crates, which turn on the DAQ electronics and boot the single-board VME computer containing the data acquisition software. The electronics are started and the high voltage is enabled an hour prior to the run's begin so they may warm up.

Our operations begin with a pedestal run in which we collect 5 seconds of data with the shutter closed, using our high-threshold internal trigger. These data allow for long-term monitoring of the PMT gain and help define our pedestal. After this, the shutter opens, another pedestal run is performed, and data acquisition begins. Data is saved in five-minute blocks and an additional 3-second pedestal run is taken between each block for monitoring purposes. Since a small number of PMTs have YAP pulsers attached, this also allows for more careful monitoring of their gain. A monitoring program logs the high-voltage at regular

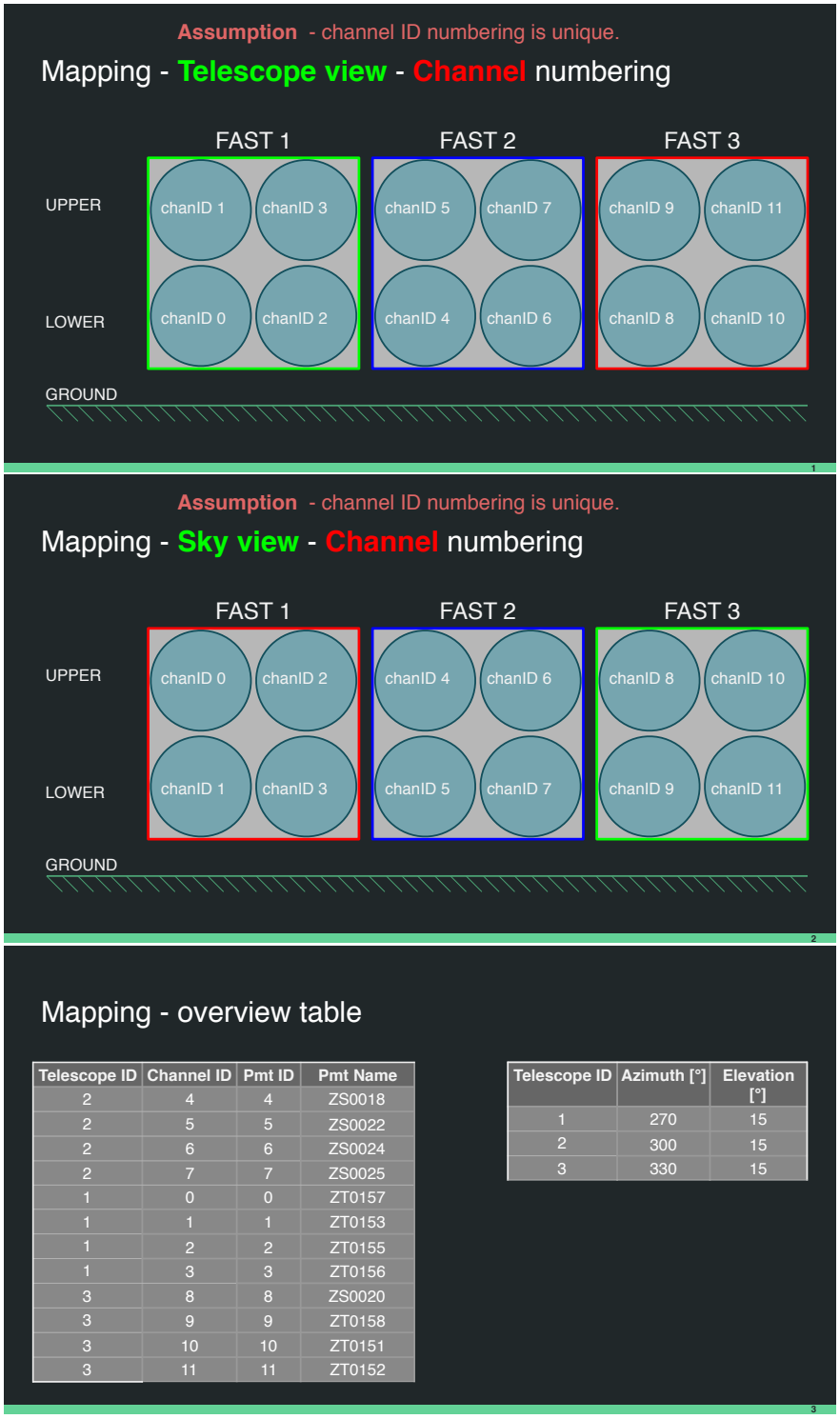

Telescope ID	Channel ID	Pmt ID	Pmt Name
2	4	4	ZS0018
2	5	5	ZS0022
2	6	6	ZS0024
2	7	7	ZS0025
1	0	0	ZT0157
1	1	1	ZT0153
1	2	2	ZT0155
1	3	3	ZT0156
3	8	8	ZS0020
3	9	9	ZT0158
3	10	10	ZT0151
3	11	11	ZT0152

Telescope ID	Azimuth [°]	Elevation [°]
1	270	15
2	300	15
3	330	15

Figure 4.30: Diagram showing the FAST numbering scheme and physical layout.

intervals to ensure there are no issues with the electronics. FAST's traces are 100 μ long, sampled at a rate of 50 MHz, and include a 10 μs buffer prior to the trigger to help estimate the pedestal for the event. A UPS system and an automated shutdown procedure ensures there is no damage to the detector in face of power outrages or loss of remote connection.

Monitoring

Throughout FAST@TA's nightly operations, we monitor the average photocathode current, weather, and sky quality.

The average photocathode current is dominated by the night-sky background (NSB). Prior to opening the shutters, FAST records a typical electronics noise of ~12 p.e./20 ns. This increases to ~98 p.e./20 ns when the shutters open. The evolution of the NSB over the course of a single FAST run is seen in Figure 4.31. Because the FAST telescopes are open to the environment during a DAQ run and the buildings are not temperature-controlled, the temperature of the electronics changes throughout the night and reflects the local weather. Since there is as much as a 30° variance in temperature over the year, and since temperature can vary by as much as 10° over a single night, this effect can be quite large. Understanding the temperature dependence of our signals (and recording the FAST camera box temperature) is important for future analyses. A YAP pulser is installed on two of the twelve FAST PMTs. The integrated YAP signal, collected from the three-second internally-triggered pedestal runs between our five-minute data acquisition periods, is used in conjunction with a temperature sensor installed in FAST 2 to examine the temperature dependence of our electronics in Figure 4.32. We determined the temperature coefficient to be -0.434 ± 0.003 % / °C, which is consistent within uncertainties of the PMT's specifications.

Two ancillary instruments have been installed on FAST 2 for monitoring purposes: the Sky-Quality Monitor (SQM) and the FAST All-Sky Camera (FASCam), used to monitor cloud coverage and night-sky brightness.

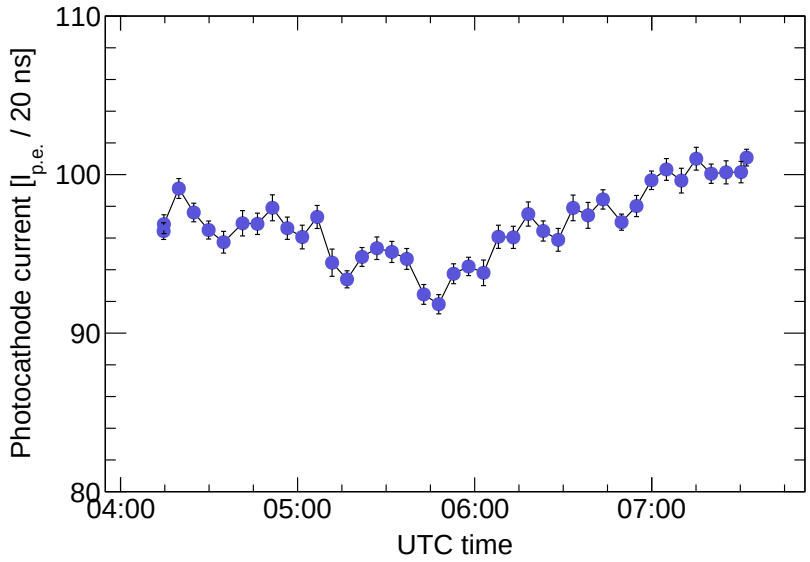

Figure 4.31: The evolution of the photocathode current during a cloud-free run on Jan. 18^{th}, 2018.

The FASCam is a CCD camera with a 180° field-of-view equipped with a Moravian Instruments G2-4000 Peltier-cooled KAI-4022 CCD chip. It features a five-position adjustable filter wheel with Johnson BVR filters and a Sigma 4.5 mm f/2.8 fish-eye lens. Mounted vertically on the exterior roof of the central FAST enclosure, it is controlled by the Raspberry Pi that initiates our DAQ startup procedure. FASCAM captures 30 s exposures of the night sky with Johnson filters and 180 s exposures through its UV filter every 10 minutes during operations. An astrometrical analaysis is performed on these data that matches observed star positions with known coordinates in each wavelength band from the Tycho-2 catalog. This provides an estimate of the cloud coverage by calculating the fraction of visible to observable stars in the field-of-view. A picture of the FASCam and an example of a FAScam analysis is shown in Figure 4.33. Measurements collected over 265 nights since the FASCam's installation in September 2017 suggest a clear sky (visible fraction ¿ 0.8) on 55% of observation nights. This analysis is automated and stored in a database for future analysis.

The Sky-Quality Monitor (SQM) is a commercial device attached to the root of FAST 2 that measures night-sky brightness in magnitudes per square arc-second with a precision of

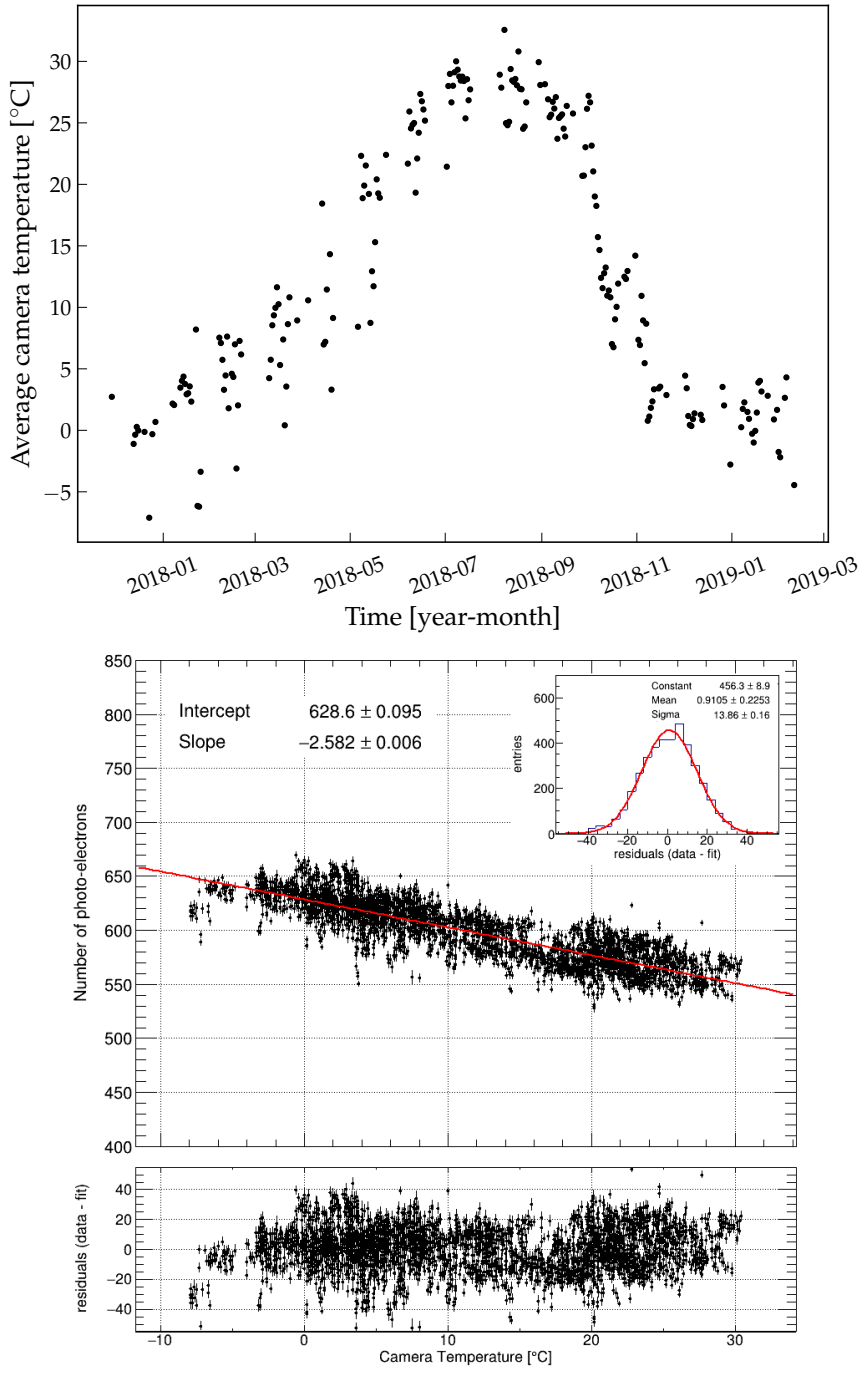

Figure 4.32: Top: Average temperature inside a FAST camera enclosure at the TA site during each night of observation over a year-long period. Bottom: Evolution of the integrated YAP signal as a function of temperature. The residuals of the fit are shown in the bottom pane.

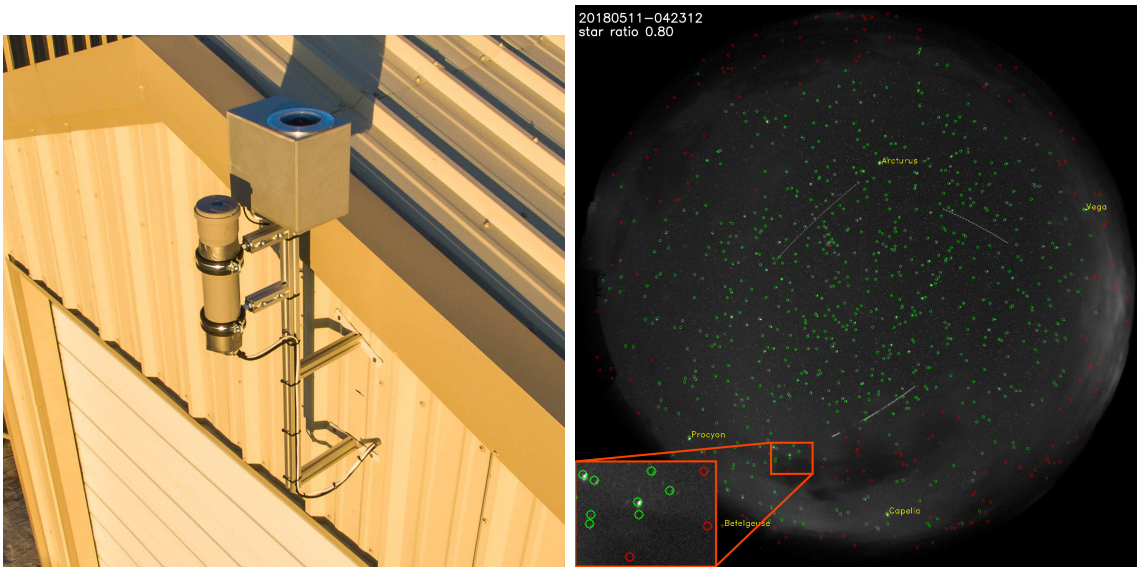

Figure 4.33: Left: The FASCam and SQM installed on the central FAST telescope. Right: An example of a FASCam analysis. Identified stars are indicated with green circles, while stars that should be observable but are obscured by cloud are shown as red circles.

± 0.1 mag/arcsec^2. Measurements taken since its installation suggest an average night-sky brightness of 21.6 mag/arcsec^2. Figure 4.34 shows coincidence measurements of night-sky brightness (from the SQM) and cloud coverage (from the FASCam) on a cloudy night (August 12, 2018). As expected, these measurements are conjugates.

Data from the FASCam and SQM, as well as high-voltage monitoring logs, are provided on a monitoring page available to remote shifters.

A final critical property to monitor is the evolving quality of the optics. As FAST telescopes are designed to be autonomously deployed over a huge array, regular cleanings of the mirrors and filters are unrealistic; it is hence important to characterize the evolving properties of the optics (including the mirror reflectivity and filter transmittance). Although each FAST is shielded from dust by a shroud, the filter is exposed and liable to collect dust particles which unpredictable scatter incident light. Prolonged exposure to UV light can also cause optical degradation.

In October 2018, when we installed the final FAST prototype, we also measured the

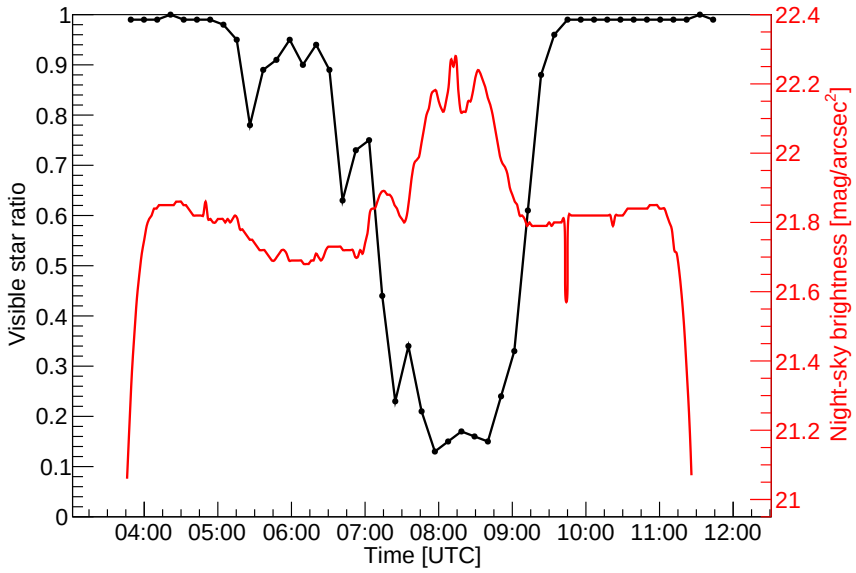

Figure 4.34: Coincident measurements of the cloud coverage and night sky brightness as recorded by the FASCam and SQM on August 12$^{\text{th}}$, 2018. The cloud coverage increases to a maximum at around 08:30 UTC, with a corresponding decrease in the night sky background light measured by the SQM. The anti-correlation between the night-sky brightness and cloud coverage early in the night is likely due to the reflection of the moon on the developing clouds.

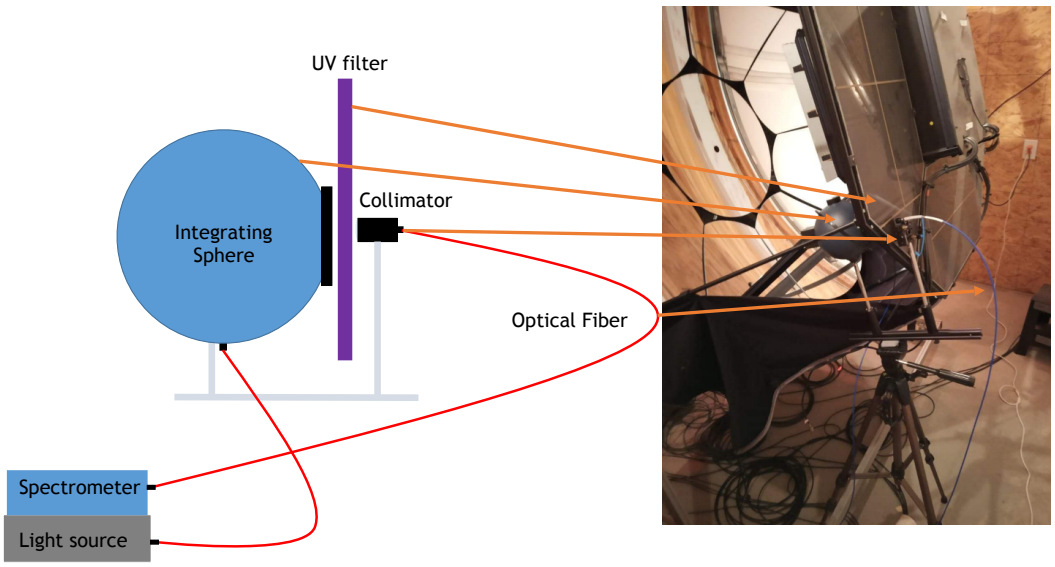

Figure 4.35: Schematic diagram showing the experimental apparatus used for *in-situ* measurement of the filter transmittance and mirror reflectivity.

filter transmittance and mirror reflectivity of the existence two telescopes. Since these were installed one and two years prior, this gives us an idea of the expected degradation of the optics over a one- and two-year period. The spectral reflectance of the mirrors was measured using a wide-band fiber-guided deuterium/halogen calibrated light source reflected off a small patch of the mirror at an 8° angle into an integrating sphere. This signal was routed to a spectrophotometer and compared to that from a similarly-measured reference surface. The absolute spectral transmittance of the mirror was measured in a similar way. A schematic of this setup is shown in Figure 4.35. We observed a decrease in the filter transmittance by approximately 5.5% and 8.5% over one and two years. The decrease in mirror reflectivity was negligible due to the shroud encompassing the telescope optics.

At this installation, we also performed a relative calibration of all FAST PMTs by repositioning the limited number of YAP pulsers to each PMT and collecting pedestal data. These data were then used to re-adjust the PMT high-voltage to ensure uniformity of the PMT gain, which is essential for proper reconstruction studies.

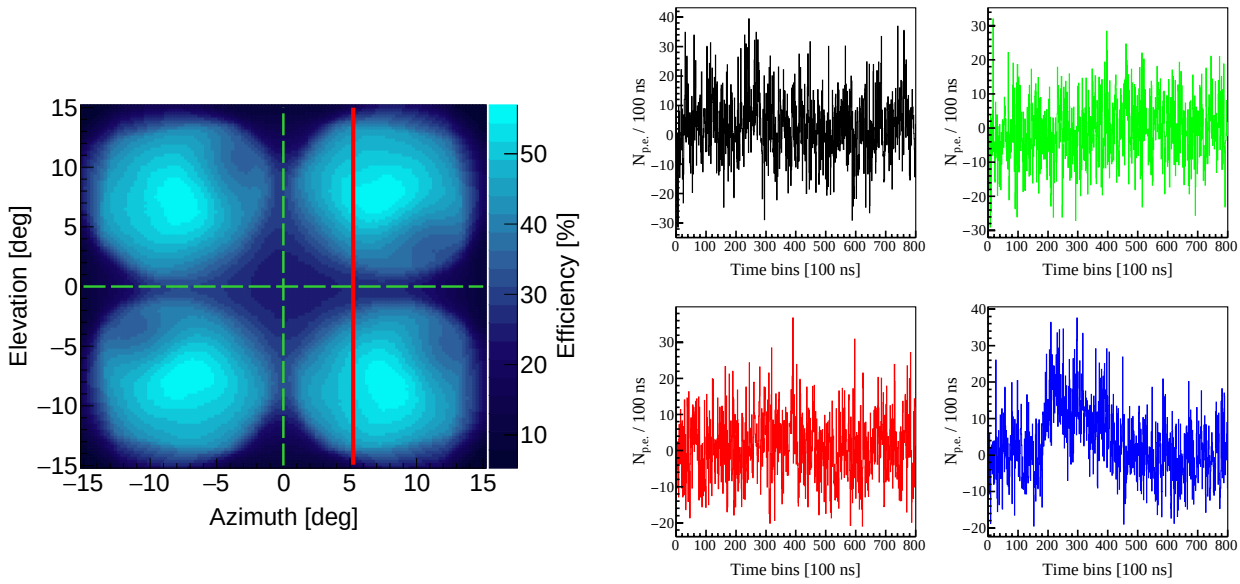

Figure 4.36: Left: Schematic showing the path of the TA CLF (in red) over the FAST camera. The contours show of the telescope, a composite of a ray-tracing simulation of the telescope optics and the azimuthally-dependent PMT response. Right: a stacked and jitter-corrected composite of ≈200 CLF shots collected over a single CLF run.

Data

In October 2016, we began our first observations with the full-scale FAST prototypes. On our first commissioning run our first milestone was detection of the TA CLF with the full telescope, which is sensitive enough to observe single laser shots. Figure 4.36 shows a schematic of the CLF path in the FAST camera, as well as one such event. Single-event observations only show significant signal in the bottom-right PMT; however, when averaging all the traces from a CLF run (typically ≈200), a clear signal in the top-right PMT is also visible. Figure 4.37 shows a stacked and averaged composite of a CLF run over all PMTs.

For our first major analysis, a UHECR event search was performed on a period of 150 h of observations in 2018. This period was chosen because it is free of significant debugging activities and artificial light source tests performed by the TA experiment. This period of data collection contained a total of approximately 1.37 million triggers. It includes data from both before and after the installation of our final telescope.

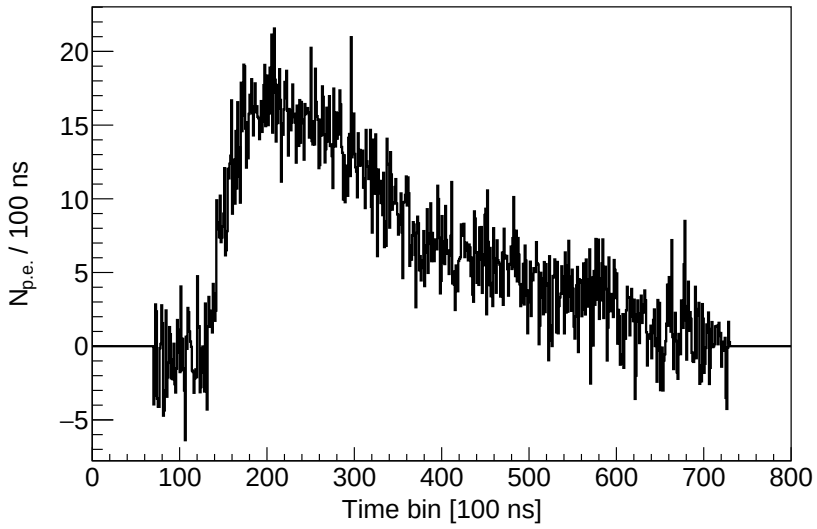

Figure 4.37: A stacked and jitter-correcetd composite trace from ≈ 200 laser shots performed over a single CLF firing run.

Because we trigger externally from the TA FD (which has a much larger field of view than our prototypes), most of these events are background. There are several reasons for this. The first is that the lower resolution of the FAST telescope means many events that are detectable with the TA FD are unresolvable from FAST. The TA FD trigger is constructed when 5 adjacent pixels fire above an internal threshold over a 12.8 μs, rather than from signals in a single large pixel. And since the TA FD's field-of-view is much larger than that of FAST, many of these triggers are due to signals that are outside of our field-of-view. From this dataset, we must extract the small subset that contains highly-significant UHECR showers. Because the amount of data we collected was much higher with these prototypes than the single-pixel test, and because we have twelve total traces that can produce significant background fluctuations instead of a single pixel, performing a manual matching procedure as done previously was unfeasible. It also not possible to use successful reconstruction as a benchmark for event detection since a bottom-up reconstruction with the FAST prototypes is not possible. We hence developed a more sophisticated and robust analysis chain

For our event search, we applied a trapezoidal finite impulse response (FIR) filter to the

data and searched for excursions above a pre-defined candidate threshold level. This filter was chosen because it allows for self-cancelation of NSB noise, and also because its similarity with the internal triggering algorithm of our DAQ system allows us to better understand possibilities for future self-triggering. We tuned the parameters of the filter to two 2.5 mus windows with a gap time of 100 μs, chosen based on the expected width of a typical shower signal and tested on a small subsample of observed events.

Since we now have access to twelve individual pixels, we can take advantage of coincidences. Coincident signals between several PMTs matching the time-profile of a shower is the strongest indicator of an UHECR event. With this in mind, we built two criteria for classification of events. There are two separate thresholds for the FIR filter: a *s*ignal threshold and a higher *c*andidate threshold to catch highly-significant showers. In order for an event to be marked as a shower candidate, one of two conditions must be met: either one pixel must have met the higher-significance *c*andidate threshold, or several pixels in coincidence must have met the lower-significance *s*ignal threshold. This way we catch both highly-significant events that strike only single pixels, such as geometrically-constrained Cherenkov events or grazing showers that leave significant signals only in one PMT, as well as events that strike multiple pixels at a lesser significance. Coincident detection by multiple PMTs (or telescopes) is the most reliable and robust method we have of finding real events. Figure 4.38 shows an air shower event detected by our signal search algorithm.

However, even with this tuning, we still observed a huge number of background events that necessitated the construction of specific background filters. FAST has four primary background sources. The first are ultraviolet laser shots from the CLF. These are important for our scientific operations and are used for monitoring purposes; however, as they resemble highly-significant air showers and there are a huge number of them every night, they must be isolated and removed from the dataset. On most nights this is straightforward, because they reliably trigger certain pixels at known time intervals, but during less-than-ideal conditions

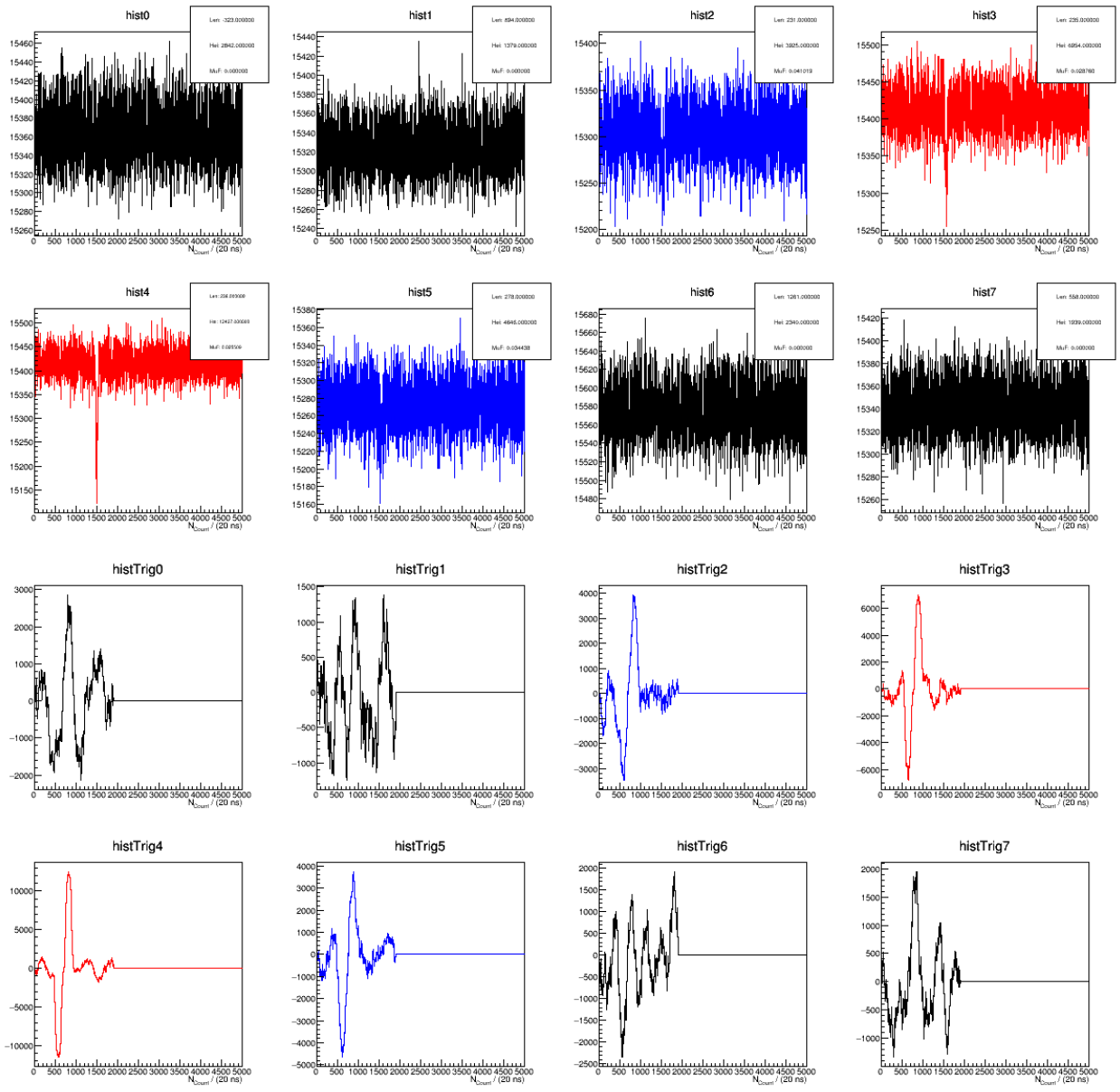

Figure 4.38: An example of an event detected by the FIR algorithm. The top half of the panel shows the FAST data traces, and the bottom half shows the output of the FIR algorithm. Traces shown in red are flagged as highly-significant, and traces shown in blue are low-significance detections.

(such as poor atmosphere quality or clouds), these patterns can be disrupted. They may be further ruled out using the fact that laser shots travel from ground level into the atmosphere, whereas UHECR showers travel from the atmosphere down to the earth. The second major background source is so-called airplane events. These are primarily triggered by airplanes flying through the field-of-view and result in periods of several hundred triggers with high-intensity, long signals seen by FAST; however, we will broadly refer to any background that follows this description to be classified as an airplane-line event. The other two backgrounds appear similarly in FAST. They include low-energy, Cherenkov-dominated events whose Cherenkov cones are directed strongly towards FAST, resulting in an extremely intense, extremely brief flash of light seen as a sudden spike in a FAST trace. A similar effect can be seen from relativistic particles passing through the camera box (eg muons) or small electromagnetic showers from decays in the atmosphere. These create localized sources of ultraviolet light that can be mistaken for an extremely fast air shower.

To deal with these backgrounds, developed a number of background-rejection techniques to reduce the number of traces we need to process. For each event, we produce two effective traces for post-processing. The first is the raw trace obtained from the FAST DAQ readout. The second is the resultant trace obtained from applying a trapezoidal FIR filter to those same traces.

A first-level rejection of airplane events is provided by comparing the leading and trailing 500 bins of each trace. If the baseline shifts significantly over this period, we flag the event as an airplane and reject it. This is an event-level filter: an event marked as an airplane will not be considered at all for the FIR processing. The threshold for this filter was tuned by examining subsets of the data. It is fixed to a difference of 40 counts. Further rejection of airplane events is performed intrinsically by the FIR filter, which removes slowly-wandering baselines by virtue of its self-subtraction. Figure 4.39 shows an example airplane event that passed our event detection threshold but was rejected by our airplane baseline shift filter.

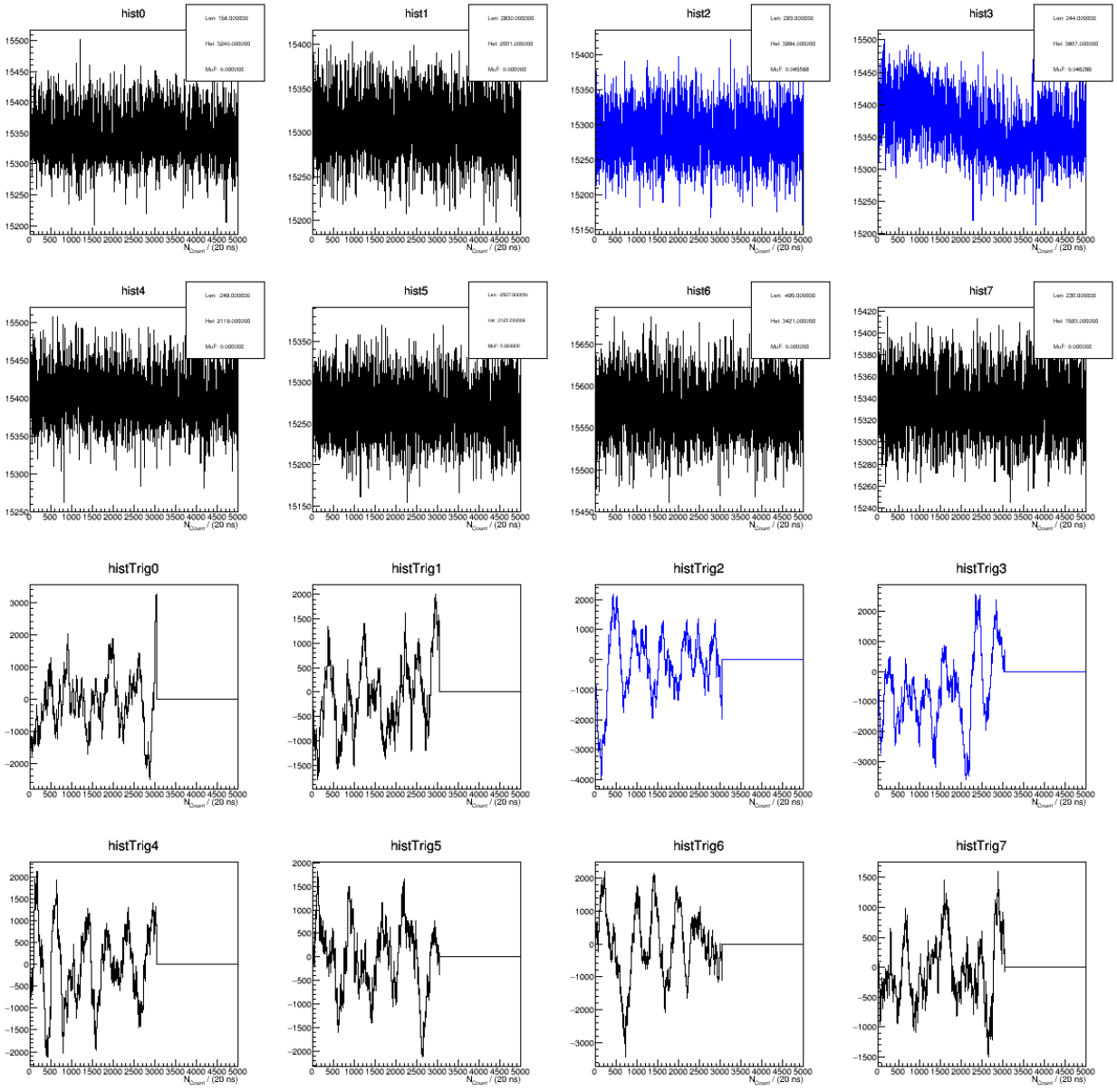

Figure 4.39: An example of airplane event that was not filtered until the baseline shift cut was applied.

Events that are sharp in time-profile produce FIR traces like step functions. Once the peaks are found in the FIR trace, we step along the trace, and if its value changes by 12% of its peak over a single bin, the trace is rejected. As these are isolated to single PMTs, this is a trace-level filter and will not interfere with the FIR processing of other traces in the event. This threshold was chosen based on examining a large number of air-shower events and muon candidates. Though this rejects a great number of events, the threshold is still conservative and these short time-profile events still dominate the FAST background. Figure 4.40 shows an example muon event that passed this filter.

Finally, a number of specific days and time windows were removed from the analysis because they were contaminated by external sources, such as TA octocoptor runs or calibration tests with ultraviolet lasers like the PLF. These are simple to detect in the output, as they result in single days or brief time windows with a huge number of qualitatively-similar events that do not resemble air shower events. These periods are excluded.

Approximately 3% of observed traces were classified as airplane events and filtered from the results. Approximately 0.2% of individual traces were flagged by the muon filter. Although these fractions are small in proportion to the entirety of the data, they overwhelmed the output of our event-search program when they were not filtered from the results. We have tuned these filters conservatively with the intent of producing a final sample of events that can be manually inspected to ensure they by-eye conform to the expectations of an air shower event.

Once we obtained our final dataset passing these cuts, we matched these in time with TA reconstructions over this same period. This gives us the full reconstructed energy and geometry for each of these events. A total of 44 highly-significant air showers were found during this period. Their core distances are shown in Figure 4.41. As with our single-pixel test, we can obtain an estimated limit on our maximum observable distance as a function of energy (Figure 4.42).

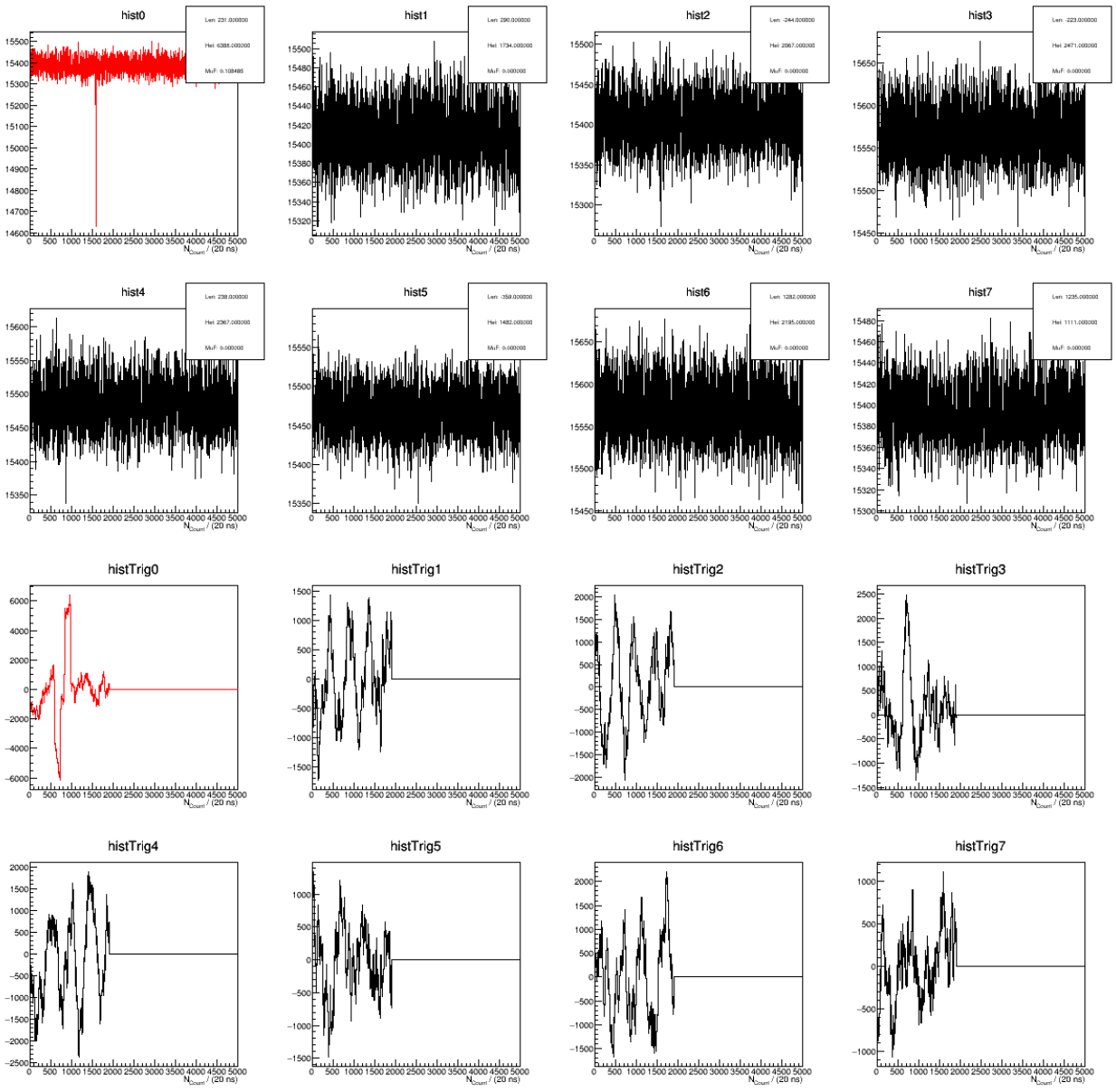

Figure 4.40: An example of a muon event that passed all muon-rejection filters. Note the extremely sharp time profile.

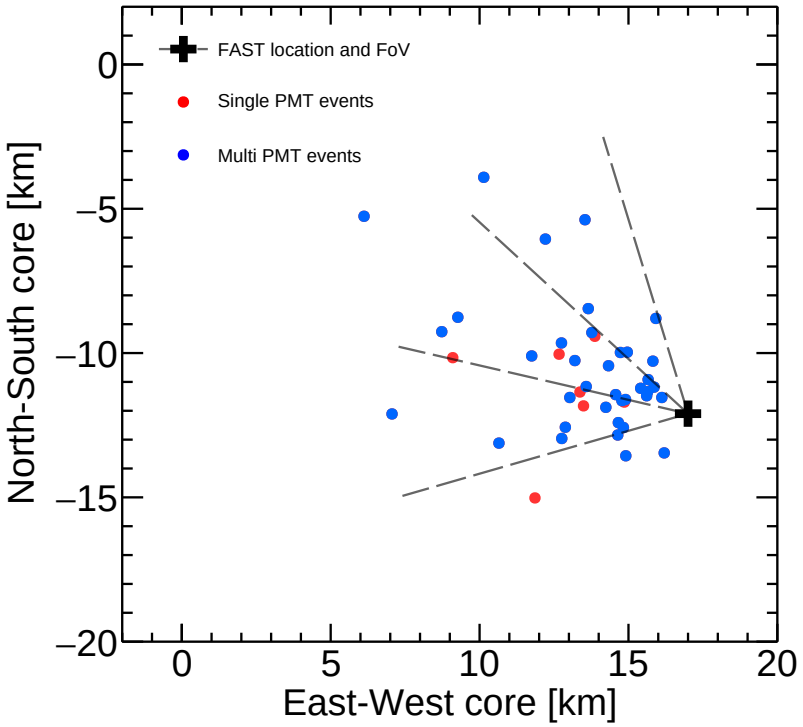

Figure 4.41: Core locations of the 44 highly-significant UHECR showers observed over the selected DAQ period by the full FAST@TA experiment. Blue dots show events with hits in multiple PMTs, and red dots show single-PMT events.

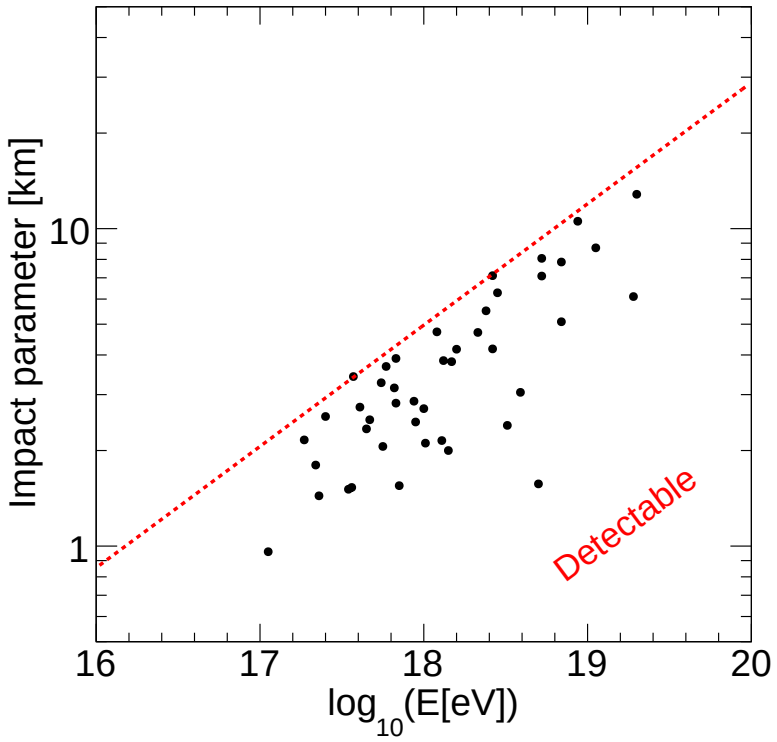

Figure 4.42: Distance of closest approach for the 44 showers observed with the FAST@TA prototypes. The red line is a rough estimate of the maximum detactable distance as a function of energy

The highest-energy event observed during this period was seen on May 15th, 2018. It is a Cherenkov-dominated event with an energy of ∼19 EeV and a zenith angle of ∼55°. Figure 4.43 shows the shower path over the FAST field-of-view and the traces measured by our telescope. By contrast, Figure 4.44 shows a high-energy fluoresence-dominated event. It has an energy of ~ 4‘ EeV and a zenith angle of $\sim 57°$.

4.5.3 FAST at Auger

After the success of the tests at the Telescope Array experiment, we began construction of new prototypes at the Pierre Auger Observatory site. We constructed a small portable hut at the site of the MIDAS experiment at the Los Leones FD site of Auger. A photograph of the hut and the fully-assembled telescope is shown in Figure 4.45. The site was chosen to maintain a shared field-of-view with Los Leones bay 4 and visibility of the CLF, whose path runs through PMTs 0 and 1. Although we originally planned to use a SLT board to externally trigger off the Los Leones FD, we have instead moved to internally triggering.

Both the observation time of FAST@Auger and the deployment of additional telescopes has been limited due to the COVID-19 pandemic, which has strained both international travel and the local Observatory staff. A number of laser shots and physical event candidates have been observed, but a robust analysis student as was performed with FAST@TA has not yet been undertaken. An example event detection is shown in Figure 4.46, and a laser calibration shot is shown in Figure 4.47.

4.6 FAST Analysis

With the robust dataset we have collected with FAST over the years, we can attempt a number of novel analyses in addition to simple overviews of the data. In this section, we will discuss our in-house atmospheric aerosol analysis and top-down reconstruction programs.

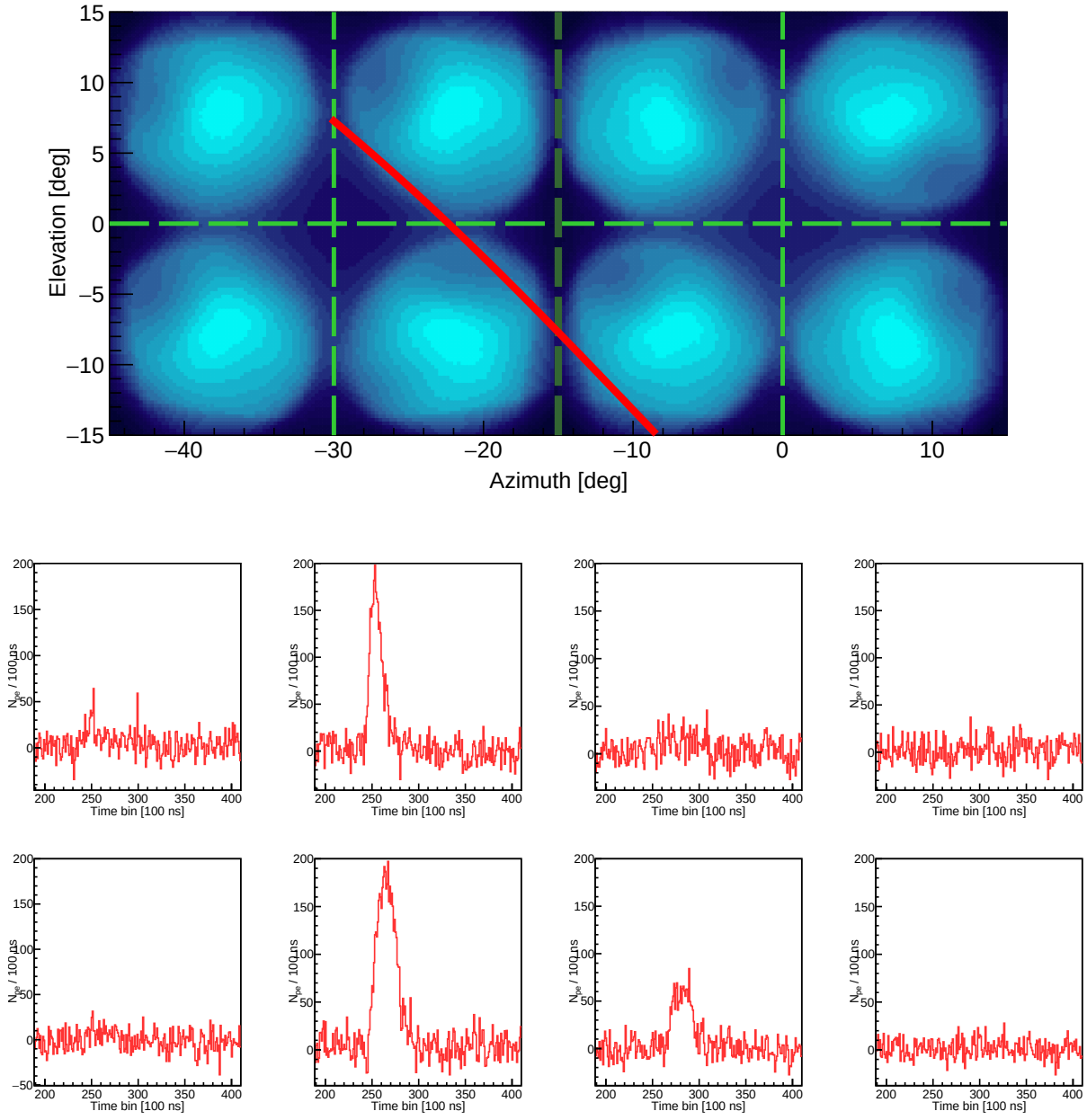

Figure 4.43: High-energy Cherenkov-dominated event measured by FAST 1 and FAST 2 on May 15$^{\text{th}}$, 2018, with an energy of $\sim 19\,\text{EeV}$ and a zenith angle of $\sim 55^{\circ}$. It is the highest-energy event observed by FAST to date. Top: The path of the shower projected onto the FAST focal surface. Bottom: The signal measured in the 8 PMTs of FAST 1 and FAST 2.

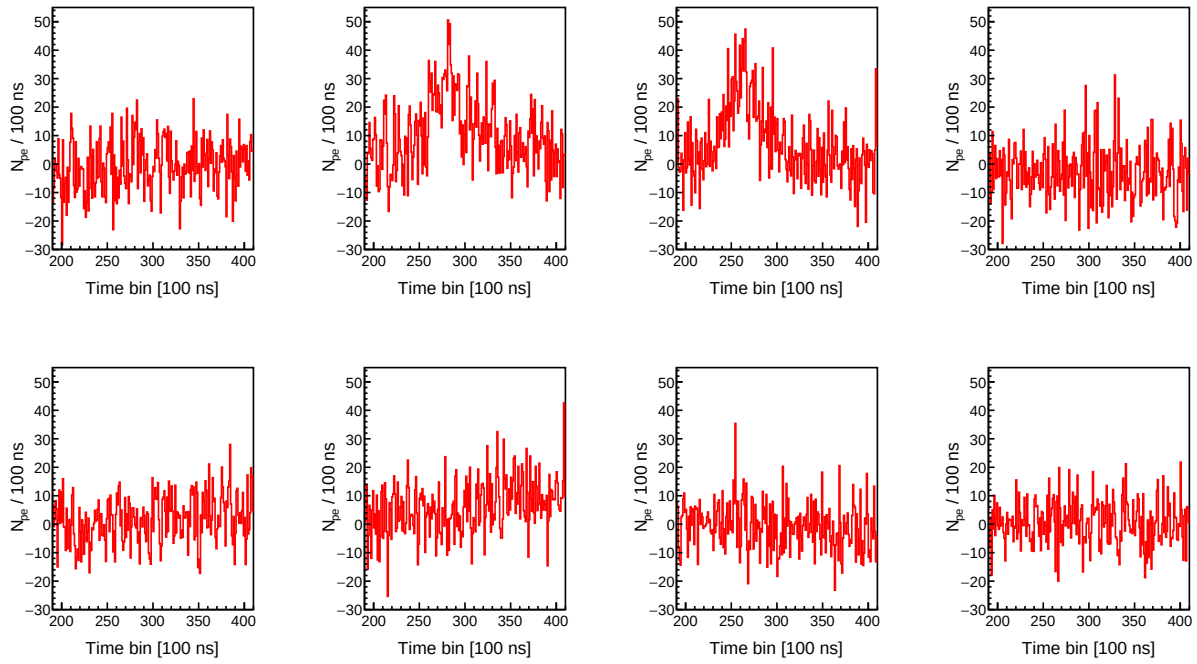

Figure 4.44: PMT signals from a typical fluorescence-dominated event. This event was measured by FAST 1 and FAST 2 on May 11$^{\text{th}}$, 2018, with an energy of $\sim 4\,\text{EeV}$ and a zenith angle of $\sim 57°$.

Figure 4.45: The FAST@Auger telescope at Los Leones inside its housing. On the right side of the photograph is the Los Leones LIDAR.

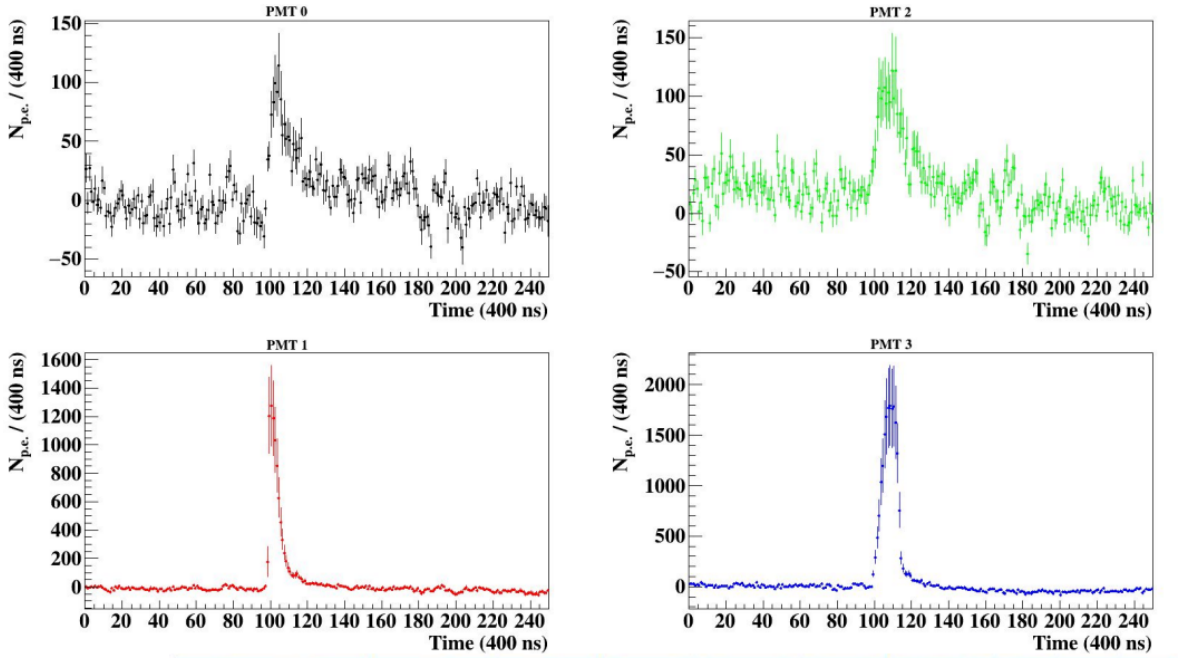

Figure 4.46: A candidate UHECR event observed with FAST@Auger, seen from the FAST event display.

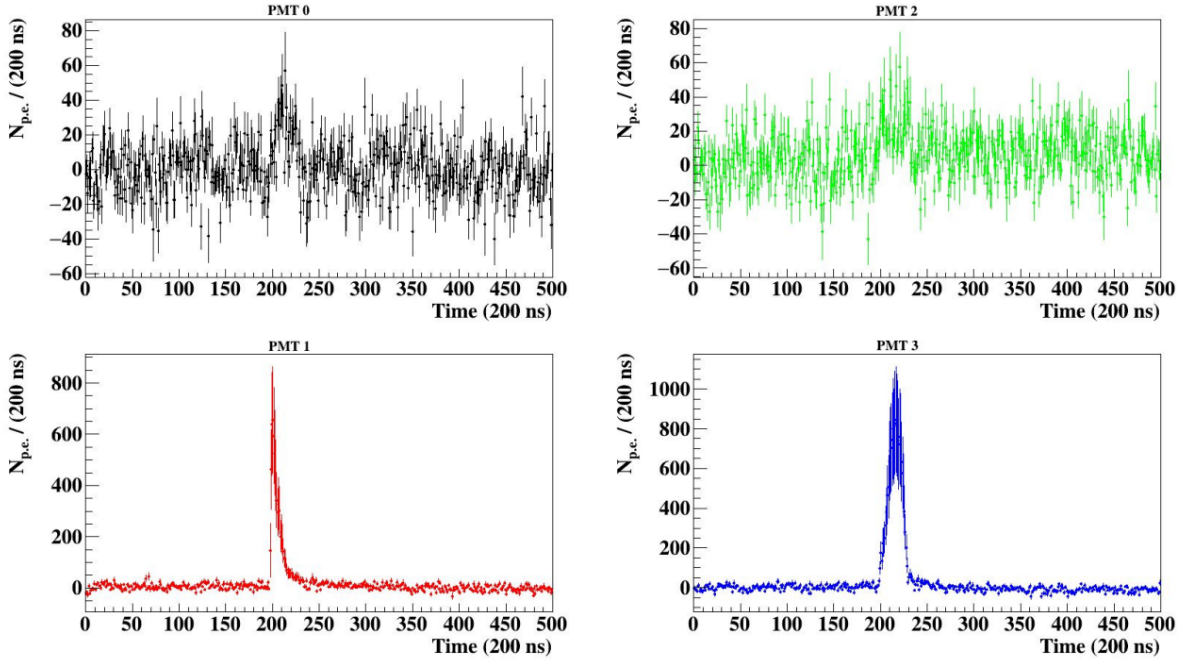

Figure 4.47: A horizontal calibration laser shot observed with FAST@Auger, seen from the FAST event display.

```
<!-- A sequence for FAST shower simulation -->
<sequenceFile>
  <enableTiming/>
  <moduleControl>

    <loop numTimes="1">

      <module> FASTProfileSimulatorCG  </module>
      <module> FASTEventGeneratorCG    </module>
      <module> ShowerLightSimulatorCG  </module>
      <module> FASTSimulatorCG         </module>

    </loop>

   </moduleControl>
</sequenceFile>
```

Figure 4.48: Module sequence used by the FASTSim program.

But first, we will begin by discussing an essential analysis tool, FASTSim.

4.6.1 FASTSim Program

An important step in the FAST analysis chain is developing a robust detector simulation. For this, we built a full-chain simulation program using the Auger Offline software, which provides an extensible, customizable framework with many existing tools, such as the ability to easily customize runs using XML configuration files; parse shower simulations from programs such as CONEX; and, most importantly, exploit existing implementations of complicated wavelength-dependent parameterizations of fluorescence yields and scattering coefficients. See Section 2.4.1 for additional information on the structure of Offline.

The Offline framework invokes a module sequence detailing a series of steps carried out by the program. Each module is written as a separate unit, transfers state to and from the master program, and is configured by a set of XML configuration files. An example module sequence used by FASTSim is shown in Figure 4.48.

The first module in the sequence is `FASTProfileSimulatorCG`. This module uses input shower parameters to generate an analytical Gaisser-Hillas profile. The functional form of

the Gaisser-Hillas function is

$$f(X) = \left(\frac{\mathrm{d}E}{\mathrm{d}X}\right)_{X_{\max}} \left(\frac{X - X_0}{X_{\max} - X_0}\right)^{\frac{X_{\max}-X_0}{\lambda}} e^{-\frac{X-X_{\max}}{\lambda}}, \tag{4.6}$$

where $(\mathrm{d}E/\mathrm{d}X)_{X_{\max}}$, the energy deposited at the shower maximum; and X_0 and λ are shape parameters. The energy deposition in bins of atmospheric depth is then calculated in a number of discrete steps. At this stage, `FASTEventGeneratorCG` builds the internal event structure used by the program, defines the number and position of telescopes in the FAST array, and performs any necessary coordinate transformations.

Next, `ShowerLightSimulatorCG` calculates the number of photons produced at each point along the shower axis using the AIRFLY model [19] [20]. This means calculating both the Cherenkov and fluorescence light. These calculations will not be reviewed here because they were covered extensively in Section 2.4.3, which may be used as a reference for the mechanics of this simulation. For laser simulation, instead the module `LaserLightSimulatorCG` runs. This module steps along the laser axis and calculates the decrease in beam intensity due to scattered light (both by molecular scattering and aerosol scattering).

Next, the module `FastSimulatorCG` runs. This is the module which contains all simulation of the FAST detector response to the photons calculated with either `LaserLightSimulatorCG` or `ShowerLightSimulatorCG`. The first step in `FastSimulatorCG` is to determine the time at which the shower enters and leaves the FAST field-of-view. This allows us to determine the time interval in which the detector will intercept photons emitted from the shower axis. Next, we propagate the photons generated from the previous modules to the diaphrahm of the FAST telescope. These depend on the aerosol and molecular attenuation coefficients at observation height.

The photons are then propagated through an end-to-end simulation of the FAST telescope. First, the wavelength-dependence of both the mirror reflectivity and the UV filter transmittance are applied. Then, we account for the efficiency of the telescope itself using

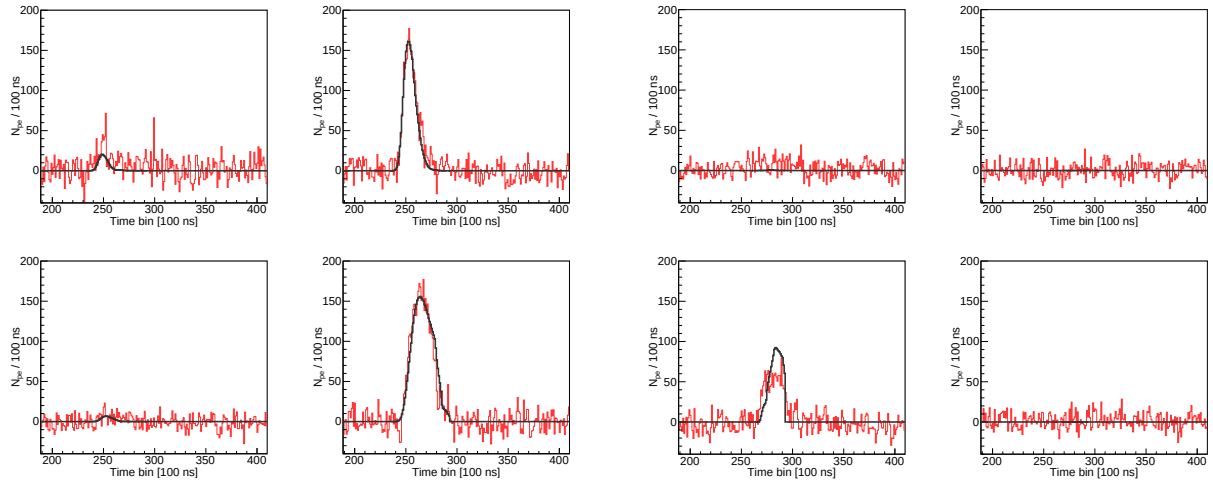

Figure 4.49: A simulation of the measured event depicted in Fig 4.43 based on the best-fit parameters given by the top-down event reconstruction in black, overlaid on the measured FAST event in red.

the results of a detailed raytracing simulation that accounts for the response of the camera and the PMT detection efficiency. From this, we calculate final traces for each of the four PMTs in the FAST camera. Finally, we apply PMT calibrations to obtain traces in number of photoelectrons.

4.6.2 Atmospheric Aerosol Analysis

A novel application of `FastSim` (using the `LaserLightSimulatorCG` module) is using FAST as an atmospheric monitoring device. Because we understand both the properties of the ultraviolet laser used at the TA CLF and the optics of our telescope, we can use laser traces to infer the aersol contents of the atmosphere. The aerosols are typically describing using the Vertical Aerosol Optical Depth (VAOD), the integral of the aerosol extinction coefficient α_A from the ground to the height h:

$$\mathrm{VAOD}(h) = \int_0^h \alpha_A(h')\mathrm{d}h'. \tag{4.7}$$

By accounting for the wavelength-dependent attenuation of CLF photons and the attenuation of scattered light towards the FAST aperture, we can infer the properties of a simple molecular and aerosol atmosphere with a volume scattering coefficient α determined by a horizontal attenuation length L, a scale height H, and a single mixing layer:

$$\begin{aligned} \alpha_{\mathrm{M}}(h) &= (1/L_{\mathrm{M}}) \cdot \exp\bigl(-(h + H_{\mathrm{g}})/H_{\mathrm{M}}\bigr) \\ \alpha_{\mathrm{A}}(h) &= \begin{cases} 1/L_{\mathrm{A}} & h < H_{\mathrm{mix}} \\ (1/L_{\mathrm{A}}) \cdot \exp(-(h - H_{\mathrm{mix}})/H_{\mathrm{A}}) & h \geq H_{\mathrm{mix}}. \end{cases} \end{aligned} \tag{4.8}$$

The use of a single mixing layer mirrors the atmospheric treatment used by the TA experiment[113]. The molecular horizontal attenuation length at sea-level for the CLF wavelength 355 nm is determined by linear interpolation from the parameters at 350 nm and 360 nm from Bucholtz [114], giving us $\sim$ 14.2 km. The fraction of laser light scattered towards a FAST telescope from a given height depends on the aerosol scattering phase functions, which can not be determined analytically. We use the modified Henyey-Greenstein phase function with backscattering parameter $f = 0.4$ and asymmetry parameter $g = 0.6$, suitable for a dry desert atmosphere, to describe the fraction of laser light per unit solid angle scattered in a particular direction be aerosols [115].

4.6.3 Top-Down Reconstruction

Traditional air shower reconstruction techniques use a bottom-up approach in which only a subset of the available recorded information, such as the total measured signal and the centroid time (signal-weighted time average) of each pixel in the telescope camera, is used to fit the shower parameters. A bottom-up reconstruction typically requires two steps: first, a fit to the shower geometry is performed using the timing information from a track of triggered pixels, and then using this reconstructed shower geometry, the measured light flux is

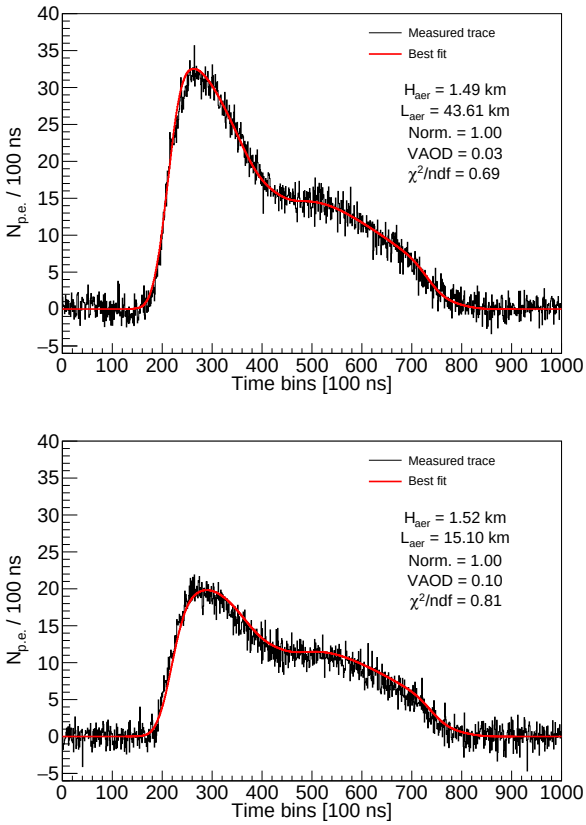

Figure 4.50: Example reconstructions of the vertical aerosol loading using a simulated FAST laser trace. The expected measured signal (from simulations) is shown in black, while the red curve is a fit to the simulated trace taking the aerosol scale height and horizontal attenuation length as free parameters. The fit result is shown on the right. Left: Aerosol atmosphere with a scale height of 1.5 km and a ground-level horizontal attenuation length of 40 km. Right: Aerosol atmosphere with a scale height of 1.5 km and a ground-level horizontal attenuation length of 15 km.

"unfolded" in order to determine the energy deposited at the shower track, usually expressed in terms of atmospheric slant depth as a Gaisser-Hillas profile. Such a reconstruction is not possible for data recorded with a FAST telescope, since only four pixels cover the same field-of-view as several hundred pixels in a traditional FD telescope. A robust top-down reconstruction algorithm is currently in development which will utilize a sound understanding of the detector response to provide estimates of measured shower parameters with acceptable resolutions.

The top-down approach uses simulations based on first-guess estimates of the shower

parameters to perform a maximum-likelihood estimation of the measured shower geometry, energy, and depth of maximum ($X_{\max}$). The maximum-likelihood estimator is built from the probability of measuring a signal of x_i photoelectrons in the i^{th} time bin of FAST pixel k, over all time bins in the traces of all FAST pixels (including those that did not measure a significant signal). The likelihood function is given by

$$\mathcal{L}(\vec{x} \mid \vec{a}) = \prod_{k}^{N_{\text{pix}}} \prod_{i}^{N_{\text{bins}}} P_k(x_i \mid \vec{a}), \tag{4.9}$$

where $\vec{a}$ represents the geometrical and physical parameters $(\theta, \phi, x, y, X_{\max})$ of the simulated shower under test. The probability density function for a single time bin is

$$P(x \mid \mu(\vec{a}), \sigma, V_{\text{g}}) = \frac{1}{\sqrt{2\pi[\sigma^2 + A\mu(1+V_{\text{g}})]}} \exp\left(\frac{-(x - A\mu)^2}{2[\sigma^2 + A\mu(1+V_{\text{g}})]}\right), \tag{4.10}$$

where the expectation value for the observed number of photo-electrons is given by μ, and the fluctuations (for large μ) are well-represented by a Gaussian of width $\sqrt{\sigma^2 + \mu(1+V_{\text{g}})}$ where σ is the baseline variance of the PMT due to the NSB, and V_{g} is the PMT's gain variance. The expected signal is modified by an energy scale factor A, a free parameter in control of the energy fit. As the total shower energy simply scales the expected signal, simulating many values of the shower energy is not required.

Preliminary tests suggest geometrical reconstruction utilizing this top-down approach will be possible with FAST operating in stereo mode (more than one FAST telescope measuring a single event), while the shower geometry may be provided by a coincident surface detector array for the reconstruction of data from a single FAST telescope. The FAST reconstruction performance and expected resolution are currently being studied using simulated events. Due to the computational expense of performing many simulations during this reconstruction procedure, a sound first guess of the shower parameters is necessary in order to minimize

the total number of required simulations. As as solution to this, we have explored a neural network solution to prove a first-guess input geometry. We have found this a surprisingly robust tool to study the efficiency of FAST.

4.6.4 Estimation of the Efficiency and Trigger Sensitivity

Since the amount of observed data with FAST is insufficient to accurately study our efficiency or obtain estimates on our reconstruction biases, we have elected to use simulations to obtain an estimate of these. We found the neural network first-guess estimation to be an effective tool for this.

The first-guess estimation is a neural network with two hidden fully-connected layers using the Keras/Tensorflow library. It uses the total signal, pulse height, and centroid time of each PMT as inputs, and outputs six parameters: $X_{\max}$, energy, zenith, azimuth, and core positions (east-west and north-south).

We used this estimator to evaluate the resolution and detection bias on $\mathrm{X_{max}}$ to simulated EAS from four primaries incident on a hypothetical FAST array: proton, helium, nitrogen, and iron, with three hadronic interaction models (EPOS-LHC, QGSJETII-04, and Sibyll 2.3c). These events are generated with uniform arrival directions and random core distances within the array's inner core. For 40 EeV events at three-fold coincidence, we estimated the resolution of each of the reconstructed parameters. The results are summarized in Table 4.2. The preliminary estimated detection bias on $\langle X_{\max} \rangle$ and $\sigma(X_{\max})$, as well as reconstructed $X_{\max}$ biases in each energy bin, are shown in Figure 4.51. An estimate of our trigger efficiency is shown in Figure 4.52 for all four primaries and all three hadronic interaction models. We estimate that we attain maximum efficiency for all primaries and all interaction models above approximately $\log E = 19.3$ EeV. We also evaluated the FAST trigger efficiency for three-fold detections (Figure 4.52).

Parameter	Resolution
Arrival Direction	4.2°
Energy	8%
Core Position	465 m
X_{max}	30 g/cm^2

Table 4.2: Resolutions of the shower parameters reconstructed with the first-guess geometry neural network. See the text for additional details on the input data.

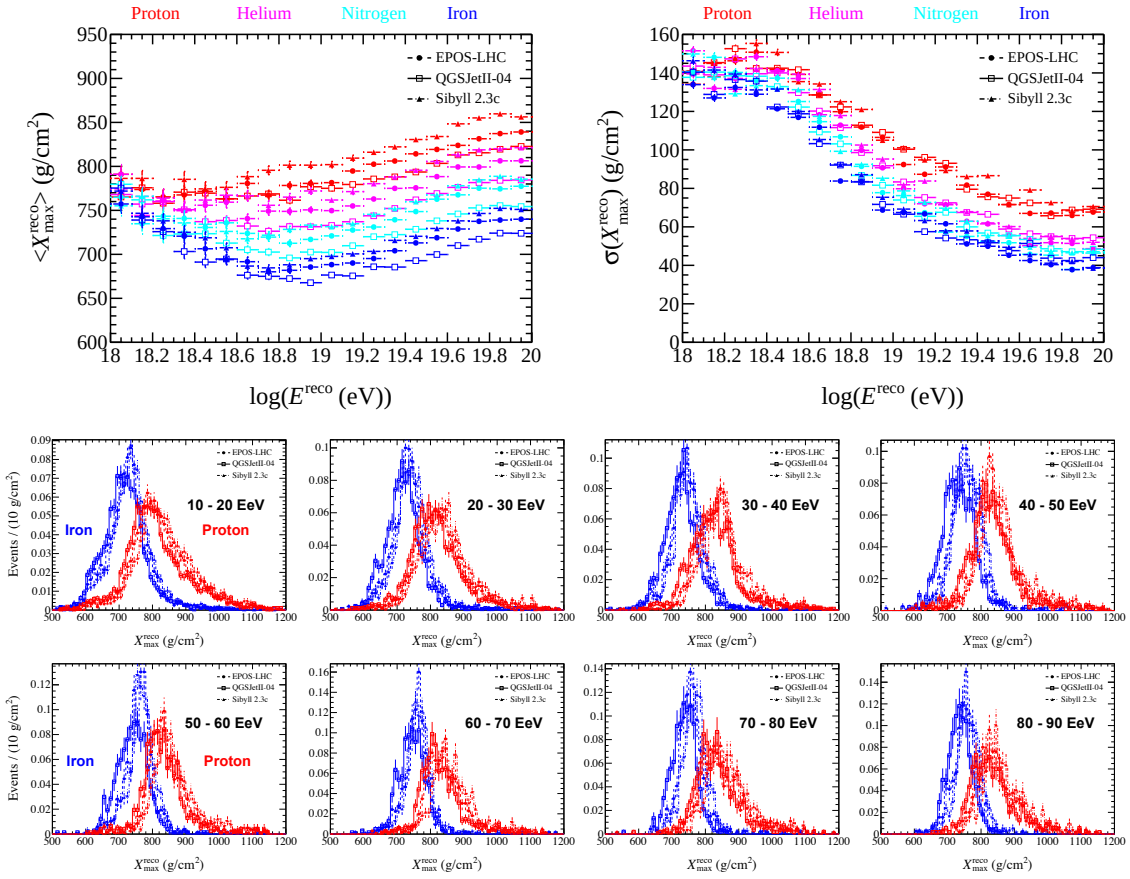

Figure 4.51: Reconstruction bias on (top left) $\langle X_{max} \rangle$ and (top right) $\sigma(X_{max})$ evaluated by only the neural network first-guess estimation. Bottom: Reconstructed X_{max} distributions in each energy bin.

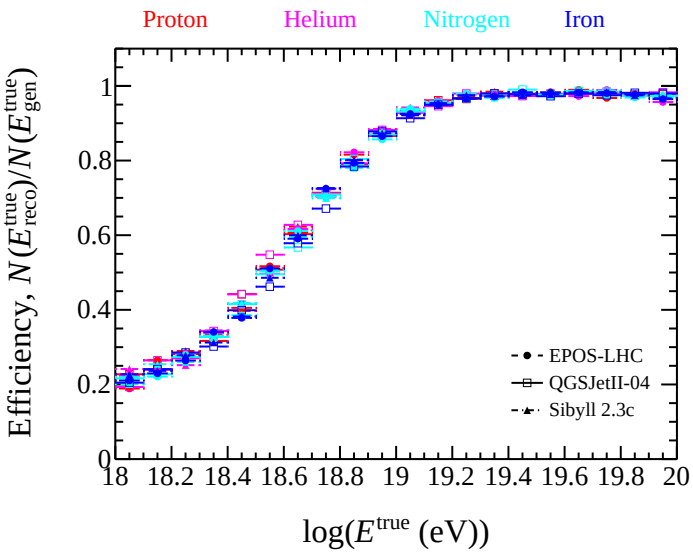

Figure 4.52: Trigger efficiency for 3-fold detections with a hypothetical FAST array.

4.7 Future

A number of improvements and advances have been made to the telescope and electronics design since the original FAST@TA prototypes. Most importantly, we are developing new FPGA-based electronics that will remove the need for the complicated and expensive NIM-and-VME electronics systems employed by FAST@TA. Further, these electronics will have low power consumption and can be solar powered, removing the need for a physical electrical connection. Hence these new electronics will both significantly reduce the cost of our following prototypes, but also will allow us to construct a free-standing FAST telescope independent of existing FD sites. We will hence be able to test observing showers in stereo, a milestone critical to the success of the FAST project.

The immediate future of FAST involves continued operation of our existing prototypes and the assembly of next test prototypes at FAST@Auger. Our next major milestone is a free-standing, independent FAST using our new low-power, FPGA-based DAQ electronics. These new electronics are significantly less expensive than the commercial VME and NIM modules used for the previous prototypes, and their lower power consumption allows them

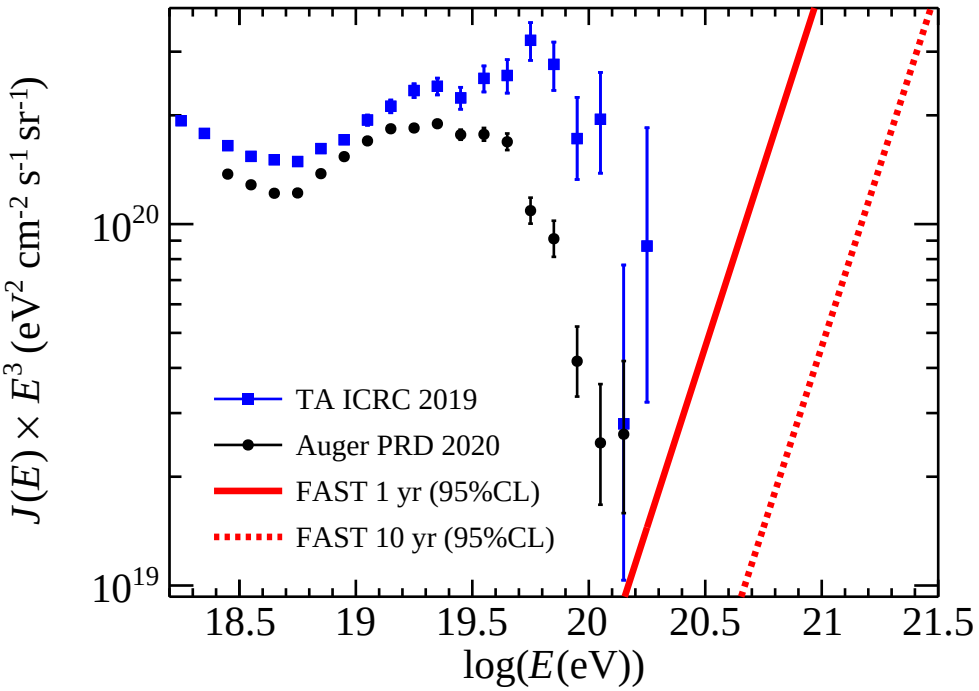

Figure 4.53: Expected 95% C.L. detectable sensitivities of the energy spectrum with the full FAST array of 500 stations compared to the spectra reported from TA [24] and Auger [25].

to be run off solar power, eliminating the need to connect FAST telescopes to the power grid. With this advancement, we can test the feasibility of stereo observation and reconstruction. Our mirror design is also being updated to reduce its expense without significantly impacting its performance by reducing the number of mirror segments from nine to four. Finally, a new, robust PMT calibration system using a robotic arm in the laboratory.

Using the first-guess reconstruction, we can project the sensitivity of a future FAST super-array (Figure 4.53). With 500 stations array and a projected exposure of 90,000 $\mathrm{km}^2\,\mathrm{sr}\,\mathrm{y}^{-1}$, we anticipate that we would exceed the exposures of current-generation detectors within one year of operations, and extend them by an order of magnitude within ten years.

Chapter 5

Conclusions

The work presented in this thesis outlines two attempts at extending the energy range of UHECR research to higher energies, through both extended analyses of data from current-generation experiments and the development and prototyping of a next-generation detector that targets the highest energies.

Chapter 3 outlines an extension of mass composition studies using the Pierre Auger Observatory surface detector using the Δ method, a technique exploiting the composition sensitivity of signal risetimes in the water-Cherenkov detectors of the surface array. It includes a robust extension of the method to higher zenith angles that accurately encapsulates the uncertainties in this new regime. The data presented here hint at lighter composition at the highest energies, as seen in Figure 3.25. Further studies of the systematics have been performed, including the bis discovered in the highest energies by the hybrid calibration technique, as seen in Figure 3.35.

Chapter 4 outlines the development of a new paradigm for ground-based UHECR observatories, targeting the highest-energy cosmic rays. The work presented here touches on every aspect of the prototyping process, including calibration of the sensors, both in the laboratory and on-site; assembly and commissioning of the telescopes; searches for UHECR and ulraviolet laser signals; and the development of DAQ software, analysis tools, and an end-to-end

simulation program forming the background of our reconstruction algorithm. The projected future sensitivity of a FAST super-array is summarized in Figure 4.53, demonstrating its capacity to extend UHECR studies by an order of magnitude in energy.

References

[1] V. Hess. On the observations of the penetrating radiation during seven balloon flights, 2018.

[2] R. Aloisio. Acceleration and propagation of ultra-high energy cosmic rays. *Progress of Theoretical and Experimental Physics*, 2017(12), 11 2017. ISSN 2050-3911. doi: 10.1093/ptep/ptx115. 12A102.

[3] A. M. Hillas. The Origin of Ultrahigh-Energy Cosmic Rays. *Ann. Rev. Astron. Astrophys.*, 22:425–444, 1984. doi: 10.1146/annurev.aa.22.090184.002233.

[4] J. Matthews. A heitler model of extensive air showers. *Astroparticle Physics*, 22(5):387–397, 2005. ISSN 0927-6505. doi: https://doi.org/10.1016/j.astropartphys.2004.09.003.

[5] John Linsley. Primary cosmic rays of energy 10**17 to 10**20-eV: The energy spectrum and arrival directions. In *8th International Cosmic Ray Conference*, 1 1963.

[6] R.M. Baltrusaitis, R. Cady, G.L. Cassiday, R. Cooperv, J.W. Elbert, P.R. Gerhardy, S. Ko, E.C. Loh, M. Salamon, D Steck, and P. Sokolsky. The utah fly's eye detector. *Nuclear Instruments and Methods in Physics Research Section A: Accelerators, Spectrometers, Detectors and Associated Equipment*, 240(2):410–428, 1985. ISSN 0168-9002. doi: https://doi.org/10.1016/0168-9002(85)90658-8.

[7] R.U. Abbasi et al. First observation of the Greisen-Zatsepin-Kuzmin suppression. *Phys.Rev.Lett.*, 100:101101, 2008. doi: 10.1103/PhysRevLett.100.101101.

[8] E. Kido. The TAx4 experiment. *PoS*, ICRC2017:386, 2018. doi: 10.22323/1.301.0386.

[9] R. Abbasi et al. Joint analysis of the energy spectrum of ultra-high-energy cosmic rays as measured at the Pierre Auger Observatory and the Telescope Array. *PoS*, ICRC2021:337, 2021. doi: 10.22323/1.395.0337.

[10] A. Aab et al. Observation of a Large-scale Anisotropy in the Arrival Directions of Cosmic Rays above 8×10^{18} eV. *Science*, 357(6537):1266–1270, 2017. doi: 10.1126/science.aan4338.

[11] R.U. Abbasi et al. Indications of Intermediate-Scale Anisotropy of Cosmic Rays with Energy Greater Than 57 EeV in the Northern Sky Measured with the Surface Detector of the Telescope Array Experiment. *Astrophys.J.*, 790:L21, 2014. doi: 10.1088/2041-8205/790/2/L21.

[12] A. Aab et al. An Indication of anisotropy in arrival directions of ultra-high-energy cosmic rays through comparison to the flux pattern of extragalactic gamma-ray sources. *Astrophys. J.*, 853(2):L29, 2018. doi: 10.3847/2041-8213/aaa66d.

[13] A. et al. Aab. Depth of maximum of air-shower profiles at the pierre auger observatory. ii. composition implications. *Physical Review D*, 90(12), Dec 2014. ISSN 1550-2368. doi: 10.1103/physrevd.90.122006.

[14] A. Yushkov. Mass Composition of Cosmic Rays with Energies above $10^{17.2}$ eV from the Hybrid Data of the Pierre Auger Observatory. *PoS*, ICRC2019:482, 2019. doi: 10.22323/1.358.0482.

[15] A. Aab et al. Inferences on mass composition and tests of hadronic interactions from 0.3 to 100 eev using the water-cherenkov detectors of the pierre auger observatory, 2017.

[16] Pedro Abreu et al. Indication of a mass-dependent anisotropy above $10^{18.7}$ eV in the hybrid data of the Pierre Auger Observatory. *PoS*, ICRC2021:321, 2021. doi: 10.22323/1.395.0321.

[17] A. V. Olinto et al. The poemma (probe of extreme multi-messenger astrophysics) observatory, 2021.

[18] K.H. Kampert and A.A. Watson. Extensive air showers and ultra high-energy cosmic rays: a historical review. *The European Physical Journal H*, 37(3):359412, Jul 2012. ISSN 2102-6467. doi: 10.1140/epjh/e2012-30013-x.

[19] M. Ave et al. Precise measurement of the absolute fluorescence yield of the 337 nm band in atmospheric gases. *Astropart.Phys.*, 42:90–102, 2013. doi: 10.1016/j.astropartphys.2012.12.006.

[20] M. Ave et al. Measurement of the pressure dependence of air fluorescence emission induced by electrons. *Astropart.Phys.*, 28:41–57, 2007. doi: 10.1016/j.astropartphys.2007.04.006.

[21] M. Unger, B.R. Dawson, R. Engel, F. Schssler, and R. Ulrich. Reconstruction of longitudinal profiles of ultra-high energy cosmic ray showers from fluorescence and cherenkov light measurements. *Nuclear Instruments and Methods in Physics Research Section A: Accelerators, Spectrometers, Detectors and Associated Equipment*, 588(3):433441, Apr 2008. ISSN 0168-9002. doi: 10.1016/j.nima.2008.01.100.

[22] P. Sánchez-Lucas. The $\langle\Delta\rangle$ method: An estimator for the mass composition of ultra-high-energy cosmic rays. *GAP-2017-005 (Ph.D thesis).*

[23] V. Verzi. Measurement of the energy spectrum of ultra-high energy cosmic rays using the Pierre Auger Observatory. *PoS*, ICRC2019:450, 2019. doi: 10.22323/1.358.0450.

[24] D. Ivanov. Energy Spectrum Measured by the Telescope Array. *PoS*, ICRC2019:298, 2020. doi: 10.22323/1.358.0298.

[25] A. Aab et al. Features of the Energy Spectrum of Cosmic Rays above 2.5 $\times$ 10^{18} eV Using the Pierre Auger Observatory. *Phys. Rev. Lett.*, 125(12):121106, 2020. doi: 10.1103/PhysRevLett.125.121106.

[26] T. Wulf. Beobachtungen ber die Strahlung hoher Durchdringungsfähigkeit auf dem Eiffelturm. *Physikalische Zeitschrift*, page 811, 1910.

[27] H. Becquerel. Sur les Radiations Émises par Phosphorescence. *Comptes rendus de lAcad. des Sciences*, page 420, 1896.

[28] D. Pacini. Penetrating radiation at the surface of and in water, 2017.

[29] V. Hess. ber Beobachtungen der durchdringenden Strahlung bei sieben Freiballonfahrten. *Phys. Z.*, 13:1084–1091, 1912.

[30] R. A. Millikan and G. Harvey Cameron. High frequency rays of cosmic origin iii. measurements in snow-fed lakes at high altitudes. *Phys. Rev.*, 28:851–868, Nov 1926. doi: 10.1103/PhysRev.28.851.

[31] W. Bothe and W. Kolhörster. Das Wesen der Höhenstrahlung. *Zeitschrift fur Physik*, 56(11-12):751–777, November 1929. doi: 10.1007/BF01340137.

[32] B. Rossi. On the magnetic deflection of cosmic rays. *Phys. Rev.*, 36:606–606, Aug 1930. doi: 10.1103/PhysRev.36.606.

[33] R. Maze P. Auger and T. Grivet-Mayer. Grandes gerbes cosmiques atmosphériques contenant des corpuscules ultrapénétrants. *Compt. Rend. Hebd. Seances Acad. Sci.*, 206(23):1721–1723, 1938.

[34] P. Auger et al. Extensive cosmic ray showers. *Rev. Mod. Phys.*, 11:288–291, 1939. doi: 10.1103/RevModPhys.11.288.

[35] J. Linsley. Evidence for a primary cosmic-ray particle with energy 10^{20} eV. *Phys. Rev. Lett.*, 10:146–148, 1963. doi: 10.1103/PhysRevLett.10.146.

[36] P. Bhattacharjee and G. Sigl. Origin and propagation of extremely high-energy cosmic rays. *Physics Reports*, 327(3-4):109247, Apr 2000. ISSN 0370-1573. doi: 10.1016/s0370-1573(99)00101-5.

[37] S. Sarkar. New physics from ultrahigh-energy cosmic rays. *Acta Phys. Polon. B*, 35: 351–364, 2004.

[38] T. Weiler. Resonant absorption of cosmic-ray neutrinos by the relic-neutrino background. *Phys. Rev. Lett.*, 49:234–237, Jul 1982. doi: 10.1103/PhysRevLett.49.234.

[39] D. Fargion, B. Mele, and A. Salis. Ultrahighenergy neutrino scattering onto relic light neutrinos in the galactic halo as a possible source of the highest energy extragalactic cosmic rays. *The Astrophysical Journal*, 517(2):725733, Jun 1999. ISSN 1538-4357. doi: 10.1086/307203.

[40] C. Hill. Monopolonium. *Nuclear Physics B*, 224(3):469–490, 1983. ISSN 0550-3213. doi: https://doi.org/10.1016/0550-3213(83)90386-3.

[41] M B Hindmarsh and T W B Kibble. Cosmic strings. *Reports on Progress in Physics*, 58(5):477562, May 1995. ISSN 1361-6633. doi: 10.1088/0034-4885/58/5/001.

[42] V. Berezinsky, M. Kachelrieß, and A. Vilenkin. Ultrahigh energy cosmic rays without greisen-zatsepin-kuzmin cutoff. *Phys. Rev. Lett.*, 79:4302–4305, Dec 1997. doi: 10.1103/PhysRevLett.79.4302.

[43] V.E. Mayes J. Ellis and D.V. Nanopoulos. Ultrahigh-energy cosmic rays particle spectra from crypton decays. *Phys. Rev. D*, 74:115003, Dec 2006. doi: 10.1103/PhysRevD.74.115003.

[44] R. Aloisio, V. Berezinsky, and M. Kachelriess. Fragmentation functions in supersymmetric qcd and ultrahigh energy cosmic ray spectra produced in top-down models. *Physical Review D*, 69(9), May 2004. ISSN 1550-2368. doi: 10.1103/physrevd.69.094023.

[45] J. Abraham, P. Abreu, M. Aglietta, C. Aguirre, D. Allard, I. Allekotte, J. Allen, P. Allison, J. Alvarez-Muiz, M. Ambrosio, and et al. Upper limit on the cosmic-ray photon flux above 1019ev using the surface detector of the pierre auger observatory. *Astroparticle Physics*, 29(4):243256, May 2008. ISSN 0927-6505. doi: 10.1016/j.astropartphys.2008.01.003.

[46] S. Petrera. Photons in the Science of the Pierre Auger Observatory. *Frascati Phys. Ser.*, 69:108–114, 2019.

[47] A. Aab et al. Limits on point-like sources of ultra-high-energy neutrinos with the pierre auger observatory. *Journal of Cosmology and Astroparticle Physics*, 2019(11):004004, Nov 2019. ISSN 1475-7516. doi: 10.1088/1475-7516/2019/11/004.

[48] E. Fermi. On the origin of the cosmic radiation. *Phys. Rev.*, 75:1169–1174, Apr 1949. doi: 10.1103/PhysRev.75.1169.

[49] First results of fast one-dimensional hybrid simulation of eas using conex. *Nuclear Physics B - Proceedings Supplements*, 151(1):159–162, 2006.

[50] D. Heck, J. Knapp, J. N. Capdevielle, G. Schatz, and T. Thouw. CORSIKA: A Monte Carlo code to simulate extensive air showers. 2 1998.

[51] S. J. Sciutto. AIRES: A system for air shower simulations. 11 1999. doi: 10.13140/RG.2.2.12566.40002.

[52] W. Heitler. *The Quantum Theory of Radiation*. Dover Books on Physics Series. Dover Publications, 1954. ISBN 9780486645582.

[53] L. Scarsi J. Linsley and B. Rossi. Extremely energetic cosmic-ray event. *Phys. Rev. Lett.*, 6:485–487, May 1961. doi: 10.1103/PhysRevLett.6.485.

[54] R. M. Tennent. The haverah park extensive air shower array. *Proceedings of the Physical Society*, 92(3):622–631, nov 1967. doi: 10.1088/0370-1328/92/3/315.

[55] D.J. Bird et al. Detection of a cosmic ray with measured energy well beyond the expected spectral cutoff due to cosmic microwave radiation. *The Astrophysical Journal*, 441:144, Mar 1995. ISSN 1538-4357. doi: 10.1086/175344.

[56] T. Abu-Zayyad et al. The prototype high-resolution Fly's Eye cosmic ray detector. *Nucl. Instrum. Meth. A*, 450:253–269, 2000. doi: 10.1016/S0168-9002(00)00307-7.

[57] N. Chiba et al. Akeno giant air shower array (AGASA) covering 100-km**2 area. *Nucl. Instrum. Meth. A*, 311:338–349, 1992. doi: 10.1016/0168-9002(92)90882-5.

[58] M. Takeda et al. Extension of the cosmic-ray energy spectrum beyond the predicted greisen-zatsepin-kuzmin cutoff. *Physical Review Letters*, 81(6):11631166, Aug 1998. ISSN 1079-7114. doi: 10.1103/physrevlett.81.1163.

[59] M. Fukushima. Telescope array project for extremely high energy cosmic rays. *Prog. Theor. Phys. Suppl.*, 151:206–210, 2003. doi: 10.1143/PTPS.151.206.

[60] T. Abu-Zayyad et al. The surface detector array of the telescope array experiment. *Nuclear Instruments and Methods in Physics Research Section A: Accelerators, Spectrometers, Detectors and Associated Equipment*, 689:8797, Oct 2012. ISSN 0168-9002. doi: 10.1016/j.nima.2012.05.079.

[61] H. Tokuno et al. New air fluorescence detectors employed in the telescope array experiment. *Nuclear Instruments and Methods in Physics Research Section A: Accelerators, Spectrometers, Detectors and Associated Equipment*, 676:5465, Jun 2012. ISSN 0168-9002. doi: 10.1016/j.nima.2012.02.044.

[62] S. Ogio. Telescope Array Low energy Extension(TALE) Hybrid. *PoS*, ICRC2019:375, 2019. doi: 10.22323/1.358.0375.

[63] A. Aab et al. The Pierre Auger Cosmic Ray Observatory. *Nucl. Instrum. Meth.*, A798: 172–213, 2015. doi: 10.1016/j.nima.2015.06.058.

[64] R. Engel J. Blmer and J.R. Hrandel. Cosmic rays from the knee to the highest energies. *Progress in Particle and Nuclear Physics*, 63(2):293338, Oct 2009. ISSN 0146-6410. doi: 10.1016/j.ppnp.2009.05.002.

[65] K. Greisen. End to the cosmic ray spectrum? *Phys. Rev. Lett.*, 16:748–750, 1966. doi: 10.1103/PhysRevLett.16.748.

[66] G.T. Zatsepin and V.A. Kuzmin. Upper limit of the spectrum of cosmic rays. *JETP Lett.*, 4:78–80, 1966.

[67] A. Aab et al. Observation of a Large-scale Anisotropy in the Arrival Directions of Cosmic Rays above 8×10^{18} eV. *Science*, 357(6537):1266–1270, 2017. doi: 10.1126/science.aan4338.

[68] A. Aab et al. Large-scale cosmic-ray anisotropies above 4 EeV measured by the Pierre Auger Observatory. *Astrophys. J.*, 868(1):4, 2018. doi: 10.3847/1538-4357/aae689.

[69] A. Aab et al. Large-scale cosmic-ray anisotropies above 4 EeV measured by the pierre auger observatory. *The Astrophysical Journal*, 868(1):4, nov 2018. doi: 10.3847/1538-4357/aae689.

[70] L. Caccianiga. Anisotropies of the Highest Energy Cosmic-ray Events Recorded by the Pierre Auger Observatory in 15 years of Operation. *PoS*, ICRC2019:206, 2019. doi: 10.22323/1.358.0206.

[71] K. Kawata et al. Updated Results on the UHECR Hotspot Observed by the Telescope Array Experiment. In *36th International Cosmic Ray Conference (ICRC2019)*, volume 36 of *International Cosmic Ray Conference*, page 310, July 2019.

[72] T. Pierog et al. EPOS LHC: Test of collective hadronization with data measured at the CERN Large Hadron Collider. *Phys. Rev. C*, 92(3):034906, 2015. doi: 10.1103/PhysRevC.92.034906.

[73] F. Riehn et al. A new version of the event generator sibyll, 2015.

[74] F. Riehn et al. Hadronic interaction model sibyll 2.3d and extensive air showers. *Physical Review D*, 102(6), Sep 2020. ISSN 2470-0029. doi: 10.1103/physrevd.102.063002.

[75] S. Ostapchenko. Monte carlo treatment of hadronic interactions in enhanced pomeron scheme: Qgsjet-ii model. *Physical Review D*, 83(1), Jan 2011. ISSN 1550-2368. doi: 10.1103/physrevd.83.014018.

[76] S. Ostapchenko. Qgsjet-ii: physics, recent improvements, and results for air showers. *EPJ Web of Conferences*, 52:02001, 2013. doi: 10.1051/epjconf/20125202001.

[77] A. Aab et al. Deep-learning based reconstruction of the shower maximum x max using the water-cherenkov detectors of the pierre auger observatory. *Journal of Instrumentation*, 16(07):P07019, Jul 2021. ISSN 1748-0221. doi: 10.1088/1748-0221/16/07/p07019.

[78] I. Allekotte et al. The Surface Detector System of the Pierre Auger Observatory. *Nucl. Instrum. Meth.*, A586:409–420, 2008. doi: 10.1016/j.nima.2007.12.016.

[79] X. Bertou et al. Calibration of the surface array of the pierre auger observatory. *Nuclear Instruments and Methods in Physics Research Section A: Accelerators, Spectrometers, Detectors and Associated Equipment*, 568(2):839846, Dec 2006. ISSN 0168-9002. doi: 10.1016/j.nima.2006.07.066.

[80] J. Abraham et al. Trigger and aperture of the surface detector array of the pierre auger observatory. *Nuclear Instruments and Methods in Physics Research Section A: Accelerators, Spectrometers, Detectors and Associated Equipment*, 613(1):2939, Jan 2010. ISSN 0168-9002. doi: 10.1016/j.nima.2009.11.018.

[81] C. Meurer and N. Scharf. Heat a low energy enhancement of the pierre auger observatory. *Astrophysics and Space Sciences Transactions*, 7(2):183186, May 2011. ISSN 1810-6536. doi: 10.5194/astra-7-183-2011.

[82] J. Abraham et al. The Fluorescence Detector of the Pierre Auger Observatory. *Nucl. Instrum. Meth.*, A620:227–251, 2010. doi: 10.1016/j.nima.2010.04.023.

[83] A. Aab et al. Spectral calibration of the fluorescence telescopes of the pierre auger observatory. *Astroparticle Physics*, 95:4456, Oct 2017. ISSN 0927-6505. doi: 10.1016/j.astropartphys.2017.09.001.

[84] R. Knapik et al. The absolute, relative and multi-wavelength calibration of the pierre auger observatory fluorescence detectors, 2007.

[85] P. Abreu et al. The rapid atmospheric monitoring system of the pierre auger observatory. *Journal of Instrumentation*, 7(09):P09001–P09001, sep 2012. doi: 10.1088/1748-0221/7/09/p09001.

[86] V.M. Harvey. Real-Time Measurements with Atmospheric Instruments at the Pierre Auger Observatory. *PoS*, ICRC2019:283, 2021. doi: 10.22323/1.358.0283.

[87] B. Fick et al. The central laser facility at the pierre auger observatory. *Journal of Instrumentation*, 1(11):P11003–P11003, nov 2006. doi: 10.1088/1748-0221/1/11/p11003.

[88] P. Abreu et al. Identifying clouds over the pierre auger observatory using infrared satellite data. *Astroparticle Physics*, 50-52:92101, Dec 2013. ISSN 0927-6505. doi: 10.1016/j.astropartphys.2013.09.004.

[89] P. Abreu et al. Description of atmospheric conditions at the pierre auger observatory using the global data assimilation system (gdas). *Astroparticle Physics*, 35(9):591607, Apr 2012. ISSN 0927-6505. doi: 10.1016/j.astropartphys.2011.12.002.

[90] S. Argir, S.L.C. Barroso, J. Gonzalez, L. Nellen, T. Paul, T.A. Porter, L. Prado Jr., M. Roth, R. Ulrich, and D. Veberi. The offline software framework of the pierre auger observatory. *Nuclear Instruments and Methods in Physics Research Section A: Accelerators, Spectrometers, Detectors and Associated Equipment*, 580(3):14851496, Oct 2007. ISSN 0168-9002. doi: 10.1016/j.nima.2007.07.010.

[91] A. Aab et al. Reconstruction of events recorded with the surface detector of the pierre auger observatory. *Journal of Instrumentation*, 15(10):P10021–P10021, oct 2020. doi: 10.1088/1748-0221/15/10/p10021.

[92] K. Kamata and J. Nishimura. The Lateral and the Angular Structure Functions of Electron Showers. *Progress of Theoretical Physics Supplement*, 6:93–155, 02 1958. ISSN 0375-9687. doi: 10.1143/PTPS.6.93.

[93] K Greisen. Cosmic ray showers. *Annual Review of Nuclear Science*, 10(1):63–108, 1960. doi: 10.1146/annurev.ns.10.120160.000431.

[94] D. Kuempel, K. H. Kampert, and M. Risse. Geometry reconstruction of fluorescence detectors revisited, 2007.

[95] A. Aab et al. Measurement of the average shape of longitudinal profiles of cosmic-ray air showers at the pierre auger observatory. *Journal of Cosmology and Astroparticle Physics*, 2019(03):018018, Mar 2019. ISSN 1475-7516. doi: 10.1088/1475-7516/2019/03/018.

[96] A. Aab et al. Reconstruction of inclined air showers detected with the pierre auger observatory. *Journal of Cosmology and Astroparticle Physics*, 2014(08):019019, Aug 2014. ISSN 1475-7516. doi: 10.1088/1475-7516/2014/08/019.

[97] B. Dawson. The Energy Scale of the Pierre Auger Observatory. *PoS*, ICRC2019:231, 2019. doi: 10.22323/1.358.0231.

[98] A. Castellina. Augerprime: the pierre auger observatory upgrade. *EPJ Web of Conferences*, 210:06002, 2019. ISSN 2100-014X. doi: 10.1051/epjconf/201921006002.

[99] A. Aab et al. Muon counting using silicon photomultipliers in the AMIGA detector of the pierre auger observatory. *Journal of Instrumentation*, 12(03):P03002–P03002, mar 2017. doi: 10.1088/1748-0221/12/03/p03002.

[100] A. Aab et al. Observation of inclined eev air showers with the radio detector of the pierre auger observatory. *Journal of Cosmology and Astroparticle Physics*, 2018(10):026026, Oct 2018. ISSN 1475-7516. doi: 10.1088/1475-7516/2018/10/026.

[101] B. Pont. A Large Radio Detector at the Pierre Auger Observatory - Measuring the Properties of Cosmic Rays up to the Highest Energies. *PoS*, ICRC2019:395, 2021. doi: 10.22323/1.358.0395.

[102] C.J. Todero Peixoto. Estimating the Depth of Shower Maximum using the Surface Detectors of the Pierre Auger Observatory. *PoS*, ICRC2019:440, 2019. doi: 10.22323/1.358.0440.

[103] M. Fukushima et al. Telescope array project for extremely high energy cosmic rays. *Prog.Theor.Phys.Suppl.*, 151:206–210, 2003. doi: 10.1143/PTPS.151.206.

[104] T. Abu-Zayyad et al. The surface detector array of the Telescope Array experiment. *Nucl. Instrum. Meth.*, A689:87–97, 2012. doi: 10.1016/j.nima.2012.05.079.

[105] H. Tokuno, Y. Tameda, M. Takeda, K. Kadota, D. Ikeda, et al. New air fluorescence detectors employed in the Telescope Array experiment. *Nucl. Instrum. Meth.*, A676: 54–65, 2012. doi: 10.1016/j.nima.2012.02.044.

[106] A. Aab et al. The Pierre Auger Observatory: Contributions to the 36th International Cosmic Ray Conference (ICRC 2019). *PoS (ICRC 2019)*, 2019.

[107] A. Aab et al. Inferences on mass composition and tests of hadronic interactions from 0.3 to 100 EeV using the water-Cherenkov detectors of the Pierre Auger Observatory. *Phys. Rev.*, D96(12):122003, 2017. doi: 10.1103/PhysRevD.96.122003.

[108] J. Biteau et al. Covering the celestial sphere at ultra-high energies. *EPJ Web Conf.*, 210:01005, 2019.

[109] T. Fujii et al. Detection of ultra-high energy cosmic ray showers with a single-pixel fluorescence telescope. *Astropart. Phys.*, 74:64–72, 2016. doi: 10.1016/j.astropartphys.2015.10.006.

[110] D. Mandat et al. The prototype opto-mechanical system for the fluorescence detector array of single-pixel telescopes. *Journal of Instrumentation*, 12(07):T07001, 2017.

[111] R. Abbasi et al. Calibration and Characterization of the IceCube Photomultiplier Tube. *Nucl. Instrum. Meth.*, A618:139–152, 2010. doi: 10.1016/j.nima.2010.03.102.

[112] K. Yamazaki et al. Calibration for the Telescope Array Fluorescence Detector using Portable UV Laser System. *Proc. of the 33th International Cosmic Ray Conference, Rio de Janeiro, Brazil (2013)*, ID0526.

[113] T. AbuZayyad. Analysis of atmospheric attenuation using the telescope array central laser data. *EPJ Web Conf.*, 197:01003, 2019. doi: 10.1051/epjconf/201919701003.

[114] A. Bucholtz. Rayleigh-scattering calculations for the terrestrial atmosphere. *Applied Optics*, 34(15):2765–2773, 1995.

[115] S.Y. BenZvi et al. Measurement of the aerosol phase function at the Pierre Auger Observatory. *Astroparticle Physics*, 28(3):312–320, 2007.